Università degli Studi di Roma *"La Sapienza"*

Dipartimento di Meccanica e Aeronautica

Dottorato di Ricerca in Meccanica Teorica e Applicata
XX ciclo

Ph.D. Thesis

Modeling of ablation phenomena in space applications

Daniele Bianchi

Supervisor: Prof. M. Onofri

2006/2007

Contents

Introduction

"...re-entry...is perhaps one of the most difficult problems one can imagine...It is certainly a problem that constitutes a challenge to the best brains working in these domains of modern aerophysics...possible means [include] mass transfer cooling, consisting of a coating that sublimates or chemically dissociates..."

-Theodore von Karman

Hypersonic aerodynamic heating

The matter of aerodynamic heating is an extremely important aspect of hypersonic vehicle design and the understanding and accurate prediction of surface heat flux is a vital part of the study and design of a hypersonic vehicle. The kinetic energy of a high-speed, hypersonic flow is dissipated by friction inside the boundary-layer. The viscous dissipation that occurs within hypersonic boundary-layers can produce very high heat-transfer rates to the surface. The surface itself must be designed in order to sustain the heat flux without collapsing and to prevent the heat load from damaging the underlying structure. Therefore surface heat transfer is usually one of the dominant aspect that drives the design of hypersonic vehicles and also of rocket nozzles. To understand why the aerodynamic heating becomes so large at hypersonic speeds, we can derive some useful relations from the flat plate theory.

The local heat-transfer coefficient can be expressed by any one of the several defined parameters, such as the *Stanton* number C_h defined as follows:

$$C_h = \frac{q_w}{\rho_e u_e (h_{aw} - h_w)} \tag{1}$$

where q_w is the heat transfer (energy per second per unit area) into the wall, h_{aw} and h_w are the adiabatic wall enthalpy and the wall enthalpy, respectively, and the subscript e denotes local properties at the outer edge of the boundary layer. If we consider the case of a flat plate parallel to the flow, these local properties are

simply freestream values, namely ρ_∞ and u_∞. The wall heat flux is therefore:

$$q_w = \rho_\infty u_\infty C_h (h_{aw} - h_w) \tag{2}$$

Assuming for simplicity a recovery factor of unity, the adiabatic wall enthalpy has the following expression:

$$h_{aw} = h_0 = h_\infty + \frac{u_\infty^2}{2} \tag{3}$$

where h_0 is the total enthalpy of the flow. Since at hypersonic speeds ${u_\infty}^2/2$ is much larger than h_∞, from (3) we obtain:

$$h_{aw} \approx \frac{u_\infty^2}{2} \tag{4}$$

Moreover, even if the surface temperature can be high in this kind of application, it is still limited by the material itself, i.e. it cannot exceed the melting or failing temperature of the protection material. Hence, the surface enthalpy h_0 is usually much smaller than h_0 at hypersonic speeds. That is, using also (4):

$$(h_{aw} - h_w) \approx h_{aw} \approx \frac{u_\infty^2}{2} \tag{5}$$

Substituting Eq. (5) into (2) we obtain the approximate relation:

$$q_w \approx \frac{1}{2} \rho_\infty u_\infty^3 C_h \tag{6}$$

The main purpose of Eq. (6) is to demonstrate that aerodynamic heating increases with the cube of flight velocity and hence increases very rapidly in the hypersonic flight regime, such is the case of an atmospheric reentry. By comparison, aerodynamic drag is given by:

$$D = \frac{1}{2} \rho_\infty u_\infty^2 S C_D \tag{7}$$

Hence, at hypersonic speeds, aerodynamic heating increasing much more rapidly with velocity than drag, and this is the primary reason why aerodynamic heating is a dominant aspect of hypersonic vehicle design.

Early Reentry Vehicles: Blunt Bodies and Ablatives

Although various people, including Wernher von Braun and other experts, had studied spaceflight during the 1940's nobody began thinking about how a vehicle

would actually return from space until the early 1950's. The few who did, like von Braun, realized that probably the best way to do it was to build a very big vehicle and circulate a fluid through its skin to soak up the heat of reentry. Clearly the problem of reentry to Earth's atmosphere was a significant challenge for the early spaceflight researchers, as they considered how best to overcome the heat generated by friction. However, not all reentry vehicles were spacecraft such as the atomic warheads launched atop ballistic missiles. They would fly up in a cannonball arc above most of the atmosphere and then come back through it at around 20 times the speed of sound, heating up tremendously.

Early research on missile reentry vehicles during the 1950's focused upon long, needle-like designs. When tested in wind tunnels, so much heat was transferred to these vehicles that they burned up. Scientist H. Julian Allen at the Ames Aeronautical Laboratory made a rather counter-intuitive discovery in 1952: he found that by increasing the drag of the vehicle, he could reduce the heat it generated. Much of the heat of reentry was actually deflected away from the vehicle. The best designs were what Allen and another scientist, Alfred J. Eggers, called "blunt-body" designs. Instead of needle-noses, they had blunt noses that formed a thick shock wave ahead of the vehicle that both deflected the heat and slowed it more quickly, thereby protecting the vehicle.

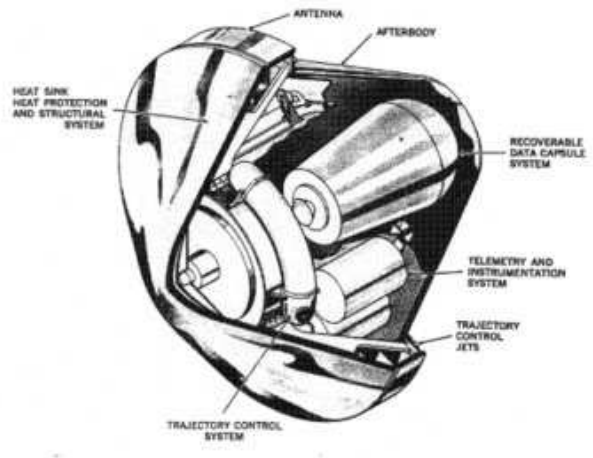

Figure 1: Prototype version of the Mk-2 reentry vehicle (RV).

Based upon this research, in 1955 General Electric (GE) engineers began work on the Mark 2 reentry vehicle (see Figure 1) for the Thor, Jupiter and Atlas missiles. The Mark 2 was a blunt body design. Much of the heat was deflected away from the vehicle via the shock wave. But some heat still reached the surface through the superheated air that formed in front of the vehicle. Getting rid of this

excess heat was a problem. GE decided to use the heat-sink concept, whereby the heat of reentry was conducted from the surface of the vehicle to a mass of material that could soak it up quickly. The key was to conduct the heat away from the surface fast enough so that the surface material itself did not melt. GE's engineers tested several materials as heat-sinks, including beryllium, cast iron, and steel. But the best proved to be copper. By putting a big mass of copper just below the outer shell of the vehicle they could prevent the craft from burning up. Figure 2 shows the copper heat sink of the intercontinental ballistic missile. A 1000 pound, copper-clad 316 stainless steel shell was manufactured by electroforming, possessing an outer skin of nickel and a reflective platinum final surface. The design was the precursor for the manned Mercury flights with beryllium heat sinks and the subsequent Gemini and Apollo flights, which had head shields instead of heat sinks, but the same blunt shapes.

Figure 2: The copper heat sink of the intercontinental ballistic missile (ICBM).

The Mark 2 had what was called a low ballistic coefficient, or *beta*. The ballistic coefficient was a calculation of weight, drag and cross-section. Vehicles with a high beta, usually slender and smoother and with less drag, travelled through the upper atmosphere without decelerating much and did most of their slowing down in the thick-lower atmosphere. They took longer to slow down and generated less heat, but experienced this heat over a longer period of time. GE's Mark 2 had a low beta. It was a flattened cone on its leading edge. It spent a lot of time in the upper atmosphere, trailing a stream of ionized gas that showed up on radar, which was not good for a warhead. Although this design was adequate, it was not ideal. What ballistic missile designers wanted was a vehicle that travelled as fast

as possible through the atmosphere so that it could not be intercepted. A high-beta vehicle was the best choice. GE engineers doubted that heat-sink technology would work for a high-beta vehicle. In addition, the heat-sink concept was heavy and the copper took up valuable payload weight.

The heat-sink's drawbacks became even more apparent when it was considered for a space vehicle. First, a space vehicle would reenter at a faster velocity than a ballistic missile and so it would get much hotter that the missile, requiring more copper, and perhaps other means of transferring the heat away from the surface. In addition, all that weight was prohibitive. Even worse, the extra-weight had cascading effects. Not only would all that copper require more fuel to get it into orbit, but it would require more fuel to get it out of orbit. An even bigger problem was the high-temperature reached by the heat-sink itself, which could be sustained by a warhead but not by a human being. A reentry at much higher velocities was needed for a lunar mission, but the metal composite heat-sink would vaporize like a meteor. The aerodynamicist's answer from experiments with gas guns and theoretical calculations was the concept of ablation by vaporizing a protection material as the thermal barrier. This was the heat shield concept in opposition to the heat-sink concept.

By the mid-1950's, GE engineers were designing lightweight, medium-beta, reentry vehicles for missile warheads. GE engineers evaluated several different concepts. One was transpirational cooling, which essentially boiled off a liquid, using the change from liquid to gas to take away the heat. Another was re-radiation, whereby the heat would be radiated away from the vehicle. Another proposal was liquid metal cooling, whereby a liquid metal, such as mercury, was circulated through the heat shield and conducted the heat away very efficiently. But the most promising proposal was a technique called ablation. By 1956, some researchers were noting that reinforced plastics had proven more resistant to heating than most other materials. They proposed using these plastics in the inlets of supersonic cruise missiles. GE engineers realized that they could use this same technique for reentry. They could coat the vehicle with a material that absorbed heat, charred, and either flaked off or vaporized. As it did so, it took away the absorbed heat.

The ablation technique worked for both spacecraft and ballistic missile requirements, for low and high-beta reentry vehicles. Ablation reduced temperatures. A blunt body, low-beta reentry vehicle returning from space could keep the external temperature relatively low. Ablative material on the vehicle would lower this temperature even further. A streamlined, high-beta missile warhead, however, would experience much higher heating for shorter periods of time. But ablation could also reduce this temperature as well, so that a missile warhead could reenter very fast and minimize its chance of interception, keeping cool by burning off layers a special plastic. The key was selecting the right material. Ultimately, they

decided upon a phenolic resin plastic. They decided to use a nylon cloth impregnated with the phenolic resin and molded into the needed shape. Eventually, this and similar materials were used to coat the surfaces of nuclear missiles warheads.

Figure 3: Mercury spacecraft ablative heat shield after recovery.

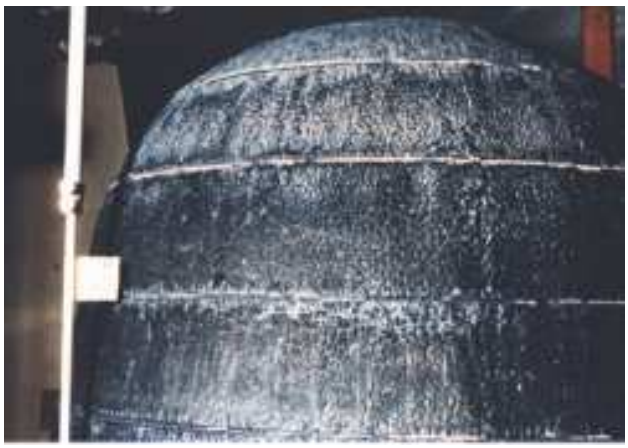

Figure 4: Charred ablative heat shield from the first KH-4 Corona mission.

The first Mercury spacecraft used a blunt body design and a heat sink, but later versions used the blunt body design and an ablative surface (see Figure 3). GE built an ablative semi-blunt (slightly rounded) reentry vehicle for Air Force and CIA Discoverer/CORONA spacecraft (see Figure 4), which returned film from

spy satellites. Other companies, such as AVCO, also developed ablative reentry vehicles for missiles. Blunt body designs and improved ablative materials were also used on the Gemini and Apollo spacecraft, advancing rapidly during 1960's. By the end of the decade, other technologies and techniques for surviving the tremendous heating of atmospheric reentry were developed.

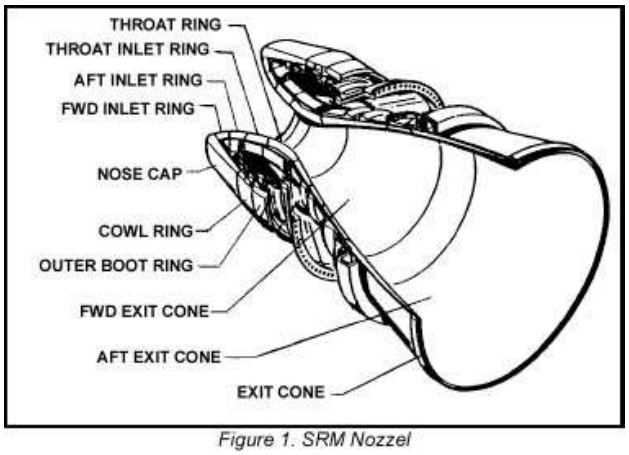

Figure 1. SRM Nozzel

Figure 5: SRM nozzle structure.

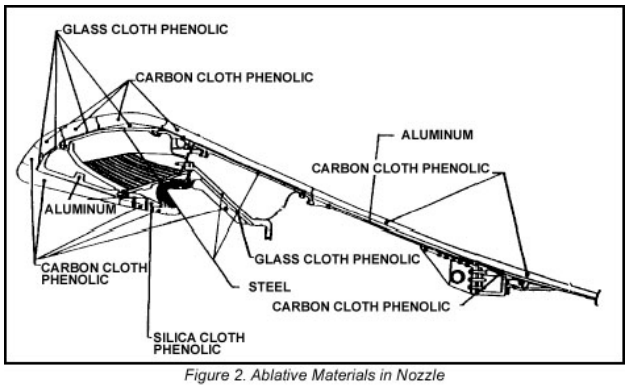

Figure 2. Ablative Materials in Nozzle

Figure 6: Ablative materials in SRM nozzles.

Ablation is affected by the freestream conditions, the geometry of the reentry body, and the surface material. Ablation occurs during the reentry of planetary expeditions or of ballistic projectiles and it occurs inside the nozzles of solid propellant rocket motors. Reentry vehicles range from blunt configurations, such as the Apollo spacecraft, to slender sphere-cone projectiles. For low heating levels,

low-temperature ablators such as teflon are used and for more demanding reentry conditions, graphites and carbon-based materials are often used.

Graphitic materials have received much attention in the last decades for application to both planetary entry probe heat shields and ballistic missile nose tip and heat shields. Ablation of graphite on atmospheric reentry continues to be actively studied, both to achieve greater fidelity of simulation and to support new concepts. Moreover carbon/carbon composites and other graphitic materials have found increasing use in the manufacture of nozzles for solid-propellant rocket motors (see Figures 5 and 6) because of their high-temperature resistance, excellent thermal and physical properties as well as low densities. In this work, graphite was selected as the ablative material.

Ablative materials

Upon exposure to ballistic reentry and rocket nozzle environments, heat-protection materials are subjected to severe thermal and mechanical conditions. Various thermal protection systems (heat sink, transpiration cooling, ablation) have been proposed and investigated quite extensively, especially from the experimental viewpoint. Among them, ablative thermal protection systems (TPS), which are characterized by the sacrificial removal of the surface material for the protection of the underlying structure, have been widely applied to reentry vehicles and solid rocket nozzles. Ablative TPS must be designed to keep the excessive heat from damaging the vehicle or its contents with a minimum weight penalty.

The thermochemical response of ablation materials to high-temperature chemically active flows has been the subject of numerous theoretical and experimental investigations. A principal goal of most of these studies has been the formulation of a rational material selection process for particular imposed (or proposed) missions. In general, investigations have been characterized by the type of ablation material and the environment to which exposure is considered. The four principal material categories are (1) high-temperature, chemically homogeneous materials which are consumed as a combined result of chemical attack and sublimation at the exposed surface (e.g., graphite), (2) composite ablation materials which decompose in depth to form a high-temperature char layer, (3) inorganic glassy materials, such as quartz and silica, which ablate due to the combined effect of vaporization, chemical reactions, and liquid removal, and (4) low-temperature organic ablators such as teflon. The environments considered include those resulting from ballistic or manned entry into the earth or other planet's atmosphere and solid (typically) or liquid rocket propellant combustion. Chemical reactions play a significant, if not dominant, role in establishing the ablation and energy transfer rates at the heated surface of most of the resultant material-environment

combinations. Principal emphasis is usually directed toward the first two material types, which are often referred to as *non-charring* and *charring* ablators, because of their relatively greater role in space exploration and space propulsive applications. The *Charring* materials are made of a filler (usually a resin) and a reinforcing material (usually carbon). When heated, the resin experiences a series of chemical reactions that release gaseous by products (pyrolysis) leaving a layer of *char* or residue. Gas pressure in the pyrolysis zone forces the pyrolysis gas to flow through the *char* into the boundary layer. The *char* itself can recede due to chemical or mechanical action by the boundary layer. For a *non-charring* ablator (such as carbon-carbon), instead, mass loss occurs only by surface ablation and mechanical erosion. Pyrolysis is an internal decomposition of the solid which releases gaseous species, whereas ablation is a combination of processes (thermo-chemical and/or mechanical) which consume the heat-shield surface material. Both the *charring* and *non-charring* ablators sacrifice some TPS material to divert the energy that would otherwise enter the vehicle.

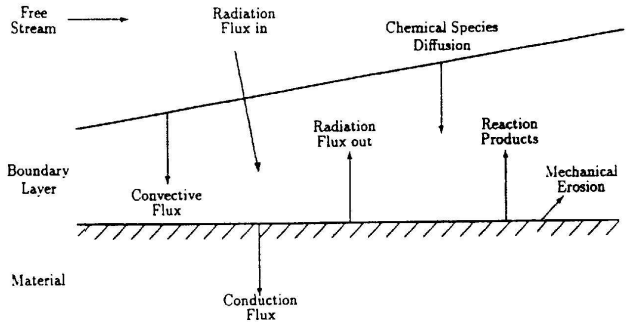

Figure 7: Energy fluxes over an ablating surface.

Figure 7 illustrates the general physico-chemical interactions between an ablating wall and the boundary-layer. The boundary-layer can heat up the surface due to convection and radiation from the hot-gases. Moreover, due to the presence of chemical reactions at wall, there are gradients of concentrations inside the boundary-layer. These concentration gradients generate a net heat flux due to species diffusion. The heat flux toward the surface is partly convected inside the material and partly re-radiated from the hot surface[1]. The chemical reactions between the solid TPS wall and the boundary-layer generate gaseous products which are injected in the boundary-layer. The chemical reactions are typically endothermic and absorb part of the incident heat; moreover, the injection of ablation product (the so-called “blowing”) produces a cooling of the boundary-layer

[1]which can reach temperatures over $3000\ K$.

and therefore reduce the convective heat flux to the wall. For strong blowing, the reduction of convective heat flux (the so-called “blockage effect”) is the primary mean to reduce the energy transmitted to the underlying structure. The friction forces at wall can also produce a mechanical erosion of the surface (called “spallation”). In this case, fragments of material are ejected from the TPS due to impact or stress. Since this phenomena is highly inefficient, TPS materials are usually reinforced in order to withstand the high thermo-mechanical stresses caused by the external environment.

The analysis of this work is directed toward the general characterization of thermo-chemical interaction between a non-charring ablation material (carbon-carbon or graphite) and its environment of arbitrary chemical composition. The ablation model considered is based on thermo-chemical ablation. Thermo mechanical ablation or spallation is neglected in this work because many researchers [11, 21, 31, 37, 45, 63] have concluded that the thermo-chemical erosion of graphite is the primary reason for the TPS recession.

CFD methods for ablating systems

Heatshields of spacecraft for planetary missions typically use thermal protection system (TPS) materials which ablate at high temperature for mass-efficient rejection of aerothermal heat load. A reliable numerical procedure that can compute surface recession rate, mass loss, surface heat flux, and internal temperature time-histories under general heating conditions is essential for the design and sizing of ablating spacecraft TPS materials.

An accurate prediction of the thermal response of TPS materials is essential to successfully carry out the design of an optimum TPS. In recent years, computational fluid dynamics (CFD) technology has continued to develop in the areas of non-equilibrium flow, multispecies kinetics, and multidimensional full Navier-Stokes capabilities. However, most codes uses primitive surface boundary conditions and cannot be realistically used to predict the aerothermal heating for the design of TPS [51]. In fact, CFD codes typically treat fluid/solid boundary conditions in a simplified manner and mass transfer is often not considered. Current methods focus their attention on some aspects of the problem at the expense of others [39, 18]. Thus aerodynamic methods concentrate on the flowfield, and rely on other methods to provide material-response characteristics; on the other hand, material-response methods concentrate on surface ablation and heat conduction in the material, using simplified models to provide the aerothermodynamic heating. However, in reality all these phenomena are highly coupled. Moreover, the heat flux to the ablating surface is often computed based on the input non-ablating heat-transfer coefficients and empirical blowing-reduction parameters to account

for the blockage effect from ablation products [32]. The uncertainty in this estimated ablating surface heat flux is high, and the predictions of surface blowing rate and temperature can be inaccurate and consequently less reliable. Thus, in order to improve estimating of the heat flux over an ablating surface, a flow solver coupled with ablating surface conditions becomes a requirement. This goal can be achieved by considering that the surface energy and mass balances, coupled with an ablation model, provide complete thermochemical boundary conditions for a solution of the fully coupled fluid-dynamics/solid-mechanics problem [15].

In this study, a general surface boundary condition with mass and energy balance coupled with a surface thermochemistry ablation model is developed for equilibrium gas states adjacent to a *non-charring* (graphite) ablating surface. Based on this formulation, a surface thermochemistry procedure is developed and integrated with a Navier-Stokes solver.

Structure of the work

The work presented in this doctorate thesis represents the synthesis of the research activities carried out by the author, during last years, at the Department of Mechanics and Aeronautics of the University of Rome “La Sapienza”; results and proceedings of these activities have also been presented in international meetings and conferences [7, 8, 9].

The aim of this work is to present the formulation of a detailed physical-mathematical model, and its numerical solution, for the analysis of the high-temperature flow over a *non-charring* (graphite) ablating surface. As previously mentioned, most flow solvers use simple surface boundary conditions and cannot be realistically used to simulate the flowfield over ablating surfaces. The general boundary conditions should include appropriate energy and multi-species mass balances together with a surface ablation model. However, rarely the available Navier-Stokes solvers include complete boundary conditions to realistically determine aerothermal heating and surface ablation rates. For aerothermal heating predictions over ablating TPS, some CFD codes have been developed [63] with surface mass and energy balances. Even when full Navier-Stokes approaches are used, a film-transfer theory (based on bulk boundary-layer transfer-coefficients) is often adopted to couple flow and material solutions via the surface mass and energy balances [15, 16, 63, 39]. In this work, efforts have been made in order to completely remove the thin-film theory assumption thus avoiding all of the problems and inaccuracies associated with the approximation of transfer coefficients.

The main objective is therefore to develop an accurate theoretical/mathematical model to describe the complex fluid-surface interactions and to numerically integrate it with a Navier-Stokes flow solver. The presentation of the work is orga-

nized in two parts:

1. **The first part** deals with the analysis of the transient thermal response of a graphitic TPS material exposed to a high temperature environment. The basic problem is to predict the temperature history inside the material exposed to some defined environment which supplies heat and which may chemically erode the material surface. The transient material response is dependent on the chemically reacting boundary-layer flow adjacent to the surface, and vice versa. In this part, heat and mass transfer-coefficients are employed to represent boundary-layer mass/energy transfer phenomena at the ablating surface. The transfer coefficient approaches have proven to be very useful for correlating theoretical as well as experimental results and have been used extensively in the reentry aerothermodynamics community. This simplified method has the advantage to have a reduced computational cost and is the most widely used engineering approach for predicting ablation.

    - ***Chapter 1*** is dedicated to the description of the physical and mathematical model developed to simulate the transient thermal response of the TPS material. A one dimensional model is assumed.
    - ***Chapter 2*** deals with the numerical technique adopted for the in-depth computation as well as the computational strategy for obtaining the coupled solution. Numerical results are also presented.

2. **The second part** deals with the full Navier-Stokes computation of surface ablation; such a computation requires detailed knowledge of complex interactions between the solid surface and the ambient gas. This is expected to be computationally intensive because a large number of chemical species and reactions must be simulated. However, because CPU technologies are significantly improved on an ongoing basis, hardware limitations may no longer be a concern. The purpose of this part, which represents the core of this work, is to obtain the full Navier-Stokes solutions with surface ablation conditions for carbon-carbon materials, to perform parametric studies to understand their performance, and to compare the results with simpler approaches. Because the entire flowfield is to be solved, the thin-film theory assumption made in the first part is no longer needed, and all of the problems associated with the approximation of transfer-coefficients are avoided.

    - ***Chapter 3*** is dedicated to the description of the thermodynamic model adopted in the flow solver.
    - ***Chapter 4*** deals with the description of the mathematical model and numerical method for the Navier-Stokes solver.

- ***Chapter 5*** is dedicated to the description of the ablation model and the surface boundary conditions based on mass and energy balances at the ablating wall.
- ***Chapter 6*** is dedicated to the presentation and the discussion of the results obtained by means of the developed tool. Supersonic laminar solutions over flat plates with different environmental gases and boundary conditions are presented. Results are also compared with the most widely used CFD approaches for this type of flows.
- ***Chapter 7*** describes the study of the erosion of carbon/carbon nozzle material in solid rocket motor (SRM) environments. The tool developed is used to numerically simulate the hot-gas flow inside the nozzle taking into account the ablation process taking place at the nozzle wall.
- ***Chapter 8*** presents the conclusions of the work.

Part I

One-dimensional transient ablation

Chapter 1

Physical approach to the ablation problem

The transient thermal response of protective materials exposed to high-energy environments is a key issue to the design of internal thermal of rocket combustion chambers and nozzles or heat shield for reentry vehicles. The basic topic to investigate is the temperature history and distribution inside the protection material when submitted to heat transfer. The solid material is ablating, i.e. it absorbs heat by increasing its temperature and changing its chemical and physical state. The changes are usually accompanied by loss of surface material. This chapter deals with the analysis of the transient thermal response of a graphitic thermal protection material exposed to a high temperature environment. The basic problem is to predict the temperature history of a non-charring thermal protection material exposed to some defined environment which supplies heat and which may chemically erode the material surface. The general prediction problem may be divided into two parts:

- in-depth behaviour computation
- heated surface boundary condition specification

In order to compute the in-depth response of the protection material, a transient heat conduction calculation has to be performed; obviously the effect of surface recession and ablation has to be taken into account and a proper surface boundary condition has to be used.

1.1 Governing equations

Analysis of a complete transient non-charring material ablation problem necessarily involves a computation of the internal thermal response of the protection

material. This section presents the fundamental assumptions and equations involved in the in-depth solution.

The theoretical model is based on the fundamental equation that governs the physical events inside the protection material, i.e. the conservation of energy (essentially the Fourier equation with a source term coming from surface recession due to ablation). For the basic in-depth solution, it is assumed that thermal conduction is one-dimensional; however, the cross section area (perpendicular to the heat flux) is allowed to vary with depth in an arbitrary manner. This correspond to a thermal stream tube. Recent studies [20] have shown that one-dimensional treatments of the in-depth response of the ablative material are generally appropriate. The one-dimensional energy differential equation is readily formulated as:

$$\rho \left(\frac{\partial hA}{\partial t} \right)_y = \frac{\partial}{\partial y} \left(kA \frac{\partial T}{\partial y} \right) \tag{1.1}$$

where the y-frame is fixed to the initial solid surface (before recession starts) and thus time independent. In Eq. (1.1) ρ is the solid density, h the solid enthalpy, k the solid conductivity, T the solid temperature, and A the cross-section area. $(.)_x$ indicates derivatives taken in the fixed frame. The first term in Eq. (1.1) is the *transient* term and the second is the *diffusion* term.

1.2 Boundary conditions

Suitable boundary and initial conditions for the energy equation 1.1 may be readily formulated. The boundary conditions at the front and back faces of the TPS are usually surface energy balances. Of these, the front or ”active” surface is the most complex. Basically, the surface energy balance may be pictured as:

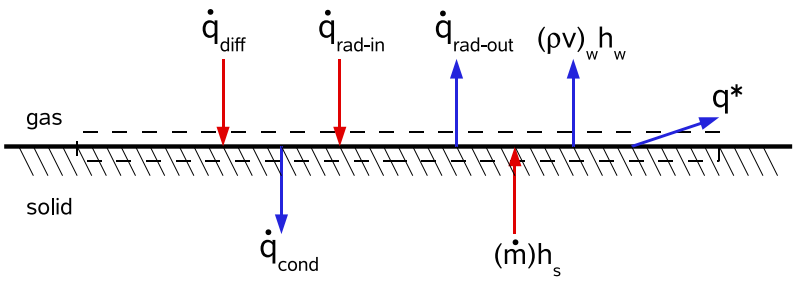

Figure 1.1: Heat fluxes over an ablating surface.

where the indicated control volume is fixed to the receding surface. Energy fluxes leaving the control volume include conduction into the material [q_{cond}], radiation away from the surface [$q_{rad_{out}}$], energy in any flow of condensed phase material such as liquid run-off and spallation [q^*], and gross blowing at the surface [$(\rho v)_w h_w$]. Energy inputs to the control volume include radiation in from the boundary layer [$q_{rad_{in}}$] and enthalpy fluxes due to solid material mass flow rates [$(\dot{m})h_s$]. The final input in the sketch is denoted [q_{diff}]. It includes all diffusive energy fluxes from the gas boundary layer. If the in-depth response computation is being coupled to an exact boundary layer solution, the term [q_{diff}] will be available directly as a single term (which is, of course, a complex function of many boundary layer properties). If, on the other hand, the in-depth response is being coupled to a simplified boundary layer scheme, such as a convective film coefficient model, then the term [q_{diff}] has a rather complicated appearance. The following sections contain a further discussion of this aspect of the total computation.

For the present, it suffices to note that computation of the surface energy balance requires the following information from the in-depth solution:

- a relation between the surface temperature and the rate of energy conducted into the material, q_{cond}

With this information the surface energy balance then determines the material consumption rate $\dot{m}$ and the surface temperature T_w. It will be useful to keep in mind that, from this point of view, the purpose of the in-depth solution at any instant is to provide information about $q_{cond}(T_w)$. In some circumstances, of course, it is of interest merely to specify the heated surface temperature T_w and surface recession rate $\dot{s} = \dot{m}/\rho$. In this case no surface energy balance is required.

It is usually of interest to have only one ablating surface. The back-wall or non-ablating wall boundary condition may be modelled with a film coefficient heat transfer equation.

1.3 Conservation of energy in moving coordinate system

Several approaches have been applied to simulate coupled ablation and conduction problems. Some efforts involve allowing the surface nodes to move, while holding the interior nodes fixed, and removing the surface nodes when they come near a neighbouring interior node [12]. Another one-dimensional approach, known as the Landau transformation [41], transforms the spatial coordinate over the thickness of the domain so that the transformed coordinate remains between zero and

one [10]. Other approaches utilize the concept of attaching a grid to the ablating surface [57], so that the nodal network is tied to the receding surface. The latter approach is adopted in this work which involves a transformation of the energy differential equation to a moving coordinate system and somewhat complicates the algebra of the difference equation modelled on this differential equation. Disposing of nodes from the front surface, however, often leads to undesirable oscillations. It is therefore convenient to base the difference formulation on a nodal network fixed to the heated surface. Since the surface will be receding, material will appear to flow into and out of the nodes. The energy differential equation presented in Eq. (1.1) thus requires a transformation to a moving coordinate system to include this aspect of the problem and to provide the proper model for differencing (described in the next chapter).

The energy equation is written first with respect to a spatially fixed coordinate system (y), for this purpose, the following functional relationships holds:

$$\begin{aligned} h &= h(T) \\ T &= T(y,t) \\ A &= A(y) \\ s &= s(t) \end{aligned}$$

where s is the amount of surface recession. The moving coordinate system (x) and the fixed coordinate system (y) are related to s by the following relation:

$$y = s + x \tag{1.2}$$

from which:

$$\left.\frac{\partial y}{\partial t}\right|_x = \frac{\partial s}{\partial t} = \dot{s} \tag{1.3}$$

The differential equation governing the conservation of energy within the solid was cited as Eq. (1.1):

$$\underbrace{\rho\left(\frac{\partial hA}{\partial t}\right)_y}_{storage} = \underbrace{\frac{\partial}{\partial y}\left(kA\frac{\partial T}{\partial y}\right)_t}_{conduction} \tag{1.4}$$

To transform the above differential equation, which is written for a point $y = constant$, to an equation written for the moving coordinate system, $x = constant$,

the storage term in the above equation may be related to its counterpart in the moving coordinate system by expanding the energy change employing the chain rule:

$$\begin{aligned} hA &= hA(y,t) \\ d(hA) &= \frac{\partial}{\partial y}(hA)_t dy + \frac{\partial}{\partial t}(hA)_y dt \end{aligned}$$

Differentiating partially with respect to time at constant x yields:

$$\frac{\partial}{\partial t}(hA)_x = \frac{\partial}{\partial y}(hA)_t \left.\frac{\partial y}{\partial t}\right|_x + \frac{\partial}{\partial t}(hA)_y$$

Introducing Eq. (1.3) and rearranging obtains:

$$\frac{\partial}{\partial t}(hA)_y = \frac{\partial}{\partial t}(hA)_x - \dot{s}\frac{\partial}{\partial y}(hA)_t \tag{1.5}$$

Substitution of Eq. (1.5) into Eq. (1.4) with the observation that partial differentiation with respect to x or y at constant time is equivalent, result in the transformed energy equation:

$$\underbrace{\rho\frac{\partial}{\partial t}(hA)_x}_{Term\ I} = \underbrace{\frac{\partial}{\partial x}\left(kA\frac{\partial T}{\partial x}\right)_t}_{Term\ II} + \underbrace{\rho\dot{s}\frac{\partial}{\partial x}(hA)_t}_{Term\ III} \tag{1.6}$$

The above terms will be considered separately below.

Term I

$$\frac{\partial}{\partial t}(hA)_x = h\left(\frac{\partial A}{\partial t}\right)_x + A\left(\frac{\partial h}{\partial t}\right)_x \tag{1.7}$$

It is convenient to express the enthalpy change rate in terms of temperature change rate so that the above equation may be written as follows:

$$\frac{\partial}{\partial t}(hA)_x = h\left(\frac{\partial A}{\partial t}\right)_x + Ac_p\left(\frac{\partial T}{\partial t}\right)_x \tag{1.8}$$

Term II

Term II in Eq. (1.6) will not require any modification.

Term III

For term III we have:

$$\rho\dot{s}\frac{\partial}{\partial x}(hA)_t = \rho\dot{s}h\left(\frac{\partial A}{\partial x}\right)_t + \rho\dot{s}A\left(\frac{\partial h}{\partial x}\right)_t \tag{1.9}$$

Now $A = A(y)$ alone, but $y = x + s$, and $s = s(t)$ alone, so we may write $A = A(x,t)$:

$$dA = \left(\frac{\partial A}{\partial x}\right)_t dx + \left(\frac{\partial A}{\partial t}\right)_x dt$$

Differentiating partially with respect to time at constant y obtains:

$$\left(\frac{\partial A}{\partial t}\right)_y = \left(\frac{\partial A}{\partial x}\right)_t \left(\frac{\partial x}{\partial t}\right)_y + \left(\frac{\partial A}{\partial t}\right)_x$$

But, since $A = A(y)$ alone, $\partial A/\partial t|_y = 0$. Also, since $y = x + s$:

$$\left(\frac{\partial x}{\partial t}\right)_y = -\frac{ds}{dt} = -\dot{s}$$

Combining the above results in:

$$\dot{s}\left(\frac{\partial A}{\partial x}\right)_t = \left(\frac{\partial A}{\partial t}\right)_x \tag{1.10}$$

Substituting Eq. (1.10) into (1.9) yields a new expression for Term III:

$$\rho\dot{s}\frac{\partial}{\partial x}(hA)_t = \rho h\left(\frac{\partial A}{\partial t}\right)_x + \rho\dot{s}A\left(\frac{\partial h}{\partial x}\right)_t \tag{1.11}$$

Substitution of Eqs. 1.8 and 1.11 into the energy differential equation 1.6 yields:

$$\rho c_p\left(\frac{\partial T}{\partial t}\right)_x = \frac{1}{A}\frac{\partial}{\partial x}\left(kA\frac{\partial T}{\partial x}\right)_t + \rho c_p\left(\frac{\partial T}{\partial x}\right)_t \dot{s} \tag{1.12}$$

The terms in equation Eqs. 1.12 represent, from left to right, the sensible energy accumulation, the net conduction, and the net energy convected as a consequence of coordinate motion. All terms are evaluated per unit volume. If the solid conductivity is constant with temperature then Eq. (1.12) simplifies to the following form:

$$\left(\frac{\partial T}{\partial t}\right)_x = \frac{1}{A}\alpha\frac{\partial}{\partial x}\left(A\frac{\partial T}{\partial x}\right)_t + \dot{s}\left(\frac{\partial T}{\partial x}\right)_t \tag{1.13}$$

where $\alpha = k/\rho c_p$ is the solid thermal diffusivity. If the cross section area A is also constant (planar surface), Eq. (1.12) assumes a still simpler form:

$$\left(\frac{\partial T}{\partial t}\right)_x = \alpha \left(\frac{\partial^2 T}{\partial x^2}\right)_t + \dot{s} \left(\frac{\partial T}{\partial x}\right)_t \tag{1.14}$$

The finite difference formulation of the above derived differential equation is presented in the next chapter.

1.4 Conservation equations for the chemically reacting boundary-layer

The purpose of this section is to present the relations governing the conservation of energy, mass, and chemical elements at the surface of an ablation material subjected to the thermochemical erosion of an external highly energetic environment. To consider the totality of the ablation process requires knowledge of:

1. The nature of the boundary-layer.
2. The in-depth response of the protection material.
3. The various surface balances which characterize the interface between the material and its environment.

In the developments presented here, the emphasis will be placed upon the surface balances. Because of the importance of the convective nature of the boundary-layer upon these balances, some initial discussion of the boundary-layer relations are presented. The boundary-layer equations are presented first, approximate correlation equations are then discussed and utilized to establish the equations for a coupled solution of a charring ablator to the boundary layer, and finally, in the next chapter, some results of the coupled solution are presented.

The boundary layer which envelops an ablating heat shield during super-orbital reentry is intimately coupled with the transient ablation processes. In addition:

- it may be laminar, transitional, or turbulent on different parts of the body and at various flight conditions.
- it may be highly non-similar, especially if there are changes of ablation materials.
- the surface material may react chemically with the environmental gas, change phase, and/or be removed mechanically by spallation or liquid-layer run-off.

- Chemical reactions will generally also occur throughout the boundary-layer.
- The homogeneous and heterogeneous reactions may be kinetically controlled.
- Incident radiant energy may be absorbed and emitted at different wave lengths.

To obtain a better basis for the consideration of mass and energy transfer to a wall, it is pertinent to consider the basic boundary-layer relations. In the present section, only the laminar boundary-layer is considered in detail. The laminar steady boundary-layer equations for two-dimensional flow can be expressed as:

- **Continuity**

$$\frac{\partial}{\partial x}(\rho u) + \frac{\partial}{\partial y}(\rho v) = 0 \tag{1.15}$$

- **Momentum**

$$\rho u \frac{\partial u}{\partial x} + \rho v \frac{\partial u}{\partial y} = -\frac{\partial p_e}{\partial x} + \frac{\partial}{\partial y}\left(\mu \frac{\partial u}{\partial y}\right) \tag{1.16}$$

- **Species**

$$\rho u \frac{\partial y_i}{\partial x} + \rho v \frac{\partial y_i}{\partial y} = -\frac{\partial j_i}{\partial y} + \dot{w}_i \tag{1.17}$$

- **Energy**

$$\rho u \frac{\partial h_0}{\partial x} + \rho v \frac{\partial h_0}{\partial y} = \frac{\partial}{\partial y}\left[\mu \frac{\partial (u^2/2)}{\partial y} + \frac{k}{c_p}\frac{\partial h}{\partial y} - \sum_i \left(j_i + \frac{k}{c_p}\frac{\partial y_i}{\partial y}\right) h_i\right] \tag{1.18}$$

- **Equation of state**

$$p = \rho \frac{\mathcal{R}}{\mathcal{M}} T \tag{1.19}$$

where $h_0 = \sum y_i h_i + u^2/2$ is the total enthalpy of the mixture, j_i is the diffusional mass flux of species i, and $\dot{w}_i$ is the mass generation of species i per unit volume as a result of chemical reaction. The diffusional mass flux of the i^{th} species can be expressed using the approximation of Fick's law:

$$\mathbf{j}_i = -\rho \mathcal{D}_{im} \nabla y_i \tag{1.20}$$

where $\mathcal{D}_{im}$ is the multicomponent diffusion coefficient.

By the very nature of a chemical reaction, the mass fractions of the individual species are altered in such a reaction, and this fact is indicated by the inhomogeneous chemical production term $\dot{w}_i$ appearing in the continuity equation for each species. However, the mass fractions of the individual chemical elements (independently of the chemical form in which they are found) are preserved in any chemical reaction[1], and these quantities are the natural counterparts of the total enthalpy in the energy equation (1.18). Let us consider the species conservation equation for chemical elements. This results directly from Eq. (1.17) upon application of the Shvab-Zeldovich transformation (multiplication by the mass of element k in species i, α_{ki}, and summation over all species) [43]:

$$\rho u \frac{\partial y_k}{\partial x} + \rho v \frac{\partial y_k}{\partial y} = -\frac{\partial}{\partial y} \sum_i \alpha_{ki} j_i \tag{1.21}$$

Note that the chemical source term $\dot{w}_i$ vanishes in the elemental approach. If the diffusion coefficient are equal, the continuity of each element Eq. (1.21) becomes:

$$\rho u \frac{\partial y_k}{\partial x} + \rho v \frac{\partial y_k}{\partial y} = \frac{\partial}{\partial y} \left(\rho \mathcal{D} \frac{\partial y_k}{\partial y} \right) \tag{1.22}$$

The y_k are often referred to as pseudo-mass fractions.

The number of independent conservational equations (Eqs. (1.16), (1.17), and (1.18)) is $N + 2$ where N is the number of molecular or ionic species present. The number of such species can be significant when chemically active ablating surfaces are involved. When diffusion coefficients are equal, the Shab-Zeldovich transformation will reduce the number of equations to $K + 2$, where K is the number of elements present in the system. In addition, the species production term is eliminated under this transformation.

The energy equation (1.18) can be expressed in a different form using the *Prandtl* and *Lewis* numbers:

$$\rho u \frac{\partial h_0}{\partial x} + \rho v \frac{\partial h_0}{\partial y} = \frac{\partial}{\partial y} \left(\frac{\mu}{Pr} \frac{\partial h_0}{\partial y} \right) + \frac{\partial}{\partial y} \left[\mu \left(1 - \frac{1}{Pr} \right) \frac{\partial}{\partial y} \frac{u^2}{2} \right] + \frac{\partial}{\partial y} \left[\rho \mathcal{D} \left(1 - \frac{1}{Le} \right) \sum_i h_i \frac{\partial y_i}{\partial y} \right] \tag{1.23}$$

where[2]

$$Pr = \frac{\mu c_p}{k} = \frac{\nu}{\alpha} \qquad Le = \frac{\rho \mathcal{D} c_p}{k} = \frac{\mathcal{D}}{\alpha}$$

[1] excluding nuclear transformations.

[2] note that the *Lewis* number is also referred to as $Le = k/\rho \mathcal{D} c_p$.

Looking at Eqs. (1.22) and (1.23), it is interesting to note that when $Le = 1$ and $Pr = 1$ the total enthalpy and the mass fractions of the individual chemical elements satisfy identical differential equations. The boundary-layer conservation equations (momentum, Eq. (1.16), and energy, Eq. (1.23)), together with elements conservation equations (1.22), constitutes a set of $K + 2$ differential equations which characterize the chemically reacting, multicomponent boundary-layer. In the following section, simplified correlation equations are proposed to characterize solutions of the above equations in terms of bulk boundary-layer transfer-coefficients. These approximation relationships are utilized to develop a set of equations requisite to obtaining a solution of ablation material response coupled to boundary-layer material interactions at the ablating surface.

1.5 Transfer-coefficient correlation equations

The transient response of an ablative material is dependent on the chemically reacting boundary-layer flow adjacent to the surface, and vice versa. This mutual dependence results in direct coupling between the ablation material response and the adjacent chemically reacting flow. Solution of this coupled problem has typically taken two avenues of approach, intimate coupling and transfer coefficient. While the first procedure yields the best solutions, the computer time required to obtain a solution for routine design problems can be very high. The film or transfer-coefficient approach attempts to simplify the problem by separating the transient heat conduction procedure from a chemically reacting boundary-layer procedure. In this method, heat and mass transfer-coefficients are employed to represent the convective heat and mass transfer rates at the ablating material surface. Heat and mass transfer coefficient approaches have proven to be very useful for correlating theoretical as well as experimental heat and mass transfer results for chemically reacting boundary-layer flows.

In this section, simplified equations are described to correlate solutions of the boundary-layer equations developed above. The form chosen for correlation equations of the multicomponent boundary-layer is such that they should be valid for a wide range of boundary conditions; that is, they include parameters appropriate to transient ablation of thermal protection materials, both for arbitrary chemical composition of the ablation material and boundary-layer edge gas.

1.5.1 Transfer-coefficient approaches

The transfer coefficient approach for representing boundary-layer heat and mass transfer characteristics has been used extensively in the reentry aerothermodynamics community. Basically, the approach is to relate wall fluxes to driving potentials

by means of transfer-coefficients. Given specific definitions of the driving potentials, the problem of representing surface heat and mass fluxes reduces to that of evaluating the transfer-coefficients for a given situation. The usual approach has been to start with a non-ablating heat transfer coefficient obtained by whatever means available, to correct this coefficient for mass addition by use of a blowing correction equation (obtained from simple boundary-layer solutions or from a correlation of experimental data), and to calculate a mass transfer coefficient through use of a relation between heat and mass transfer-coefficients.

1.5.2 Element conservation equation

Let us rewrite the element conservation equation (1.22) for a reacting boundary-layer:

$$\rho u \frac{\partial y_k}{\partial x} + \rho v \frac{\partial y_k}{\partial y} = \frac{\partial}{\partial y}\left(\rho \mathcal{D} \frac{\partial y_k}{\partial y}\right) \tag{1.24}$$

For simple Couette flow (with constant properties and no pressure gradient), the terms on the left-hand side vanish and the equation may be integrated directly to yield the elemental mass flux at the wall, $j_{w,k}$, in terms of the channel height δ:

$$j_{w,k} = \rho_e u_e C_m (y_{w,k} - y_{e,k}) \tag{1.25}$$

where the simple Couette flow mass-transfer coefficient is $\rho_e u_e C_m = \rho\mathcal{D}/\delta$. The subscript w and e refer to properties evaluated at the wall and at edge of boundary-layer, respectively. Thus, for simple Couette flow, the mass-transfer coefficient is related directly to the diffusion coefficient, $\mathcal{D}$. When the convective terms on the left-hand side of the element conservation equation (1.24) cannot be ignored, the transfer-coefficient driving-potential Eq. (1.25) is still appropriate for calculating the elemental mass flux. The "driving potential" is clearly represented by the mass fraction difference across the boundary-layer $(y_{w,k} - y_{e,k})$, but the mass-transfer coefficient must now include the effects of mass transfer by both convective and diffusive mechanisms. Therefore, solution of equation (1.24) is often correlated by an expression like (1.25) relating the diffusion mass flux of element k to the product of a mass-transfer coefficient and mass fraction difference. The mass-transfer coefficient is expressed as the product of the boundary-layer edge mass velocity, $\rho_e u_e$, and a Stanton number for mass-transfer, C_m.

Equation (1.25) is the desired form for a transfer-coefficient approach to mass transfer in the chemically reacting, multicomponent boundary-layer.

The mass-transfer coefficient C_m is related approximately to the heat-transfer coefficient C_h (Stanton number) by:

$$C_m = C_h (Le)^{\frac{2}{3}} \tag{1.26}$$

which is called the Chilton-Colburn relation. When the Lewis number is unity the mass and energy transfer coefficients are equal and this corresponds to the fact that the element and energy conservation equations (1.22) and (1.23) are identical with the further assumption that $Pr = 1$ (in the following section we will show that the effect of nonunity Prandtl number in the energy equation lies in the use of the recovery enthalpy instead of the total enthalpy in the driving potential expression).

1.5.3 Surface mass balance

Consider the fluxes of chemical elements k entering and leaving a control surface fixed to the ablating surface. The graphite surface material may be visualized as moving into the surface at a rate $\dot{s}$. If it is assumed that no material is being removed in a condensed phase (solid or liquid), then the surface and the fluxes of the k^{th} chemical element may be illustrated as:

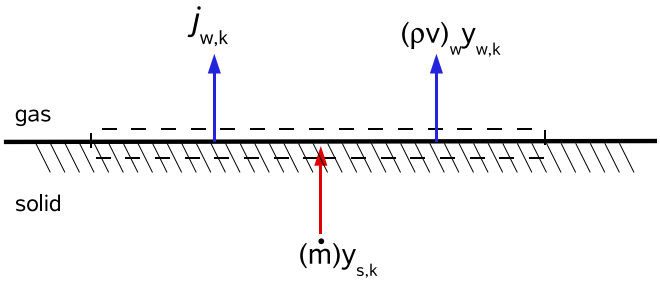

Figure 1.2: Element mass fluxes over an ablating surface.

Terms subscripted by k represent the total mass fraction or flux of element k, independent of molecular configuration. Thus:

$$y_{w,k} = \sum_{i=1}^{N} \alpha_{ki} y_{i,w} \qquad\qquad j_{w,k} = \sum_{i=1}^{N} \alpha_{ki} j_{i,w}$$

where k pertains to element k, i pertains to species i, and α_{ki} is the mass fraction of element k in species i. The subscript s denotes the surface material. Fluxes of element k away from the surface consist of boundary layer diffusion and gross motion of the fluid adjacent to the surface due to the injection flux $\dot{m}$ (rate of consumption of surface material: $\dot{m} = \rho_s \dot{s}$). Note that for graphite surfaces the quantity $y_{s,k}$ is unity for $k = C$ and zero for $k \neq C$ (where C represents the element carbon). From the above sketch, requiring that chemical elements be

conserved at the ablating surface, yields:

$$j_{w,k} + (\rho v)_w y_{w,k} = \dot{m} y_{s,k} \tag{1.27}$$

Summing Eq. (1.27) over all elements k yields the total mass continuity equation (for the case where there is no condensed phase material removal):

$$(\rho v)_w = \dot{m} \tag{1.28}$$

The elemental mass balance at the surface of the ablation material is obtained employing Eq. (1.25) to express the diffusional flux of element k in Eq. (1.27), yielding:

$$\rho_e u_e C_m (y_{w,k} - y_{e,k}) + \dot{m} y_{w,k} = \dot{m} y_{s,k} \tag{1.29}$$

1.5.4 Energy equation

When a gas contains more than one chemical species, heat energy is transported not only by heat conduction but also by diffusion currents carrying chemical enthalpy. In two-dimensional or axially-symmetric flows of boundary-layer type the rate of energy transport at wall is given by:

$$q_w = -k \frac{\partial T}{\partial y} + \sum \rho y_i u_i h_i \tag{1.30}$$

where $h_i = \int_0^T c_{p_i} dT + h_i^0$ and h_i^0 is the heat of formation of the i^{th} species. u_i is the diffusion velocity of species i. In the important special case of a binary mixture, Fick's law states that:

$$\rho y_i u_i = -\rho \mathcal{D} \frac{\partial y_i}{\partial y} \tag{1.31}$$

therefore:

$$q_w = k \frac{\partial T}{\partial y} + \rho \mathcal{D} \sum h_i \frac{\partial y_i}{\partial y} \tag{1.32}$$

Now the complete static enthalpy, which includes both the thermal and chemical enthalpies, is defined by the relation $h = \sum y_i h_i$, so that $dh = c_p dT + \sum h_i dy_i$, where $c_p = \sum y_i c_{p_i}$, and the expression for q_w is rewritten as follows:

$$q_w = \frac{k}{c_p} \left[\left(\frac{\partial h}{\partial y} - \sum h_i \frac{\partial y_i}{\partial y} \right) + \frac{\rho \mathcal{D} c_p}{k} \sum h_i \frac{\partial y_i}{\partial y} \right] \tag{1.33}$$

In other words, the relative magnitude of the heat energy transported by the two processes depends on the ratio of chemical to thermal enthalpy, and also on the parameter $\rho \mathcal{D} c_p / k$, which is the Lewis number. When $Le = 1$:

$$q_w = \frac{k}{c_p} \frac{\partial h}{\partial y} \tag{1.34}$$

independently of the mechanism of heat transfer, or of the magnitude of the chemical reaction rates in the mixture. Thus the heat transfer rate at the wall depends principally on the enthalpy difference across the flow, and therefore, on the differences in temperature and mass fractions. When $Le = 1$ the detailed chemical reaction rates influence this heat transfer rate only through their effect on the transport properties and on the mass fractions of the individual species at the surface.

An approximate correlation equation for the boundary-layer energy equation can also be rationalized. If the $Pr = Le = 1$ the energy equation (1.23) can be written in the following form:

$$\rho u \frac{\partial h_0}{\partial x} + \rho v \frac{\partial h_0}{\partial y} = \frac{\partial}{\partial y}\left(\mu \frac{\partial h_0}{\partial y}\right) \tag{1.35}$$

By analogy to Eq. (1.24), solutions to (1.35) are conveniently expressed in terms of a dimensionless heat-transfer coefficient C_h where, remembering Eq. (1.40)[3]:

$$q_w = \left(\frac{k}{c_p}\frac{\partial h_0}{\partial y}\right)_w = \rho_e u_e C_h (h_{0,e} - h_w) \tag{1.36}$$

where $h_{0,e}$ is the total enthalpy at the edge of the boundary-layer:

$$h_{0,e} = h_e + \frac{u_e^2}{2} \tag{1.37}$$

For nonunity Prandtl and Lewis numbers, the transfer-coefficient formulation for the boundary-layer energy flux is not straightforward as that discussed for the mass transfer Eq. (1.25) in the previous section. This is because the boundary-layer energy equation is no longer of the similar form as Eq. (1.24) and (1.35) and thus a transfer-coefficient formulation cannot be justified purely by analogy.

When the *Prandtl* number is not unity, the viscous dissipation and heat conduction terms in the boundary-layer energy equation (1.23) cannot be combined (leading to Eq. (1.35)), thus rendering the equation inhomogeneous. Solutions to this equation indicate that the driving potential in the transfer-coefficient expression for the surface heat flux should be defined in terms of a recovery enthalpy in place of the actual boundary-layer edge total enthalpy of Eq. (1.36), leading to:

$$q_w = \rho_e u_e C_h (h_{r,e} - h_w) \tag{1.38}$$

where $h_{r,e}$ is the recovery enthalpy:

$$h_{r,e} = h_e + r_c \frac{u_e^2}{2} \tag{1.39}$$

[3]note that, at wall, $\left.\frac{\partial h_0}{\partial y}\right|_w = \left.\frac{\partial h}{\partial y}\right|_w$.

where r_c is the so-called *recovery factor* which is:

$$\begin{cases} r_c \approx \sqrt{Pr} & \text{for laminar boundary-layer} \\ \\ r_c \approx Pr^{\frac{1}{3}} & \text{for turbulent boundary-layer} \end{cases}$$

Note that for $Pr = 1$, $r_c = 1$, and Eq. (1.39) reduces to Eq. (1.36).

When the *Lewis* number is not unity, the terms in the boundary-layer energy equation (1.23) representing energy transfer by heat conduction and chemical species diffusion cannot be combined, again rendering the equation inhomogeneous. The energy flux to the surface is given by Eq. (1.39) where the first term characterizes the heat conducted to the surface as a result of the temperature gradient in the gas adjacent to the surface, and the second term represents the effect of endothermic and exothermic chemical reactions at the surface. The appropriate transfer coefficient form of Eq. (1.39) is suggested in [35, 43, 69]:

$$q_w = \rho_e u_e C_h (h_r - h_w)_e + \rho_e u_e C_m \sum_{i=1}^{N} (y_{e,i} - y_{w,i}) h_{w,i} \tag{1.40}$$

In Eq. (1.40) the driving potential in the first term is the recovery enthalpy at the boundary-layer edge minus the enthalpy of the boundary-layer edge gases frozen at the edge composition and at the surface temperature, and $h_{w,i}$ represents the enthalpy of chemical species i evaluated at the surface temperature. It can be shown that for $Le = 1$ and $C_m = C_h$, (1.40) collapses to (1.38) as expected[4]. However when Le 1, the heat and mass transfer coefficients are generally unequal and a correlation frequently employed is represented by Eq. (1.26).

1.5.5 Surface energy balance

Consider the fluxes of energy entering and leaving a control surface fixed to the ablating surface. For the no condensed phase removal ablation case being considered, these fluxes may be illustrated as in Figure 1.3.

At the surface heat energy is transported from the gas to the solid by conduction and diffusion at the rate $q_{diff} = \left(k\frac{\partial T}{\partial y} + \rho \mathcal{D} \sum h_i \frac{\partial y_i}{\partial y} \right)$. At the same time enthalpy is transported away from the interface by the normal current at the rate $(\rho v)_w h_w$ in the gas, and toward the interface at the rate $\dot{m} h_s$ in the solid. Energy is also transported to the solid interior by thermal conduction (q_{cond}). The energy balance at the surface of an ablating material may be written utilizing Eq. (1.40) to express the boundary-layer heat transfer by conduction and diffusion (q_{diff}).

[4]Note that, in Eq. (1.40), $\sum_i (y_{e,i} - y_{w,i}) h_{w,i} = h_{w,e} - h_w$.

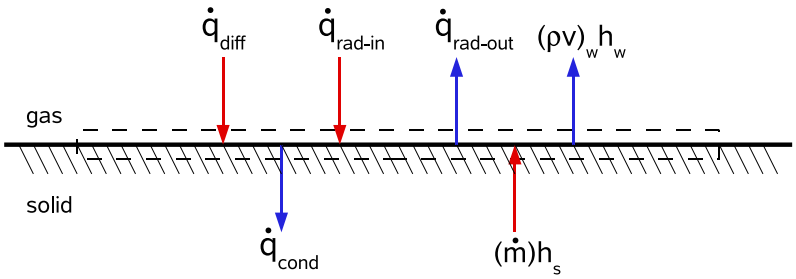

Figure 1.3: Heat fluxes over an ablating surface.

Referring to the above sketch, which depicts the primary energy transfer terms appropriate to an ablating surface and requiring that energy be conserved at the ablating surface, yields:

$$\underbrace{\rho_e u_e C_h (h_r - h_w)_e + \rho_e u_e C_m \sum_{i=1}^{N} (y_{e,i} - y_{w,i}) h_{w,i}}_{q_{diff}} + \dot{m} h_s + q_{rad_{in}} = \\ = (\rho v)_w h_w + \sigma \epsilon {T_w}^4 + q_{cond} \quad (1.41)$$

where $\sigma \epsilon {T_w}^4$ represents the surface re-radiation flux $q_{rad_{out}}$.

1.5.6 Blowing correction of heat-transfer coefficient

The transfer-coefficient model has provided simple expressions for the diffusive transport rates of mass and energy through the boundary-layer to the wall. To employ the film coefficient formulation just described, firstly the heat-transfer coefficient C_h needs to be evaluated. Two practical problems must be settled in this respect:

- How is C_m related to C_h?
- Can be both C_m and C_h be specified as functions of edge conditions (i.e. of time) independent of the subsequent problem solution (i.e. mass transfer rates and body shape)?

In answer to the first question it may be stated that within the present formulation it is adequate to take the ratio C_m/C_h constant. The value of this constant is a measure of the ratio of the mean mass transfer aspects of the boundary-layer

to the mean heat-transfer aspects. For equal mass diffusion coefficients, a vast amount of experimental data suggest the correlation $C_m/C_h = Le^{\gamma}$ just like in Eq. (1.26).

The answer to the second question, changes of C_h with body shape (which changes due to surface recession) are occasionally of interest and may be easily accounted for. A more important problem concerns the dependence of C_h on the actual rate of mass transfer. The value of C_h depends fairly strongly on $\dot{m}$ and the heat transfer rate is reduced in this case by the well-known "blocking effect" of mass addition at the surface. If we denote the C_h with $\dot{m}$ as C_{h_0}, this dependence can be represented by the following blowing reduction equation:

$$C_h = C_{h_0}\left[\frac{\phi}{e^{\phi}-1}\right] \tag{1.42}$$

or

$$C_h = C_{h_0}\left[\frac{\ln[1+2\lambda\dot{m}/(\rho_e u_e C_h)]}{2\lambda\dot{m}/(\rho_e u_e C_h)}\right] \tag{1.43}$$

where

$$\begin{aligned}
\phi &= 2\lambda\dot{m}/(\rho_e u_e C_{h_0}) \\
\dot{m} &= \text{amount of material injected into the boundary-layer} \\
\lambda &= \text{blowing-rate parameter (empirical)} \\
\rho_e u_e C_{h_0} &= \text{nonablating (unblown) heat-transfer coefficient} \\
\rho_e u_e C_h &= \text{heat-transfer coefficient corrected for blowing}
\end{aligned}$$

with $\lambda = 0.5$ both equations (1.42) and (1.43) reduces to the classical blowing correction often expressed as [69, 32]:

$$\frac{C_h}{C_{h_0}} = \frac{\ln[1+\dot{m}/(\rho_e u_e C_h)]}{\dot{m}/(\rho_e u_e C_h)} \tag{1.44}$$

which is useful for a wide range of problems.

Other values of λ allows to fit blowing correction curves of C_h/C_{h_0} versus $\dot{m}/(\rho_e u_e C_h)$ or $\dot{m}/(\rho_e u_e C_{h_0})$ to account for special effects. In view of the uncertainties it is usually recommended that $\lambda = 0.5$ be used for laminar flow. For turbulent flow a $\lambda = 0.4$ appears to be slightly better.

1.6 Ablation thermochemistry

In a hypersonic heating environment, non-charring TPS materials, such as carbon-carbon and silica, lose mass only by ablation and melt/fail mechanisms. Detailed

analysis of the performance of such TPS materials must consider the in-depth energy equation, the surface mass and energy balances, and ablation modeling. The latter aspect will be described in this section.

For non-charring TPS materials, several ablation models are available with varying degrees of sophistication [51]. The least-general ablation model is an $\dot{s}$ vs T_w model which specifies the recession rate as a function of surface temperature. This empirical model relies on experimental data for ablation in the pressure range of interest.

The Q^* model is the most common engineering-level model for ablation. In this model, Q^* is the effective heat of ablation:

$$\dot{m} = \dot{s}\rho_s = q_w/Q^* \qquad \text{for } T_w \geq T_{abl} \tag{1.45}$$

where $\dot{m}$ is the ablation mass flux, ρ_s is the material density, and q_w is the net aerothermal heat flux. The Q^* model is most useful for hig-heating conditions and for low-conductivity materials where steady-state recession is a good approximation. This model cannot predict accurately the surface temperature history and heat soak for a TPS material.

Thermochemical ablation is the most general and widely applicable TPS ablation model [33, 34]. Thermochemical ablation models are obtained from a solution of the equations for thermodynamic equilibrium (typically) or non-equilibrium between the TPS material and the atmosphere of interest, coupled with surface mass and energy balances and boundary-layer transfer-coefficients. The net result of the calculations is a set of thermochemical tables relating surface temperature and pressure to the dimensionless surface mass flux owing to ablation. These tables numerically represent a general ablation function $\mathcal{F}(T, p, B^{'}) = 0$ for a specific TPS material, such as carbon, and a specific boundary-layer edge gas, such as air. In the thermochemical tables, the surface mass fluxes are nondimensionalized with the mass transfer coefficient to define the dimensionless variable $B^{'} = \dot{m}/\rho_e u_e C_m$. The shape of $B^{'}$ curves depends on the material composition, the choice of allowable surface and gas-phase species, the atmospheric composition, and whether or not kinetically limited reactions occur. Experience, insight, and experimental data are all important ingredients in the development of accurate thermochemical tables for a selected TPS material and environment. However, once such tables have been generated, they are applicable over a wide range of aerothermal heating conditions. The next section describes the thermochemical ablation model for thermodynamic equilibrium at the surface.

1.6.1 ablation rate

In order to employ the surface mass balance (1.29) and surface energy balance (1.41) to assess the material ablation rate, it is necessary to consider the degree of

chemical equilibrium at the surface, since the terms $y_{w,i}$ and h_w depend strongly on the molecular composition of the gases at the surface. The results presented thus far are valid independent of the degree of chemical equilibrium achieved in the boundary-layer and at the ablating surface. In this section, this degree of generality will be abandoned in order to indicate how solutions to the equations may be obtained for the limiting case of chemical equilibrium. Employing the definition of a blowing parameter:

$$B^{'} = \frac{(\rho v)_w}{\rho_e u_e C_m} \tag{1.46}$$

the surface mass balance (1.29) can be expressed as:

$$(1 + B^{'}) y_{w,k} = B^{'} y_{s,k} + y_{e,k} \tag{1.47}$$

and solving (1.47) for the total mass fractions of element k at the wall yields:

$$y_{w,k} = \frac{B^{'} y_{s,k} + y_{e,k}}{1 + B^{'}} \tag{1.48}$$

The element flux balance (1.47) ensures that the correct elemental composition is obtained in the gas phase at the surface. Given the relative amount of chemical elements specified by (1.48), the chemical and thermodynamic state of the gases adjacent to the ablating surface may be calculated from equilibrium relations.

Chemical equilibrium relations may be written considering formation reactions of each gaseous species from the elemental gaseous species. We consider here an accounting of equations and unknowns for the case of equilibrium chemistry in the control volume across the ablative surface. The control volume contains a mixture of K elements including N gaseous species and L condensed species (solid or liquid), i.e. the surface species[5]. Some species may have negligible concentrations, but there must be at least one gaseous species containing each element. To begin, K gaseous species are selected (denoted as N_k) to represent *base species* for the elements in the system. Non-base gaseous species N_i can be represented by formation reactions of the base species:

$$\sum_k \nu_{ki} N_k \rightarrow N_i \tag{1.49}$$

where ν_{ki} is the number of atoms of element k in a molecule of species i. Similarly, for the formation of condensed phase species from the gaseous elements:

$$\sum_k \nu_{kl} N_k \rightarrow N_l \tag{1.50}$$

[5]For a carbon-carbon (graphite) material there is only one condensed species which is solid carbon.

The equations of chemical equilibrium corresponding to Eq. (1.49) and (1.50) may be written in terms of the equilibrium constant $K_p(T)$ for each reaction. For each gas-phase formation reaction [Eq. (1.49)], the following equilibrium relation applies:

$$K_{pi}(T) = p_i \prod_k {p_k}^{-\nu_{ki}} \Rightarrow \ln p_i - \sum_k \nu_{ki} \ln p_k = \ln K_{pi}(T) \tag{1.51}$$

If chemical equilibrium is achieved between the gas phase and the surface material (considered made of a single solid species), the following equilibrium relation may be written introducing the temperature dependent equilibrium constants for the condensed phase formation reactions:

$$K_{pl}(T) = \prod_k {p_k}^{-\nu_{kl}} \Rightarrow -\sum_k \nu_{kl} \ln p_k \leq \ln K_{pl}(T) \tag{1.52}$$

The equality in Eq. (1.52) implies the existence of condensed species l; if the condensed species is not present, the inequality applies. When considering systems such the ablation of graphite in air, the surface is most certainly carbon.
Other easily defined quantities are the total pressure:

$$p = \sum_i p_i \tag{1.53}$$

and the elemental gaseous mass fraction at the wall:

$$y_{w,k} = \frac{1}{p\mathcal{M}} \sum_i \alpha_{ki} p_i \mathcal{M}_i = \frac{\mathcal{M}_k}{p\mathcal{M}} \sum_i \nu_{ki} p_i \tag{1.54}$$

where the unscripted $\mathcal{M}$ is the gas-phase average molecular weight.

In the absence of material failure, the unknown quantities in Eqs. (1.48),(1.51-1.54) are the N gaseous partial pressures p_i, the K mass fractions $y_{w,k}$, the temperature T, and the molecular weight $\mathcal{M}$, for a total of $N + K + 2$ unknowns. The equations are $N - K$ equilibrium expressions Eq. (1.51), K wall mass fractions definitions Eq. (1.54), K elements flux balances Eq. (1.48), the pressure sum Eq. (1.53), and one equilibrium expression for the condensed phase Eq. (1.52), for a total of $N + K + 2$ equations for closure of the equation set.

The simultaneous solution of Eqs. (1.48),(1.51-1.54) yields the surface temperature and molecular composition of the gases adjacent to the surface for a specified ablation rate B' and surface pressure p. By specifying a parametric array of pressures and of B', a map of boundary conditions satisfying the mass balances and equilibrium constraints is obtained. Figure 1.4 shows $B'(T, p)$ for pure thermochemical ablation (no material failure) of carbon in air. As the pressure is

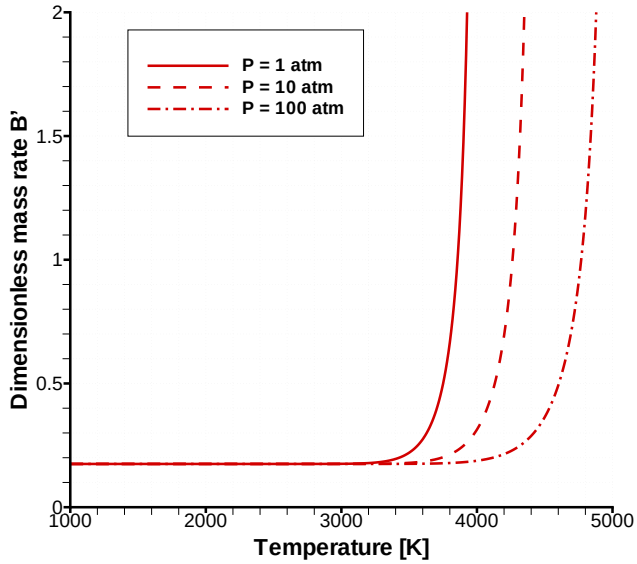

Figure 1.4: Dimensionless ablation rate for carbon in air.

increased, a higher surface temperature is needed to reach the same dimensionless ablation rate. For any pressure, at the highest ablation rates, carbon sublimation is the primary mass loss mechanism, and $C_3(g)$ is the predominant ablative species. However, below $B' = 0.2$, surface oxidation reactions dominate, and CO is the major species leaving the surface. Figure 1.5 shows the predicted gas-phase mass fractions at the surface[6]. C_3 is the major ablative species only at the highest temperatures and ablation rates. Whichever the surface temperature, the oxygen mass fraction at the surface is always zero because it completely reacts with solid carbon to form carbon monoxide.

The thermochemical tables may be employed in conjunction with the surface energy equation (1.41) and relations describing the in-depth response of the ablation material to obtain coupled solutions of the ablation problem.

1.7 Boundary-layer and material response coupling

The analysis of ablative-material thermal protection systems for highly energetic, chemically active environments requires theoretical techniques to characterize the

[6]only the major ablating species are showed: CO and C_3

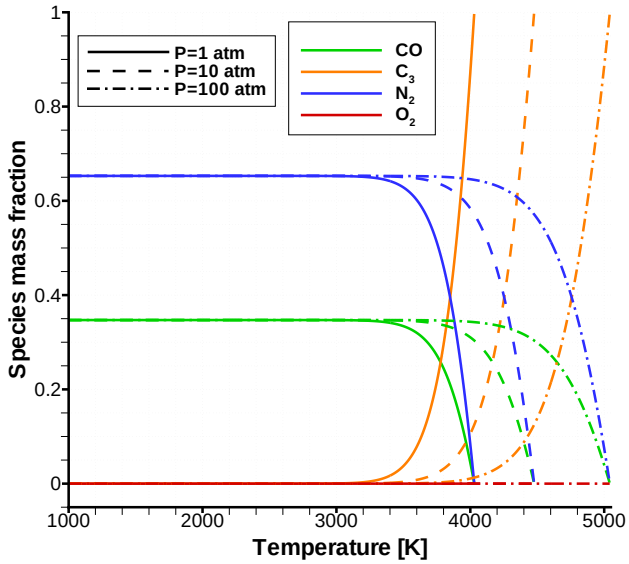

Figure 1.5: Surface chemical species for carbon ablation in air.

material thermal response and to represent the heated-surface boundary condition. In the previous sections, mathematical models have been described for representing the transient thermal response of a non-charring ablative material type and for representing boundary-layer transport phenomena necessary for evaluating the heated-surface boundary conditions. Because an intimate coupling exists between boundary-layer transport phenomena and ablative material thermal response, the need for a coupled solution is apparent. The procedure described herein employs correlation equations that relate surface conditions directly to boundary-layer-edge conditions through the use of over-all convective transfer-coefficients. A film coefficient model for boundary-layer heat and mass transfer with chemical reactions has been derived for the governing differential equations of the boundary-layer. Of the resulting transfer-coefficient expressions, those for mass transport has been coupled to a chemistry routine to provide boundary conditions for an in-depth response calculation. The boundary information and the in-depth calculation are coupled through the transfer-coefficient energy balance, providing a complete link between the boundary-layer and the solid material.

The finite difference equations for the in-depth solution are developed and presented in the next chapter, as well as the computational strategy for obtaining the coupled solution.

Chapter 2

Numerical approach to the ablation problem

Since the phenomenon presented in the previous chapter involves transient one-dimensional heat conduction, the following sections will explain how to numerically model the heat transfer problem with ablation and how to couple the transient solution to the transfer-coefficient boundary-layer model.

2.1 Finite-difference method for the in-depth solution

Let us consider the in-depth energy balance in the moving coordinate system expressed by Eq. (1.14):

$$\frac{\partial T}{\partial t} = \alpha \frac{\partial^2 T}{\partial x^2} + \dot{s} \frac{\partial T}{\partial x} \tag{2.1}$$

which holds for a planar surface and constant thermal conductivity. The finite difference expression for the simplified energy equation (2.1) will be described for the sake of comprehension. The added complexity due to the variable area and variable properties somewhat complicates the algebra of the difference form of the equation (see Appendix C) but the solution philosophy remains the same.

2.2 Nodal coordinate layout

The basic solution procedure is of the *finite difference* type. Nodal position are specified by defining the total number of node and their thickness (it is common practice to concentrate the number of nodes near the ablating wall where the temperature gradients are higher). In harmony with the shifting x-coordinate system

introduced in section 1.3, nodal coordinates are tied to the heated surface. The following principles of nodal sizing have been followed:

- The nodes have a fixed size. This avoids the slight additional computation complexity of shrinking nodes, and more importantly, makes the next principle easier to satisfy, in addition to preserving a useful nodal spacing throughout the history of a given problem.

- Since the nodes are fixed in size, not all of them can be retained if the surface of the material is receding due to chemical erosion. From time to time a node must be dropped, and experience shows that it is much more preferable to drop node from the back (non-ablating) face of the material rather than from the front ablating face in order to avoid numerical instabilities. This means that the nodal network is tied to the receding surface, and that material appears to be flowing through the nodes. That is the reason why the energy equation has been transformed to a moving coordinate system.

To this end, suppose the domain we will work on is rectangular with x ranging from x_{min} to x_{max} and t ranging from 0 to T. Divide $[0, T]$ into I equally spaced intervals at t values indexed by $i = 0, 1, ..., I$, and $[x_{min}, x_{max}]$ into N intervals at x values indexed by $n = 1, ..., N + 1$. The length of these intervals is Δt in the time direction and Δx in the spatial direction. In general the quantity Δx can vary from node to node.

We seek an approximation to the true values of temperature T at the $(I + 1) \times (N + 1)$ gridpoints. Let T_n^i denote our approximation at the gridpoint where $x = x_{min} + n\Delta x$ and $t = i\Delta t$ and T_n^{i+1} denote our approximation at the gridpoint where $x = x_{min} + n\Delta x$ and $t = (i + 1)\Delta t$. From now on, without the risk of confusion, the quantities T_n^i and T_n^{i+1} will be referred to as T_n and T_n', respectively. The following sections will explain the numerical algorithm for solving the energy equation for the case of planar surface, constant properties and constant nodal size (Δx). This will help the reader in understanding the solving algorithm structure and its coupling to the ablating surface mass/energy balances. The general algorithm for the case of variable properties, variable cross-section area and variable nodal size is reported in Appendix C.

2.3 Crank-Nicholson algorithm

The implicit finite difference scheme is based on the Crank-Nicholson algorithm, which has the virtue of being unconditionally stable and also is second order accurate in both x and t directions. The first step is to approximate the partial derivatives of T at each gridpoint by finite difference expressions. The expression for

T_t, T_x, and T_{xx} are the following:

$$\begin{aligned} T_t &= \frac{T_n^{'} - T_n}{\Delta t} \\ T_x &= \frac{(T_{n+1}^{'} - T_{n-1}^{'}) + (T_{n+1} - T_{n-1})}{4\Delta x} \\ T_{xx} &= \frac{(T_{n+1}^{'} - 2T_n^{'} + T_{n-1}^{'}) + (T_{n+1} - 2T_n + T_{n-1})}{2\Delta x^2} \end{aligned}$$

2.3.1 Interior nodes

Substituting the above into the Eq. (2.1), results in:

$$\begin{aligned} \frac{T_n^{'} - T_n}{\Delta t} &= \frac{\alpha}{2\Delta x^2}\left(T_{n+1}^{'} - 2T_n^{'} + T_{n-1}^{'} + T_{n+1} - 2T_n + T_{n-1}\right) + \\ &+ \frac{\dot{s}}{4\Delta x}\left(T_{n+1}^{'} - T_{n-1}^{'} + T_{n+1} - T_{n-1}\right) \end{aligned} \tag{2.2}$$

multiplying (2.2) through by $4\Delta x^2 \Delta t$ to eliminate the denominators, and collecting all the terms involving the unknowns $T_n^{'}$ on the left hand side results in:

$$\begin{aligned} -(2\alpha\Delta t - \dot{s}\Delta x\Delta t)T_{n-1}^{'} + (4\Delta x^2 + 4\alpha\Delta t)T_n^{'} - (2\alpha\Delta t + \dot{s}\Delta x\Delta t)T_{n+1}^{'} &= \\ (2\alpha\Delta t - \dot{s}\Delta x\Delta t)T_{n-1} + (4\Delta x^2 - 4\alpha\Delta t)T_n + (2\alpha\Delta t + \dot{s}\Delta x\Delta t)T_{n+1} & \end{aligned} \tag{2.3}$$

for each interior node $n = 2, N$. It is apparent that the $T_n^{'}$ cannot individually be written as simple linear combinations of the T_n, but are simultaneously determined as the solution to this system of linear equations. Since equation (2.3) applies only to the interior gridpoints, at each time step appropriate boundary conditions (e.g. at x_{min} and x_{max}) have to be used to calculate all the $T_n^{'}$.

2.3.2 The surface node

We almost have a procedure for recursively determining the entire grid of $T_n^{'}$ starting from the given initial values. Substitution of the difference expressions into the differential equation only gave us a linear equation for each interior point in the grid. That gives $N - 1$ equation at each time step, which is not sufficient to determine the $N + 1$ unknowns. The missing two equations must be provided by boundary conditions applied at each time step. It would be desirable for these to

be representable in a form that preserves the tri-diagonal form of the system and thus the efficiency of the solution.

It will be recalled from the introductory section 1.2 on boundary conditions that one of the key purpose of the in-depth response solution is to provide a function $q_{cond}(T_w)$. How this is finally accomplished will become clear in the next section, but it is clear enough that the quantity q_{cond}, which ultimately will be calculated as a part of the surface energy balance, will play the central role in linking the in-depth solution to the surface energy balance.

Therefore the energy input to the first node ($n = 1$) will be left simply as q_{cond}, which will replace the terms of the form:

$$\frac{(T_{n+1} - T_{n-1})}{2\Delta x} = -\frac{q_{cond}}{k}$$

$$\frac{(T'_{n+1} - T'_{n-1})}{2\Delta x} = -\frac{q'_{cond}}{k}$$

where k is the material thermal conductivity. Thus we have the energy difference equation for the first node as:

$$\begin{aligned} \frac{T'_1 - T_1}{\Delta t} &= \frac{\alpha}{2\Delta x^2}\left(2T'_2 - 2T'_1 + \frac{2\Delta x}{k}q'_{cond} + 2T_2 - 2T_1 + \frac{2\Delta x}{k}q_{cond}\right) + \\ &+ \frac{\dot{s}}{4\Delta x}\left(-\frac{2\Delta x}{k}q'_{cond} - \frac{2\Delta x}{k}q_{cond}\right) \end{aligned} \tag{2.4}$$

multiplying (2.4) through by $4\Delta x^2 \Delta t$ to eliminate the denominators, and collecting all the terms involving the unknowns T'_n and q'_{cond} on the left hand side results in:

$$\begin{aligned} &(4\Delta x^2 + 4\alpha\Delta t)T'_1 - (4\alpha\Delta t)T'_2 - 2\frac{\Delta x \Delta t}{k}(2\alpha - \dot{s}\Delta x)q'_{cond} = \\ &(4\Delta x^2 - 4\alpha\Delta t)T_1 + (4\alpha\Delta t)T_2 + 2\frac{\Delta x \Delta t}{k}(2\alpha - \dot{s}\Delta x)q_{cond} \end{aligned} \tag{2.5}$$

2.3.3 The last node

The energy equation for the last node ($n = N + 1$) must also be considered separately. The last node does not of course conduct energy to an adjacent node. Hence the conduction term is replaced by a temperature-potential convective transfer

communicating with a "reservoir" at temperature T_{res}:

$$\frac{(T_{n+1} - T_{n-1})}{2\Delta x} = -\frac{h_{res}}{k}(T_n - T_{res})$$

$$\frac{(T'_{n+1} - T'_{n-1})}{2\Delta x} = -\frac{h_{res}}{k}(T'_n - T_{res})$$

where h_{res} is the heat-transfer coefficient with the external ambient. Thus we have the energy difference equation for the last node as:

$$\begin{aligned} & \frac{T'_{N+1} - T_{N+1}}{\Delta t} = \\ = \; & \frac{\alpha}{2\Delta x^2}\left(2T'_N - 2T'_{N+1} - 2\Delta x\frac{h_{res}}{k}T'_{N+1} + 2T_N - 2T_{N+1} - 2\Delta x\frac{h_{res}}{k}T_{N+1} + 4\Delta x\frac{h_{res}}{k}T_{res}\right) + \\ + \; & \frac{\dot{s}}{4\Delta x}\left(-2\Delta x\frac{h_{res}}{k}T'_{N+1} - 2\Delta x\frac{h_{res}}{k}T_{N+1} + 4\Delta x\frac{h_{res}}{k}T_{res}\right) \end{aligned} \tag{2.6}$$

multiplying (2.6) through by $4\Delta x^2\Delta t$ to eliminate the denominators, and collecting all the terms involving the unknowns T'_n and q'_{cond} on the left hand side results in:

$$\begin{aligned} - \; & (4\alpha\Delta t)T'_N + \left[4\Delta x^2 + 4\alpha\Delta t + 2\Delta x\Delta t\frac{h_{res}}{k}(2\alpha + \dot{s}\Delta x)\right]T'_{N+1} = \\ & (4\alpha\Delta t)T_N + \left[4\Delta x^2 - 4\alpha\Delta t - 2\Delta x\Delta t\frac{h_{res}}{k}(2\alpha + \dot{s}\Delta x)\right]T_{N+1} + \\ & 4\Delta x\Delta t\frac{h_{res}}{k}(2\alpha + \dot{s}\Delta x)T_{res} \end{aligned} \tag{2.7}$$

2.3.4 Tri-diagonal matrix form

The system made up of Eq. (2.3) fort the interior nodes and (2.5) and (2.7) for the two boundary nodes has a very convenient structure. Written in a matrix form:

$$\begin{pmatrix} B_1 & C_1 & 0 & 0 & 0 & 0 & ... & 0 \\ A_2 & B_2 & C_2 & 0 & 0 & 0 & ... & 0 \\ 0 & A_3 & B_3 & C_3 & 0 & 0 & ... & 0 \\ 0 & & ... & ... & ... & & & 0 \\ 0 & & & ... & ... & ... & & 0 \\ 0 & ... & 0 & 0 & A_{N-1} & B_{N-1} & C_{N-1} & 0 \\ 0 & ... & 0 & 0 & 0 & A_N & B_N & C_N \\ 0 & ... & 0 & 0 & 0 & 0 & A_{N+1} & B_{N+1} \end{pmatrix} \begin{pmatrix} T'_1 \\ T'_2 \\ T'_3 \\ ... \\ ... \\ T'_{N-1} \\ T'_N \\ T'_{N+1} \end{pmatrix} = \begin{pmatrix} D_1 \\ D_2 \\ D_3 \\ ... \\ ... \\ D_{N-1} \\ D_N \\ D_{N+1} \end{pmatrix} \tag{2.8}$$

The expressions for the coefficients A_n, B_n, C_n and D_n are readily apparent from the finite difference energy equations (2.3), (2.5) and (2.7). For the interior nodes:

$$\begin{cases} A_n &= -(2\alpha\Delta t - \dot{s}\Delta x\Delta t) \\ B_n &= (4\Delta x^2 + 4\alpha\Delta t) \\ C_n &= -(2\alpha\Delta t + \dot{s}\Delta x\Delta t) \\ D_n &= -A_nT_{n-1} + (4\Delta x^2 - 4\alpha\Delta t)T_n - C_nT_{n+1} \end{cases} \qquad n = 2, ..., N \tag{2.9}$$

while for the first node:

$$\begin{cases} B_1 &= (4\Delta x^2 + 4\alpha\Delta t) \\ C_1 &= -(4\alpha\Delta t) \\ D_1 &= \mathcal{F}(q'_{cond}) \end{cases} \tag{2.10}$$

with

$$D_1 = (4\Delta x^2 - 4\alpha\Delta t)T_1 - C_1T_2 + 2\frac{\Delta x\Delta t}{k}(2\alpha - \dot{s}\Delta x)(q'_{cond} + q_{cond})$$

and for the last node:

$$\begin{cases} A_{N+1} &= -(4\alpha\Delta t) \\ B_{N+1} &= \left[4\Delta x^2 + 4\alpha\Delta t + 2\Delta x\Delta t\frac{h_{res}}{k}(2\alpha + \dot{s}\Delta x)\right] \\ D_{N+1} &= \mathcal{F}(h_{res}, T_{res}) \end{cases} \tag{2.11}$$

with

$$\begin{aligned} D_{N+1} = \; &- \; A_{N+1}T_N + \left[4\Delta x^2 - 4\alpha\Delta t - 2\Delta x\Delta t\frac{h_{res}}{k}(2\alpha + \dot{s}\Delta x)\right]T_{N+1} + \\ &+ \; 4\Delta x\Delta t\frac{h_{res}}{k}(2\alpha + \dot{s}\Delta x)T_{res} \end{aligned}$$

For a given node n, except the first or last, the finite difference energy relation involves three unknown temperatures, T'_{n-1}, T'_n, and T'_{n+1}. For the last node $N+1$, there are only two unknown temperatures, T'_N and T'_{N+1}, while the first node equation involves only T'_1 and T'_2, in addition to the unknown heat flux q'_{cond}.

2.4 Computational strategy for the coupled solution

It is now possible to see clearly what needs to be done for each time step Δt of the solution in order to prepare for coupling to the surface energy balance. First, using the current values of $\dot{s}$ and T_n, the coefficients of the tri-diagonal energy equation matrix can be computed. Once this matrix is set up, the required surface energy relation $q_{cond} = q_{cond}(T_w)$ may be obtained directly, as described in the next section.

2.4.1 Reduction of the Tri-diagonal matrix

Referring to the array of in-depth energy equations set down symbolically in Set (2.8), it may be seen that, beginning with the last node, the highest-indexed unknown temperature may be eliminated from each equation of Set (2.8) in turn (this is the standard first step in the routine reduction of a tri-diagonal matrix). The resulting simpler set of equations is the following:

$$\begin{pmatrix} B_1^* & 0 & 0 & 0 & 0 & 0 & ... & 0 \\ A_2^* & B_2^* & 0 & 0 & 0 & 0 & ... & 0 \\ 0 & A_3^* & B_3^* & 0 & 0 & 0 & ... & 0 \\ 0 & & ... & ... & ... & & & 0 \\ 0 & & & ... & ... & ... & & 0 \\ 0 & ... & 0 & 0 & A_{N-1}^* & B_{N-1}^* & 0 & 0 \\ 0 & ... & 0 & 0 & 0 & A_N^* & B_N^* & 0 \\ 0 & ... & 0 & 0 & 0 & 0 & A_{N+1}^* & B_{N+1}^* \end{pmatrix} \begin{pmatrix} T_1' \\ T_2' \\ T_3' \\ ... \\ ... \\ T_{N-1}' \\ T_N' \\ T_{N+1}' \end{pmatrix} = \begin{pmatrix} D_1^* \\ D_2^* \\ D_3^* \\ ... \\ ... \\ D_{N-1}^* \\ D_N^* \\ D_{N+1}^* \end{pmatrix} \tag{2.12}$$

It will be noted that this reduction implies that the A, B, C, and D terms involve only known quantities evaluated at the beginning of the time step. In particular, the surface recession rate $\dot{s}$ is treated in this explicit manner. This cause little error since the energy term involving $\dot{s}$ are small compared to the other energy terms. The expressions for the coefficients A_n^*, B_n^*, C_n^* and D_n^* are easily expressed. For the last node ($n = N + 1$):

$$\begin{cases} A_{N+1}^* &= A_{N+1} \\ B_{N+1}^* &= B_{N+1} \\ D_{N+1}^* &= D_{N+1} \end{cases} \tag{2.13}$$

for the interior nodes ($n = 2, ..., N$):

$$\begin{cases} A_n^* &= A_n \\ B_n^* &= B_n - C_n \dfrac{A_{n+1}^*}{B_{n+1}^*} \\ D_n^* &= D_n - C_n \dfrac{D_{n+1}^*}{B_{n+1}^*} \end{cases} \tag{2.14}$$

for the first node ($n = 1$):

$$\begin{cases} B_1^* &= B_1 - C_1 \dfrac{A_2^*}{B_2^*} \\ D_1^* &= D_1 - C_1 \dfrac{D_2^*}{B_2^*} \end{cases} \tag{2.15}$$

Of the reduced set of equations (2.12), only the top-most equation is of immediate interest. It may be arranged as:

$$q_{cond} = \mathcal{F}_s(T_w) \tag{2.16}$$

where $\mathcal{F}_s$ is a simple linear relation and T_w is the unknown surface temperature. In fact, from Set (2.12):

$$B_1^* T_1^{'} = D_1^*$$

now from the expression of B_1^* and D_1^* it can be easily found that:

$$q_{cond}^{'} = \frac{B_1^*}{\mathcal{C}_2} T_1^{'} - \frac{\mathcal{C}_1}{\mathcal{C}_2} + \frac{C_1}{\mathcal{C}_2} \frac{D_2^*}{B_2^*} - q_{cond} \tag{2.17}$$

with

$$\begin{cases} \mathcal{C}_1 &= (4\Delta x^2 - 4\alpha\Delta t)T_1 + (4\alpha\Delta t)T_2 \\ \mathcal{C}_2 &= 2\dfrac{\Delta x \Delta t}{k}(2\alpha - \dot{s}\Delta x) \end{cases}$$

Eq. (2.17) is a simple linear relation of the form:

$$q_{cond}^{'} = A_s T_1^{'} + B_s \tag{2.18}$$

Since $T_1^{'} = T_w$, Equation (2.18) is the desired relation between q_{cond} and T_w implied by the in-depth solution.

It is now necessary to harmonize this in-depth relation with the surface energy balance (SEB). This will be discussed in the following section.

2.4.2 Coupling in-depth response to SEB

If the surface boundary condition involves an energy balance with convective energy input, the final in-depth relation Eq. (2.18) must now be coupled to the surface energy balance illustrated in Figure 1.3. In this most general case, events at the heated surface are determined by convective heating and by surface thermochemical interactions with the boundary-layer gases. The surface energy balance equation employed is of the convective transfer coefficient type expressed in section 1.5.5:

$$\underbrace{\rho_e u_e C_h (h_r - h_w)_e}_{q_{sen}} + \underbrace{\rho_e u_e C_m \sum_{i=1}^{N} (y_{e,i} - y_{w,i}) h_{w,i} - \dot{m} h_w + \dot{m} h_s +}_{q_{chem}}$$

$$+ q_{rad_{in}} - \underbrace{\sigma \epsilon {T_w}^4}_{q_{rad_{out}}} - q_{cond} = 0 \tag{2.19}$$

The surface energy balance Eq. (2.19) may be rewritten with the use of the dimensionless blowing parameter $B^{'} = \dot{m}/\rho_e u_e C_m$ defined in section 1.6:

$$\rho_e u_e C_h (h_r - h_w)_e + \rho_e u_e C_m \left[h_{w_e} - (1 + B^{'}) h_w \right] + \dot{m} h_s +$$

$$q_{rad_{in}} - \sigma \epsilon {T_w}^4 - q_{cond} = 0 \tag{2.20}$$

where we remember that h_{w_e} is the enthalpy of the boundary-layer edge gases frozen at the edge composition and at the surface temperature. Note that if the mass and energy transfer coefficients are equal, the SEB simplifies to the following form:

$$\rho_e u_e C_h \left[h_r - (1 + B^{'}) h_w \right] + \dot{m} h_s + q_{rad_{in}} - \sigma \epsilon {T_w}^4 - q_{cond} = 0 \tag{2.21}$$

where the term h_{w_e} is no longer present.

In Eq. (2.19), the term q_{sen} represents the *sensible* convective heat flux, it excludes all *chemical* energy contributions. It has the advantage that the driving force involves only edge gas states. The energy transfer-coefficient $\rho_e u_e C_h$ and the recovery enthalpy h_r are function of boundary-layer solution and must be known for the solution of the surface energy balance. The quantity h_{e_w} is part of the input thermochemical data discussed below.

The term q_{chem} represents the net of a number of fluxes of chemical energies at the surface. The y difference term represents transport of chemical energy associated with chemical reactions at the wall; it is the chemical energy parallel to

the sensible convective heat flux term. The $\dot{m}h_s$ term represents energy fluxes arriving at the surface from within the solid material and $\dot{m}h_w$ term represents energy leaving the surface in the gross motion (blowing) of the gas adjacent to the surface. Of the quantities in the q_{chem} expression, the convective mass transfer coefficient $\rho_e u_e C_m$ is obtained from the input values of $\rho_e u_e C_h$ using relations such as Eq. (1.26). The enthalpy h_s is obtained from the material thermodynamic properties $h_s = h_{s_0} + \int_T^{T_0} c_{p_s} dT$. Remaining quantities to discuss are $B^{'}$, $\sum y_{e,i} h_{w,i} = h_{w_e}$, $\sum y_{w,i} h_{w,i} = h_w$, and T_w (which does not compare explicitly but is necessary to evaluate h_s). The quantity h_{w_e} is known form the edge input composition $y_{e,i}$ and the surface temperature. The quantity $B^{'}$ can be obtained from the thermochemical tables shown in section 1.6, given the edge pressure p and the surface temperature T_w. Finally, the wall enthalpy h_w is obtained from the wall temperature and composition, the latter obtained by the thermochemical tables.

The radiative energy flux to the surface $q_{rad_{in}}$, when present, must be supplied by the user as all the others boundary-layer input terms. The re-radiative energy term, $\epsilon {T_w}^4$, is a function of temperature only. The conduction energy term, q_{cond}, is delivered by the in-depth solution as described in the previous sections.

Finally we have shown that, coupling the procedure with a thermochemical ablation model (thermochemical tables), all the unknown terms in the surface energy balance Eq. (2.20) are function of T_w which is therefore the only unknown. The energy balance solution procedure is now described. An initial guess of the surface temperature T_w is obtained in some manner. The quantities in the SEB Eq. (2.20) are evaluated from the boundary-layer solutions, the thermochemical tables, and the initial guess surface temperature. Then the surface energy balance can be computed. In general, however, the sum of the terms will not equal zero but some non-zero quantity $\mathcal{E}$ called the error. Some appropriate iterative procedure must be devised to select successively better estimates of T_w which drive the error ϵ to zero. Experience shows that Newton's procedure, in which the derivative of the error with respect to T_w is used to compute the next guess $(k+1)$ for T_w, gives good results:

$$T_{w_{k+1}} = T_{w_k} - \frac{\epsilon}{\left(\partial \mathcal{E} / \partial T\right)_k}$$

This scheme converges rapidly to the solution. The above-described procedure to solve the surface energy balance may be summarized as follows:

1. Evaluate h_r, $\rho_e u_e C_{h_0}$, p, and $q_{rad_{in}}$ from a previous solution of the boundary-layer. The edge composition $y_{e,i}$ must also be determined.

2. Obtain values of A_s and B_s in the expression $q^{'}_{cond} = A_s T_w + B_s$ from in-depth nodal energy balance solution.

3. Guess an initial value for the surface temperature T_w
4. Evaluate $B^{'}$ from surface thermochemical table $B^{'} = \mathcal{F}(p, T_w)$.
5. Use blowing correction equation (1.43) to evaluate $\dfrac{C_h}{C_{h_0}}$ and calculate $\rho_e u_e C_h$.
6. Compute $\rho_e u_e C_m$ from C_h and the ratio C_m/C_h, the latter evaluated using Eq. (1.26).
7. Use p and T_w to obtain values for $B^{'}$, h_w, and h_{w_e} from the thermochemical tables.
8. with T_w evaluate ϵ and h_s from material properties.
9. Construct Eq. (2.20).
10. Adjust T_w to reduce the error $\mathcal{E}$ using Newton-Raphson iteration technique.
11. Go back to step 4 and continue until a convergence criterion is satisfied.

2.4.3 Completing the in-depth solution

Once the surface energy balance has been satisfied, the new surface temperature $T_1^{'}$ may be substituted in the reduced array of temperature (2.12). Since $T_1^{'}$ is now known, the second equation of Set (2.12) yields $T_2^{'}$ directly, then the third equation yields $T_3^{'}$, and so on until the new temperature set $T_n^{'}$ is complete:

$$T_n^{'} = \frac{D_n^{'}}{B_n^{'}} - \frac{A_n^{'}}{B_n^{'}} T_{n-1}^{'}, \qquad n = 2, N+1 \tag{2.22}$$

With the surface temperature T_w and the dimensionless mass blowing rate $B^{'}$ coming from the SEB solution, the mass blowing rate $\dot{m}$ can be evaluated. The surface recession term is then updated to its new value $\dot{s} = \dot{m}/\rho_s$. As a final step, new values for temperature dependent properties can be selected for each node and the entire system is then ready for a new time step.

2.4.4 Solution without energy balance

The surface boundary condition need not, of course, be an energy balance. Surface temperature T_w and recession rate $\dot{s}$ might be specified as time-dependent input parameters. In that case $T_1^{'}$ is known, and the solution of Set (2.12) can be completed at once as shown in the previous section. The quantity q_{cond} being only of cultural interest in that case. This option can be useful for parametric studies

matching internal temperature response predictions to the measured thermocouple responses, using measured surface temperature and recession data as input, in order to obtain thermal conductivity data via an inverse procedure. This option can be also used to compare the numerical solution with known analytical solutions.

2.5 Results

This section reports the results of a number of computational simulations aimed at studying the transient response of graphite TPS for typical reentry and rocket nozzle applications. The obtained results will give useful information for the understanding of the behaviour of such TPS materials exposed to a realistic thermochemical environment typical of the applications of interest.

2.5.1 Solution check-out

This section presents the results of a series of check-out computations testing the heat conduction aspects of the developed numerical code.

As a first check out, a constant properties semi-infinite slab was simulated with a thickness large enough to ensure that the final node showed no temperature response during the computation. Property values were taken as:

$$k = 30\ W/m^2\ K$$

$$c_p = 2000\ J/kg\ K$$

$$\rho = 1850\ kg/m^3$$

The exact solution to the semi-infinite solid problem with uniform initial temperature T_0 and step surface temperature T_s at time $t = 0$ is a similarity solution:

$$\frac{T - T_0}{T_s - T_0} = 1 - \text{erf}(x^*)$$

where

$$x^* = \frac{x}{2\sqrt{\alpha t}}$$

where α is the solid thermal diffusivity: $\alpha = k/\rho c_p$. The surface and initial temperature, T_s and T_0, are taken equal to $4000\ K$ and $300\ K$, respectively. The material thermal response is simulated over a period of 30 seconds with a material thickness of $20\ cm$ which ensures satisfactorily the condition of no temperature rise of the last node. The time step selected is equal to $0.1\ s$ and the nodal size is equal to $1\ mm$ for each node with a total number of 200 nodes.

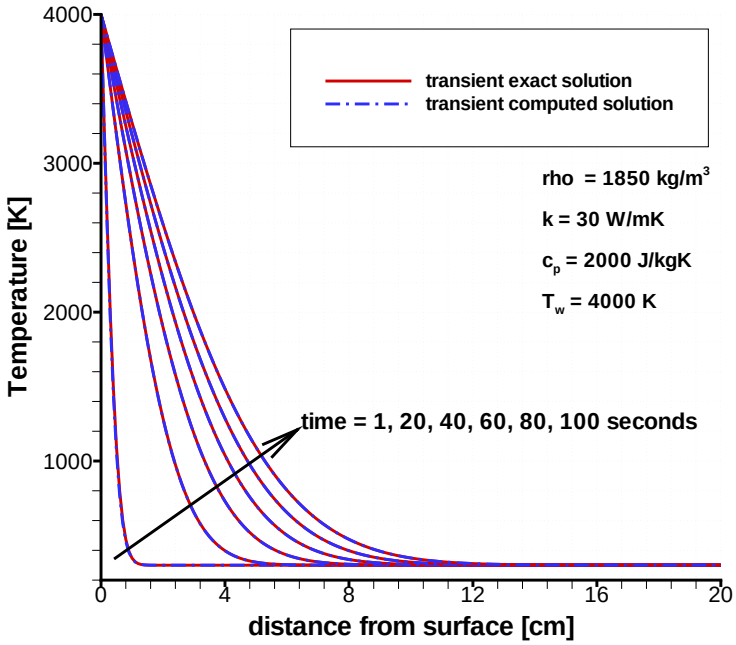

Figure 2.1: Temperature profiles of a constant properties semi-infinite solid exposed to a step in surface temperature.

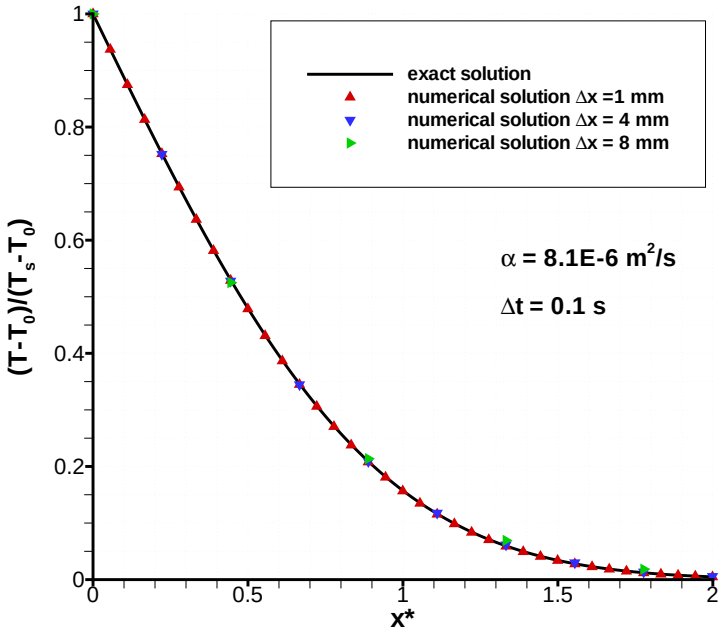

Figure 2.2: Transient response after $1\ s$ of a constant properties semi-infinite solid exposed to a step in surface temperature.

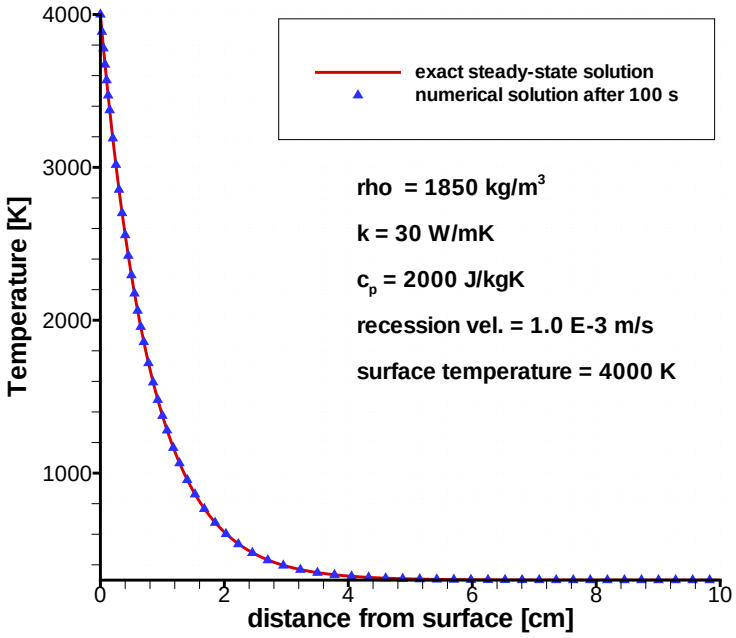

Figure 2.3: Steady-state temperature profile of semi-infinite solid exposed to a step in surface temperature and to a step in surface recession rate.

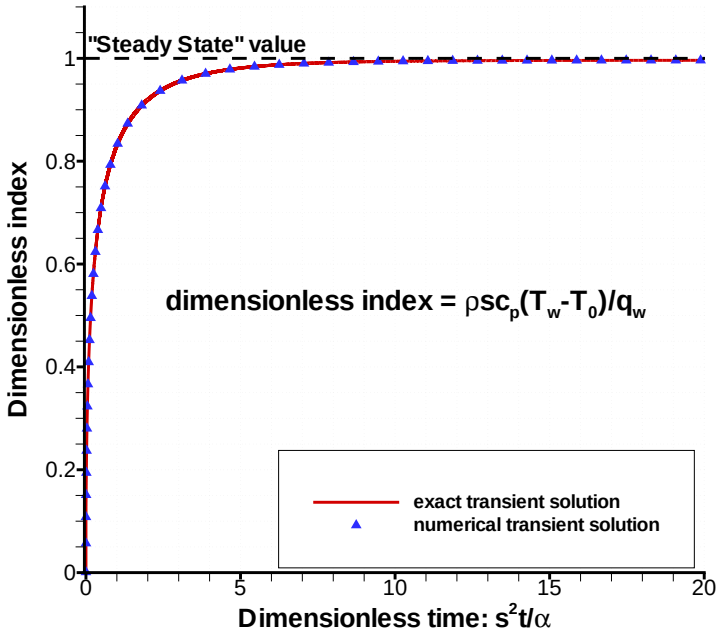

Figure 2.4: Transient response of semi-infinite solid exposed to a step in surface temperature and to a step in surface recession rate.

Figure 2.1 shows the exact transient temperature profiles and the computed ones. The agreement between the exact and computed solution is excellent even at the early times. To better check this agreement Figure 2.2 shows the exact similarity profile compared to the computed profile after 1 second. The numerical solution is performed with different nodal sizes corresponding to 200, 50, and 25 nodes. Even at this early time the computed profile is very close to the exact profile. For the case of 200 and 50 nodes the agreement is excellent.

Check-out of the convection aspects of the computation requires a problem with surface recession. An analytical solution is available for the transient response of a semi-infinite solid initially at uniform temperature exposed to a step in surface temperature and to a step in surface recession rate $\dot{s}$. For the constant properties problem it can be readily shown that the temperature profile approaches a quasi-steady form:

$$\frac{T - T_0}{T_s - T_0} = e^{-\frac{\dot{s}x}{\alpha}}$$

where the x coordinate origin is tied to the receding surface. A useful measure of the approach to steady-state is provided by the variable:

$$\frac{\rho c_p \dot{s}(T_s - T_0)}{q_{cond}}$$

comparing the amount of solid convection pick-up to the amount of energy conducted into the solid. This term is initially zero and approaches unity in the steady-state.

Figure 2.3 shows the exact steady-state temperature profile compared to the computed profile after 100 seconds. This time is long enough to reach the steady-state for the present conditions and the agreement between computed and exact profile is excellent. Figure 2.4 shows the exact transient response compared to computed results for a problem with the same nodal size distribution as the semi-infinite slab problem previously described. The specified surface recession rate $\dot{s}$ is set to $1\ mm/s$. The agreement between computed results and the exact solution is again excellent.

The most widely used numerical approach in the U.S. aerospace industry for predicting ablation was developed by the Aerotherm Corporation in the late 1960 [33, 1]. Since then, the CMA code has been widely used in the aerospace industry for analysis of ablating TPS materials on re-entry vehicles and SRM nozzles. This technique solved the one-dimensional internal energy balance coupled with the ablating surface energy balance condition to simulate the response of ablative heat shields in hypersonic flows. This approach has been widely used for many engineering applications [19], and the predictions provide satisfactory accuracy with minimum computational cost.

Table 2.1: Surface boundary conditions

B.L. edge conditions	
edge pressure:	$1\ [bar]$
edge temperature:	$4000\ [K]$
edge total enthalpy:	$8500\ [kJ/kg]$
heat-transfer coefficient:	$3.5\ [kg/m^2 s]$
edge composition:	equilibrium air
Prandtl number:	0.7
Lewis number:	1.0
surface emissivity:	0.9
blowing-rate parameter λ:	0.5

A suitable test case has been defined in order to verify the consistency and accuracy of the developed code in comparison with the CMA code. This test case calculates the transient thermal response of a carbon-carbon TPS with thermochemical tables for carbon ablation in air. The thermochemical tables were generated with an equilibrium routine based on the NASA Chemical Equilibrium with Application (CEA) open source code [28]. The material is exposed to a convective heat flux over a period of 100 seconds in air environment. The material has a total thickness of $10\ cm$; the time step selected is equal to $0.1\ s$ and the nodal size is equal to $1\ mm$ for each node. The material properties are the same used in the previous solutions and the "heated surface" boundary conditions are expressed in table 2.1. The material initial temperature is set to $300\ K$. The recovery enthalpy is evaluated from the edge conditions assuming a laminar flow:

$$\frac{h_r - h}{h_0 - h} = r \qquad \text{with} \qquad r = \sqrt{Pr}$$

The heat-transfer coefficient is corrected using the classical blowing correction equation (1.44) with $\lambda = 0.5$. In this test case, since $Le = 1.0$, the mass-transfer coefficient is equal to the heat-transfer coefficient.

Figure 2.5 shows the comparison of the surface recession variation with time evaluated with the developed code and the CMA code. The same comparison is made over the surface temperature in Figure 2.6. Finally, Figure 2.7 shows the comparison of the temperature profiles at different times. The agreement between the developed code and the CMA code is excellent.

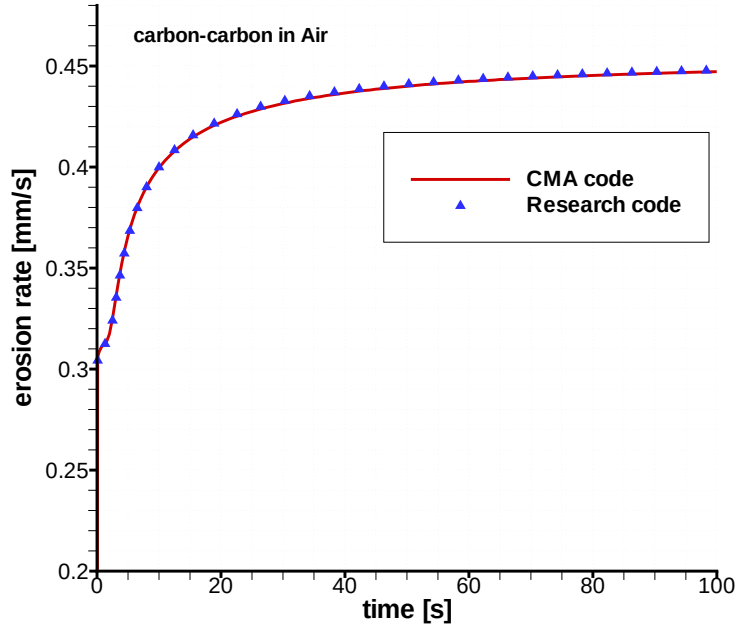

Figure 2.5: Surface recession rate variation with time.

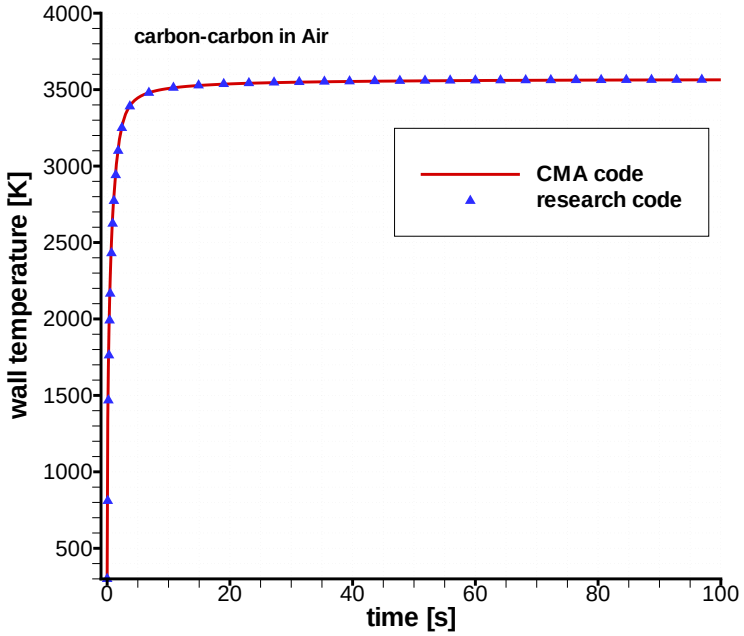

Figure 2.6: Surface temperature variation with time.

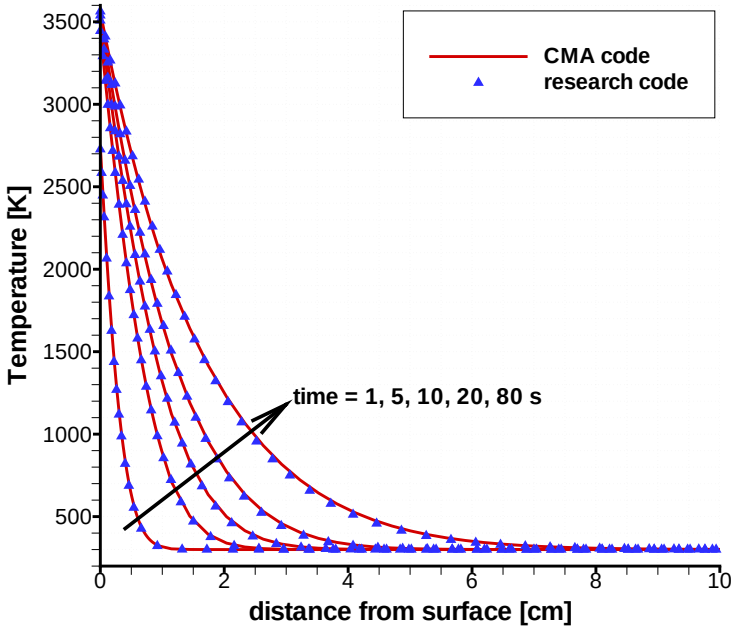

Figure 2.7: Temperature profiles at different times.

2.5.2 Blunt body analysis

The developed numerical procedure has been used to simulate the thermal response of the TPS in the stagnation point of an Earth re-entry vehicle. The example problem is a hypersonic test vehicle with a small nose radius ($1.75\ cm$) and graphite TPS which travels near Mach 16 and at an altitude of $30.5\ km$. This test case has been taken from [51]. The problem data and "edge" boundary conditions are reported in table 2.2. The surface heat flux is evaluated with the approximation formula from [71]:

$$q_w = \rho_\infty^N V_\infty^M C \tag{2.23}$$

where the units for q_w, V_∞, and ρ_∞ are W/cm^2, m/s, and kg/m^3, respectively. For the stagnation point case the following values hold:

$$M = 3, \qquad N = 0.5, \qquad N = 1.83 \cdot 10^{-8} R^{-1/2} \left(1 - \frac{h_w}{h_r}\right) \tag{2.24}$$

Table 2.2: Blunt body test case parameters

Problem data	
nose radius (cm)	1.75
material	graphite
thickness (cm)	8.0
duration ($seconds$)	60.0
Boundary layer "edge" conditions	
height (km)	30.5
Mach	≈ 16
Prandtl number:	0.72
Lewis number:	1.0
h_0 (kJ/kg)	$11.5 \cdot 10^3$
p_∞ (Pa)	$1.197 \cdot 10^3$
T_∞ (K)	226.5
ρ_∞ (kg/m^3)	$1.841 \cdot 10^{-2}$
blowing-rate parameter λ:	0.5

where R is the nose radius in meters and h_w and h_r are as usual the wall enthalpy and the recovery enthalpy, respectively. The non-ablating heat-transfer coefficient can be easily evaluated from Eqs. (2.23), (2.24) and from its definition:

$$\rho_e u_e C_{h_0} = \frac{q_w}{(h_r - h_w)}$$

The surface pressure at the stagnation point is evaluated from the Newtonian flow theory:

$$p = p_\infty + \frac{1}{2}\rho_\infty V_\infty^2 \sin^2\theta \tag{2.25}$$

where $\sin\theta$ is equal to 1 at the stagnation point. The chemical equilibrium CEA code is used to evaluate the "edge" chemical composition after the normal shock. The chemical composition at the edge of the boundary-layer, in fact, is a major parameter which must be provided in order to solve the surface energy balance Eq. (2.19). Since the physical properties (thermal conductivity and specific heat) of graphitic TPS strongly vary with temperature, a variable properties material has been considered. The properties used for graphite are taken from NIST TRC

Thermodynamic Tables and from experimental results and are reported in Figure 2.8.

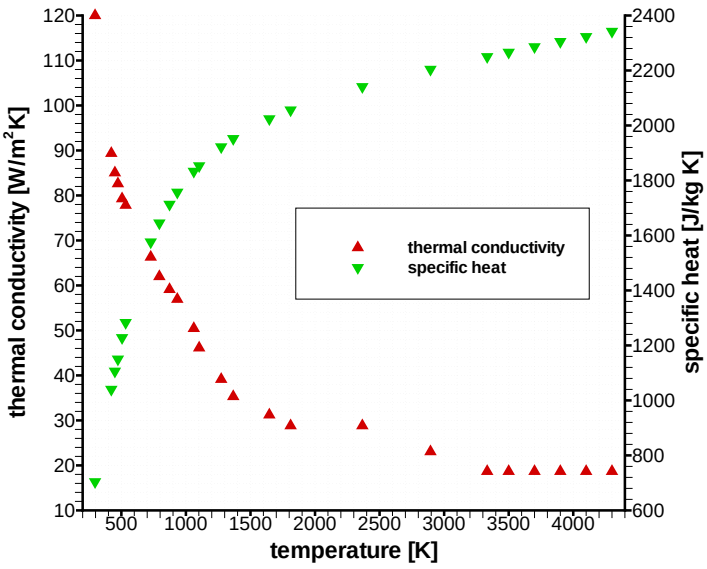

Figure 2.8: Graphite properties variation with temperature.

Figure 2.9 shows the temperature profile inside the TPS at various times. Note that the temperature profiles are fixed to the receding surface so that recession of the material can be seen from the back surface. It is worth noting that the heating of the TPS in this environment (Earth reentry) is pretty fast, with the surface temperature reaching almost $2000\ K$ in the first second of exposure. Figure 2.10 shows the surface temperature variation with time and the surface total recession (cm) variation with time. The computed solution is also compared with the results presented in [51]. The agreement is very good both for the surface recession and the surface temperature.

The reentry velocity is now varied to see its effect on the TPS thermal response. The velocity is increased 1.25 and 1.5 times the initial value, keeping untouched the other parameters. Figures 2.11 and 2.12 show the erosion rate and wall temperature variation with time for the three velocities. Obviously both the erosion rate and the surface temperature increase with increasing reentry velocity but some differences in their behaviours can be noted. It can be seen that the erosion rate is almost flat for the smallest velocity and shows a more marked variation at early times for the higher velocities. The opposite behaviour can be observed

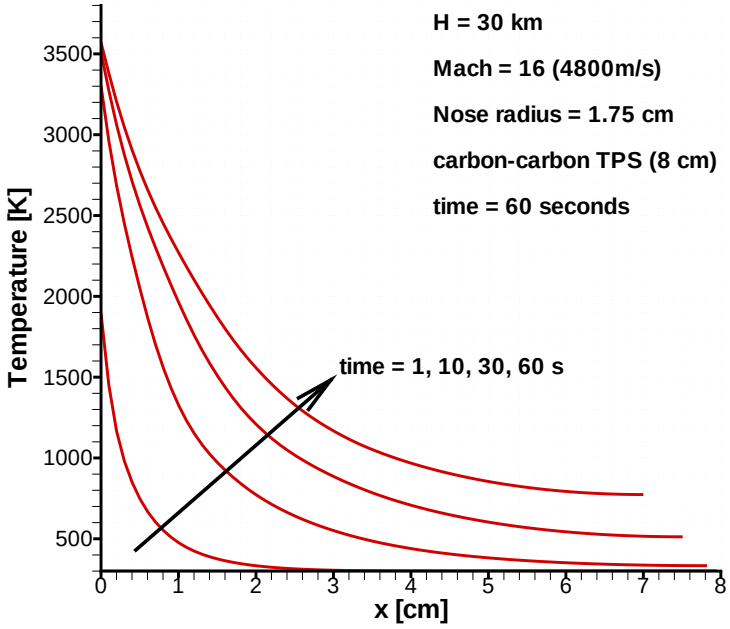

Figure 2.9: Temperature profiles at different times.

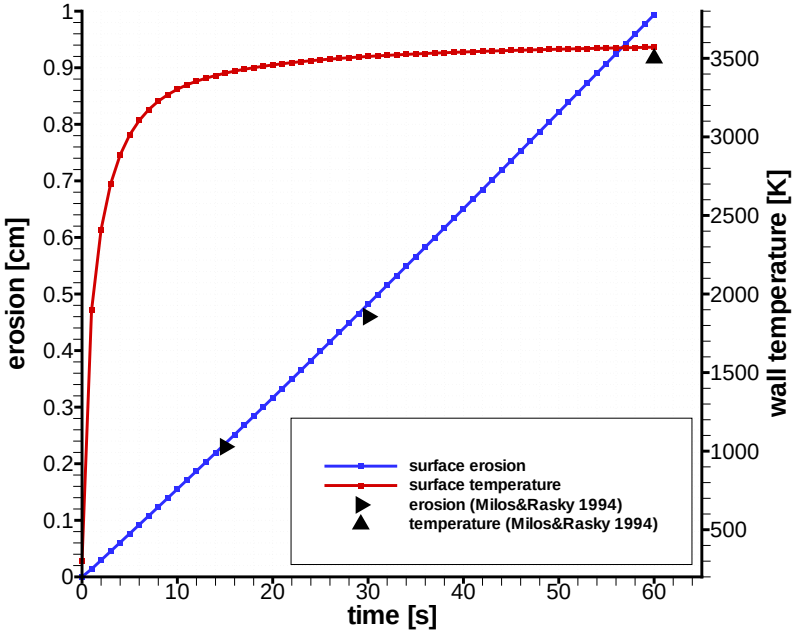

Figure 2.10: Surface recession and surface temperature variation with time.

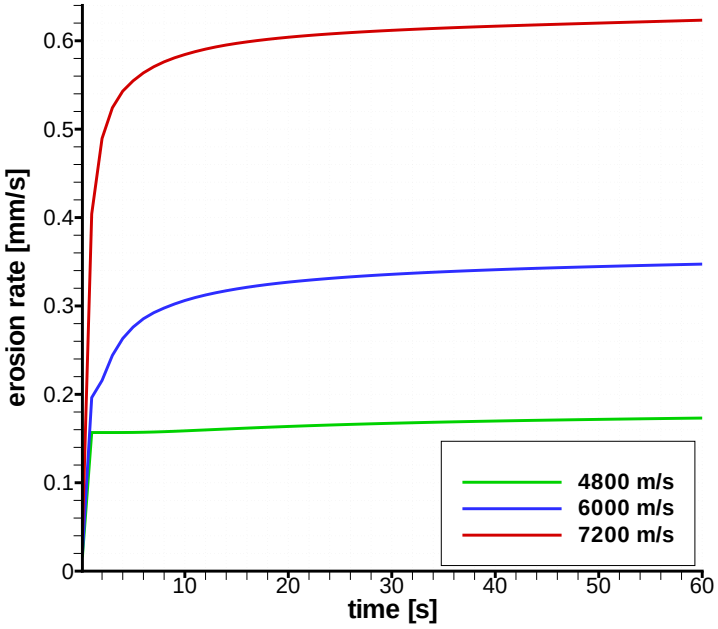

Figure 2.11: Erosion rate time-variation for three different velocities.

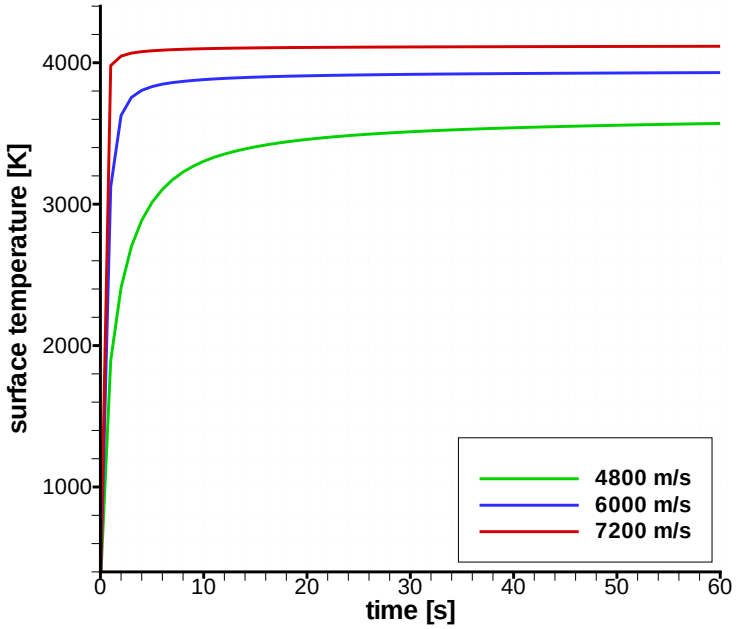

Figure 2.12: Surface temperature time-variation for three different velocities.

for the surface temperature. This kind of TPS materials (such as graphite and carbon-carbon) have the distinctive feature to show a limit in the temperature reached by the exposed wall. This is due to the fact that, when the surface is exposed to a higher heat flux, the blowing becomes more and more intense with the increase of surface temperature (see Figure 1.4) and the heat absorption due to the surface chemical reactions becomes dominant as well as the blockage effect due to ablation products injection. When the surface is close to the sublimation temperature[1], an increase of the incident wall heat flux produces a strong increase of the mass blowing rate and a slight increase of surface temperature. This behaviour is clear from Figures 2.11 and 2.12. The wall temperature shown in Figure 2.12 rises rapidly from the initial value ($300\ K$) to the steady-state value and this rise is quicker with increasing reentry velocity (which affects directly the convective heat flux). The erosion rate, instead, is almost uniform at the lowest velocity because surface oxidation is dominant. As seen in Figure 2.13, in the

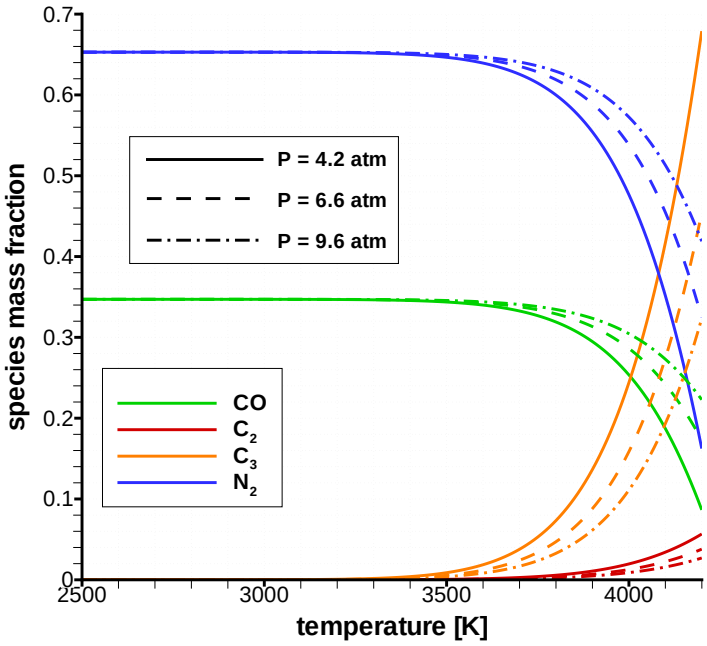

Figure 2.13: Surface equilibrium chemical composition for three velocities.

oxidation regime (with CO formation) surface composition is not varying with surface temperature; on the contrary, in the sublimation regime (C_3 formation)

[1]the sublimation temperature of graphite is about $4000\ K$ at $1\ bar$ and $4400\ K$ at $10\ bar$.

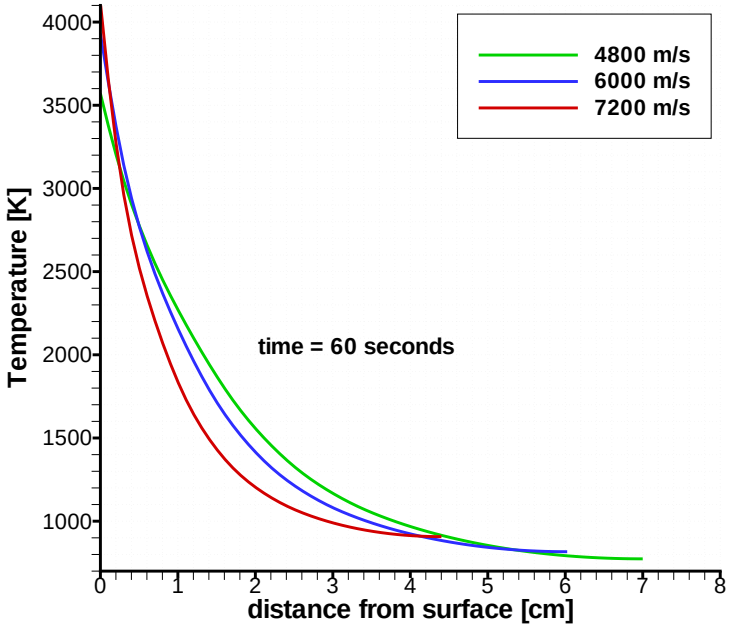

Figure 2.14: Temperature profiles after $60\ s$ for three different velocities.

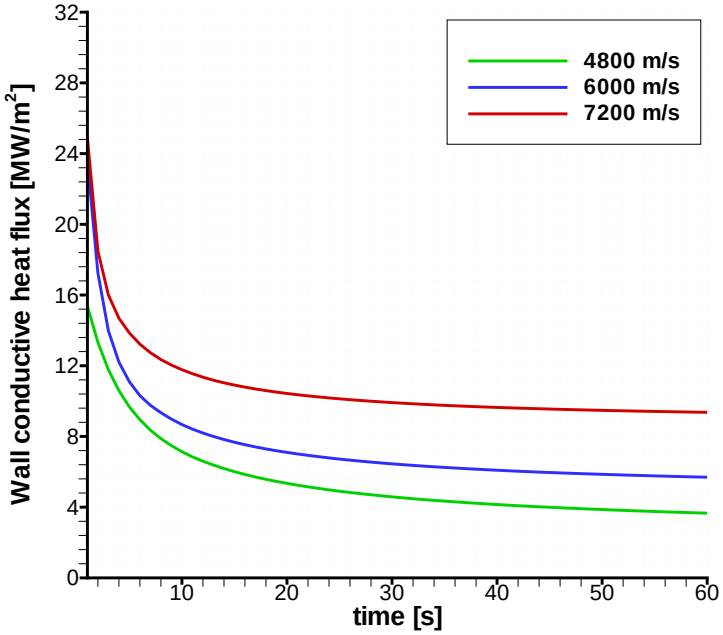

Figure 2.15: Wall conductive heat flux time-variation for three different velocities.

there is a strong variation of the wall composition with temperature. The transition between the oxidation regime and the sublimation regime depends on pressure as Figure 2.13 clearly shows (the three pressures represented in this figure correspond to the stagnation pressures for the three reentry velocities). Looking at figure 2.11 at the lowest reentry velocity the TPS is in the oxidation regime and the erosion rate is almost constant; at the higher velocities, instead, the sublimation regime is dominant due to the higher wall temperature and this causes a more pronounced variation of the erosion rate in the early times (first 10 seconds).

Finally, Figure 2.14 shows the temperature distribution after $60\ s$ of exposure. The three profiles are similar with the higher-velocity profiles showing a higher wall temperature and a lower internal temperature. Obviously the total recession is greater for the higher-velocity cases. The three profiles show a tendency of the temperature to experience higher gradients inside the material. This is a consequence of the higher heat flux and consequently of the higher recession rate: the steady-state condition is reached quickly and the temperature profile inside the material is steeper at the higher reentry velocities. Figure 2.15 shows the variation with time of the heat flux conducted in the solid. The heat flux shows a strong variation with time during the first seconds and then rapidly tends to be uniform showing the approaching of the steady-state condition. At the higher velocities the time period over which the heat flux is strongly varying is reduced and the steady-state condition is approached earlier.

2.5.3 SRM nozzle throat analysis

The developed numerical procedure has been used to simulate transient thermal response at the throat location of a carbon-carbon nozzle exposed to the solid propellant combustion gases. The example problem is a typical SRM nozzle application with a chamber pressure of $55\ bar$, a chamber pressure of $3500\ K$, and a throat radius of $8.2\ cm$. The problem data and "edge" boundary conditions are reported in table 2.3. Graphite is usually used to protect the throat region of SRM nozzle. However, an insulation material (such as carbon-phenolic or silica-phenolic) is usually inserted between the carbon-carbon and the aluminium structure to limit the temperature rise of the structure itself. Carbon-carbon is an extremely effective ablator for SRM nozzle application but it has a relatively high thermal conductivity if compared to other insulator materials. Carbon-carbon has a thermal conductivity of about $80\ W/m^2K$ at $500\ K$ which is rather high if compared to about $1\ W/m^2K$ of carbon-phenolic at the same temperature. A complete nozzle TPS has been analysed in this test, with a main ablator material, an insulator back-up, and finally the structural material (relative thickness are expressed in table 2.3).

Table 2.3: SRM nozzle throat test case parameters

Problem data	
chamber pressure (bar)	55
chamber temperature (K)	3500
throat radius (cm)	8.2
main TPS material (cm)	graphite (6.0)
insulation material (cm)	carbon-phenolic (1.5)
structural material (cm)	aluminium (1.5)
fire duration ($seconds$)	110.0
Nozzle conditions	
specific heat ratio	1.13
Prandtl number:	0.5
Lewis number:	1.8
combustion gases viscosity ($Pa \cdot s$)	$1.0 \cdot 10^{-4}$
characteristic velocity (m/s)	1600
total enthalpy (kJ/kg)	$1.69 \cdot 10^3$
throat velocity (m/s)	1000
throat temperature (K)	3300
throat pressure (bar)	32
blowing-rate parameter λ:	0.4
Gas-phase mass fractions	
CO:	0.3485
CO_2:	0.0303
HCl:	0.3030
H_2:	0.0152
H_2O:	0.1364
N_2:	0.1514
OH:	0.0152

The mass fraction of the combustion species at the nozzle inlet, shown in table 2.3, are based on chemical equilibrium calculations at the chamber pressure for an AP/HTPB composite propellant. All the relevant chamber parameters are evaluated with an equilibrium routine as well as the throat conditions assuming a one-dimensional equilibrium expansion. The surface heat flux is evaluated with the approximation formula from Bartz [4]:

$$\rho_e u_e C_{h_0} = \left[\frac{0.026}{D_t^{0.2}} \left(\frac{\mu^{0.2}}{Pr^{0.6}}\right)_0 \left(\frac{p_c}{c^*}\right)^{0.8}\right] \cdot \left(\frac{A_t}{A}\right)^{0.9} \cdot \sigma \qquad (2.26)$$

where c^* is the characteristic velocity and D_t and A_t are the throat diameter and area, respectively. The term σ is a dimensionless factor accounting for property variations across the boundary-layer [4]. The recovery enthalpy is evaluated from the edge conditions assuming a turbulent flow:

$$h_r = h_0 - (1-r)\frac{U^2}{2} \qquad \text{with} \qquad r = \sqrt[3]{Pr}$$

Since the nozzle surface is not planar, a variable cross-sectional area (linear with the radius) has been considered in the energy equation.

Figure 2.16 shows the temperature profile inside the TPS at various times. The TPS transient response in this environment shows a similar behaviour to that of the reentry application: the heating of the TPS is very quick, with the surface temperature reaching almost $2000\ K$ in the first second of exposure and then approaching rapidly a steady-state value (below $3000\ K$). An abrupt change in the slope of the temperature profiles is clearly visible and this is due to the change of thermal conductivity passing from the main to the insulating back-up material. There is another change in the slope passing from the back-up to the structural (aluminium) material. The temperature distribution is constant inside the aluminium due to its high thermal conductivity. Figure 2.17 shows the surface temperature variation with time and the surface erosion rate (mm/s) variation with time. The surface erosion rate is completely flat during the whole firing time. This is due to the fact that the carbon-carbon TPS is always operating in the oxidation regime where the B' curve is flat and the surface composition shows no variation with temperature as Figure 2.18 clearly shows. For the present throat pressure, carbon-carbon sublimation starts above $3500\ K$ and a so-high temperature is never reached at wall during the motor operation time. In Figure 2.18 the three oxidizing species (CO_2, H_2O, and OH) are not represented because they react completely with the solid carbon to form CO species. Finally Figure 2.19 shows the variation with time of the heat flux conducted in the solid. As for the reentry case, the heat flux shows a large variation during an initial transient and then tends to be uniform showing the approaching of the steady-state condition.

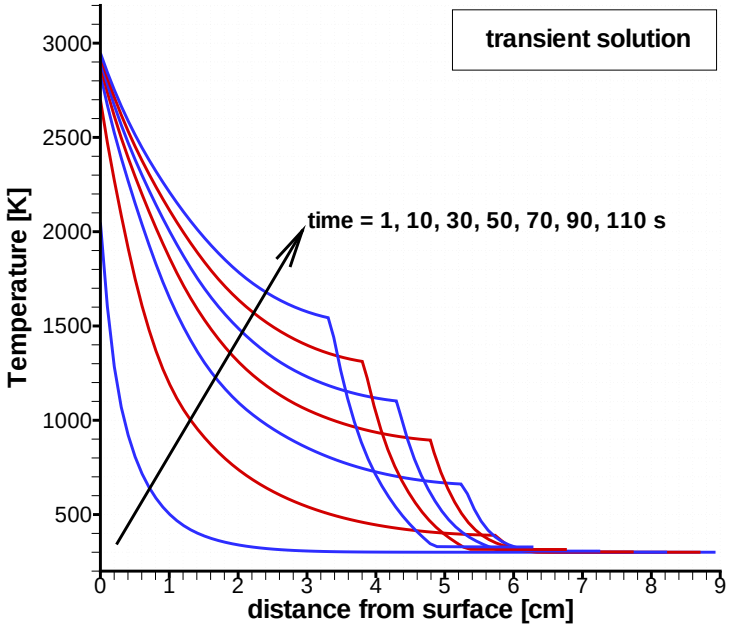

Figure 2.16: Temperature profiles at different times.

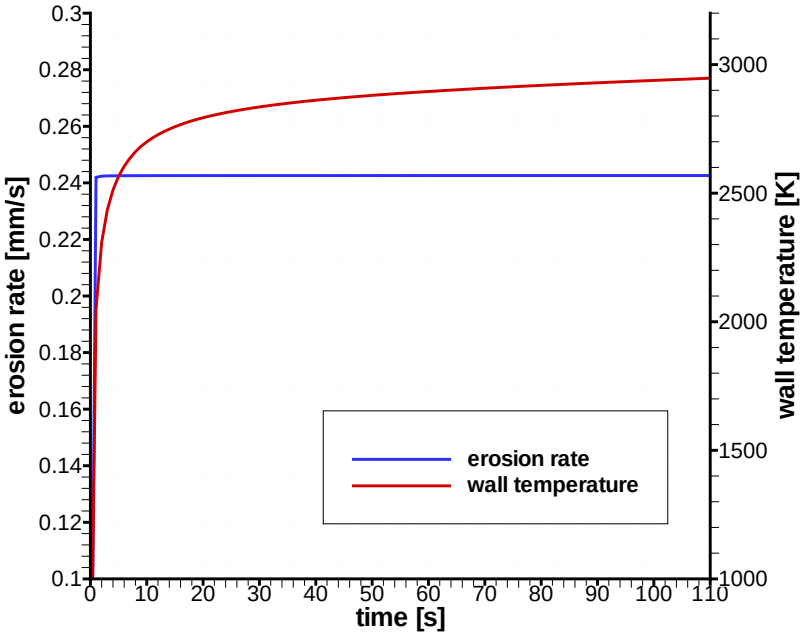

Figure 2.17: Surface recession rate and surface temperature variation with time.

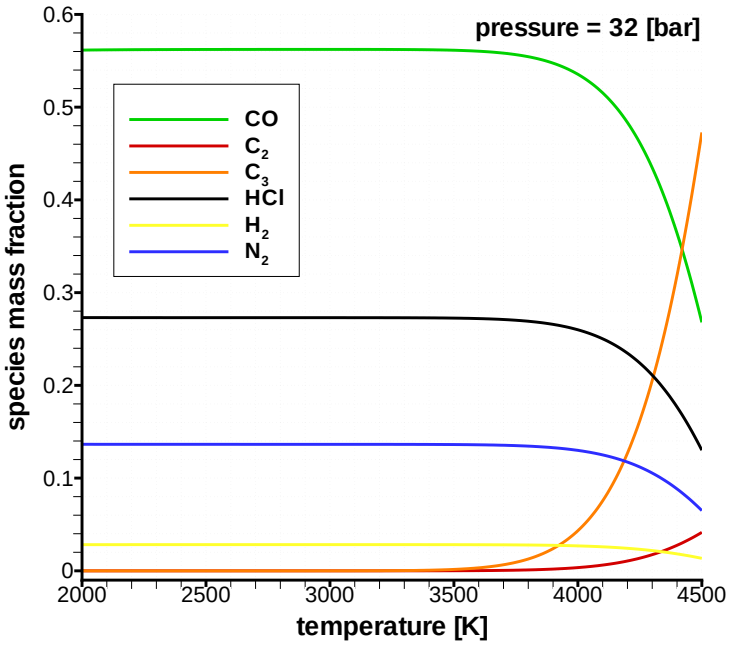

Figure 2.18: Surface composition for carbon ablation in SRM environment.

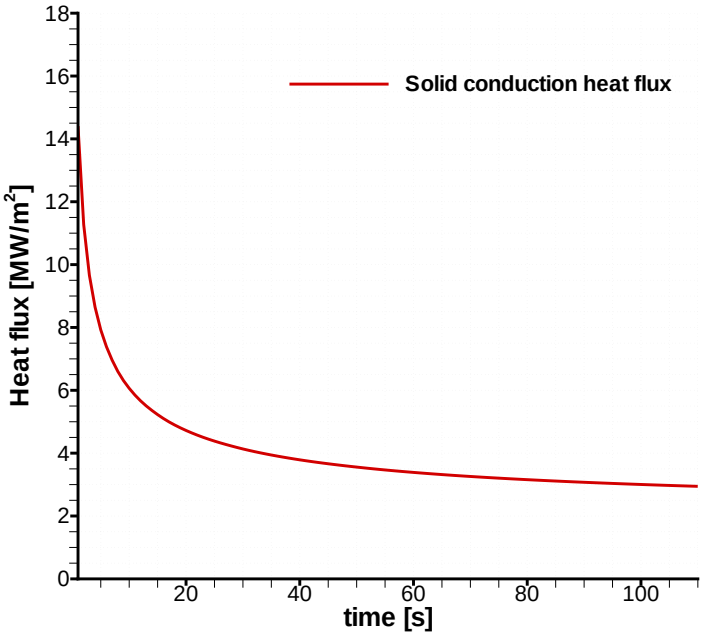

Figure 2.19: Wall conductive heat flux time-variation.

It is worth noting that the erosion rate depends strongly on the local pressure. The results presented herein assume that the chamber pressure remains constant during the firing duration; in SRM nozzle the chamber pressure depends on propellant, burning surface, and throat area. Assuming a constant throat area (negligible area-variation due to throat erosion) and a given propellant, the chamber pressure time-history is a direct result of the burning surface time-history and therefore of propellant grain geometry. The effect of variable chamber pressure due to grain geometry has not been considered in this test case but it could be easily done assigning the pressure time-variation as boundary condition. However, this is outside the scope of this part, whose main goal is the analysis of carbon-carbon TPS transient thermal response under realistic environments to obtain useful information for the following part of this work.

Pressure has a strong influence on erosion rate because it affects the heat flux convected from the hot-gases to the wall (see Eq. (2.26)). Pressure also affects the mass transfer across the boundary-layer: higher pressures, in fact, increase the mass-transfer coefficient and consequently the erosion mass rate. The same test case has been repeated considering the effect of throat erosion on chamber pressure. While throat is eroding, in fact, the throat area is increased and this causes the chamber pressure to drop and consequently alters the erosion rate. The effect of pressure drop due to erosion is shown in Figures 2.20 and 2.21 for the erosion rate and the eroded thickness, respectively. For a solid rocket motor the chamber pressure is obtained by the following relation:

$$p_c = \left(\rho_p \cdot a \cdot c^* \cdot \frac{S_b}{A_t} \right)^{\frac{1}{1-n}} \tag{2.27}$$

where ρ_p is the propellant density, S_b is the burning surface, and a and n are the burning rate constant and exponent, respectively. The burning rate $\dot{r}$ is represented by $\dot{r} = a \cdot p_c^n$. Form Eq. (2.27) the following relation holds:

$$p_c \propto \left(\frac{1}{r_t} \right)^{\frac{2}{1-n}} \tag{2.28}$$

where r_t is the throat radius. From the Bartz equation (2.26):

$$C_h \propto \frac{p_c^{0.8}}{r_t^{0.2}} \tag{2.29}$$

combining Eqs. (2.28) and (2.29) gives:

$$C_h \propto \left(\frac{1}{r_t} \right)^{\frac{1.8-0.2n}{1-n}} \tag{2.30}$$

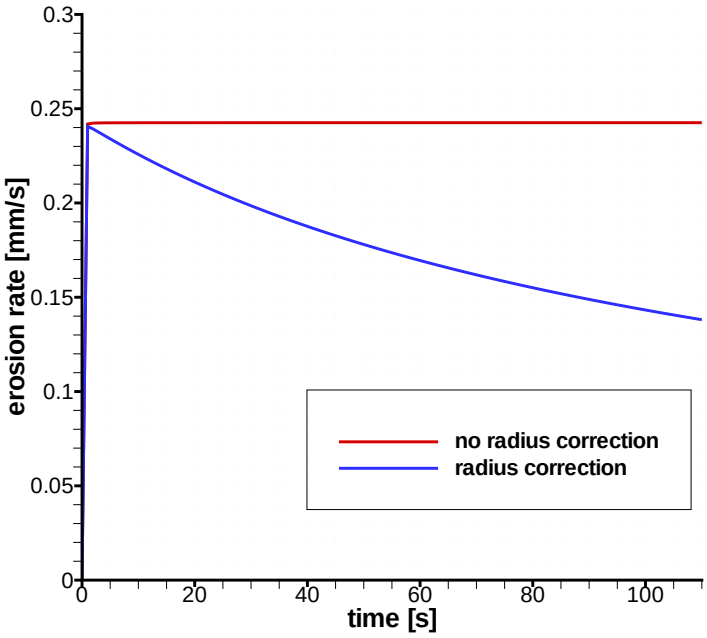

Figure 2.20: Erosion rate time-variation with and without radius correction.

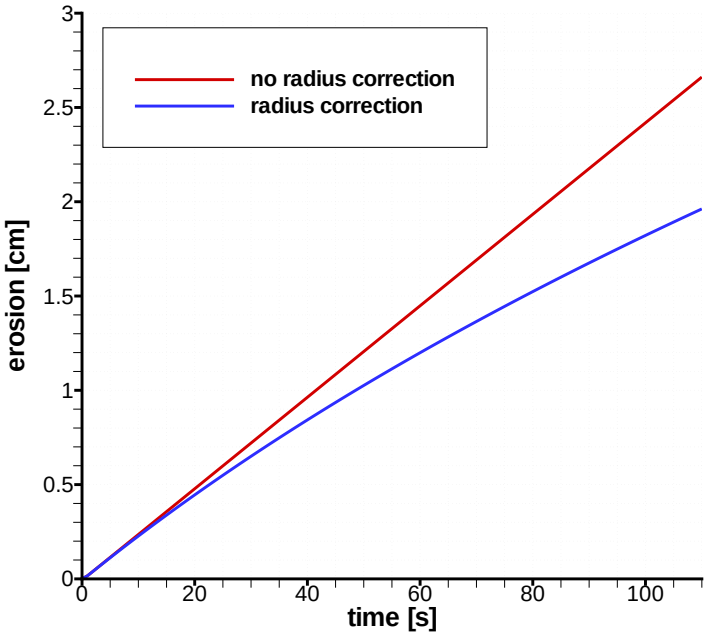

Figure 2.21: Erosion time-variation with and without radius correction.

Eq. (2.30) is used to correct the heat-transfer coefficient during the transient computation to take into account the effect of throat erosion with the increase of r_t. At the same time Eq. (2.28) is used to vary the chamber pressure due to throat erosion. Chamber pressure, in fact, affects the thermochemical tables modifying the equilibrium composition: this effect, however, is only seen in the sublimation regime (nozzle environment is not sufficiently energetic to trigger sublimation).

Figures 2.20 and 2.21 show the effect of throat erosion during the firing on the erosion rate and the eroded surface, respectively. The erosion rate (Fig. 2.20) is decreasing with time due to chamber pressure drop and consequently the erosion (Fig. 2.21) is no more linear with time. This effect is obviously more important for small nozzles (such as the one used in this example) where the throat area variation due to erosion is not negligible. For the present case ($r_t = 8.2\ cm$) the final throat area is about 55% bigger than the initial area. For a bigger nozzle (booster), with a nozzle radius of $40\ cm$, this increase would be of only 10% and the effect of throat erosion on chamber pressure could be neglected.

2.6 Conclusions

An unsteady quasi-one-dimensional ablation thermal response code for carbon-carbon materials based on a nodal network tied to the receding surface has been developed and verified. An ablation model based on thermochemical tables have been also proposed and coupled with the thermal response code. Special attention is devoted to simulate the effect of ablation on the surface mass and energy balance, using a transfer-coefficient boundary-layer model. The model has shown excellent agreement with known analytical solutions and with the widely used CMA code. In particular this model is finalized to be used as a time-efficient engineering tool for the TPS analysis, prediction and design. Numerical results have been presented for different environmental conditions with different environmental gases: i) stagnation point of an Earth re-entry vehicle ii) nozzle throat section of a solid rocket motor. The major result of these computations is that, despite the different kind of application ranging from rocket nozzle to Earth reentry environment, these kind of materials show a similar behaviour characterized by a quick heating and a short transient period in which surface conditions strongly vary with time. When steady-state condition is reached the temperature profile and the surface conditions do not change with time provided that the boundary condition are not changing. Results have shown that the temperature profile inside the material experiences a noticeable variation with time particularly in the inner part of the solid. However, the presented results have also shown that the surface parameters (temperature, erosion rate, heat conduction into solid) are much faster in reaching the steady conditions than the in-depth temperature profile. This permits

to conclude that, for what concern the surface conditions, a steady-state assumption is acceptable to study the complex interaction between hot-gas flow and TPS material. On the contrary, if one is interested in the temperature rise inside the material and in particular at the interface with the structure, a transient solution is mandatory.

In the next part of this work, where the author concentrated much of his efforts, the interaction between the hot-gas layer and the TPS will be studied assuming steady-state condition but completely removing the transfer-coefficient approach using a full Navier-Stokes solver to model with more accuracy the heat and mass transfer mechanisms.

Part II

CFD method for ablating surfaces

Chapter 3

Thermodinamic model

Computational fluid dynamics (CFD) and computational solid mechanics (CSM) codes typically treat fluid/solid boundary conditions in a very simplified manner such as constant prescribed temperature or heat flux and with zero mass transfer. However, in energetic hypersonic environments, TPS materials interact with the flow through diverse thermochemical and thermophysical mechanisms including ablation, shape change, pyrolysis, melt flow, spallation, solid thermal conduction. The specific application of this part is the modeling and analysis of the interaction between carbon-carbon TPS and highly energetic hypersonic flowfields. Solution of the coupled material flowfield problem is of critical importance for the TPS design, sizing, and optimization for hypersonic vehicles and rocket nozzles. TPS are traditionally designed with one and two-dimensional engineering codes similar to the tool described in the previous chapter. Occasionally, a detailed computational solution is obtained, but these solutions rarely contain the correct surface boundary conditions. To compensate for uncertainties in the analyses, a safety margin of extra TPS material is added to the final design, and the structure weight must also be increased. The TPS/structural weight is typically significantly larger [3] than the payload weight and therefore a reduction in the TPS weight has a cascade effect: the structural weight is also reduced, resulting in a direct increase in payload and scientific capability. Clearly there is a need for more accurate, multidimensional computational tools which can be used to reduce the uncertainties in TPS analysis and to optimize the TPS design. Nowadays, CFD technology continues to develop in the areas of non-equilibrium flow, multispecies kinetics and transport properties, radiation transport, and three dimensional capabilities. However, most codes use primitive surface boundary conditions and cannot realistically be used for TPS analysis and design. To obtain a suitable tool for the analysis of flowfield with ablation, CFD codes must take into account spatially varying surface temperature and heat flux, a realistic surface energy and mass balance, thermal soak into the TPS material, and thermochemical ablation modeling. It must be noted, how-

ever, that the computational expense of these advanced CFD methods can limit their utility. This and the next chapters will deal with the modeling of these surface and near-surface thermochemical phenomena and their interface with a CFD code.

In order to study the complex flowfield over an ablating surface, a Navier-Stokes approach is used in this work. The physics of the hot-gases over a solid surface is modeled by the chemically reacting Navier-Stokes governing equations, which are solved by a 2-D axisymmetric solver based on the approach described by Nasuti & Onofri [61, 60] and Martelli [47]. The main features of this method are to discretize the convective terms according to the *lambda scheme* [54]. Because of the chemically active surface, further physical modeling is necessary for the fluid-surface interaction. The latter aspect, which will be described in chapter 5, requires the addition of a mathematical model of the hot-gas-flow boundary condition which describes the physics of the surface phenomena. In this chapter the thermodynamic model is described, while in the next chapter the flow governing equations and the numerical method used will be discussed.

3.1 High-temperature gas dynamics

During an atmospheric entry as well as in rocket engine applications the high-temperature effects are important and must be accounted for. The thermodynamic and transport properties are varying with temperature and mixture composition which, in turn, changes due to chemical reactions. Moreover, the additional transport mechanism of diffusion becomes important. These kind of flows are characterized by strong variations of temperatures and velocities. Consequently, the hypothesis of ideal gas cannot be made due to chemical reactions. Moreover, the vibrational levels of molecules are exited by the high temperatures, causing the variation of specific heats.

The kinetic energy of a high-speed, hypersonic flow is dissipated by the influence of friction within the boundary layer. The viscous dissipation that occurs within hypersonic boundary layers can create very high temperatures, high enough to excite vibrational energy internally within molecules and to cause dissociation and even ionization within the gas. If the surface of a hypersonic vehicle is protected by an ablative heat shield, the product of ablation are also present in the boundary layer, giving rise to complex chemical reaction with the atmosphere. Therefore the surface of a hypersonic vehicle can be wetted by a *chemically reacting boundary layer*. For a hypersonic flow, the boundary layer and also the shock layer can be dominated by high-temperature chemically reacting flow. In introductory studies of thermodynamics and compressible flow, the gas is assumed to have constant specific heats; hence, the ratio $\gamma = c_p/c_v$ is also constant. This

leads to some results for pressure, density, temperature and Mach number variations in a flow. However, when the gas temperature is increased to high values, the gas behaves in a *non-ideal* way, specifically as follows:

- The vibrational energy of the molecules becomes excited, and this causes the specific heats c_v and c_p to become functions of temperature. It turn, the ratio of specific heats, $\gamma = c_p/c_v$, also becomes a function of temperature.

- As the gas temperature is further increased, chemical reactions can occur. For a chemically reacting gas, c_v and c_p are function of both temperature and pressure, and hence γ.

All of these phenomena are called *high-temperature effects*. High-temperature chemically reacting flows can have an influence on lift, drag, ad moments on a hypersonic vehicle. For example, such effects have been found to be important for estimating the amount of body-flap deflection necessary to trim the space shuttle during high-speed reentry. However, by far the most dominant aspect of high temperatures in hypersonics is the resultant high heat-transfer rates to the surface. Aerodynamic heating dominates the design of all hypersonic machinery, whether it be a flight vehicle, a rocket engine to power such a vehicle, or a wind tunnel to test the vehicle. This aerodynamic heating takes the form of heat transfer from the hot boundary layer to the cooler surface, which consequently must be protected to sustain the heat flux and keep the excessive heat from damaging the vehicle. Clearly, high-temperature effects are a dominant aspect of hypersonic aerodynamics.

In the subsequent sections important physical and thermodynamic variables and relations (equation of state) are discussed which will be useful in the following description of the governing equations given in Chapter 4.

3.2 Internal energy

The internal energy per unit mass of a single gaseous species in a mixture of thermally perfect gases can be expressed as a function of temperature only:

$$e_i = \int_{T_{ref}}^{T} c_{v_i}(T)dT + h_{f_i} \tag{3.1}$$

where $c_{v_i} = de_i/dT$ is the specific heat at constant volume, function of temperature only according to the thermally perfect gas hypothesis, and h_{f_i} is the heat of formation of the i^{th} species at the temperature $T = T_{ref}$. The internal energy per

unit mass of the mixture can be written as:

$$e = \sum_{i=1}^{N} \frac{\rho_i}{\rho} e_i = \sum_{i=1}^{N} y_i e_i \tag{3.2}$$

where N is the total number of species, ρ_i is the density of the i^{th} species, $\rho = \sum \rho_i$ is the density of the mixture, and y_i is the mass fraction. For each *individual* chemical species present in the mixture (assuming a perfect gas) the internal energy will be function of temperature only. However, the internal energy for a chemically reacting mixture depends not only on e_i, but also on how much of each species is present. Therefore for a chemically reacting mixture of perfect gases, in the general non-equilibrium case, we write:

$$e = e\left(T, y_1, y_2, y_3, ..., y_N\right) \tag{3.3}$$

Dealing with chemically reacting mixtures it is convenient to introduce the frozen specific heats (at constant pressure and volume), obtained assuming the flow to be frozen [2]:

$$c_v = \sum_{i=1}^{N} y_i c_{v_i}, \qquad c_p = \sum_{i=1}^{N} y_i c_{p_i} \tag{3.4}$$

It is also possible to define a mixture specific gas constant, that is:

$$R = \sum_{i=1}^{N} y_i R_i = c_p - c_v \tag{3.5}$$

where $R_i = R_u/\mathcal{M}_i$, with R_u being the *universal gas constant* and $\mathcal{M}_i$ the i^{th} species molecular weight. Finally the frozen specific heats ratio can be introduced:

$$\gamma = \frac{c_p}{c_v} \tag{3.6}$$

In the adopted model only mixtures in thermal equilibrium are considered and every contribution to the internal energy (such as the vibrational energy) is included into the c_{v_i} expression.

3.3 Equation of state

In the previous section a chemically reacting mixture made of (thermally) perfect gases has been assumed. For a perfect gas the internal energy is function of temperature only. A *perfect gas* is a gas where intermolecular forces are negligible while a *real gas* is a gas where intermolecular forces are important and

must be accounted for. At distances approximately 10 molecular diameters away from the molecule, the magnitude of the intermolecular force is negligible. Because the molecules are in constant motion, and this motion is what generates the macroscopic thermodynamic properties of the system, then the intermolecular force might affect these properties. For most problems in aerodynamics, the assumption of a perfect gas is very reasonable. Conditions that require the assumption of a real gas are very high pressures ($p = 1000\ atm$) and/or low temperatures ($T = 30\ K$); under these conditions the molecules are packed closely together and move slowly with low inertia. Thus, the intermolecular force can act on the molecules modifying the macroscopic properties of the system. In contrast, at lower pressures and higher temperatures, the molecules are widely spaced and move more rapidly with higher inertia. Thus, the intermolecular force has little effect on the particle motion and therefore on the macroscopic properties of the system. Again, we can assume such a gas to be a *perfect gas*, where the intermolecular forces can be ignored. A perfect gas is assumed in this work, and this is a reasonably assumption given the conditions of pressure and temperature in the applications of interest.

Consequently, a relationship between pressure and temperature (equation of state) of this kind can be written:

$$p = \sum_{i=1}^{N} p_i = \sum_{i=1}^{N} \rho_i R_i T \tag{3.7}$$

which is called the *perfect-gas equation of state*. For a mixture of perfect gases the Dalton's law holds, which express the fact that the pressure of the gas mixture is made up of the individual partial pressures p_i of the i^{th} species. By definition, the partial pressure of species i, p_i, is the pressure that would exist in the system if all of the other species were removed, and the particles of the i^{th} species were the only ones occupying the whole system at the volume V and temperature T.

3.4 Frozen speed of sound

The appropriate speed of sound in a thermally equilibrated reacting mixture of gases is the *frozen speed of sound* given by:

$$a^2 = \left(\frac{\partial p}{\partial \rho}\right)_{s,y_i} \tag{3.8}$$

where not only the process through the sound wave is isentropic ($s = const$) but it is also frozen ($y_i = const$). From the definition of pressure, Eq. (3.7), and internal

energy, Eq. (3.2), it is clear that $p = p(\rho, e, y_i)$, from which it is possible to obtain:

$$a^2 = \left(\frac{\partial p}{\partial \rho}\right)_{e,y_i} + \left(\frac{\partial p}{\partial e}\right)_{\rho,y_i} \left(\frac{\partial e}{\partial \rho}\right)_{s,y_i} \tag{3.9}$$

where the last derivative can be obtained from the first law of thermodynamics:

$$\left(\frac{\partial e}{\partial \rho}\right)_{s,y_i} = \frac{p}{\rho^2} \tag{3.10}$$

and the other two derivatives can be expressed as:

$$\left(\frac{\partial p}{\partial \rho}\right)_{e,y_i} = RT \tag{3.11}$$

$$\left(\frac{\partial p}{\partial e}\right)_{\rho,y_i} = \rho R \left(\frac{\partial T}{\partial e}\right)_{y_i} \tag{3.12}$$

where the temperature derivative can be obtained from the definition of internal energy, Eq. (3.1) and Eq. (3.2):

$$\left(\frac{\partial T}{\partial e}\right)_{y_i} = \frac{1}{c_v} \tag{3.13}$$

Substituting we find the interesting result:

$$a^2 = \gamma RT = \gamma \frac{p}{\rho} \tag{3.14}$$

which is not an approximation, but it is the frozen speed of sound for reacting mixtures.

3.5 Thermodynamic data

The thermodynamic properties of the chemical species are evaluated with the thermodynamic database used in the chemical equilibrium composition computer program developed by Gordon and McBride [28].

The data are selected from a number of sources, but the principal current sources are Chase et al. [14], Cox et al. [22], Gurvich et al. [30], and Marsh et al. [46]. McBride et al. [48] documented the sources and the data for 50 reference elements. The thermodynamic data are provided in the form of least-square coefficients.

3.5.1 Data for individual species

For each chemical species the thermodynamic functions specific heat, enthalpy, and entropy as functions of temperature are given in the form of least-square coefficients. The general form of these equations is as follows:

$$\begin{aligned} \frac{C_p^0}{R} &= \sum a_i T^{q_i} \\ \frac{H^0}{RT} &= \frac{\int C_p^0 dT}{RT} \\ \frac{S^0}{R} &= \int \frac{C_p^0}{RT} dT \end{aligned} \tag{3.15}$$

Where R is the gas constant equal to 8314.51 $[\frac{J}{kmole \cdot K}]$, C_p^0 is the molar heat capacity at constant pressure for standard-state $[\frac{J}{kmole \cdot K}]$, H^0 is the standard-state molar enthalpy $[\frac{J}{kmole}]$, and S^0 is the standard-state molar entropy $[\frac{J}{kmole \cdot K}]$ for the generic species. The set of least-square coefficients consists of seven terms for C_p^0/R and corresponding terms for enthalpy and entropy as well as the integration constants a_8 and a_9 as follows:

$$\frac{C_p^0}{R} = a_1 T^{-2} + a_2 T^{-1} + a_3 + a_4 T + a_5 T^2 + a_6 T^3 + a_7 T^4$$

$$\frac{H^0}{RT} = -a_1 T^{-2} + a_2 T^{-1} \ln T + a_3 + a_4 \frac{T}{2} + a_5 \frac{T^2}{3} + a_6 \frac{T^3}{4} + a_7 \frac{T^4}{5} + \frac{a_8}{T}$$

$$\frac{S^0}{R} = -a_1 \frac{T^{-2}}{2} - a_2 T^{-1} + a_3 \ln T + a_4 T + a_5 \frac{T^2}{2} + a_6 \frac{T^3}{3} + a_7 \frac{T^4}{4} + a_9$$

The temperature intervals are fixed. These intervals are 200 to $1000K$, 1000 to $6000K$, and, for some gases, 6000 to $20000K$.

Generally, the three functions are fit simultaneously. The fit is constrained to match the functions exactly at $T = 298.15K$. Thus, the least-square coefficients reproduce heats of formation at $T = 298.15K$ exactly.

3.5.2 Mixture properties

Once the thermodynamic data for each species i are known, the mixture properties can be evaluated as follows:

$$H = \sum_i X_i H_i^0$$

$$S = \sum_i X_i S_i$$

$$S_i = S_i^0 - R \ln X_i - R \ln P$$

$$C_{p_{frozen}} = \sum_i X_i C_{p,i}^0$$

where X_i is the mole fraction of the i^{th} species and all properties are molar properties (*upper-case letters*). The specific properties (*lower-case letters*) can be easily obtained from the molar properties:

$$h = \frac{1}{M} \cdot H$$

$$s = \frac{1}{M} \cdot S$$

$$c_{p_{frozen}} = \frac{1}{M} \cdot C_{p_{frozen}}$$

where M is the molecular weight of the mixture.

Chapter 4

Mathematical model and numerical method

4.1 Governing equations

The flow of a compressible chemically reacting mixture of thermally perfect gases is governed by the conservation principles of mass, momentum, and energy. From these conservation principles the Navier-Stokes equations can be derived. However, Navier-Stokes equations can be expressed in a different fashion depending on the numerical method used for their solution. In particular, the mathematical method used in this work is based on the *lambda scheme* which takes advantage from the hyperbolic nature of the Euler equations, decoupling between the convective operator and the diffusive operator (treated as a source term). The equations are written in quasi-linear form, in terms of $b = a/\delta$[1], $\mathbf{v}$, s, y_i.

The nondimensional reacting Navier-Stokes equations written in terms of y_i, b, $\mathbf{v}$, s are as follows (details on their derivation are given in Appendix A):

$$\begin{cases} \dfrac{Dy_i}{Dt} = V_{y_i} \qquad i = 1, ..., N-1 \\ \dfrac{1}{c_1}\dfrac{Db}{Dt} + a\nabla \cdot \mathbf{v} - \dfrac{a}{\gamma R}\dfrac{Ds}{Dt} = V_b + A \\ \dfrac{D\mathbf{v}}{Dt} + \dfrac{a}{c_1}\nabla b - \dfrac{a^2}{\gamma R}\nabla s + \dfrac{a^2}{\gamma R}\sum Q_i \nabla y_i = \mathbf{V}_m \\ \dfrac{Ds}{Dt} = V_s \end{cases} \tag{4.1}$$

[1] $a = \sqrt{\gamma RT}$ and $\delta = \frac{\gamma - 1}{2}$.

where the source terms, grouped on the right-end side of Eqs. (4.1), have the following expression:

$$\begin{aligned} V_{y_i} &= \frac{\dot{w}_i}{\rho} - \frac{1}{\rho}\nabla \cdot \mathbf{j}_i \\ V_b &= \frac{1}{c_1}\beta + \frac{a}{\gamma R}(\gamma - 1)V_s \\ \mathbf{V}_m &= \frac{1}{\rho}\nabla \cdot \mathbf{T} \\ V_s &= -\frac{1}{T}\sum \mu_i V_{y_i} + \frac{R}{p}(-\nabla \cdot \mathbf{q} + \nabla \mathbf{v} : \mathbf{T}) \end{aligned} \tag{4.2}$$

The reacting inviscid equations can be obtained neglecting the viscous terms ($\mathbf{T} = 0$, $\mathbf{q} = 0$ and $\mathbf{j}_i = 0$) from Eqs. (4.2). The *Euler* equations (inviscid and non-reacting) can be obtained simply putting the source terms (V_{y_i}, V_b, $\mathbf{V}_m$, and V_s) equal to zero.

4.2 Numerical technique

The Navier-Stokes equations (4.1) hold independently from the dimension of the space or from the adopted reference frame. Here the equations for two-dimensional problems (planar or axisymmetric) are numerically solved following the *lambda scheme* using a curvilinear orthogonal frame, in order to have a grid well adapted to the geometry of the body, which is transformed to a Cartesian grid (called the computational plane) by conformal mapping. The *lambda scheme* is a technique developed for the Euler equations and extended to the Navier-Stokes equations decoupling between the convective operator and the diffusive operator (treated as a source term), according to their different physical nature. This technique is second-order accurate in both space and time and is described in details in Appendix B.

The equations in the computational plane are:

$$\begin{cases} b_t = c_1 \left(f_1^x + f_2^x + f_1^y + f_2^y + V_b^{'} + \dfrac{a}{\gamma R} s_t - \dfrac{a}{\gamma R} \sum Q_i y_{i,t} + A \right) \\ u_t = f_1^x - f_2^x + f_3^y + V_u \\ v_t = f_1^y - f_2^y + f_3^x + V_v \\ s_t = f_4^x + f_4^y + V_s \\ y_{i,t} = f_i^x + f_i^y + V_{y_i} \qquad i = 1, ..., N-1 \end{cases} \tag{4.3}$$

The terms f_p^q represent the convective part and are discretized with *upwind* differencing while the terms $V_b^{'}$, V_u, V_v, V_s, and V_{y_i} represent the chemical and diffusive source terms which are discretized with central differencing. The terms Q_i and c_1 represent partial derivatives of γ and R with respect to temperature and species mass fractions.

The technique is second-order accurate, and no errors are introduced at the boundaries: the *boundary conditions*, according to the chosen model of the "outside world", can be enforced with utmost simplicity and without using arbitrary elements. Among the advantages of this method over other techniques, one is simplicity, which is also responsible for reducing computational time, and another is easiness in handling boundary points and boundary conditions. This simplicity and accuracy in treating the boundaries is obviously useful for the treatment of complex boundary conditions, as in the case of ablation. Equations like (B.13) and (B.14), in addition to local terms, contain terms, the f_p^q, which express physical contributions from one side or the other. Terms with express contributions from outside are not computed from inside the computational region. They must be determined using some appropriate, physical boundary condition. The calculation at boundary points, therefore, is not affected by arbitrariness.

4.3 Boundary conditions

An appealing technique for specifying boundary conditions for hyperbolic systems is to use relations based on characteristic lines, i.e., on the analysis of the different waves crossing the boundary. It is well known that the Navier-Stokes equations are not hyperbolic as the addition of viscous terms changes the mathematical nature of the system by increasing its order. However, Navier-Stokes equations certainly propagate waves like Euler equations do and, from a physical point of view, Euler boundary conditions appear as first-order candidates to

treat Navier-Stokes boundary conditions. However, Navier-Stokes equations require more boundary conditions than Euler equations do. To build Navier-Stokes boundary conditions, the approach used here is to take conditions corresponding to Euler conditions (the *inviscid conditions*) and to supply additional relations (the *viscous conditions*) which refer to viscous effects. The term *viscous* is used here to describe all processes which are specific to Navier-Stokes, i.e., viscous dissipation, thermal diffusion, species diffusion, etc. These additional conditions must have a negligible effect when the viscosity goes to zero and their implementation is not done at the same level as the inviscid conditions. The viscous conditions are used only to compute the viscous terms in the conservation equations at the boundary and, therefore, are not strictly enforced.

Boundary conditions must be applied at four boundaries: 1. lower wall, 2. upper wall, 3. entrance and 4. exit. The main types of boundary conditions are: inflow and outflow of the gas, viscous wall, and inviscid wall (axis of symmetry). In the computational plane, which is a box $[0,1]\times[0,1]$ (see Appendix B), the four boundaries are identified by the lines $\hat{x}=0$ (left), $\hat{x}=1$ (right), $\hat{y}=0$ (down) and $\hat{y}=1$ (up).

4.3.1 Inflow and outflow conditions

The inflow or outflow conditions are usually assigned to the left and right boundaries ($\hat{x}=0$ and $\hat{x}=1$). To assign inflow (or outflow) boundary conditions the first step is to identify which terms (corresponding to space derivatives in the $\hat{x}$ direction) express contributions from outside, either at the left boundary, or at the right boundary. The unknown f_p^x are clearly the ones corresponding to the positive λ_i^x for the left boundary, and to the negative λ_i^x for the right boundary. These terms from the "outside world" cannot be computed from inside the computational region and therefore they must be determined by some physical boundary conditions. We will hereby derive the boundary conditions for the left boundary, being the conditions for the other boundaries based on the same logic. On the entry (or exit) boundary the flow may be supersonic or subsonic:

- **Supersonic inflow**. In this case the condition $u>a$ holds. The three λ_i^x are all positive and therefore $4+(N-1)$ boundary conditions must be assigned for the corresponding unknown terms: f_1^x, f_2^x, f_3^x, f_4^x, and the $(N-1)$ f_i^x. This equals to assigning the inflow conditions.

  1. Steady flow and equal to the initial condition.

The unknown f_p^x can be obtained from:

$$\begin{cases} b_t = 0 \\ u_t = 0 \\ v_t = 0 \\ s_t = 0 \\ y_{i,t} = 0, \quad , i = 1, N-1 \end{cases} \tag{4.4}$$

If a planar flow and uniform in the $\hat{y}$ direction is assigned, the simple condition $f_1^x = f_2^x = f_3^x = f_4^x = f_i^x = 0$ is obtained from (4.4) and (4.3). If this is not the case, the unknown terms can be nevertheless obtained from (4.4) and (4.3), after the space derivatives in the $\hat{y}$ direction have been evaluated.

- **Subsonic inflow**. In this case the condition $a > u > 0$ holds. $3 + (N-1)$ signals come from outside the computational region: f_1^x, f_3^x, f_4^x, and f_i^x are unknown while f_2^x can be correctly evaluated from inside the computational region, being $\lambda_2^x < 0$.

  1. The impinging flow has clearly defined total temperature, total pressure, and species mass fractions. Moreover the flow is considered directed along the $\hat{y} = cost$ lines. The conditions can be expressed in terms of time derivatives, that is: $(T_0)_t = \mathcal{F}(t)$, $(p_0)_t = \mathcal{G}(t)$, $(y_i)_t = \mathcal{Y}_i(t)$ and $V_t = 0$. With the equation of state these relations can be transformed in terms of b,u,v and s. The condition of defined total temperature and total pressure can be expressed in terms of total enthalpy $(h_0)_t$ and entropy, respectively.

$$\begin{cases} (T_0)_t = \mathcal{F}(t) \\ (p_0)_t = \mathcal{G}(t) \\ y_{i,t} = \mathcal{Y}_i(t) \\ V_t = 0 \end{cases} \quad \Rightarrow \quad \begin{cases} (h_0)_t = Fbb_t + uu_t = \hat{\mathcal{F}}(t) \\ s_t = \hat{\mathcal{G}}(t) \\ y_{i,t} = \mathcal{Y}_i(t) \\ v_t = 0 \end{cases} \tag{4.5}$$

where

$$F = \frac{(\gamma - 1)/2}{\left[1 - \frac{\gamma+1}{\gamma-1}\frac{T}{\gamma}\frac{\partial \gamma}{\partial T}\right]}$$

The assumption that $\alpha = 0$ has been also made for the entry boundary so that the relation $v = V$ holds. Eqs. (4.5) allow to evaluate the unknown signals (f_1^x, f_3^x, f_4^x, f_i^x) from known quantities, i.e. the derivatives in the $\hat{y}$ direction. Note that if the inflow conditions do not vary with time (which is the usual condition), then $\mathcal{F}(t)$, $\mathcal{G}(t)$, and $\mathcal{Y}_i(t)$ are set to zero.

- **Supersonic outflow**. In this case $u < -a$ holds. The λ_i^x are all negative and all the signals come from inside the computational region. No boundary conditions are needed because all the space derivatives are correctly evaluated inside the computational region.

- **Subsonic outflow**. In this case $-a < u < 0$ holds. $3 + (N-1)$ signals (f_2^x, f_3^x, f_4^x, f_i^x) come from inside the computational region. A single condition is needed to evaluated the only unknown signal f_1^x.

  1. Assigned pressure
     The condition for this case is $p_t = \mathcal{F}(t)$, expressed in terms of a time derivative. With the expression of entropy and the equation of state the pressure condition can be expressed in terms of b_t, s_t, and $y_{i,t}$:

     $$\mathcal{F}(b_t, s_t, y_{i,t}) = \hat{\mathcal{F}}(t) \tag{4.6}$$

     the above condition allows f_1^x to be evaluated from known quantities. If the pressure do not vary with time (usual condition), then $\mathcal{F}(t)$ is set to zero.

  2. Non-reflecting (radiative) condition
     With this condition [73] the signals coming from the outside are assumed to be zero. In this case the boundary condition becomes simply:

     $$f_1^x = 0 \tag{4.7}$$

  3. Extrapolation
     In this case the unknown values of all the variables (b, u, v, s, and y_i) are extrapolated from the corresponding values from inside the computational region. This condition is not mathematically correct but can be useful for problems where no appropriate physical conditions are known at the boundary. A typical case is the exit condition for the subsonic boundary-layer of a supersonic flow.

4.3.2 Wall conditions

To assign wall conditions, as for the case of inflow or outflow, the first step is to identify which terms (corresponding to space derivatives in the $\hat{y}$ direction) express contributions from outside, either at the upper boundary $\hat{y} = 1$, or at the lower boundary $\hat{y} = 0$. The unknown f_p^x correspond to the positive λ_i^y for the lower wall, and to the negative λ_i^y for the upper wall. We will hereby derive the boundary conditions for the lower wall, being the conditions for the other wall

based on the same logic. Two kind of walls can be defined: inviscid wall, viscous wall and axis of symmetry. The special case of an ablating wall will be discussed in the following chapter. If the lower (or upper) boundary is not a wall or an axis of symmetry then inflow or outflow conditions can be enforced exactly in the same way shown for the $\hat{x} = cost$ boundaries.

- **Inviscid wall**. The boundary conditions on inviscid walls are easily treated. In this case the condition $v = v_t = 0$ holds. For a rigid wall, in fact, v must vanish at all of its points; this is called the *flow tangency* condition and it is the only condition which has to be specified for an inviscid flow. Consequently $\lambda_1^y > 0$, $\lambda_2^y < 0$, and $\lambda_3^y = 0$ and $3 + (N-1)$ boundary conditions must be assigned for the corresponding unknown terms: f_1^y, f_3^y, f_4^y, and the $(N-1)$ f_i^y. The term f_1^y can be derived from the third of (4.3), imposing $v_t = 0$:

  $$f_1^y = f_2^y - f_3^x - V_v \tag{4.8}$$

  The other unknown signals, are easily derived:

  $$f_3^y = f_4^y = f_i^y = 0 \tag{4.9}$$

  the above condition is obtained from (B.14) imposing $\lambda_3^y = 0$.

- **Viscous wall (non-reacting)**. The λ-scheme specifies the boundary conditions using relations based on characteristic lines, i.e., on the analysis of the different waves crossing the boundary. To build Navier-Stokes boundary conditions, the approach used here is to take conditions corresponding to Euler conditions (*inviscid*) and to supply additional relations, i.e. the *viscous* conditions. According to signal propagation, the viscous and inviscid conditions are exactly the same. The difference lies in the added conditions which must be assigned on space derivatives for a viscous flow [65]. This can be made directly specifying the flow parameters at wall. The usual flow tangency condition for an inviscid flow changes drastically for a viscous flow. Because of the existence of friction, the flow can no longer slip at the wall and we have the *no-slip* condition at the wall, namely the velocity vector is zero at the wall:

  $$u = v = 0 \tag{4.10}$$

  The zero-pressure gradient at the wall is also enforced:

  $$\left(\frac{\partial p}{\partial y}\right)_w = 0 \tag{4.11}$$

In addition, because of energy transport by thermal conduction, we require an additional boundary condition at the wall involving temperature. Different cases can be considered [2]:

1. Isothermal wall:

$$T = T_w \tag{4.12}$$

where T_w denotes the specified wall temperature. Usually the wall will not be at constant temperature. If we know a priori the distribution of temperature along the surface (for example from an experiment) then the above condition is modified with $T_w(\hat{x})$ instead of T_w, where $T_w(\hat{x})$ is the specified wall temperature variation as a function of distance along the surface (the $\hat{y} = 0$ line in the computational plane). Unfortunately, in a high-speed flow problem, the wall temperature is usually one of the unknowns and the isothermal wall condition is, therefore, not usable in this case.

2. Heat-transfer wall boundary condition:

$$q_w = -k \left(\frac{\partial T}{\partial y} \right)_w \tag{4.13}$$

where q_w is the heat transfer (energy per second per unit area) into or out of the wall, and $(\partial T/\partial y)_w$ is the normal temperature gradient existing in the gas immediately at the wall. In general, the wall heat transfer (and hence the wall-temperature gradient) are unknowns of the problem, and, therefore, in the most general case this boundary condition must be matched to a separate heat-conduction analysis describing the heat distribution within the surface material itself, and both the flow problem and the surface material problem must be solved in a coupled fashion. A special case of the above condition is the *adiabatic wall* condition, wherein by definition the heat transfer to the wall is zero.

3. Adiabatic wall:

$$\left(\frac{\partial T}{\partial y} \right)_w = 0 \tag{4.14}$$

Note that here the boundary condition is not on the wall temperature itself, but rather on the temperature *gradient*. The resulting wall temperature, which comes out as part of the solution, is defined as the *adiabatic wall temperature* T_{aw}.

Although the choice of an appropriate boundary condition for temperature at the wall appears somewhat open ended from the preceding discussion, the majority of high-speed viscous flow calculations assume one of the two extremes, that is, they either treat a uniform, constant-temperature wall or an adiabatic wall. However, for a detailed and accurate solution of many practical problems, such is the case of an ablative surface, a heat-transfer wall boundary condition must be employed along with a coupled solution of the heat-conduction problem in the surface material itself.

- **Viscous wall (reacting)**. As for the non-reacting viscous wall, the standard, no-slip boundary conditions on velocity at the wall Eq. (4.10) hold for a chemically reacting viscous flow as well. For a constant-temperature wall with known temperature T_w, the (4.12) holds as well. In contrast, for an adiabatic wall, the boundary condition becomes:

$$\left(\frac{\partial T}{\partial y} + \rho \sum_{i}^{N} \mathcal{D}_{im} h_i \frac{\partial y_i}{\partial y}\right)_w = 0 \tag{4.15}$$

where $\mathcal{D}_{im}$ is the multicomponent diffusion coefficient. For a chemically reacting mixture, in fact, there is also an energy transport caused by diffusion. That is, as species i diffuses through the gas, it carries with it the enthalpy of species i, h_i, which is a form of energy transport. Hence, in a chemically reacting flow for an adiabatic wall the normal temperature gradient is not necessarily zero.

In a chemically reacting flow, the mass fraction of species i is one of the dependent variables. Therefore boundary conditions for y_i are needed as well as for u, v, and T already discussed. At the wall, the boundary condition on y_i deserves some discussion because it involves, in general, a surface chemistry interaction with the gas at the wall. The wall can be made of a material that tends to catalyze chemical reactions at the surface or it can ablate or melt due to the incoming heat flux. To get familiar with wall-flow chemical interactions, the *catalytic wall* conditions will be discussed:

1. Fully catalytic wall:
   A fully catalytic wall is one where all atoms are recombined, irrespective of the mass fraction of atoms that would be allowed to exist at local chemical equilibrium conditions (pressure and temperature at the wall). The boundary condition is simply the following:

$$(y_A)_w = 0 \tag{4.16}$$

   where $(y_A)_w$ is the mass fraction of atomic species at the surface.

2. Equilibrium catalytic wall:
   An equilibrium catalytic wall is one at which chemical reactions are catalyzed at an *infinite* rate, that is, the mass fractions at the wall are their local equilibrium values at the local pressure and temperature at the wall. The boundary condition is simply as follows:

$$(y_i)_w = (y_i)_{eq} \tag{4.17}$$

   where $(y_i)_{eq}$ is the equilibrium composition at the wall pressure and temperature. Note that, if the wall temperature is sufficiently low, the equilibrium value of y_A is essentially zero. In this case the fully catalytic and the equilibrium catalytic wall conditions are exactly the same.

3. Partially catalytic wall:
   A partially catalytic wall is one at which chemical reactions are catalyzed at a finite rate. Let $\dot{w}_c$ denote the catalytic rate at the surface (mass of species i per second per unit area). $\dot{w}_c$ is positive for species i consumed at the surface and negative for species i produced at the surface. At the surface the amount of species i produced or destroyed as a result of the catalytic rate must be balanced by the rate at which species i is diffused to the surface. Hence:

$$(\dot{w}_c)_i = \rho \mathcal{D}_{im} \left(\frac{\partial y_i}{\partial y} \right)_w \tag{4.18}$$

   Equation (4.18) is the boundary condition for a surface with finite catalyticity. It dictates the gradient of the mass fraction at the surface.

4. Noncatalytic wall:
   A noncatalytic wall is one where no recombination occurs at the wall, that is, $(\dot{w}_c)_i = 0$. For this case, from (4.18):

$$\left(\frac{\partial y_i}{\partial y} \right)_w = 0 \tag{4.19}$$

The subjects of surface chemical reactions with the flow and the associated boundary conditions just discussed for a catalytic surface are serious matters for the analysis of chemically reacting viscous flows, because they can strongly affect the aerodynamic heating. The more complex case of an ablating surface and the associated boundary conditions will be discussed in chapter 5.

- **Axis of symmetry**. This condition corresponds to the inviscid wall condition, both for the Euler and Navier-Stokes equations. The symmetry condition, in fact, dictates that $v = -v$ and therefore $v = v_t = 0$.

4.3.3 Error accumulation on the boundaries

For each of the described cases (inflow, outflow, rigid wall), the problem of truncation errors accumulation in time can arise [54]. To avoid this problem, the boundary conditions must be enforced not only on space derivatives but also on variables themselves. Terms, such as f_1^y in (4.8), re-evaluated at the boundaries, are used in (4.3) to udate the boundary points themselves. In principle, v originally equal to zero on the wall, should remain equal to zero because (4.8) assures the vanishing of v_t. Similarly, T_0 and p_0 should remain constant because of (4.5), and p should remain constant because of (4.6). In practice, it may not be so because the updating of v, T_0, p_0, and p is affected by almost imperceptible truncation errors in time. After a number of steps, one can observe a departure from the original values, producing an increase or decrease in total energy and/or a non-vanishing v (expressing an addition or loss of mass through the wall). It is necessary, therefore, to reset certain quantities to maintain T_0, p_0, p, and v constant at the entry, exit, and wall boundary, respectively. This can be done easily at the wall because v is one of the variables of the system while it can be a little more complicated for outflow or inflow conditions, where the conserved parameters (T_0, p_0, p) are a combination of the dependent variables. For example the task is accomplished, at the entrance, by computing:

$$\begin{aligned} (h_0)^{k+1} &= h_0 \\ (R_2^x)^{k+1} &= (b)^{k+1} - (u)^{k+1} \end{aligned} \tag{4.20}$$

Since h_0 is a function of T_0, the system (4.20) can be used to obtain the corrected values of $(b)^{k+1}$ and $(u)^{k+1}$. From these values and the knowledge of p_0, the corrected value of $(s)^{k+1}$ can be obtained.

4.3.4 Multi-block technique

In many practical problems the computational region is complex to discretize using a single grid obtained with conformal mapping. A common solution consists in considering multiple computational regions, which have one or more boundaries in common and where the flowfield continuity must be enforced (*Multi-block technique*). In this work the multi-block technique described in [60, 59, 47] is adopted for multicomponent reacting flows.

Chapter 5

Ablation model and boundary conditions

In a hypersonic heating environment, non-charring TPS materials, such as carbon-carbon, lose mass only by ablation and melt/fail mechanisms. Detailed analysis of the performance of such TPS materials must consider the in-depth energy equation, the surface mass and energy balances, and ablation modeling. However, to predict the aerothermal heating over an ablating surface, the CFD code has to be integrated with a computational surface thermochemistry technique. The surface mass and energy balances, in fact, include terms which involve gradients and which are consequently expressed differently depending on the solver's structure; thus the mass and energy balances must be considered part and parcel of the CFD code's boundary conditions. An accurate evaluation of the boundary-layer mass and energy transfer mechanism is a key issue to predict the correct mass blowing rate and consequently the heat flux over an ablating surface. To obtain a better evaluation of the ablating flowfield, the mass and energy exchange mechanisms must be accurately modeled using the information from the full Navier-Stokes solver; this is performed including the ablating surface conditions inside the flow solver.

Approaches based on boundary-layer transfer-coefficients (see Chapter 2) permit to express the gradients across the boundary-layer as a function of values at wall and at the boundary-layer edge with the use of suitable nondimensional numbers (*Stanton* numbers for mass and energy transfer). Approaches based on these simplified boundary-layer models require less CFD code modifications but rely on a less accurate modeling which can limit the accuracy in the estimation of surface blowing rate and surface temperature. Thus, in order to improve the estimation of the heat flux over an ablating surface, a flow solver with ablating surface conditions becomes a requirement.

The inclusion of mass and energy balance in the equation solver's boundary

conditions and the coupling with the ablation model will be explained in details in the next sections.

5.1 Surface mass and energy balance

The physics of the hot-gases over a solid surface is modeled by the chemically reacting Navier-Stokes governing equations, which are solved by the code based on the lambda scheme [54] described in Appendix A and B. Because of the chemically active surface, further physical modeling is necessary for the fluid-surface interaction. The latter aspect requires the addition of a mathematical model of the hot-gas-flow boundary condition which describes the physics of the surface phenomena.

Consider the fluxes of energy entering and leaving a control surface fixed to the ablating surface. The graphite surface material may be visualized as moving into the surface at a rate $\dot{s} = \dot{m}/\rho_s$. If it is assumed that no material is being removed in a condensed phase (solid or liquid), then the general boundary conditions for a chemically reacting, *non-charring* ablating surface can be written as [51, 15]:

$$k \left.\frac{\partial T}{\partial y}\right|_w + \sum_i^{N_c} h_i \rho D_i \left.\frac{\partial y_i}{\partial y}\right|_w + q_{rad} + \dot{m} h_s = (\rho v) h_w + \epsilon \sigma T^4 + q_{cond} \qquad (5.1)$$

which is the surface energy balance (SEB), and:

$$\rho D_i \left.\frac{\partial y_i}{\partial y}\right|_w + \dot{m} y_{s,i} = (\rho v) y_{w,i} + \sum_r^{N_r} \omega_i^r \qquad i = 1, ..., N_c \qquad (5.2)$$

which is the surface mass balance (SMB) for the i^{th} species. N_c is the number of chemical species of the system and the subscripts w and s denote gas and solid properties at the wall, respectively.

The terms on the left-end side of Eq. (5.1) are the heat fluxes entering the surface due to conduction, diffusion, radiation from the gas to the surface, and solid material mass flow rate, while the terms of the right-end side are the heat fluxes leaving the surface due to blowing, re-radiation, and conduction in the material. The conduction term q_{cond} is an input for the CFD analysis, which has to be provided by numerical or semi-analytic CSM (Computational Solid Mechanics) computation.

The terms on the left-end side of Eq. (5.2) are the mass flux entering the surface due to diffusion and solid material injection flux, while the terms on the right-end side are the mass fluxes leaving the surface due to blowing and surface reactions (different from ablation, i.e. catalysis). The term ω_i^r is the mass

flux of species i due to surface reaction r, and $y_{s,i}$ is the mass of species i produced or consumed in the ablation process per mass of TPS material ablated, i.e. $y_{s,i} = \dot{m}_i/\dot{m}$. The $y_{s,i}$ are positive for ablation products, negative for species which are consumed in the ablation process and sum to unity. Eq. (5.1) and (5.2) can also be applied to a non-ablating surface, with $\dot{m} = 0$. A summation of Eq. (5.2) over all the species, considering that the summation made over the diffusive and chemical terms is zero because of mass conservation, yields:

$$(\rho v) = \dot{m} \tag{5.3}$$

Where ρ and v are the density of the gaseous mixture at the wall and the gas-phase injection velocity, respectively. With the use of Eq. (5.3), Eq. (5.1) and (5.2) can be cast into a more appealing form:

$$k \left.\frac{\partial T}{\partial y}\right|_w + \sum_i^{N_c} h_i \rho D_i \left.\frac{\partial y_i}{\partial y}\right|_w + q_{rad} = \dot{m}(h_w - h_s) + \epsilon\sigma T^4 + q_{cond} \tag{5.4}$$

$$\rho D_i \left.\frac{\partial y_i}{\partial y}\right|_w = \dot{m}(y_{w,i} - y_{s,i}) + \sum_r^{N_r} \omega_i^r \tag{5.5}$$

With the energy and mass balances in this form, each term has a more perceivable physical significance.

It is interesting to note that a suitable combination of Eq. (5.4) and (5.5) allows to express the so-called *heat of ablation* term. This can be obtained by multiplying Eq. (5.5) for h_i and summing over all the species:

$$\sum_i^{N_c} h_i \rho D_i \left.\frac{\partial y_i}{\partial y}\right|_w = \dot{m} \left(\sum_i^{N_c} h_i y_{w,i} - \sum_i^{N_c} h_i y_{s,i} \right) + \sum_i^{N_c} \sum_r^{N_r} h_i \omega_i^r \tag{5.6}$$

The term $\sum_i \sum_r h_i \omega_i^r$ is the chemical energy flux due to surface reactions different from ablation. Substituting Eq. (5.6) into Eq. (5.4) and noting that the term $\sum_i h_i y_{w,i}$ is the enthalpy of the mixture of gases at wall h_w, yields:

$$k \left.\frac{\partial T}{\partial y}\right|_w + \dot{m} \left(h_w - \sum_i^{N_c} h_i y_{s,i} \right) + \sum_i^{N_c} \sum_r^{N_r} h_i \omega_i^r + q_{rad} = \dot{m}(h_w - h_s) + \epsilon\sigma T^4 + q_{cond} \tag{5.7}$$

Defining the term $H_{abl} = \sum_i h_i y_{s,i} - h_s$ and rearranging, Eq. (5.7) becomes:

$$k \left.\frac{\partial T}{\partial y}\right|_w + \underbrace{\sum_i^{N_c} \sum_r^{N_r} h_i \omega_i^r - \dot{m} H_{abl}}_{chemical\ heat\ flux} + q_{rad} = \epsilon\sigma T^4 + q_{cond} \tag{5.8}$$

The term H_{abl} is the so-called heat of ablation, which is the difference between the enthalpies of the species created or consumed by the ablation mechanism and the enthalpy of the solid material at the surface temperature; therefore it represents the energy absorbed (or released) by the thermochemical ablation process. The term $\sum_i \sum_r h_i \omega_i^r - \dot{m} \cdot H_{abl}$ is therefore the heat flux due to the surface chemical reactions which will be referred to as *chemical heat flux*. If the heat of ablation H_{abl} is positive and the surface reactions are only due to ablation ($\omega_i^r = 0$), then the chemical heat flux is negative and heat is absorbed by the ablation process. The opposite happens when the heat of ablation is negative. The chemical heat flux has the following equivalent expressions:

$$q_{chem} = \sum_{i}^{N_c} \sum_{r}^{N_r} h_i \omega_i^r - \dot{m} H_{abl} \tag{5.9}$$

and

$$q_{chem} = \sum_{i}^{N_c} h_i \rho D_i \left. \frac{\partial y_i}{\partial y} \right|_w - \dot{m}(h_w - h_s) \tag{5.10}$$

5.1.1 Steady-state surface energy balance

The conduction term q_{cond} in the surface energy balance Eq. (5.4) is an input for the CFD analysis, which has to be provided by a numerical or semi-analytical CSM (Computational Solid Mechanics) computation. However, when a coupling with a material response code is not available, further hypothesis have to be made in order to compute the conduction term. A *radiative equilibrium* SEB solution [15] can be achieved by setting $q_{cond} = 0$ while retaining all the other terms in Eq. (5.4). However, this is rarely a reasonable assumption for an ablating surface because the energy conduction in the material cannot be neglected. A better approximation is represented by the *steady-state* ablation [29, 6]. For low-conductivity materials or at high ablation rates, the conduction term q_{cond} is approximately equal to the steady-state value [66]:

$$q_{cond}{}^{ss} = \dot{m}(h_s - h_{s_i}) \tag{5.11}$$

where h_s is the enthalpy of the solid material at the wall temperature, while h_{s_i} is the enthalpy of the material at the initial (in-depth) temperature. With the steady-state assumption, relative to the ablating (moving) surface, things do not change with time. Thus, it is possible to define a control volume such that it moves along with the receding surface and includes the entire temperature layer. The lower surface of this control volume is aligned with the start of the in-depth material at the initial temperature T_i and enthalpy h_{s_i}. The upper surface of this control

volume is aligned with the gas-phase interface that is adjacent to the receding surface. It should be noted that the lower surface of this control volume is taken sufficiently in-depth such that, at any instant, $T = T_i$ and $\partial T/\partial y = 0$. The integration of the energy balance Eq. (1.12) across the control volume gives the result of Eq. (5.11) assuming steady-state ($\partial T/\partial t = 0$).

Substituting the steady-state conduction term Eq. (5.11) in the SEB Eq. (5.4) leads to the "steady-state" energy balance (called SSEB):

$$\underbrace{k\left.\frac{\partial T}{\partial y}\right|_w}_{convective} + \underbrace{\sum_i^{N_c} h_i \rho D_i \left.\frac{\partial y_i}{\partial y}\right|_w - \dot{m}(h_w - h_s)}_{chemical} + \underbrace{q_{rad}}_{radiative} = \underbrace{\epsilon\sigma T^4}_{re-radiative} + \underbrace{\dot{m}(h_s - h_{s_i})}_{solid\ conduction} \tag{5.12}$$

The *steady-state* SEB is a better assumption than the *radiative equilibrium* SEB because the conduction heat flux is, in general, larger than the steady-state value and tends to it asymptotically with time (provided that the external conditions are not varying). When the CFD solution is not coupled with a material response code, the steady-state ablation is a common assumption [6, 29]. Moreover, the results presented in Chapter 2 have shown that the steady-state assumption is a reasonable approximation for carbon-carbon composite material.

5.1.2 Surface equilibrium assumption

For an ablating surface, the SMB takes different forms depending on whether or not the flow is in chemical equilibrium with the solid phase. For equilibrium flow, it is convenient to use elemental mass fraction y_k, which are known for the TPS material and which are variables in the CFD solutions. The term y_k represent the total mass fraction of element k independent of molecular configuration, i.e. $y_k = \sum_i \alpha_{ki} y_i$.

A summation of Eq.(5.5) over all the species yields a balance equation for each element k, and consequently eliminates the surface reaction term:

$$\sum_i^{N_c} \alpha_{ki} \rho D_i \left.\frac{\partial y_i}{\partial y}\right|_w = \dot{m} \sum_i^{N_c} \alpha_{ki}(y_{w,i} - y_{s,i}) \tag{5.13}$$

which, introducing $y_{w,k} = \sum_i \alpha_{ki} y_{w,i}$ and $y_{s,k} = \sum_i \alpha_{ki} y_{s,i}$, can be expressed as:

$$\sum_i^{N_c} \alpha_{ki} \rho D_i \left.\frac{\partial y_i}{\partial y}\right|_w = \dot{m}(y_{w,k} - y_{s,k}) \qquad k = 1, ..., N_{el} \tag{5.14}$$

N_{el} represents the total number of chemical elements in the system. The term $y_{w,k}$ is the elemental mass fraction of the gaseous mixture at the wall while $y_{s,k}$ is

the mass of element k produced in the ablation process per mass of TPS material ablated, i.e. $y_{s,k} = \dot{m}_k/\dot{m}$. Clearly the $y_{s,k}$ must be equal to the elemental composition of the TPS material. If the diffusion coefficients D_i are all equal, Eq. (5.10) becomes:

$$\rho D \left.\frac{\partial y_k}{\partial y}\right|_w = \dot{m}(y_{w,k} - y_{s,k}) \tag{5.15}$$

The use of Eq. (5.10) or (5.13) together with the assumption of chemical equilibrium at wall permits to bypass the entire discussion about governing processes and intermediate steps concerning the number of species, reaction mechanisms, and the associated reaction rates, especially for the complex flowfields with ablation. The advantage of using Eq. (5.10) instead of Equation (5.5) lies in the fact that the source term due to chemical reactions vanishes in the elemental approach. Moreover, the term $y_{s,k}$ only depends on the material composition while its species' counterpart, the term $y_{s,i}$, also depends on the reaction mechanism with the atmosphere.

The surface equilibrium approach provides satisfactory accuracy with reduced computational cost, although ablating surface non-equilibrium should be taken into account. However, only few data are available to validate gas-surface kinetic models which strongly affect the prediction of mass blowing rate [75, 31, 19]. For these reasons the surface equilibrium approach has been used here: this is equivalent to assume that the regime is always diffusion controlled.

5.2 Thermochemical ablation model

Solving the energy and mass surface balances, Eqs. (5.4) and (5.14), is only possible if the ablation term is suitably modeled. Thus it occurs to prescribe some relationships among the blowing mass flow rate $\dot{m}$ and the surface thermodynamic state (wall pressure and temperature). Two different ablation models have been considered in the present study: a classical *thermochemical table model* and a *fully-coupled ablation model*. Both models rely on the assumption of surface equilibrium.

5.2.1 Thermochemical table model

The *thermochemical table* ablation models [51, 34], which are the most widely used for TPS materials, are obtained from a solution of the equations for thermodynamic equilibrium between the TPS material and the atmosphere of interest, coupled with surface mass balance and simplified boundary-layer transfer potential methodology. The *thermochemical table* ablation model has been described

in Chapter 1 and only the major framework of the model is repeated here. With the transfer coefficient approach the elemental mass balance Eq. (5.15) becomes:

$$y_{e,k} + B^{'} y_{s,k} = (1 + B^{'}) y_{w,k} \tag{5.16}$$

where $B^{'} = \dot{m}/\rho_e u_e C_m$ is the dimensionless mass flux due to ablation and $()_e$ refers to the edge of the boundary layer. For each value of $B^{'}$, Eq. (5.16) permits to find the wall elemental composition ($y_{e,k}$ and $y_{s,k}$ are known). Once the $y_{w,k}$ are known, the wall temperature can be determined by the wall pressure and the assumption of chemical equilibrium using a free energy minimization procedure [28]. The net result of the calculations is a set of thermochemical tables $\mathcal{F}(p, T, B^{'}) = 0$ relating surface temperature and pressure to a dimensionless ablation mass flux. Figure 1.4 shows $B^{'}(T, p)$ for thermochemical ablation of carbon in air. At each pressure and temperature corresponds a dimensionless mass flux and a mixture composition in equilibrium with the solid phase.

The advantage of using these tables is that, once they have been generated, they are applicable over a wide range of aerothermal heating conditions. The disadvantage is that they are obtained with a very simplified boundary layer approach based on transfer coefficients to model species diffusion across the boundary-layer. From the definition of $B^{'}$ it is clear that the diffusion coefficient C_m plays a dominant role in determining the surface ablation rate $\dot{m}$, and thus the uncertainty in this estimated mass blowing rate can be high. The mass-transfer coefficient C_m is usually obtained via the convective heat transfer coefficient C_h and semi-empirical relations such as Eq. (1.26). Sometimes they are even taken as simply being equal as in [38]. The uncertainty in this estimated mass transfer coefficient is high, and consequently the predictions of mass blowing rates ($\dot{m}$), surface temperatures, and heat fluxes can be inaccurate. An error on the mass transfer coefficient C_m, in fact, has a great influence not only on the mass blowing rate but also on surface temperature and heat fluxes, since the term $\dot{m}$ affects the surface energy balance as well through injection and blowing terms.

In a typical computation using $B^{'}$ tables, the surface temperature, mass blowing rate, and composition are computed from the material response code and then used as input conditions for the CFD code which then computes the wall pressure and heat flux. The final temperature is thus determined through coupled iterations between the flow solver and the material code. However, the surface mass and energy balance are solved by the material response code using a simplified transfer potential methodology. Even modern approaches [16, 63, 18, 38] rely on the use of transfer coefficient approaches because of the difficulty of imposing directly the mass and energy balance as boundary condition for the CFD code. The simplified surface energy balance assumes typically the form expressed in Chapter 1

(see, for example, [17]):

$$\rho_e u_e C_h (h_r - h_w)_e + \rho_e u_e C_m \sum_{i=1}^{N} (y_{e,i} - y_{w,i}) h_{w,i} + \rho_e u_e C_m B^{'} (h_s - h_w) + \\ + q_{rad_{in}} - \sigma \epsilon {T_w}^4 - q_{cond} \tag{5.17}$$

where the first two terms are the transfer-coefficient expressions for the convective and diffusive heat flux. During the iterations, the heat transfer coefficient C_h is determined from the CFD solution so that the convective heat flux is exactly equal to that computed from the Navier-Stokes solver. However, the simplified mass transfer model remains both in the diffusive heat flux and in the $B^{'}$ term. In case of steady-state ablation the expression of Eq. (5.11) can be substituted into Eq. (5.18) to obtain the steady-state transfer-coefficient expression for the SEB.

5.2.2 Fully-coupled ablation model

Thermochemical tables are based on a simplified boundary-layer diffusion model which is a very limiting assumption. An accurate evaluation of the mass/energy transfer mechanism is a key issue to predict the correct mass blowing rate and temperature and consequently the heat flux over an ablating surface; thus, a full Navier-Stokes approach is needed to solve the coupled material/flow problem: the advantage of using pre-generated $B^{'}(T, P)$ tables and transfer potential mass and energy balances is lost but the simplified boundary-layer approach can be completely removed.

Assuming chemical equilibrium, the surface chemical composition can be computed basing on equilibrium relations between the wall mixture of gases and the solid material (details are given in the next section). Tables are created representing the wall chemical composition at different pressures and temperatures. These tables are then used by the main code as boundary conditions to solve the mass balance equation and to determine the correct mass blowing rate of each wall node. With the pressure coming from the flowfield (assuming zero-pressure gradient at wall) and with the wall temperature assigned, the chemical composition at wall ($y_{w,i}$) can be obtained from pre-generated tables. The wall elemental composition ($y_{w,k}$) is then easily obtained as well as the wall diffusive mass flux of element k:

$$\begin{aligned} y_{w,k} &= \sum_i \alpha_{ki} y_{w,i} \\ j_{w,k} &= \sum_i \alpha_{ki} \rho D_i \left. \frac{\partial y_i}{\partial y} \right|_w \end{aligned}$$

where the species mass fraction gradient at wall $\partial y_i/\partial y|_w$ can be evaluated from the surface and flowfield solution. Finally, with the elemental composition and the elemental diffusive mass flux at wall, the mass blowing rate $\dot{m}$ can be evaluated with the use of the surface mass balance Eq. (5.14). Among the N_{el} equations of this type there are $N_{el}-1$ relations due to the fact that the elemental compositions of the atmosphere and of the surface material are known; the only unknown is their relative amount at the wall. Therefore the mass blowing rate can be obtained from Eq. (5.14) using any of the elements of the system. During the computation, the mass blowing rate boundary condition and the wall chemical composition are continuously updated until the steady-state condition is reached. Mass blowing rate must be updated continuously because it depends on the boundary layer solution (via the diffusive mass fluxes) and at the same time it affects its development. When steady-state is reached, the mass blowing rate is everywhere consistent with the mass balance Eq. (5.14) and the wall composition is in chemical equilibrium with the wall material at the wall pressure and temperature. Unlike the *thermochemical table* model, the mass balance equation is not inserted in the chemical tables but is part of the solver's boundary conditions, through Eq. (5.14), and thus no simplified mass transfer model has to be introduced.

If the surface temperature is not assigned, it must be derived from the surface energy balance. Assuming steady-state ablation, the unknown wall temperature can be obtained solving the steady-state energy balance (SSEB) reported in Eq. (5.12). An initial value for the temperature is assumed for each wall node; from this value all terms of the SSEB can be computed but, in general, the SSEB will not be satisfied. Therefore the Newton's procedure is adopted to select successively better estimates of the wall temperature until the SSEB is verified. It is clear that, when the wall temperature is changed, all the temperature-dependent parameters must be consequently updated. At each CFD iteration, the wall temperature and consequently the composition and mass blowing rate are computed according to the above procedure. It is important to stress that the mass and energy balances are inserted as boundary conditions in the flow solver and then solved during the CFD computation without introducing any simplification in the mass/energy transport mechanism.

5.2.3 Evaluation of wall chemical composition

Consider a system made up of N_{el} chemical elements. In general, these elements will interact to form a number of chemical species[1] N_c (gas phase) and N_l (condensed phase). If enough time has elapsed so that thermodynamic and chemical equilibrium is established, the thermodynamic state of the system, including the

[1]"Chemical species" includes both molecular and atomic species.

relative amount of chemical species present, is completely determined if two independent thermodynamic variables are known (for example temperature and pressure). Thus, assigning the elemental composition (regardless of molecular configuration) of the environmental gas (such as air) and of the wall material (such as carbon) together with pressure and temperature, the equilibrium chemical composition can be determined. Obviously, among the chemical species present, there is also a condensed phase (solid carbon). Knowing the relative amount of each species (solid and gaseous) the chemical composition of the sole gaseous mixture can be easily determined:

$$y_{i_{\text{gas}}} = \frac{y_i}{1 - y_{i_{\text{solid}}}}$$

When a chemical equilibrium calculation is made, the relative amount of each component (the environmental gas and the TPS material) must be specified, either in mole or in mass fractions. In this case, since we are only interested in the composition of the gaseous mixture at wall, the relative amount of the solid phase is irrelevant. However, it is a base requirement to have the presence of solid phase in the equilibrium composition. According to this, calculations are made with excess of solid component (carbon). The elemental compositions are assigned and fixed once the environmental gas and TPS material have been selected. Tables can be created representing the wall chemical composition at different pressures and temperatures. These tables are then used as boundary conditions to solve the mass balance equation (5.14) and to determine the correct mass blowing rate. Unlike *thermochemical ablation* model (see Figure 1.4), the mass balance equation is not inserted in the chemical tables but is part of the solver's boundary conditions, as shown in the previous section. In this way, no simplified boundary-layer transfer coefficient model has to be introduced.

Tables with surface composition at different pressures and temperatures are created by an equilibrium routine once for all prior to the CFD run. The equilibrium program is a version of the NASA Chemical Equilibrium with Application (CEA) open source code[2] [28]. The CEA code is organized in modules to facilitate adding or deleting applications of the program. Only the needed modules of CEA have been retained in the equilibrium routine and the equilibrium module has been modified to compute the composition of the gaseous mixture in equilibrium with the solid phase. The output is a file containing the mass fractions of each species of the system as a function of temperature and pressure. The range of pressure (*Pmin*, *Pmax*) and temperature (*Tmin*, *Tmax*) as well as their increment (*deltaP*, *deltaT*) can be assigned to the equilibrium routine.

[2]Web site:
http://www.grc.nasa.gov/WWW/CEAWeb/ or
http://www.openchannelfoundation.org/projects/CEA/.

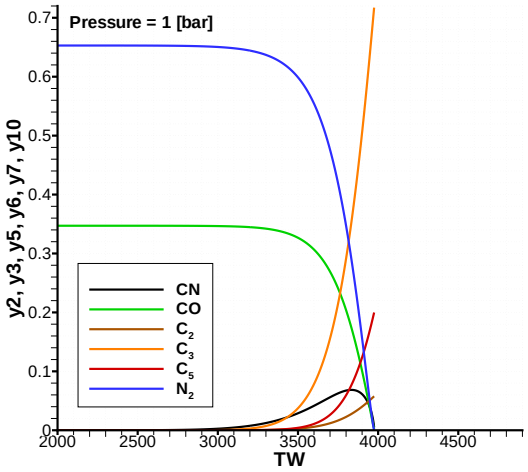

Figure 5.1: Carbon ablation in air at $1\ bar$: equilibrium composition.

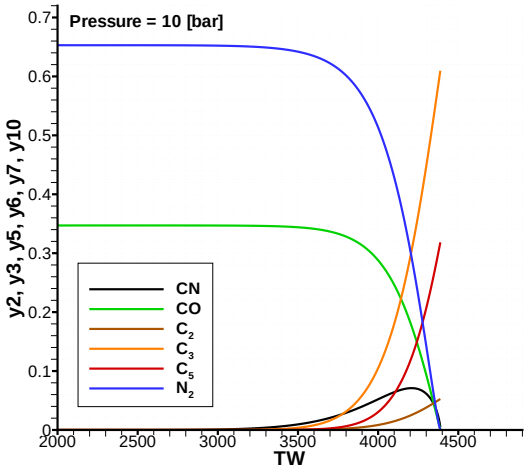

Figure 5.2: Carbon ablation in air at $10\ bar$: equilibrium composition.

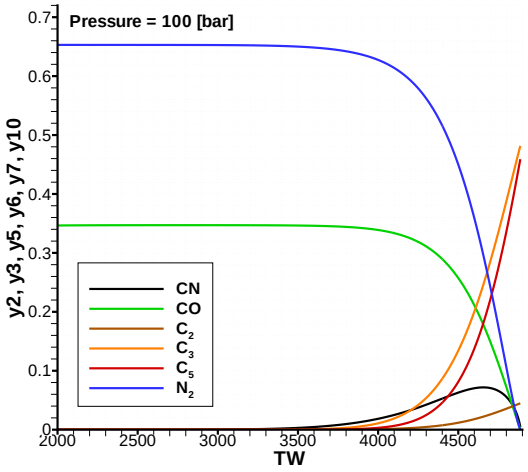

Figure 5.3: Carbon ablation in air at $100\ bar$: equilibrium composition.

The species mass fractions are ordered in columns; each record of the tabular file represents one wall pressure and one wall temperature. The equilibrium routine generates separate groups for each pressure; these groups are ordered on pressure (ascending). Within each pressure group the temperature is is ascending order. Figures 5.1-5.3 show the wall composition for pure carbon ablation in air at three different pressures. The surface composition can be evaluated for temperatures below the sublimation temperature, above which graphite is not present in solid phase. The sublimation temperature depends on pressure: around $4000\ K$ at $1\ bar$, $4400\ K$ at $10\ bar$ and $4900\ K$ at $100\ bar$. Figures 5.1-5.3 show that the major sublimation product is the species C_3, with C_5 playing an important role only at very high pressures.

The chemical composition database file (graphically represented in Figures 5.1-5.3) is read once for all by the main code and stored into an array. During each time step the surface composition at the local wall temperature and pressure is evaluated using a bi-linear interpolation function. Reading (and interpolating) the composition from a pre-build database permits to save computational time.

5.3 Implementing the ablative boundary conditions

As shown in the previous sections, the surface mass and energy balances, coupled with a surface thermochemical ablation model, provide complete boundary conditions for the solution of a flowfield with surface ablation. The surface mass and energy balances Eqs. (5.14) and (5.12) are connected with the Navier-Stokes solver because of the presence of gradients which involve the knowledge of variables both at wall and inside the flow. The way these gradients are expressed is highly dependent on the numerical scheme adopted for the solver (they can involve multiple nodes, metric terms, etc.); thus, for the ablation problem, the SMB and SEB have to be considered part and parcel of the CFD code's boundary conditions and cannot be put as an external routine. The thermochemical ablation model, instead, can be an external module which provides surface composition for a given wall thermodynamic state (pressure and temperature). The ablation model provides the chemical composition at the surface given its thermodynamic state. With the wall composition and the solution inside the flowfield (to compute all the relevant gradients), the mass balance boundary condition provides the mass blowing rate. Finally, with the mass blowing rate, the wall composition, and the solution inside the flowfield, the energy balance boundary condition provides the wall temperature.

5.4 Inviscid conditions

As described in Chapter 4 (see also Appendix B), the λ-scheme specifies the boundary conditions using relations based on characteristic lines, i.e., on the analysis of the different waves crossing the boundary. To build Navier-Stokes boundary conditions, the approach used here is to take conditions corresponding to Euler conditions (*inviscid*) and to supply additional relations, i.e. the *viscous* conditions, which refer to viscous effects. To assign wall conditions, as discussed in Chapter 4, the first step is to identify which terms express contributions from outside, either at the upper boundary $\hat{y} = 1$, or at the lower boundary $\hat{y} = 0$. We will hereby derive the boundary conditions for the lower wall, being the conditions for the upper wall based on the same logic. The unknown f_p^x correspond to the positive λ_i^y for the lower wall. Assuming a positive subsonic injection (blowing) velocity the condition $a > v > 0$ holds. Consequently $\lambda_1^y > 0$, $\lambda_2^y < 0$, and $\lambda_3^y > 0$ and $3+(N-1)$ boundary conditions must be assigned for the corresponding unknown terms: f_1^y, f_3^y, f_4^y, and the $(N-1)$ f_i^y.

As previously mentioned, the λ-scheme permits to enforce the boundary conditions with utmost simplicity and without using arbitrary elements. For the case of an ablating surface the following *"steady-state"* conditions are used:

$$\begin{cases} u_t = u = 0 \\ \dot{m}_t = 0 \\ T_t = 0 \\ y_{i,t} = 0, \qquad i = 1, .., N-1 \end{cases} \tag{5.18}$$

Since "steady-state" solutions are computed, surface mass blowing, surface temperature, and surface composition are constant when convergence is reached. "Steady-state" conditions are imposed at wall. The condition on the mass blowing rate can be expressed as a function of the integration variables, that is $b = a/\delta$, $\mathbf{v}$, s, and y_i. Since $\dot{m} = \rho v$ and $s_t = -\dfrac{R}{\rho}\rho_t$[3], the equations expressed in (5.18)

[3]when $y_{i,t} = 0$ and $T_t = 0$.

become:

$$\begin{cases} u_t = u = 0 \\ \rho v_t = \dfrac{\rho v}{R} s_t \\ b_t = 0 \\ y_{i,t} = 0, \qquad i = 1, .., N-1 \end{cases} \tag{5.19}$$

Substituting equations (4.3) into (5.19) we obtain:

$$\begin{cases} f_1^x - f_2^x + f_3^y + V_u = 0 \\ \rho \left(f_1^y - f_2^y + f_3^x + V_v \right) - \dfrac{\rho v}{R} s_t = 0 \\ f_1^x + f_2^x + f_1^y + f_2^y + V_b^{'} + \dfrac{a}{\gamma R} s_t + A = 0 \\ f_i^x + f_i^y + V_{y_i} = 0, \qquad i = 1, .., N-1 \end{cases} \tag{5.20}$$

Rearranging the 2^{nd} and 3^{rd} equation of (5.20) with the use of the expression of s_t from (4.3), we obtain the final expression for the unknown f_p^q terms:

$$\begin{cases} f_3^y = f_2^x - f_1^x - V_u \\ f_1^y = \dfrac{a}{a + \gamma v} \left[f_2^y - f_3^x - V_v - \dfrac{\gamma v}{a} \left(f_1^x + f_2^x + f_2^y + V_b^{'} + A \right) \right] \\ f_4^y = \dfrac{\gamma R}{a + \gamma v} \left(-f_1^x - f_2^x + f_3^x - 2 f_2^y + V_v - V_b^{'} - A \right) - f_4^x - V_s \\ f_i^y = -f_i^x - V_{y_i}, \qquad i = 1, .., N-1 \end{cases} \tag{5.21}$$

If the ablative surface is on the upper wall, the unknown signals are: f_2^y, f_3^y, f_4^y, and f_i^y. Their expression is the following:

$$\begin{cases} f_3^y = f_2^x - f_1^x - V_u \\ f_2^y = \dfrac{a}{\gamma v - a} \left[-f_1^y - f_3^x - V_v - \dfrac{\gamma v}{a} \left(f_1^x + f_2^x + f_1^y + V_b^{'} + A \right) \right] \\ f_4^y = \dfrac{\gamma R}{\gamma v - a} \left(f_1^x + f_2^x + f_3^x + 2 f_1^y + V_v + V_b^{'} + A \right) - f_4^x - V_s \\ f_i^y = -f_i^x - V_{y_i}, \qquad i = 1, .., N-1 \end{cases} \tag{5.22}$$

These conditions are implemented into the main code's boundary conditions.

5.5 Viscous conditions

Apart from the above conditions, which come from the *eulerian* part of the equations, there are the conditions related to the *"viscous"* terms, which are:

1. No slip condition for axial velocity component $[u = 0]$
2. Specified surface ablation rate $[\dot{m}]$ coming from the *elemental* SMB Eq. (5.14)
3. Isothermal wall condition or variable surface temperature $[T_w]$ coming from the iterative solution of the steady-state SEB Eq. (5.12)
4. Zero-pressure derivative in the normal direction $[\partial p/\partial y = 0]$
5. Wall mixture of gases $[y_i]$ in equilibrium with the solid material at the wall pressure and temperature

The isothermal ablation viscous conditions will be described first, followed by the more complex case of variable surface temperature according to the steady-state surface energy balance.

5.5.1 Isothermal ablation

The wall derivatives are evaluated using a three-nodes (second-order) expression, that is:

$$\left.\frac{\partial A}{\partial y}\right|_w = G\hat{y}_\eta \frac{-A_4 + 4 \cdot A_3 - 3 \cdot A_2}{2 \cdot \Delta\hat{y}} \tag{5.23}$$

where A is a generic variable and G and $\hat{y}_\eta$ are the metric terms to transform derivatives expressed in the computational plane $(\hat{x}, \hat{y})$ into derivatives expressed in the physical plane (x, y)[4]. The *subscripts* 2, 3, and 4 represent the wall node and the two nodes above it, respectively.

For each time step firstly the wall pressure is evaluated from the zero-pressure derivative condition. With the expression (5.23) for derivatives, the wall pressure is:

$$p_2 = \frac{4 \cdot p_3 - p_4}{3}$$

[4] see Appendix B.

Since the pressure is not part of the integration variables, it is derived from entropy, temperature and chemical composition using the following expression:

$$\frac{p}{p_0} = \frac{\exp\left[-\frac{s}{R} + \sum_i x_i M_i \left(s_{0_i} + \int c_{p_i} \frac{dT}{T}\right)\right]}{\prod {x_i}^{x_i}}$$

With the wall pressure known and with the assigned wall temperature, the composition[5] of the wall mixture of gases is obtained using the routine described in section 5.2.3. Once the wall chemical composition and surface temperature are known, all the mixture properties (specific heats, ratio of specific heats, mixture gas constant) are updated. The wall density is obtained via the equation of state:

$$\rho = \frac{p}{RT}$$

The mass blowing rate is evaluated from the elemental SMB:

$$\dot{m} = \frac{-j_{w,k}}{(y_{w,k} - y_{s,k})} \tag{5.24}$$

y_k is the wall chemical elemental composition and can be easily obtained from the wall composition while $y_{s,k}$ is the elemental composition of the TPS material and is known once the material has been selected. The term $j_{w,k}$ is the elemental diffusive mass flux at the surface, which can be expressed with a summation of the species diffusive mass fluxes:

$$j_{w,k} = -\sum_i^{N_c} \alpha_{ki} \rho D_i \left.\frac{\partial y_i}{\partial y}\right|_w$$

$\left.\frac{\partial y_i}{\partial y}\right|_w$ is the wall normal derivative of the species mass fraction and can be expressed using expression (5.23) (note that the wall chemical composition has been previously calculated):

$$\left.\frac{\partial y_i}{\partial y}\right|_w = G\hat{y}_\eta \frac{-y_{i_4} + 4 \cdot y_{i_3} - 3 \cdot y_{i_2}}{2 \cdot \Delta\hat{y}}$$

The mass blowing rate can be evaluated with the expression (5.24) written for any of the elements of the system. Once the mass blowing rate has been calculated, the blowing velocity can be obtained from the relation:

$$v = \frac{\dot{m}}{\rho}$$

[5] in terms of species mass fractions.

The wall axial velocity is assigned equal to zero according to the no-slip condition at wall:

$$u = 0$$

The wall condition ($\mathbf{v}, \rho, p, T, y_i$) is thus completely known. Since the integration variables are $b = a/\delta$, $\mathbf{v}$, s, y_i, wall entropy is evaluated through wall temperature, pressure, and composition:

$$s = \sum_i y_i s_i$$

with

$$s_i = s_{0_i} + \int_{T_0}^{T} c_{p_i} \frac{dT}{T} - R_i \ln \frac{x_i p}{p_0}$$

Finally, the speed of sound a and the integration variable $b = a/\delta$ are evaluated with the following expressions:

$$a = \sqrt{\gamma R T}$$

$$b = \frac{a}{\delta}, \qquad \delta = \frac{\gamma - 1}{2}$$

5.5.2 Steady-state ablation

If the wall condition is not isothermal, the SSEB Eq. (5.12) must be used to select successively better estimates of the wall temperature until the sum of the terms of the SSEB will equal zero.

Firstly with the initial value for surface temperature, both wall composition and mass blowing are evaluated with the previously described procedure. With pressure, temperature, composition, and mass blowing rate, all the wall heat fluxes can be evaluated and the SSEB can be computed. In general, however, the sum of the terms of the SSEB will not equal zero but some non-zero quantity $\mathcal{E}$. At each time step the SSEB is computed and the error $\mathcal{E}$ is calculated; then the wall temperature is slightly perturbed and all the temperature-dependent parameters are updated, together with the SSEB. With a new value of $\mathcal{E}$, its derivative with respect to temperature can be numerically evaluated. The new temperature is then obtained with the following expression (Newton's method):

$$T_w{}' = T_w - \frac{\mathcal{E}}{\partial \mathcal{E} / \partial T} \tag{5.25}$$

Once the "new" wall temperature is known, wall composition and mass blowing rate are consequently updated as in the case of fixed temperature. The SSEB is evaluated once again with the "new" temperature and the procedure is repeated until the error goes below a defined tolerance or after a maximum number of cycles is reached.

5.6 Computational Requirements

Beside its simplicity and availability, a chemical equilibrium routine can be very time-consuming. For this reason, the gas chemical composition in equilibrium with the solid phase for a given pressure and temperature is obtained from a pre-generated table and then stored into an array by the main program. This permits to save computational time without loosing accuracy since tables can be created with many temperature and pressure intervals with no increase in computational time. Once stored into an array, in fact, the time required to interpolate among tabulated values is the same regardless of the dimension of the array.

Once the wall composition has been evaluated, the procedure for obtaining the mass blowing rate through the SMB is straightforward and fast. If the wall temperature is evaluated through the SSEB, each time step the Newton's iterative procedure must be accomplished. However, this procedure converges rapidly so that few iterations are needed. The best results have been obtained solving the SSEB every time step with a maximum of 2 iterations at a time. Updating the wall temperature through the SSEB after a finite number of time steps is not a good choice since the time required for convergence is increased and often convergence problems are encountered. As previously described, during the iterative solution of the SSEB, when a new wall temperature is reached all the temperature-dependent parameters must be consequently updated. Updating the composition and consequently the mass blowing rate $\dot{m}$ is a key issue to obtain SSEB convergence during each time step since the response of the material to the new temperature is mainly due to the change of the blowing mass flow rate. Without the use of a chemical equilibrium database table, the Newton's iterative procedure to solve the SSEB would be very time-consuming because it requires a call to an equilibrium routine for each iteration performed. The use of pre-generated tables permits to reduce drastically the computational time to perform a steady-state solution.

The general boundary conditions, including mass and energy balances, of chemically equilibrated gas adjacent to an ablating surface have been derived. An efficient computational procedure based on these conditions has been developed and integrated with a Navier Stokes solver. The surface mass and energy balances, coupled with a surface thermochemical ablation model, provide complete boundary conditions for the solution of a flowfield with surface ablation. The following chapters will show the results obtained.

Chapter 6

2-D planar results

The procedure described above is applied to a flat plate made up of pure carbon (graphite). Supersonic laminar solutions with different environmental gases and boundary conditions are presented in this study to examine their effects on the predictions of flow structure and surface conditions. Chemical reactions between the wall material and the environmental gas are considered to determine the composition of the mixture of gases at wall. The effect of kinetically controlled chemical reactions in the boundary-layer and their effect on surface ablation is also investigated.

6.1 Existing approaches

The important fact which is explained by the thermochemical ablation model, as shown in Figure 1.4, is that there is a unique relation between temperature and mass blowing rate. Even modern approaches rely on the use of such tables because of the difficulty of imposing directly the mass balance equation as boundary condition for the CFD code. The design and analysis of a TPS involves transient CSM (Computational Solid Mechanics) analyses of the material and a sequence of steady-state CFD analyses to determine the time-history of the aerothermal heating and coupled mass and energy balance boundary conditions, as reported in [16] and [63]. When a coupling with a transient CSM code is not included in the analysis the steady-state ablation is commonly assumed [5, 29]. In all of these approaches the flowfield boundary conditions at the wall consist of a specified surface ablation rate $\dot{m}$ and a specified wall temperature T_w. When the procedure is coupled with a transient CSM analysis, wall temperature and mass blowing rate come from the material code (which makes use of thermochemical tables); when the procedure is based on the steady-state assumption, the mass blowing rate comes from the energy equation written in the steady-state form Eq. (5.12),

while temperature can be the sublimation temperature [29] or is simply assigned to an arbitrary value [5].

Assigning both temperature and mass blowing rate as boundary conditions can be misleading especially when the steady-state assumption is made; in this case, in fact, the steady-state wall temperature depends on the flowfield and it can be difficult to assign it beforehand [6]. When the wall temperature is specified, and with the wall pressure coming from the flowfield solution, the thermochemical ablation model dictates that there is a unique mass blowing rate coming from mass balance and from thermochemical equilibrium or non-equilibrium reactions between the gas mixture adjacent to the wall and the wall material. Therefore, assuming a fixed wall temperature, the mass blowing rate should be an output instead of an input. When temperatures and blowing rates come from a CSM code, the relation between blowing rate and temperature is guaranteed by the use of thermochemical tables. As we have seen, however, these tables rely on a very simplified boundary layer model and the error in the estimation of the mass transfer coefficient C_m to calculate the dimensional mass blowing $\dot{m}$ can compromise the accuracy of the following full Navier-Stokes solution (which has the calculated mass blowing rate as boundary condition).

In this work, efforts have been made in order to bring the process at the base of the thermochemical ablation model inside the CFD code. The advantage of using pre-generated tables is lost but the simplified boundary layer transfer-coefficient approach has been totally removed.

6.2 Isothermal ablation results

The fully-coupled procedure described in the previous chapter is applied to a flat plate made of pure carbon (graphite). Isothermal solutions with different surface temperatures are presented to examine their effects on flow predictions. Chemical reactions between the wall material and the environmental gas are considered only at the surface using an equilibrium approach. Once the wall composition has been calculated, the species are not allowed to react as they are diffusing across the boundary layer. The effect of finite rate chemical reactions inside the boundary-layer is studied in section $6.2.5$. The diffusion model used is based on binary diffusion coefficients using a constant Lewis number. In this section the isothermal ablation results are presented while the steady-state ablation results will be presented in section 6.3.

Table 6.1: Freestream conditions for Test Case 1

Freestream Conditions	
pressure:	1 [bar]
temperature:	4500 [K]
Mach number:	1.8
Composition:	100% He

6.2.1 Test case 1: Helium environment

First, an inert environmental gas (helium) is analysed. Two kind of wall boundary conditions are investigated. The first with assigned temperature and mass blowing rate and the second with assigned temperature and chemical composition. In the last case the composition at wall is the one in chemical equilibrium with the solid material (graphite) at the temperature and pressure of the wall. Since pressure is varying during the computational transitory, the wall composition is constantly updated. The respect of the elemental mass balance Eq. (5.14) is invoked in both cases. In the first case the mass balance is used to compute the elemental composition, while in the second case it is used to compute the corresponding mass blowing rate. The freestream conditions are expressed in table 6.1. The wall temperature is kept constant and equal to $3500\ K$. At this temperature and for pressures near $1\ bar$ the primary ablation product is gaseous C_3 (85%)[1]. The equilibrium assumption is acceptable because the wall temperature is sufficiently high [34]. Figure 6.1 shows the C_3 mass fraction at wall along the x direction, with mass blowing rate imposed as boundary condition. As in the work of [6], the ablation species (C_3) shows a gradual buildup in the streamwise direction and then asymptote to some value which is less than 1. Figure 6.2 instead, is obtained imposing the composition at wall to be in chemical equilibrium with the solid material (graphite) at the temperature and pressure of the wall. Wall composition is almost constant because the wall pressure is weakly varying. Mass blowing rate instead is strongly varying in the streamwise direction according to the growing of the boundary layer. Higher mass blowing rates are experienced near the leading edge of the flat plate where the diffusional mass fluxes are higher as shown in Figure 6.3. Imposing the wall composition is surely a more adequate boundary condition because it ensures a physical relation between the wall mixture of gases at wall and the solid material.

[1] for higher temperatures also the production of C_5 becomes important.

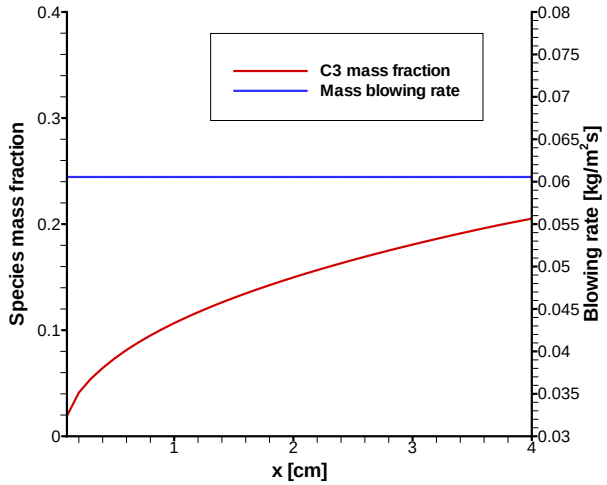

Figure 6.1: Mass blowing rate (imposed) and C_3 mass fraction at wall.

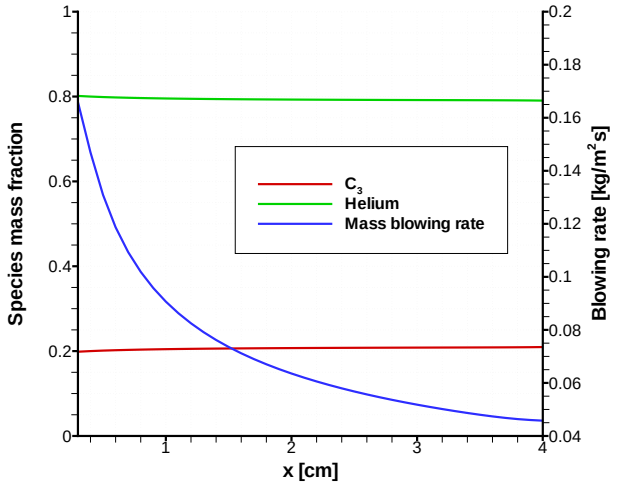

Figure 6.2: Mass blowing rate and species mass fraction (equilibrium) at wall.

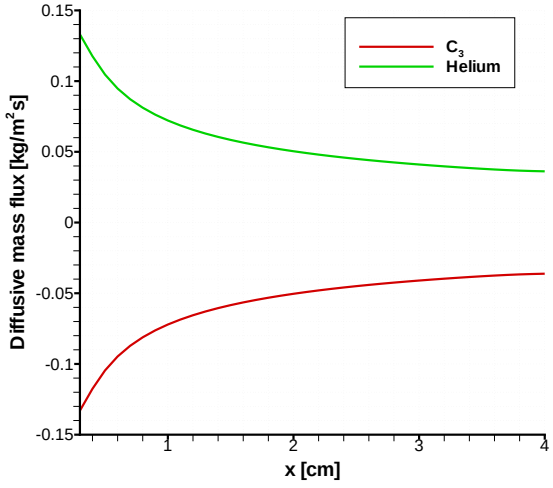

Figure 6.3: Species diffusive mass fluxes at wall.

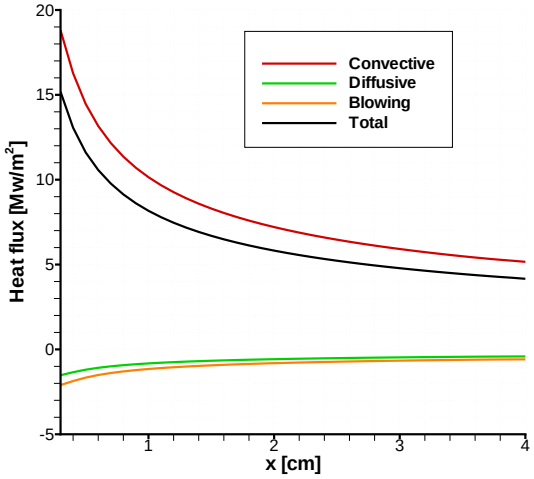

Figure 6.4: Wall heat fluxes.

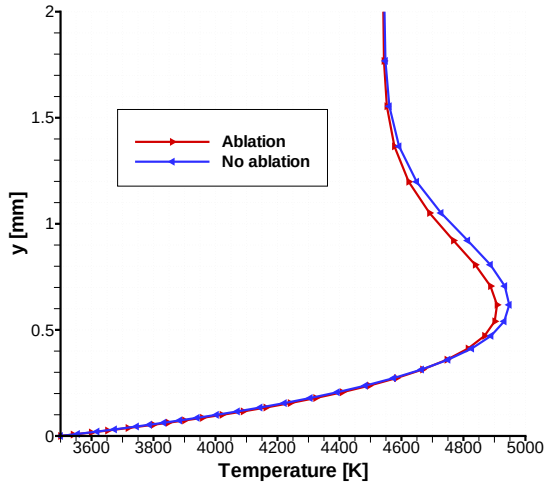

Figure 6.5: Temperature boundary-layer profile with and without ablation.

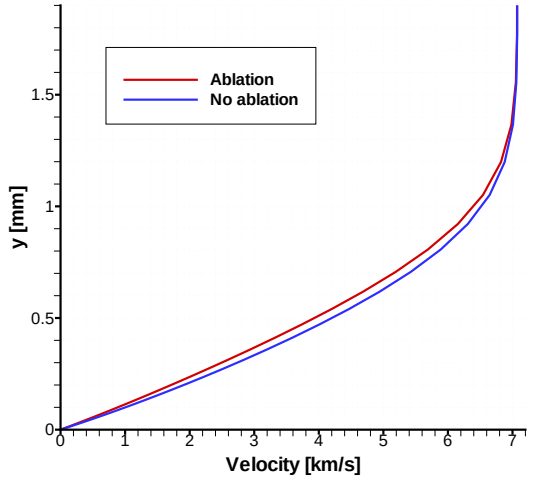

Figure 6.6: Velocity boundary-layer profile with and without ablation.

Since the wall temperature is assigned, the SEB is not imposed in this test case; however, it is interesting to evaluate the heat fluxes due to conduction (from the gas), diffusion, and convection. Figure 6.4 shows the wall heat fluxes computed according to SEB:

$$\underbrace{k\left.\frac{\partial T}{\partial y}\right|_w}_{convective} + \underbrace{\sum_i^{N_c} h_i \rho D_i \left.\frac{\partial y_i}{\partial y}\right|_w}_{diffusive} \underbrace{-\dot{m}(h_w - h_s)}_{blowing} - \epsilon\sigma T^4 - q_{cond} = 0$$

The diffusive and blowing heat fluxes are negative in accordance to the fact that the mechanism of ablation reduces the total wall heat load. As shown in Eqs. (5.9) and (5.10) the sum of the diffusive and blowing heat fluxes is the chemical heat flux which represents the heat absorption due to the *heat-of-ablation*[2]. Heat is absorbed because of the sublimation reaction of graphite with formation of gaseous C_3. The heat-of-ablation is therefore positive.

Figures 6.5 and 6.6 show the temperature and velocity boundary-layer profiles at the end of the flat plate with and without ablation. The blowing of the ablation species generates a cooling of the boundary-layer with a reduction in the temperature gradient at the wall and consequently a reduction in the convective heat flux to the surface. This effect is usually referred to as *blockage effect*. The surface blowing also produces a reduction in the velocity gradient at the wall as shown in Figure 6.6. The blockage effect will be more evident in the next test case.

[2]In the absence of catalytic reactions.

6.2.2 Test case 2: Nitrogen environment

Table 6.2: Freestream conditions for Test Case 2

Freestream Conditions	
pressure:	1 [bar]
temperature:	5000 [K]
Mach number:	3.5
Composition:	100% N_2

In this case the environmental gas is molecular nitrogen and the ablation products considered are C_3, C_5, and CN. With the use of a non-inert environmental gas there are also reactions between the solid material and the gas itself (e.g. nitridation of carbon). The freestream conditions are expressed in table 6.2. The wall temperature is kept constant and equal to $3800\ K$. In this case freestream conditions and wall temperature are more severe in order to produce a higher ablation rate. The equilibrium composition between gas phase and solid phase is imposed at wall. The four species considered (C_3, C_5, CN, and N_2) make up more than 95% of the equilibrium mixture for the actual condition of pressure and temperature. Species with minor concentrations have been neglected. Figure 6.7 shows the composition at wall and the mass blowing rate. In this case the blowing rate is more intense because of the higher wall temperature and freestream Mach number. The higher wall temperature increases the ablation products' mass fraction at wall and, together with the higher freestream velocity, increases the species' gradients inside the boundary layer and consequently the diffusional mass fluxes as shown in Figure 6.8. Figure 6.9 shows the species mass fractions profiles across the boundary-layer at the end of the flat plate. Created species are diffused from the surface to the edge of the boundary-layer. The environmental gas (nitrogen) is diffusing toward the surface. It's important to stress that at the surface there is a non-zero normal velocity, so that species diffusing to the wall are also transported away from the wall due to convection. Figure 6.10 shows the wall heat fluxes. In this case the heat absorption due to the ablation process is much more evident and the total incoming heat flux (convective + chemical) is highly reduced.

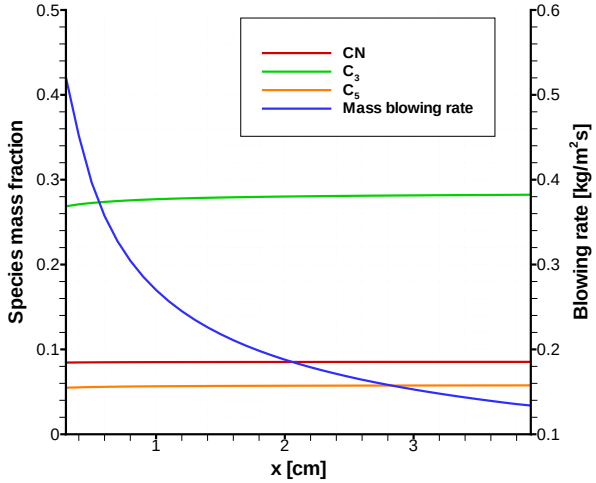

Figure 6.7: Mass blowing rate and species mass fraction (equilibrium) at wall.

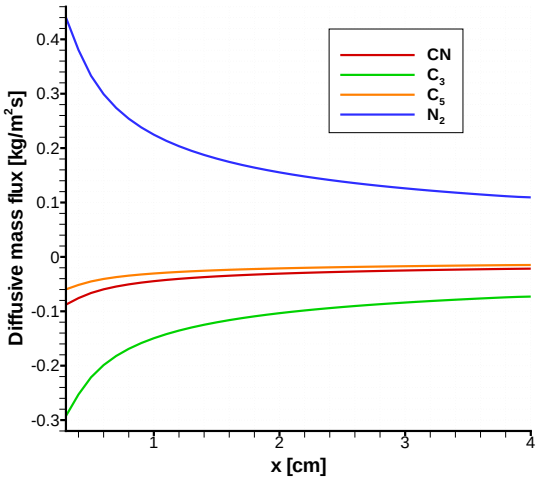

Figure 6.8: Species diffusive mass fluxes at wall.

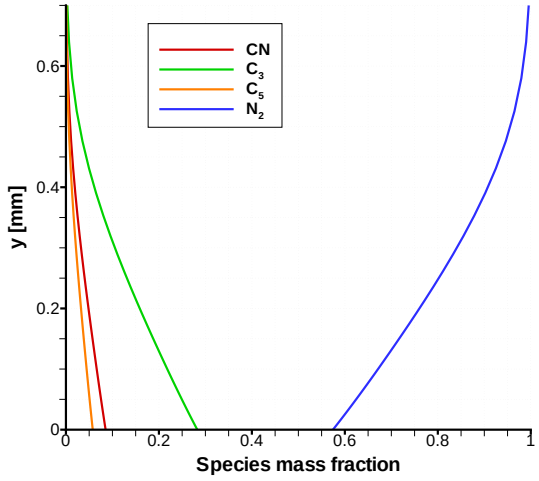

Figure 6.9: Species mass fractions boundary-layer profiles.

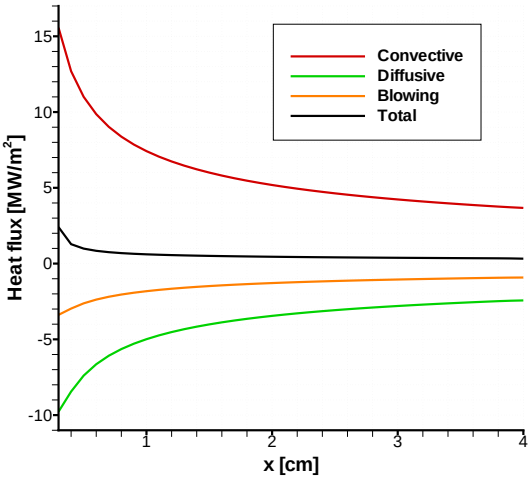

Figure 6.10: Wall heat fluxes.

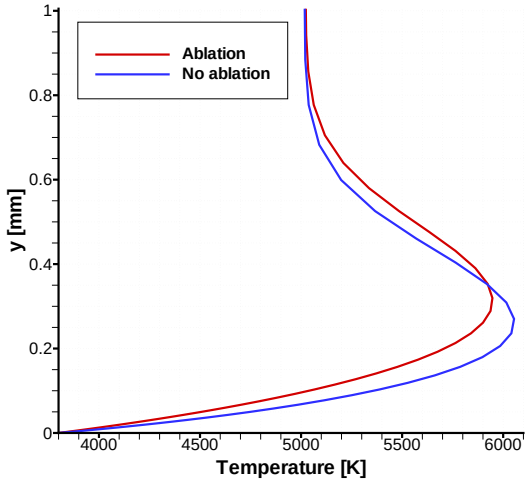

Figure 6.11: Temperature boundary-layer profile with and without ablation.

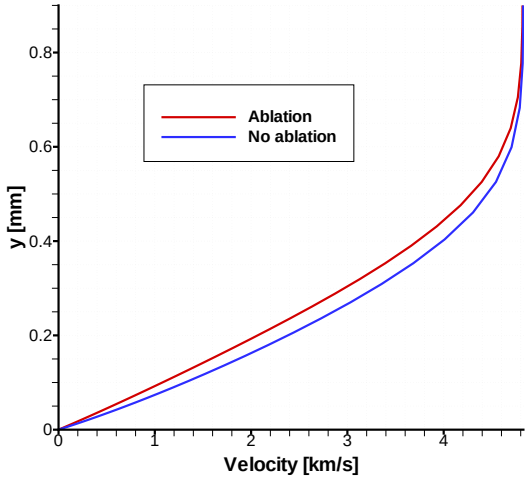

Figure 6.12: Velocity boundary-layer profile with and without ablation.

Figures 6.11 and 6.12 show the temperature and velocity boundary-layer profiles at the end of the flat plate with and without ablation. In this case due to more severe condition, the blockage effect and the consequent reduction of wall temperature and velocity gradients is evident. The peak temperature inside the boundary-layer away from the wall is also reduced by blowing.

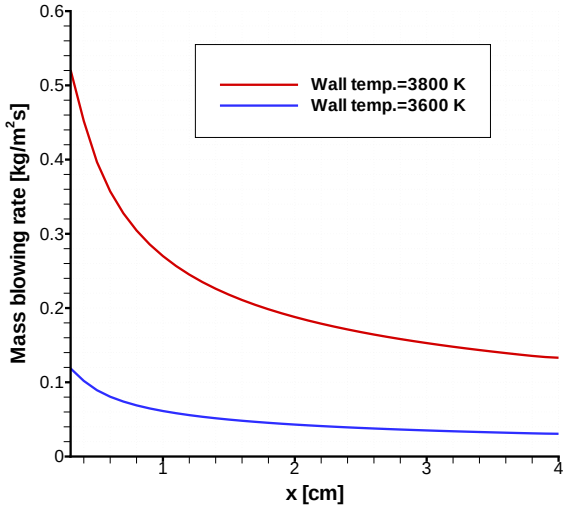

Figure 6.13: Effect of wall temperature on mass blowing rate.

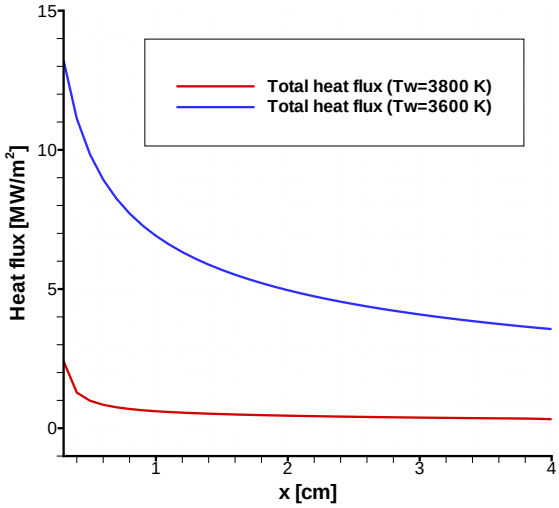

Figure 6.14: Effect of wall temperature on total wall heat flux.

The same test case has been repeated with the same freestream conditions and a lower wall temperature of $3600\ K$. Figures 6.13 and 6.14 show the effect of a reduction in wall temperature on the mass blowing rate and total heat flux, respectively. A 5% reduction in wall temperature produces an average mass blowing reduction of approx. 75% and an average total heat load increase of approx. 85%. This is because wall temperature is close to the sublimation temperature. Looking at the thermochemical table of Figure 1.4 it can be seen that, in the knee region of the curve, a slight temperature variation causes a great mass blowing variation.

6.2.3 Test case 1 and Case 2: comparison with blowing correction equation

In many cases, CSM and CFD codes are loosely coupled, and the heat flux to the ablating surface is usually computed based on the input non-ablating heat transfer coefficients corrected with empirical blowing reduction equations. This procedure provides reduced computational cost at the expense of accuracy. In fact, the uncertainty in the estimated ablating heat flux can be high, and consequently the predictions of mass blowing rate and temperature are somewhat inaccurate. As seen in Chapter 1, using a convective transfer coefficient approach the convective heat flux from the gas to the surface can be expressed as [17, 18]:

$$q_{conv} = k \left. \frac{\partial T}{\partial y} \right|_w = \rho_e u_e C_h (h_r - h_w)_e \tag{6.1}$$

where $h_{w,e}$ is the enthalpy of edge gases evaluated at wall temperature and h_r is the recovery enthalpy of the edge gases. As discussed in Chapter 1, the term C_h is the transfer coefficient ($Stanton$ number) for heat transfer. A blowing correction allows for the reduction in transfer coefficient due to the transpiration or blowing effect of gases being injected into the boundary layer. The most commonly used blowing rate correction equation is represented by Eq. (1.42) [17, 18]:

$$C_h^{'} = C_{h_0} \left[\frac{\phi}{e^{\phi} - 1} \right] \tag{6.2}$$

where λ is a blowing reduction parameter (equal to 0.5 in the laminar case) and $\phi = 2\lambda \dot{m}/(\rho_e u_e C_{h_0})$. Eq. (6.1) can be used to evaluate the unblown $Stanton$ number C_{h_0} from the convective heat flux computed via a non-ablating CFD computation, Eq. (6.2) is then used to evaluate the corrected heat transfer coefficient $C_h^{'}$ provided that the mass blowing rate $\dot{m}$ is known. With the corrected heat transfer coefficient the ablative surface heat flux can be evaluated via Eq. (6.1).

Figures 6.15 and 6.16 show the computed conductive heat fluxes for Test case 1 and 2 with and without ablation. Results are compared with the corrected non-ablating heat flux using the methodology above mentioned. The mass blowing rate $\dot{m}$ used in the blowing correction equation is the one previously evaluated with the fully coupled ablation model so that the only blowing correction equation is tested here. For Test case 1 the conductive heat flux is reduced approximately by 10% and the corrected curve shows a perfect agreement with the computed one. For Test case 2, with a more intense blowing, the reduction is approximately of 15% and the agreement between computed and corrected heat flux is slightly worse. The blowing reduction equation seems to work better in case of lower ablation rates, as one would easily expect.

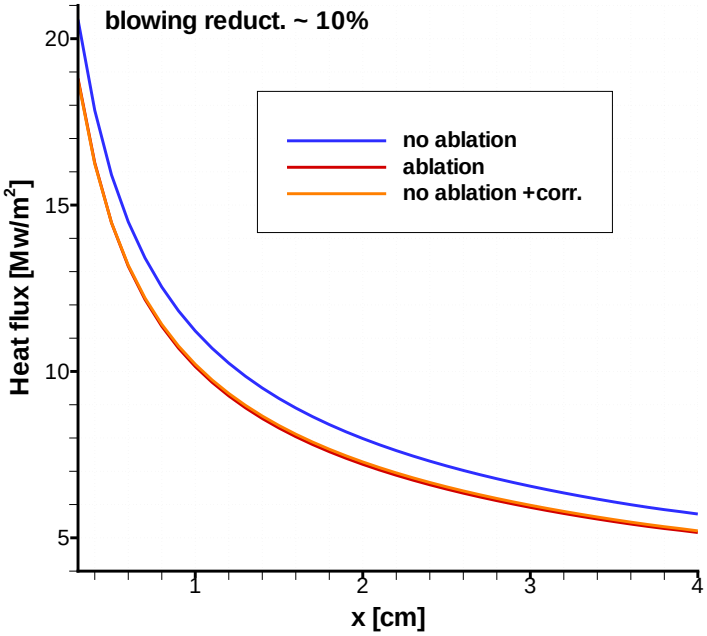

Figure 6.15: Test case 1: comparison with blowing correction equation.

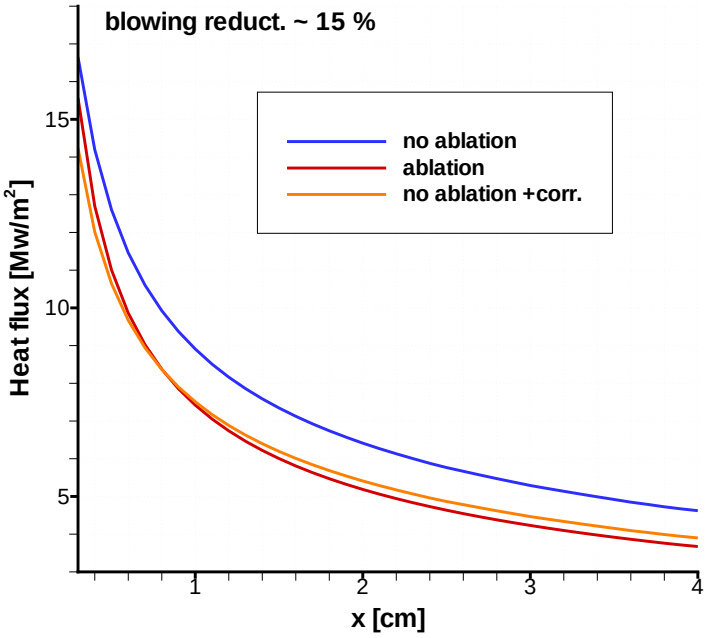

Figure 6.16: Test case 2: comparison with blowing correction equation.

6.2.4 Effect of surface temperature

The supersonic ($M = 4$) flow of air over a graphite flat plate is analysed. Three different surface temperatures are considered: a) $T_w = 2500\ K$; b) $T_w = 3800\ K$; and c) $T_w = 3900\ K$. The environmental gas is frozen air with equilibrium composition at the freestream thermodynamic state ($p = 1\ bar$, $T = 4000\ K$, $y_{N_2} = 0.767$, $y_O = 0.233$). The equilibrium composition between gas phase and solid phase is imposed; two ablation species are considered (CO and C_3) which make up more than 85% of the equilibrium mixture for the actual conditions of pressure and temperature. Species with minor concentrations have been neglected.

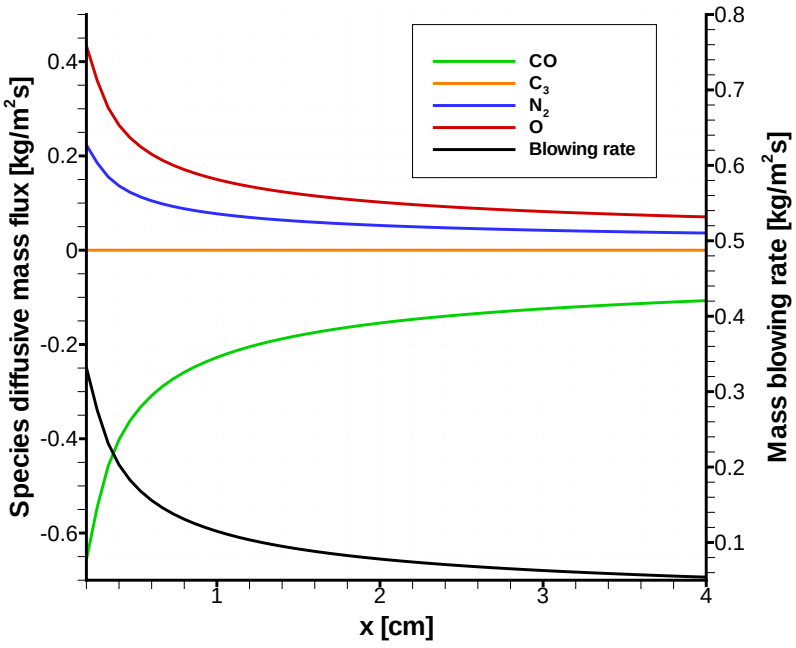

Figure 6.17: Species diffusive mass fluxes and mass blowing rate for $T_w = 2500\ K$.

Figures 6.17 and 6.18 show the wall diffusive mass flux of each species (CO, C_3, N_2, O) together with the mass blowing rate for two different wall temperatures. As shown in previous results the mass blowing rate is strongly varying in the streamwise direction according to the growth of the boundary layer: higher mass blowing rates are experienced near the leading edge of the plate where the diffusional mass fluxes are higher. The diffusional mass fluxes are positive for the

atmospheric species and negative for the ablation products created at the surface. The surface temperature of $2500\ K$ is too low to trigger surface sublimation (with formation of C_3) and the only ablation mechanism is the oxidation of carbon.

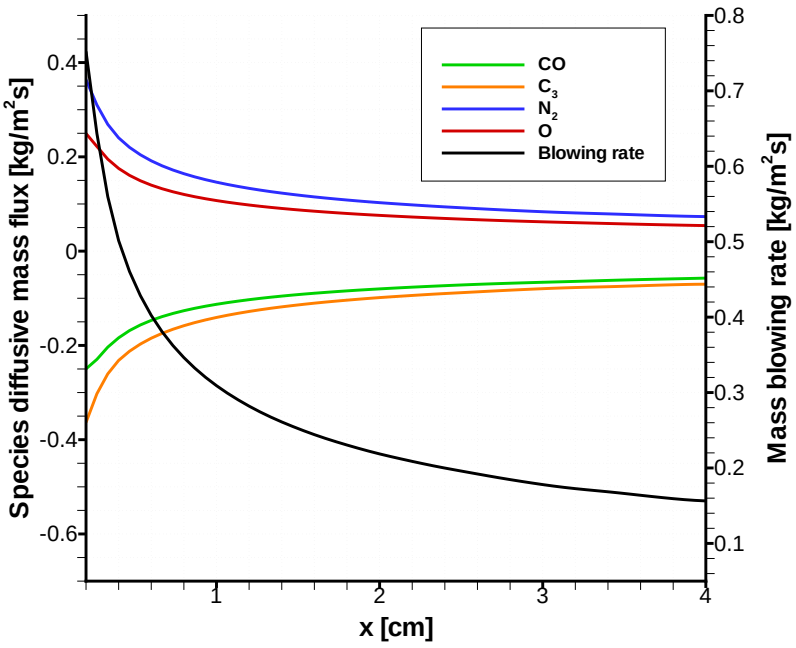

Figure 6.18: Species diffusive mass fluxes and mass blowing rate for $T_w = 3800\ K$.

Figure 6.19 shows the mass blowing rate which is strongly varying with the surface temperature. The mass blowing rate increases with temperature, especially in the sublimation regime ($T_w = 3800\ K$ and $T_w = 3900\ K$). In this regime, a slight increase of the surface temperature causes a large increase of the mass blowing rate. This behaviour has been previously shown by the sudden increase of B' with temperature in the thermochemical table model (see Fig. 1.4). The surface convective heat flux ($k \cdot \partial T/\partial \eta$) shown in Figure 6.20 is reduced in part due to the increase of wall temperature and mainly due to the so called *blockage effect* caused by the blowing of ablation product. The dashed lines in Figure 6.20 represent the same solution without ablation. The effect of *blockage* is evident in the sublimation regime where the heat flux is highly reduced if compared to the non-ablating case. The blowing of ablation products thus generates a cooling of the boundary layer which consequently reduces the wall heat flux. This can be

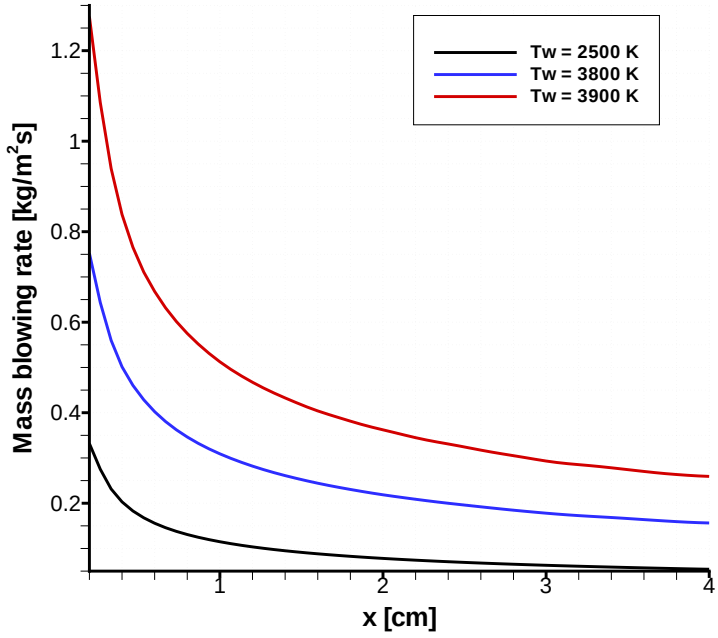

Figure 6.19: Mass blowing rate for three wall temperatures.

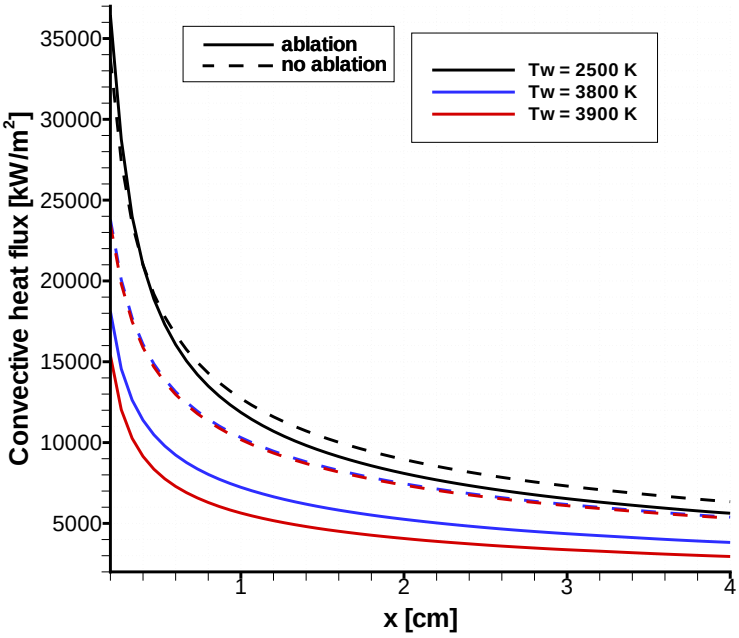

Figure 6.20: Convective heat flux for three wall temperatures.

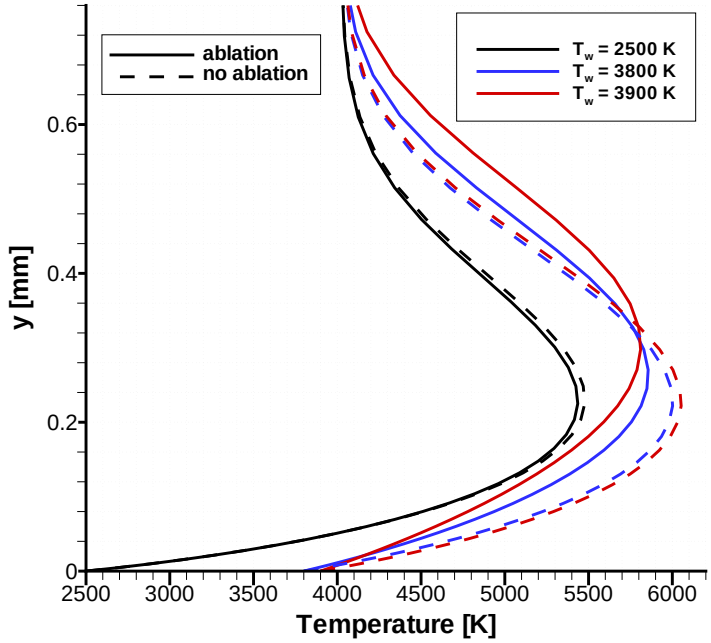

Figure 6.21: Temperature profile for three wall temperatures.

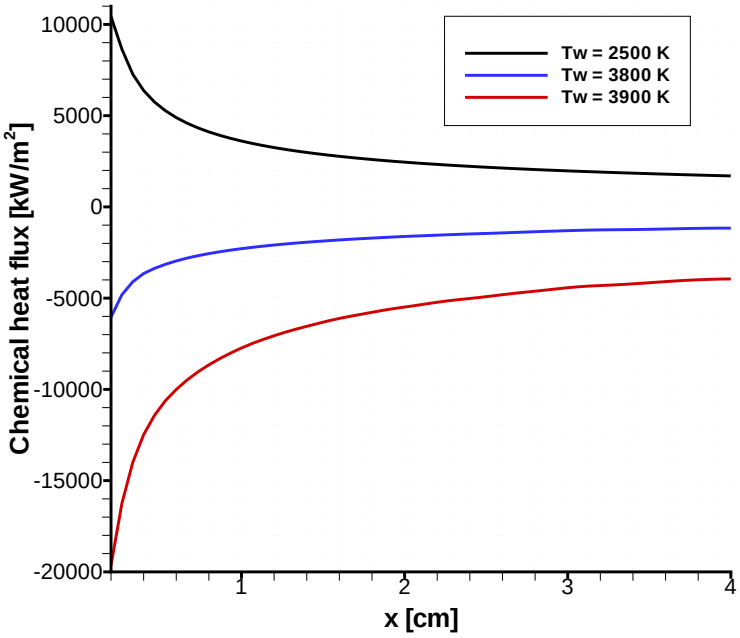

Figure 6.22: Chemical heat flux for three wall temperatures.

seen looking at the temperature profiles shown in Figure 6.21. For strong blowing the blockage effect is one of the major mechanism to limit the temperature rise inside the material. Finally, Figure 6.22 shows the *chemical heat flux* for the three cases. It can be seen that in the oxidation regime ($T_w = 2500\ K$) the chemical flux is positive, while in the sublimation regime it is negative. Therefore in the former regime the chemical reactions at wall are releasing heat, whereas in the latter they are absorbing it. This is due to the fact that the oxidation reaction of graphite (with formation of CO) is and exothermic process whereas the vaporization process (with formation of C_3) is endothermic.

6.2.5 Effect of boundary-layer finite-rate chemistry

The temperature rise inside the boundary layer can be considerable due to the viscous dissipation which converts kinetic energy into heat. In the previous solutions the temperature rises above $5500\ K$ inside the boundary layer away from the surface (see Figure 6.21). A new computation is performed at $M = 6$ to reach a peak temperature of nearly $8000\ K$ inside the boundary-layer. Such a high temperature can trigger thermal decomposition of ablation species which is another mechanism to divert energy which otherwise would reach the wall.

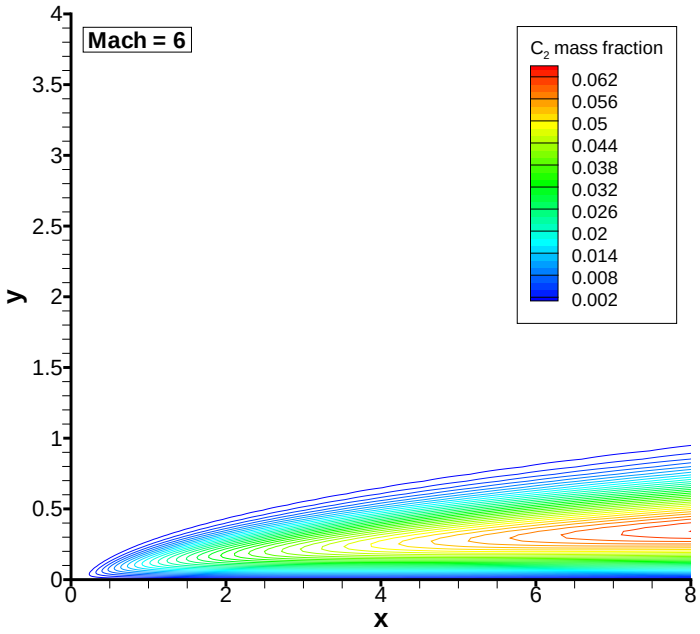

Figure 6.23: C_2 mass fraction spatial distribution (not in scale).

In the previous solutions ablation species were not allowed to react with each other as they were diffusing across the boundary layer. In order to study the effect of these chemical reactions, a finite-rate kinetic model based on the work of Park [64] has been adopted to model the thermal decomposition of the two ablating species CO and C_3 created at wall:

$$CO = C + O, \qquad C_3 = C_2 + C, \qquad C_2 = C + C$$

Figure 6.23 shows the C_2 mass fraction spatial distribution which can be considered as an index of the thermal decomposition of C_3.

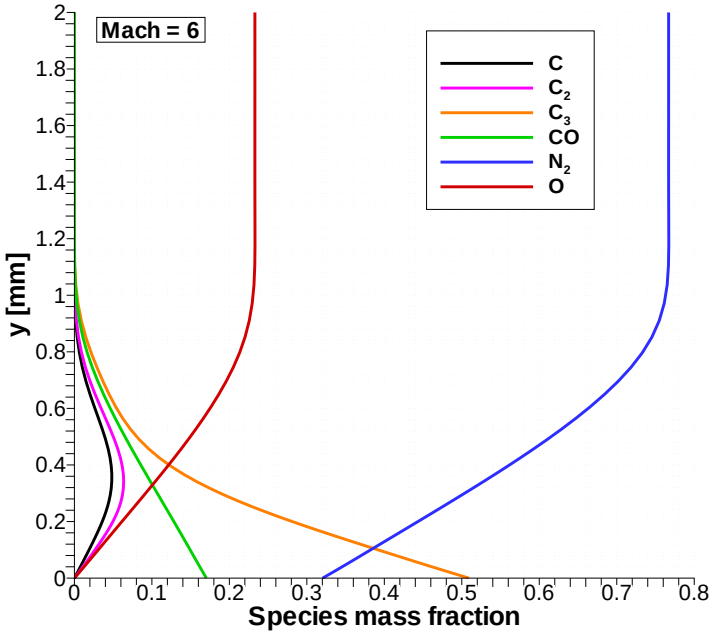

Figure 6.24: Species mass fractions profiles.

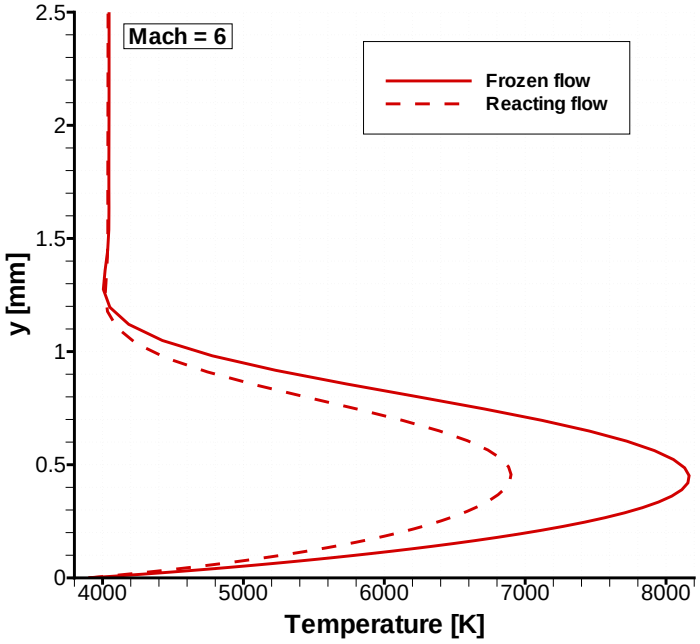

Figure 6.25: Temperature profiles.

The creation of the species C and C_2 inside the boundary-layer and away from the wall (where the temperature is higher) is shown in Figure 6.24 which shows the species mass fractions profiles at the end of the flat plate. It is clear that a certain amount of C_3 and CO are thermally decomposed and these reactions produce a cooling of the boundary layer as Figure 6.25 clearly shows. However, the effect of these decomposition reactions can be seen on the mass blowing rate and wall convective heat flux. The effect, even if weak, is a reduction both in mass blowing rate and convective heat flux as shown in Figure 6.26.

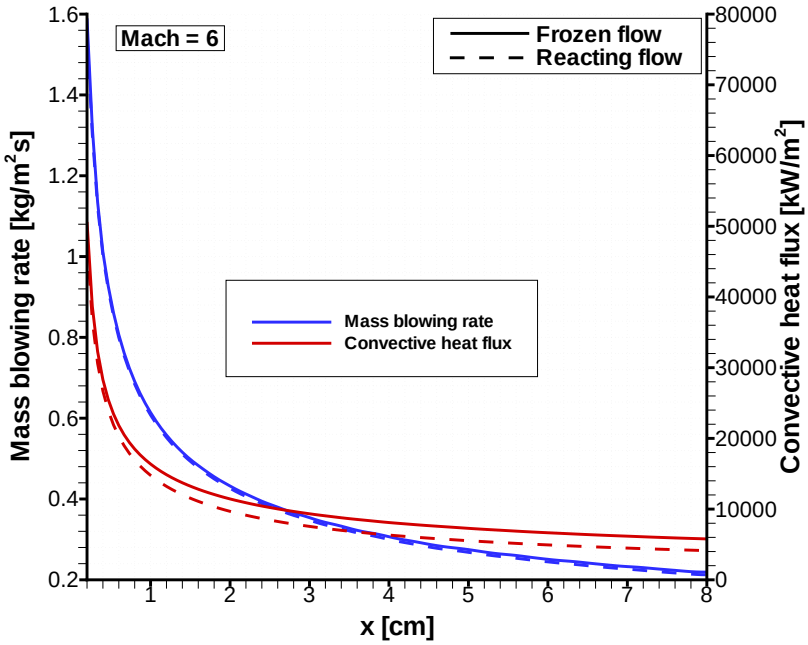

Figure 6.26: Mass blowing rate and convective heat flux.

6.2.6 Comparison with thermochemical table approaches

With the procedure developed in this work, the mass balance equation is solved inside the CFD code, through the boundary condition. However, in many cases CFD codes are loosely coupled with the material and often the flowfield solutions are obtained using ablating boundary conditions with $B^{'}$ tables [16, 63, 18, 38] or even non-ablating boundary conditions corrected with blowing reduction equations [17, 15, 21].

When a *thermochemical table* approach is used coupled with ablative CFD solutions, the mass blowing rate at the surface is obtained by the use thermochemical tables such as those in Figure 1.4. To obtain the mass blowing rate $\dot{m}$ from the tables, surface pressure and temperature must be known together with the mass transfer coefficient C_m. In the isothermal case, surface temperature is assigned while surface pressure can be obtained from the flowfield solution and the zero-pressure gradient condition. Finally, the diffusion coefficient C_m is derived from semi-empirical relations such as [69]:

$$C_m = C_h \cdot Le^{-2/3} \tag{6.3}$$

and the heat transfer coefficient C_h is evaluated from the ablative CFD solution by its definition:

$$C_h = \frac{k \left.\dfrac{\partial T}{\partial \eta}\right|_w}{\rho_e u_e (h_r - h_w)_e} \tag{6.4}$$

In this case the heat-transfer coefficient needs not to be corrected for blowing because it is obtained from an ablative CFD solution. Eq. (6.4) is used to evaluate the heat transfer coefficient from the CFD solution and C_h is then used with Eq. (6.3) to compute C_m. With C_m and the $B^{'}$ value coming from the table, the mass blowing rate can be finally evaluated. The procedure must be iterated until convergence because the mass blowing rate $\dot{m}$ affects the CFD solution changing the heat transfer coefficient C_h which, in turns, alters the mass blowing rate. This procedure is typically used when coupling the CFD code to a material thermal response code [16, 63, 17, 18, 38]. However, even if ablative CFD computations are performed, the simplified mass transfer model at the base of thermochemical tables together with Eq. (6.3) can affect the accuracy of the CFD solution.

When *non-ablating boundary conditions* are used in the CFD solution (no mass injection and no chemical reactions at the surface), a blowing correction is typically adopted to reduce the computed heat flux to take into account of the blockage effect due to the ablation gases injected into the boundary layer. The

blowing-correction equation is the usual:

$$C_h = C_{h_0}\left[\frac{ln\left(1+2\lambda\dot{m}/\left(\rho_e u_e C_h\right)\right)}{2\lambda\dot{m}/\left(\rho_e u_e C_h\right)}\right] = C_{h_0}\left[\frac{ln\left(1+2\lambda B' C_m/C_h\right)}{2\lambda B' C_m/C_h}\right] \quad (6.5)$$

When a non-ablating CFD solution is performed, Eq.(6.4) is used to compute the non-ablative heat transfer coefficient C_{h_0} which is then reduced with the use of Eq.(6.5). The corrected C_h is finally used to evaluate the mass blowing rate as in the case of thermochemical table approach with ablating boundary conditions. In this case there is no iterative coupling between TPS and CFD solution, since thermochemical tables and blowing correction equations are used to obtain TPS properties (such as the mass blowing rate $\dot{m}$ in this case) without updating the CFD solution (which is non-ablating). The computational cost is reduced when non-ablating boundary conditions are adopted, both because a simpler solution (with no species injected and no surface reactions) is performed, and also because no iteration are needed to couple the CFD solution with the thermochemical table model. Obviously all this at the expense of accuracy.

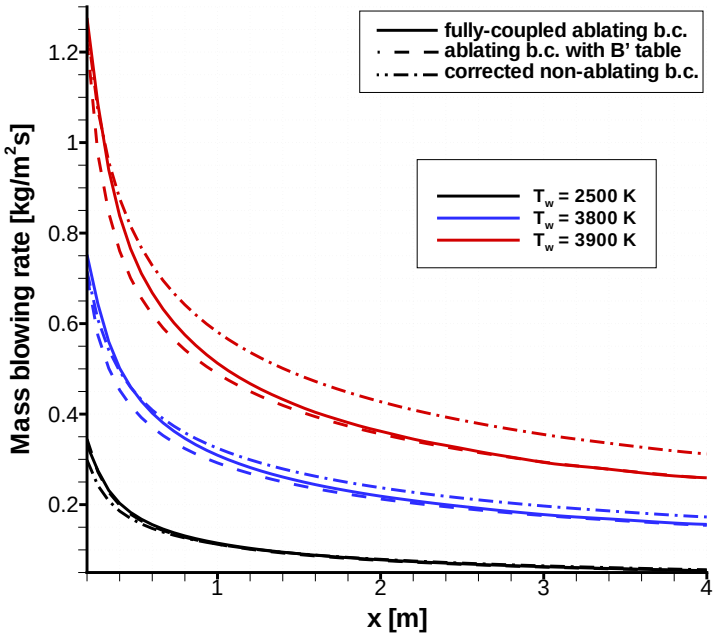

Figure 6.27: Mass blowing rate for different wall temperatures with three different boundary conditions.

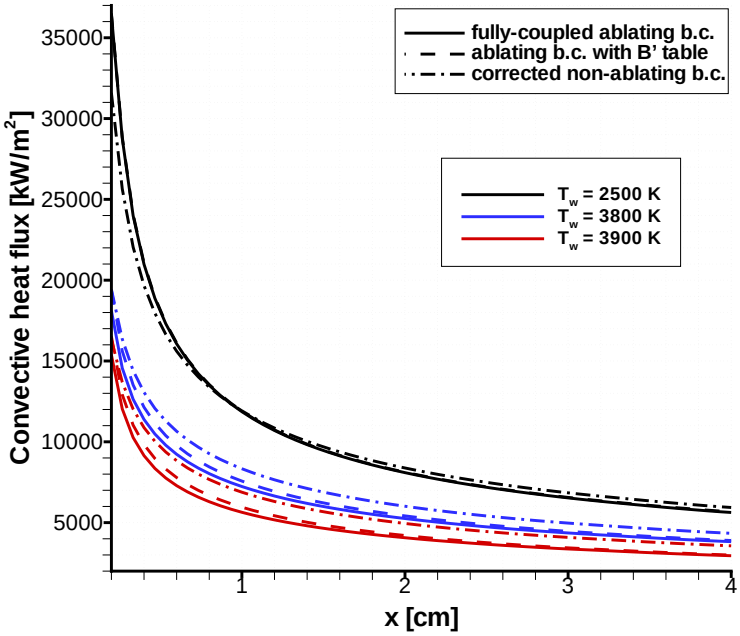

Figure 6.28: Convective heat flux for different wall temperatures with three different boundary conditions.

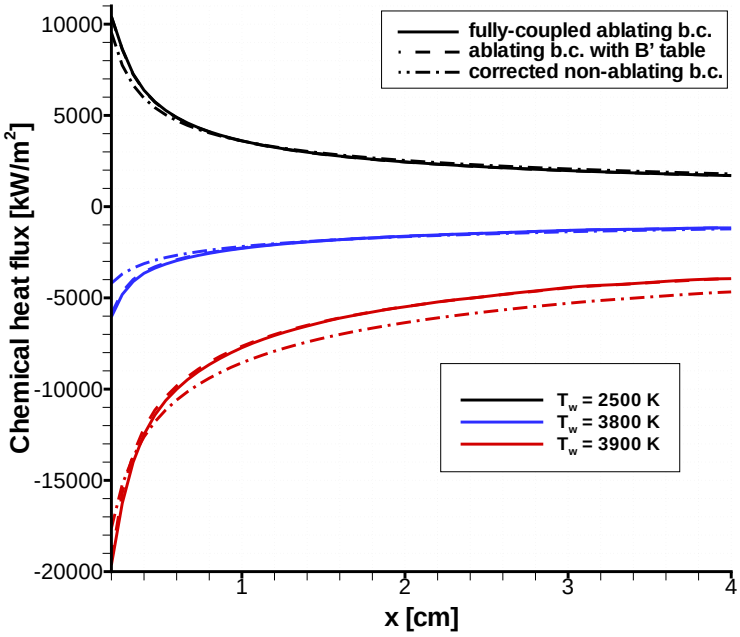

Figure 6.29: Chemical heat flux for different wall temperatures with three different boundary conditions.

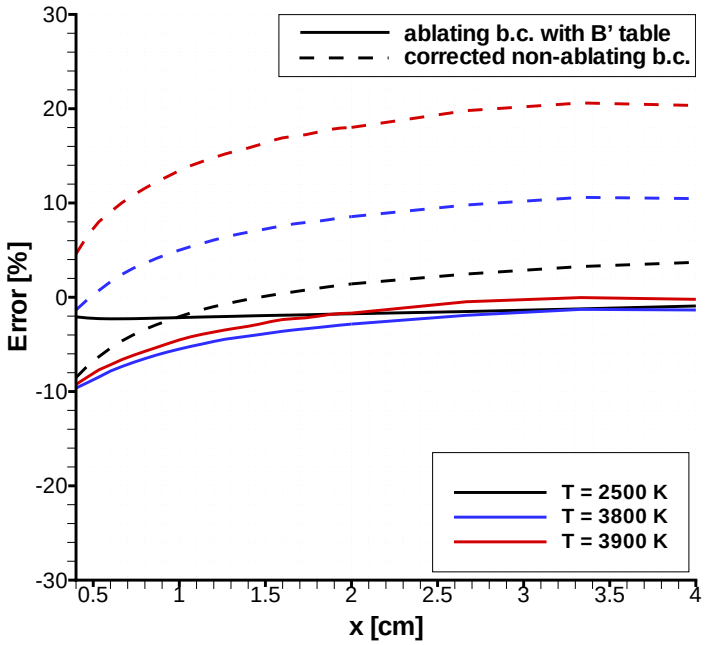

Figure 6.30: Differences on the mass blowing rate between the present method and the simplified approaches.

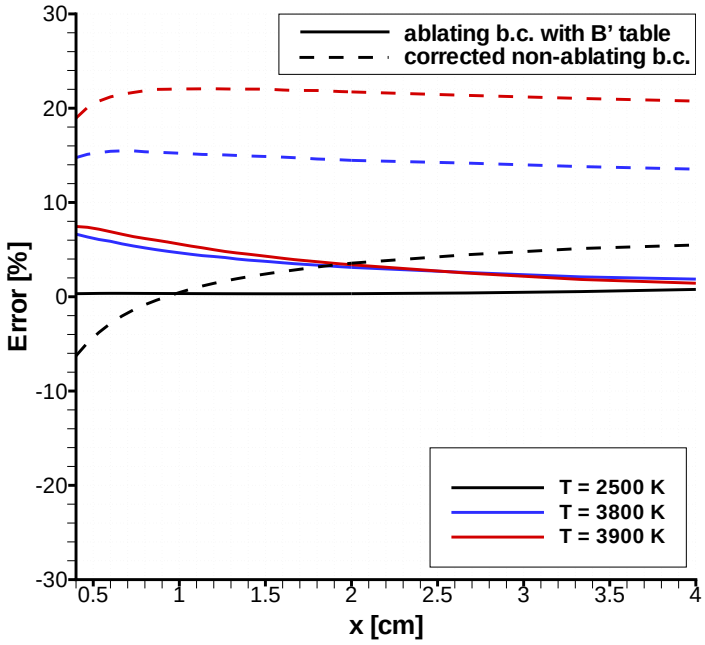

Figure 6.31: Differences on the convective heat flux between the present method and the simplified approaches.

Figures 6.27, 6.28, and 6.29 show the mass blowing rate, convective heat flux, and chemical heat flux (respectively) for the three wall temperatures, computed with three different boundary conditions: fully-coupled ablating boundary conditions, ablating boundary conditions coupled with $F(T, p, B')$ thermochemical tables, and non-ablating boundary conditions coupled with thermochemical tables and blowing correction equation. Both the blowing rate and the heat flux clearly show the error introduced by the simplified boundary conditions. The agreement between the table approach and the fully-coupled approach is very good at the lowest temperature but gets worse as the temperature and consequently the mass blowing rate are increased. Figures 6.30 and 6.31 show the percentage errors between the fully coupled approach and the two simplified approaches for the mass blowing rate and convective heat flux, respectively. Obviously the non-ablating approach is the one leading to major errors. Figures 6.30 and 6.31 clearly show that the agreement between the fully-coupled and the simplified approaches get worse as the temperature and therefore the mass blowing rate is increased.

The comparison between the cases with ablating boundary conditions shows that at the higher surface temperatures the table-predicted mass blowing rate and heat flux are affected by a certain degree of inaccuracy. These results show the limitations of the *thermochemical-table* approaches due to the simplified boundary-layer diffusion model expressed by Eq. (1.25), which was developed from the laminar boundary-layer theory over flat plates [34]; thus the present comparisons between the two approaches are made in the most favourable condition.

Table 6.3: Freestream conditions for Test Case 3

Freestream Conditions	
pressure:	1 [bar]
temperature:	5000 [K]
Mach number:	1.8
Composition (equil. air):	77.787%N_2 22.213% O

6.3 Steady-state ablation results

The fully-coupled procedure described in Chapter 5 for steady-state ablation is applied to a flat plate made of pure carbon (graphite). Chemical reactions between the material and the environmental gas at the surface are accounted for using an equilibrium approach. The effect of finite rate chemical reactions inside the boundary-layer is studied in section $6.3.3$.

6.3.1 Test case 3: Air environment

In this case the environmental gas is air and the "steady-state" energy balance Eq. (5.12) is used to compute the correct wall temperature distribution across the axial direction. The freestream conditions are expressed in table 6.3. The ablation products considered are CN, CO, and C_3. Wall temperature distribution across the axial direction is set initially at $3000K$, then the code makes use of the SSEB to find the correct steady-state value.

Figure 6.32 shows the mass blowing rate and the wall temperature. It is evident the strong variation in the streamwise direction of both temperature and mass blowing rate. Higher wall temperatures are experienced near the leading edge of the flat plate where the incoming heat fluxes are higher. Mass blowing rate is strongly varying in the streamwise direction (if compared to the previous isothermal solutions) both because of the growth of the boundary layer and also because of the decrease of surface temperature. Since the wall temperature is not constant, the wall chemical composition is consequently varying, as shown in figure 6.33. Near the leading edge wall temperature is sufficiently high to produce graphite sublimation (with formation of C_3) and carbon nitridation (with formation of CN). Away from the leading edge these species tend to vanish because the surface is getting colder and CO production dominates. Therefore, for an air environment and in this range of wall temperatures, surface oxidation reactions

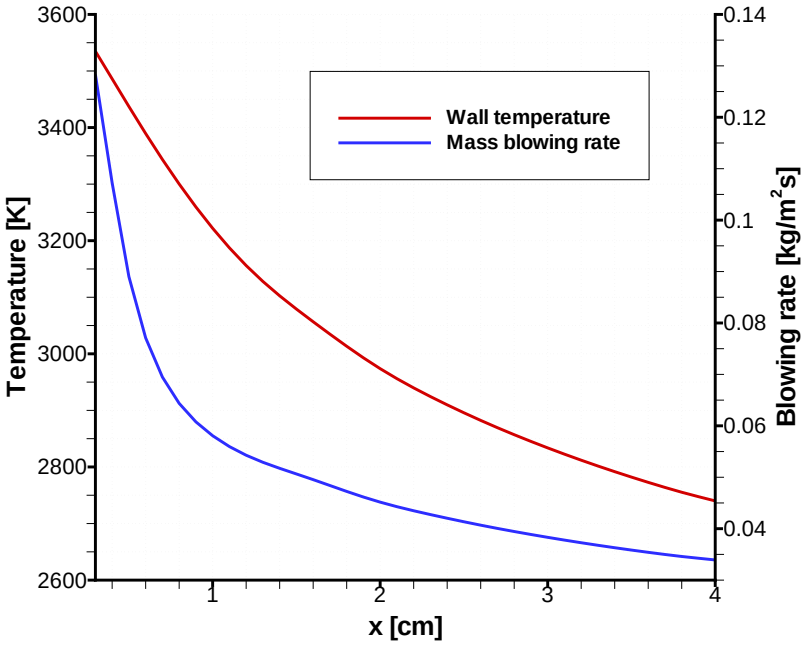

Figure 6.32: Wall temperature and mass blowing rate.

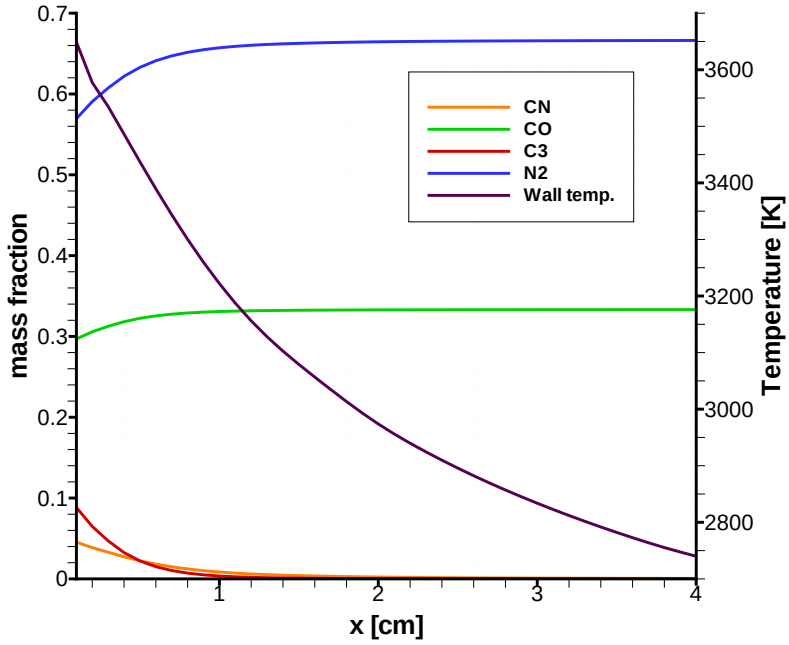

Figure 6.33: Wall temperature and composition.

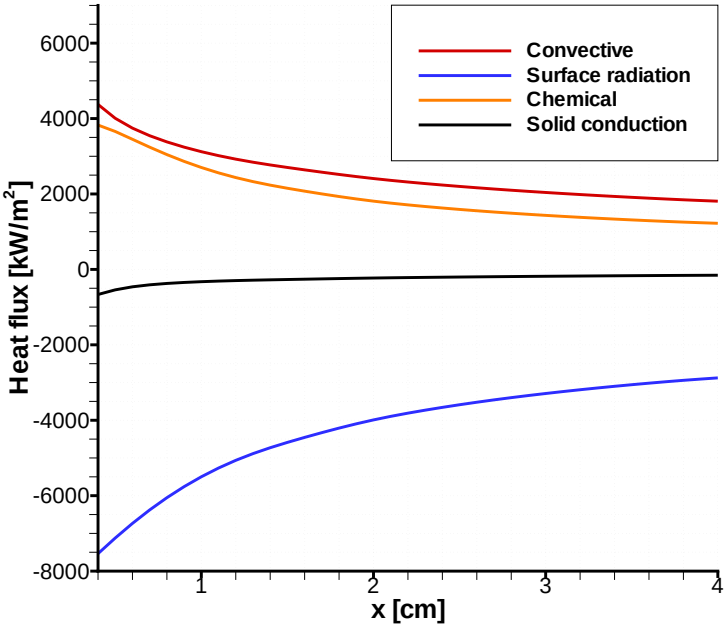

Figure 6.34: -*Air*- Wall heat fluxes

dominate and CO is the major species leaving the surface. The carbon oxidation reaction ($C + \frac{1}{2}O = CO$) is an exothermic reaction and this affects strongly the surface energy balance. Looking at figure 6.34, in fact, the chemical heat flux is positive (so the *heat-of-ablation* is negative); this means that in this condition the process of ablation is generating heat. The only mechanisms to cool the wall are surface radiation (which is strong since wall temperature is high) and heat soak into the solid. When the surface temperature reaches values close to $4000K$[3], however, carbon sublimation (which is endothermic) becomes dominant and CO formation falls off rapidly as shown in the next section.

[3]for wall pressures in the range of 1 bar.

6.3.2 Effect of Mach number

The supersonic laminar flow of air over a graphite flat plate is analysed. Three different Mach numbers are considered: a) $M = 2$; b) $M = 4$; and c) $M = 6$. The environmental gas is frozen air with equilibrium composition at the freestream thermodynamic state ($p = 1\ bar$, $T = 4000\ K$, $y_{N_2} = 0.767$, $y_O = 0.233$). The equilibrium composition between gas and solid phase is imposed at wall; two ablation species are considered (CO and C_3) which make up more than 85% of the equilibrium mixture for the actual conditions of pressure and temperature. Species with minor concentrations have been neglected. Chemical reactions between the wall material and the environmental gas are considered only at the surface; once the wall composition has been calculated, the species are not allowed to react with each other as they are diffusing across the boundary layer. Mass blowing rate and surface temperature are computed solving the mass and steady-state energy balance Eqs. (5.14) and (5.12), respectively. The radiative heat flux from the gas to the surface in the surface energy balance has been neglected.

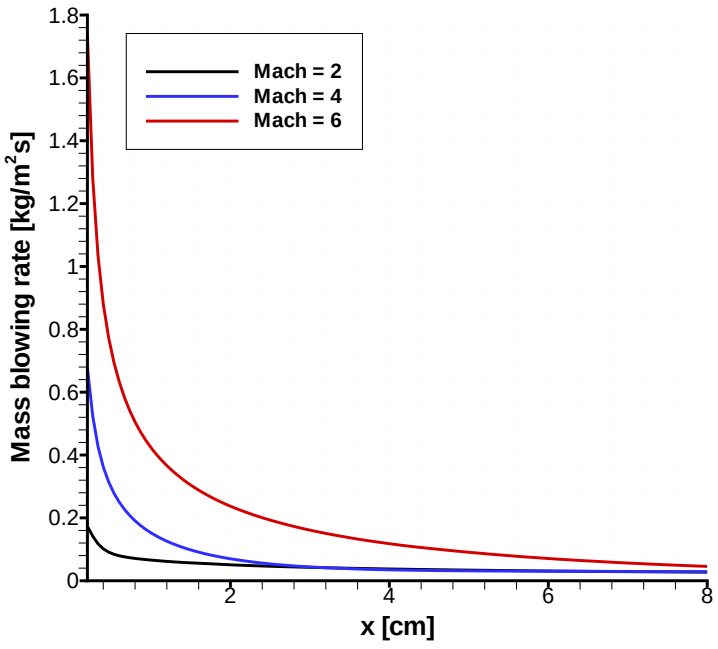

Figure 6.35: Mass blowing rate at different Mach numbers.

Figures 6.35 and 6.36 shows the mass blowing rate and wall temperature profiles for the three different Mach numbers. Both the blowing rate and wall tem-

perature are increasing with M due to the increase of the convective heat flux to the wall. The mass blowing rate, as shown in the previous solutions, is rapidly decreasing because of the combined effect of boundary layer growth and decreasing wall temperature. Moreover it can be seen that, at the highest Mach number, the wall temperature tends to be uniform. This is due to the fact that, for each pres-

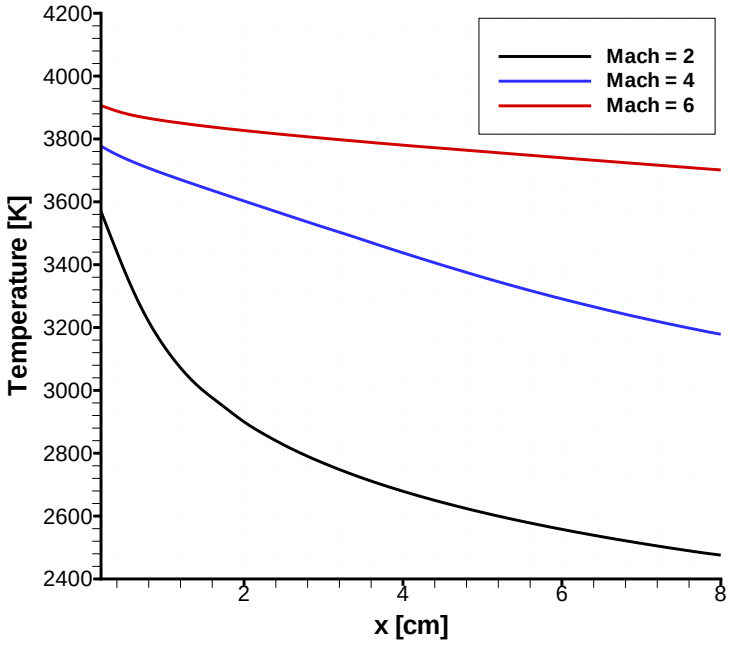

Figure 6.36: Surface temperature at different Mach numbers.

sure, there is a limit temperature (i.e. the sublimation temperature) which cannot be exceeded. When the temperature is close to the sublimation temperature, the effect of increasing the heat flux is a large increase of mass blowing rate and only a minor increase of surface temperature. This behaviour has been previously shown by the sudden increase of B' with temperature in the thermochemical table model (see Figure 1.4). Figure 6.36 clearly shows this behaviour: passing from $M = 4$ to $M = 6$, the temperature near the leading edge of the plate is only increased by 3.5% while the mass blowing rate is increased by more than 150%.

Figures 6.37 and 6.38 show the wall convective heat flux (with and without ablation) and the wall chemical heat flux according to Eq. (5.12). The non-ablative solutions have been obtained with the commonly assumed [15] radiative equilibrium energy balance and with frozen surface chemistry. Figure 6.37 clearly shows

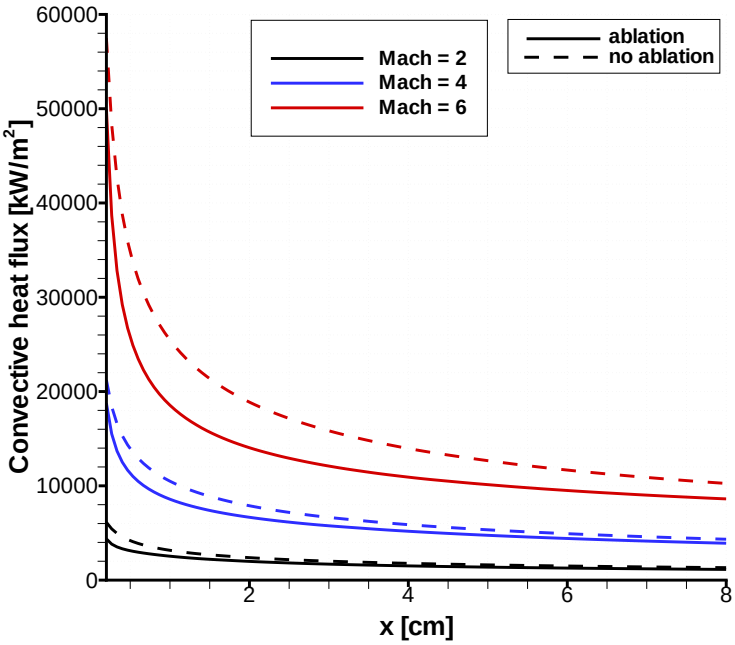

Figure 6.37: Convective heat fluxes with and without ablation at different Mach numbers.

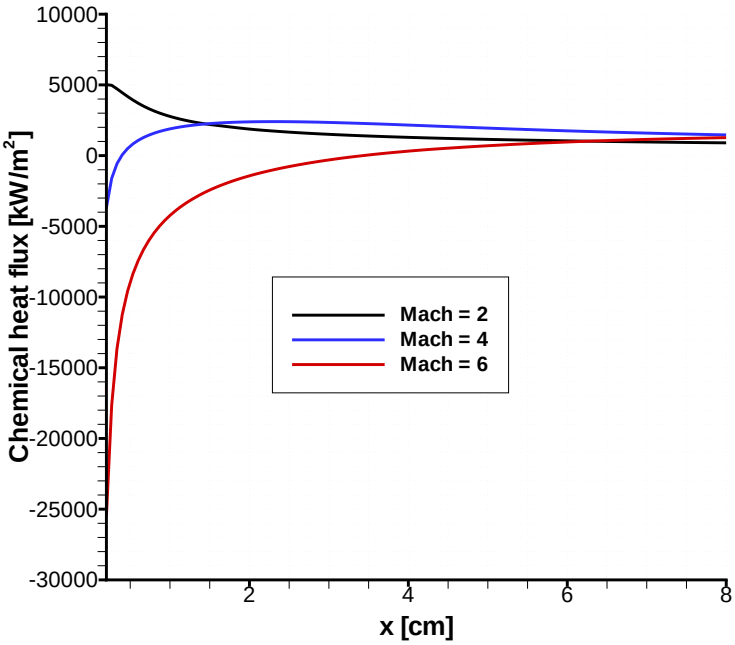

Figure 6.38: Chemical heat fluxes at different Mach numbers.

the reduction of the surface heat flux due to the *blockage effect*. The effect of *blockage* is more evident in the sublimation regime where the heat flux is highly reduced if compared to the non-ablating case. Figure 6.38 shows the *chemical heat flux* for the three cases. For $M = 2$ the chemical heat flux is always positive, for $M = 4$ it is negative in the leading edge zone, and for $M = 6$ it is negative in the first half of the plate. This behaviour is due to the transition between the oxidation and the sublimation regime caused by the variable surface temperature. In the former regime the graphite oxidation (with formation of CO) is the primary mass loss mechanism while in the latter the sublimation of graphite dominates and C_3 is the major species leaving the surface. Since graphite oxidation is an exothermic process the chemical reactions at wall are releasing heat, causing the wall chemical heat flux to be positive; graphite sublimation, instead, is an endothermic process causing the wall chemical heat flux to be negative.

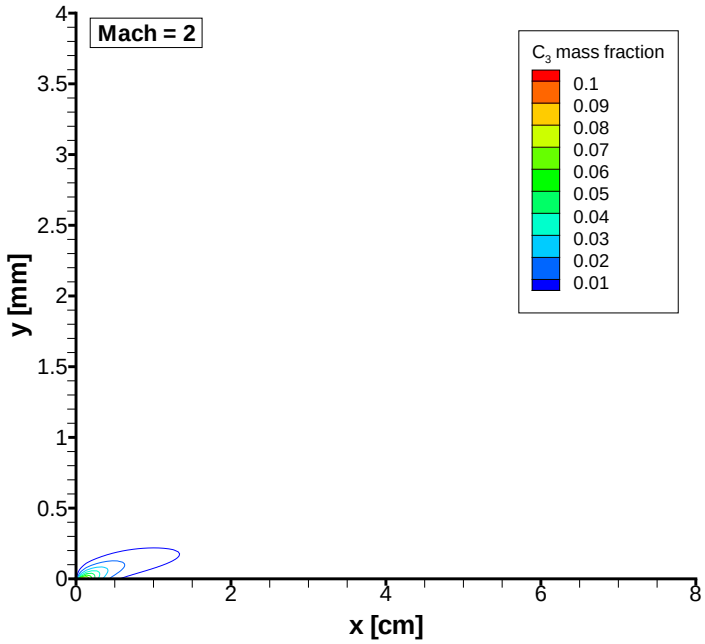

Figure 6.39: C_3 mass fraction spatial distribution at $M = 2$ (not in scale).

Figures 6.39, 6.40, and 6.41 show the C_3 mass fraction spatial distribution in the flowfield at the three Mach numbers. The sublimation of carbon is almost absent for $M = 2$ (graphite oxidation dominates) because of a too-low wall temperature, while it is dominant for $M = 6$. These results help explaining the behaviour of Figure 6.38 and show the transition between the two regimes.

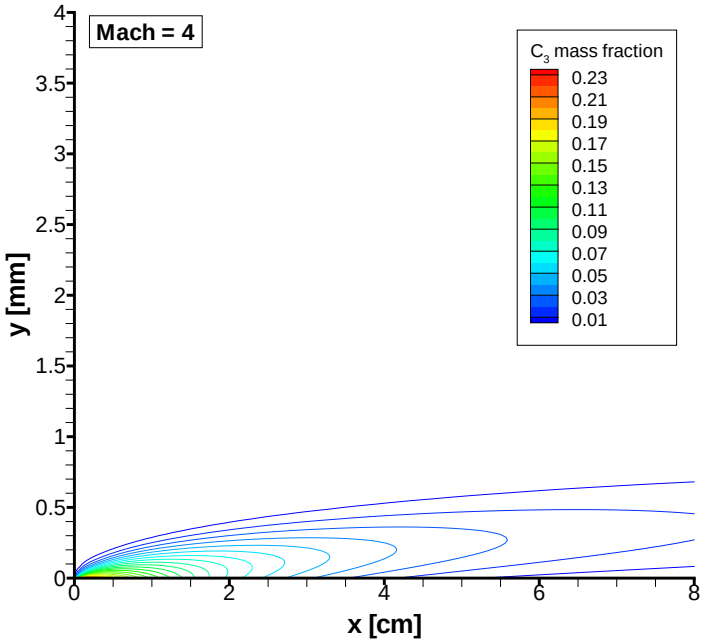

Figure 6.40: C_3 mass fraction spatial distribution at $M = 4$ (not in scale).

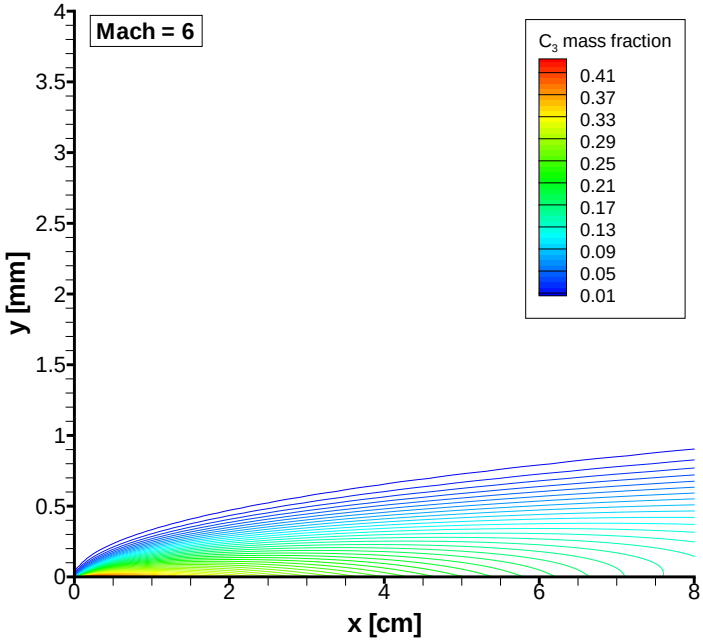

Figure 6.41: C_3 mass fraction spatial distribution at $M = 6$ (not in scale).

Figures 6.42, 6.43, and 6.44 show the wall heat fluxes for the three different Mach numbers. The heat fluxes are computed according to the SSEB Eq. (5.12) where the radiative heat flux from the gas to the surface (q_{rad}) has been neglected. For $M = 2$, since the chemical heat flux is always positive due to carbon oxidation, the only mechanism of cooling the surface is re-radiation from the wall. For $M = 6$, instead, the surface temperature is sufficiently high to produce carbon sublimation almost everywhere. In the first half of the plate the heat flux absorption is mainly due to graphite ablation (chemical heat flux) with the re-radiation from the surface playing a minor role in cooling the surface. The results of Figures 6.42-6.44 also show the strong variation of the (steady-state) solid conduction heat flux due to the varying flowfield conditions.

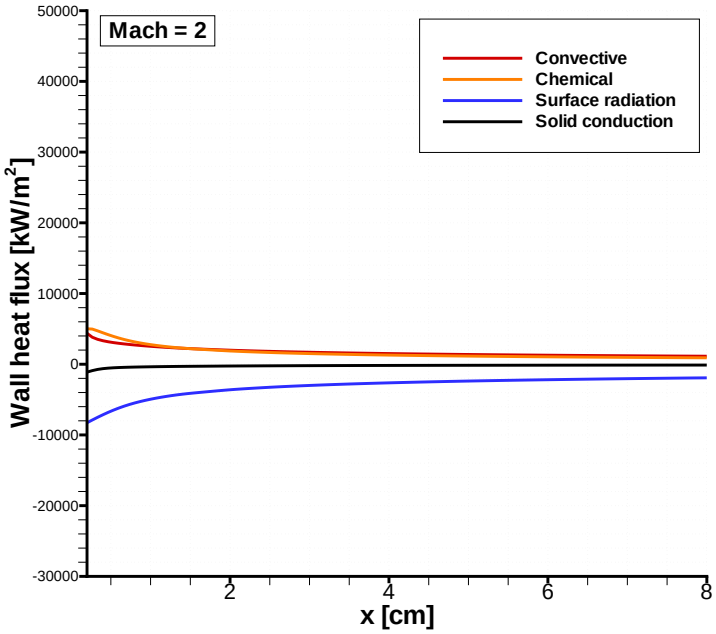

Figure 6.42: Wall heat fluxes at $M = 2$.

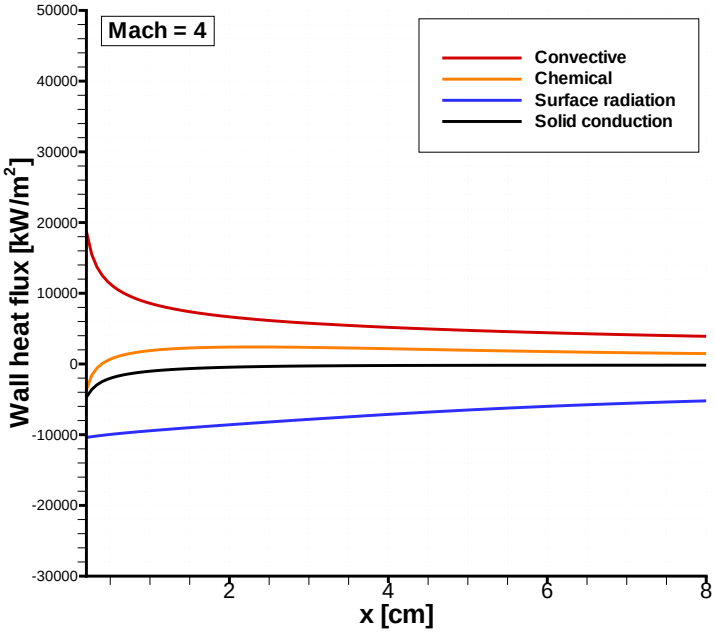

Figure 6.43: Wall heat fluxes at $M = 4$.

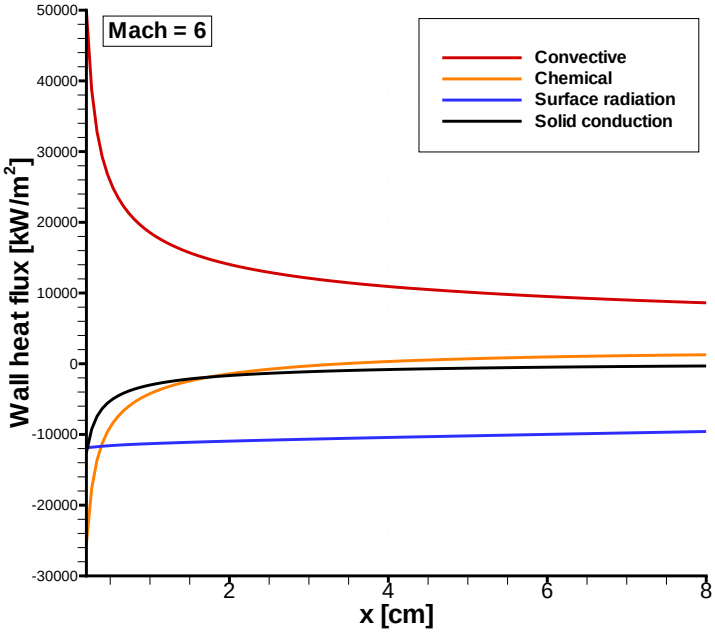

Figure 6.44: Wall heat fluxes at $M = 6$.

6.3.3 Effect of boundary-layer finite-rate chemistry

The temperature rise inside the boundary layer can be considerable, especially for the higher M cases. High temperature inside the boundary-layer can trigger thermal decomposition (endothermic reactions) of ablation species which in turn can alter the mass and energy balances at the surface. In order to study the effect of these chemical reactions, the same finite-rate kinetic model shown in section $6.2.5$ and based on the work of Park [64] has been adopted to model the thermal decomposition of the two ablating species CO and C_3 created at wall.

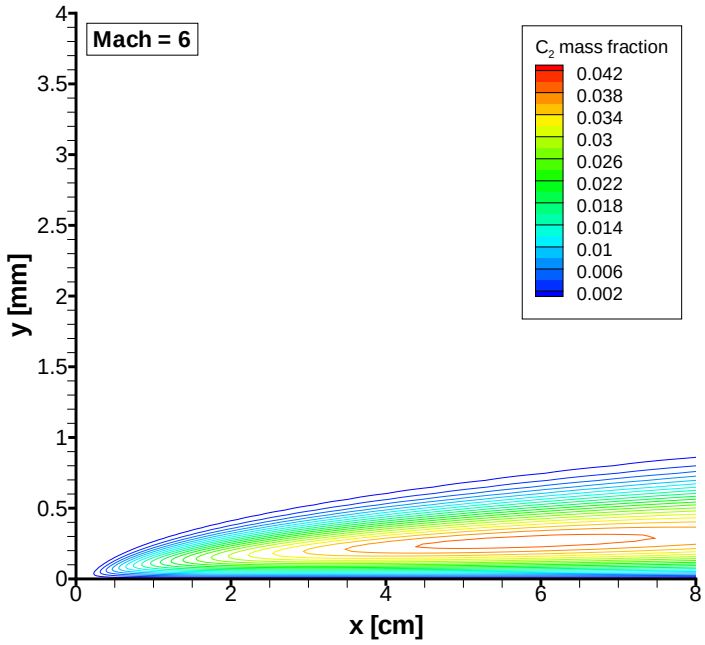

Figure 6.45: C_2 mass fraction spatial distribution (not in scale).

Figure 6.45 shows the C_2 mass fraction spatial distribution for the highest Mach case. A certain amount of C_2 and C are produced from the decomposition reaction of the ablation species C_3 and CO. Figure 6.47 shows the species mass fractions profiles at the end of the flat plate. Comparing Figure 6.47 and 6.46 it is clear that the species produced by the thermal decomposition reach a maximum mass fraction where the temperature reaches the peak value. These decomposition reactions produce a cooling of the boundary layer as Figure 6.46 clearly shows. The peak temperature in the boundary-layer (at the end of the flat plate) is decreased by nearly $1000\ K$. However, the effect of the decomposition reactions

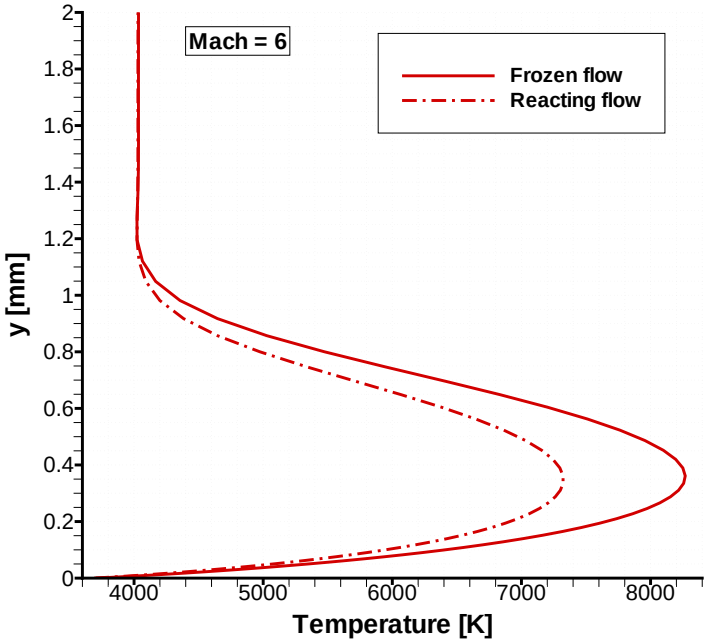

Figure 6.46: Temperature profile.

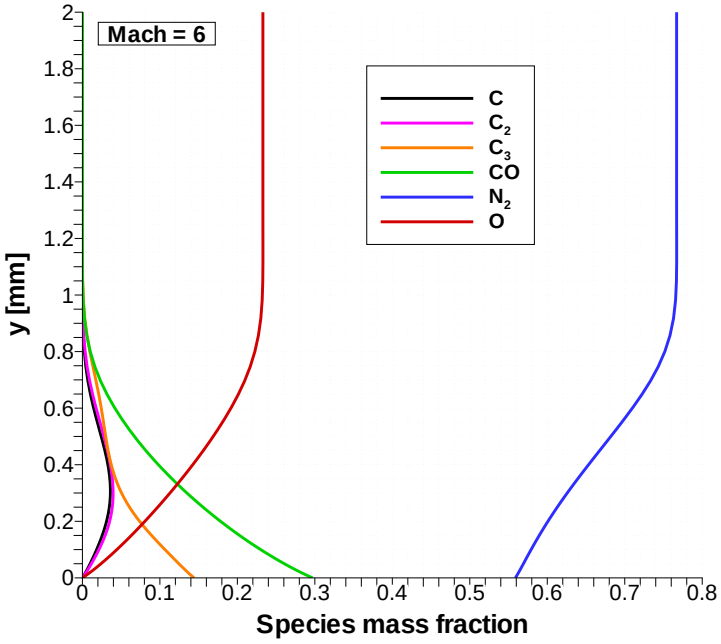

Figure 6.47: Species mass fractions profile.

is barely seen on the surface temperature and mass blowing rate. The effect, even if weak, is a reduction both in surface temperature and mass blowing rate as shown in Figure 6.48.

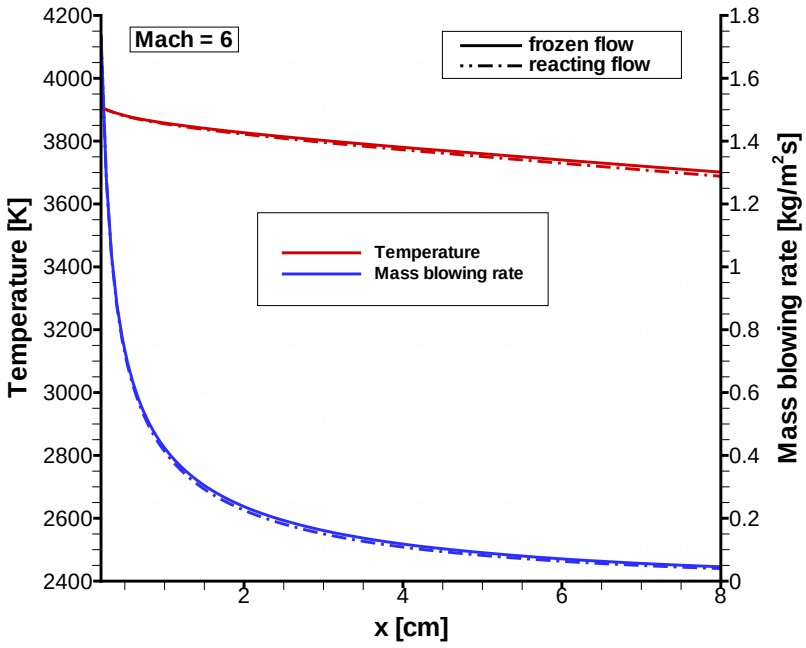

Figure 6.48: Wall temperature and blowing rate.

6.3.4 Comparison with thermochemical table approaches

As discussed in section $6.2.6$, in many cases CFD codes are loosely coupled with the material and often the flowfield solutions are obtained using ablating boundary conditions coupled with $B^{'}$ thermochemical tables and transfer-coefficient energy balance (see Eq. (2.20)) or even non-ablating boundary conditions corrected with blowing reduction equations.

When a *thermochemical table* approach is used, the mass blowing rate is obtained by thermochemical tables and by the heat transfer coefficient C_h evaluated from the ablative CFD computation as described in section $6.2.6$ for the isothermal case. The difference in this case is that, since the surface temperature is not assigned, it must be derived from the surface energy balance. In this simplified model, the surface energy balance is solved outside the CFD code (usually by the thermal response code) using a transfer-coefficient energy balance such as that expressed by Eq. (2.20). The transfer-coefficient SEB (in the steady-state form for the present comparison) is used to compute the surface temperature through coupled iterations with the CFD code: when temperature changes, a new CFD solution is evaluated (with the new temperature and mass blowing rate) to update the heat transfer coefficient C_h until convergence is reached. The use of simplified transfer-coefficient mass balance (which is part of the thermochemical table) and transfer-coefficient energy balance can reduce the accuracy of the material-flow coupled computation.

When *non-ablating* boundary conditions are used the "unblown" CFD solution is computed assuming a radiative-equilibrium wall condition (no mass injection and no gas/solid chemical reactions) [21]; as usual, a blowing correction is then adopted to reduce the wall heat flux. After computing a non-ablating CFD solution, Eq. (6.5) is used to reduce the non-ablative heat transfer coefficient C_{h_0} obtained from the CFD solution. The mass transfer coefficient C_m is evaluated from the corrected heat-transfer coefficient C_h using semi-empirical relations such as (6.3). The transfer-coefficient surface energy balance Eq. (2.20) in the steady-state form is then used to compute the surface temperature with a simple iterative technique (usually the Newton's method) without performing new CFD computations. In this simpler case there is no iterative coupling between material and CFD solution, since transfer-coefficient balances and blowing correction equations are used to obtain TPS properties (mass blowing rate $\dot{m}$ and surface temperature T_w) without updating the CFD solution (which is non-ablating). The computational cost is reduced in this simpler case because a single CFD computation is performed without chemical interaction with the TPS material. The accuracy of this method is obviously reduced.

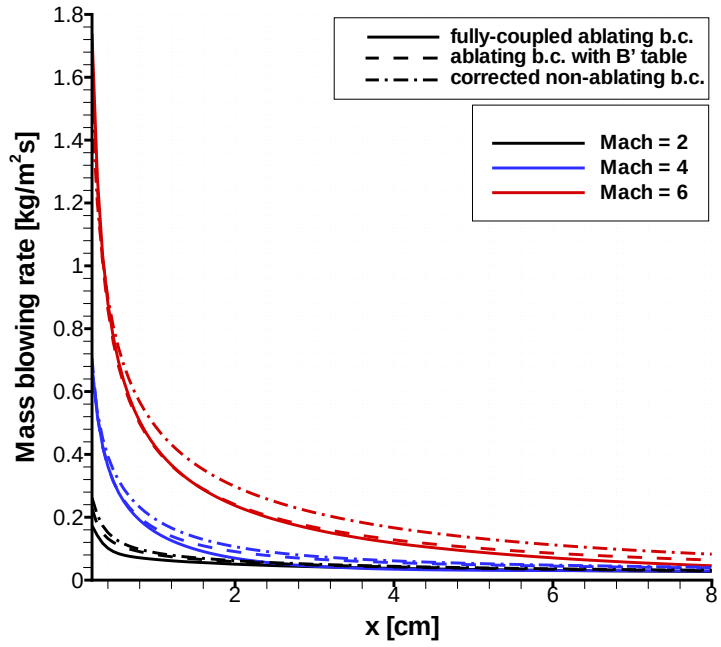

Figure 6.49: Mass blowing rate.

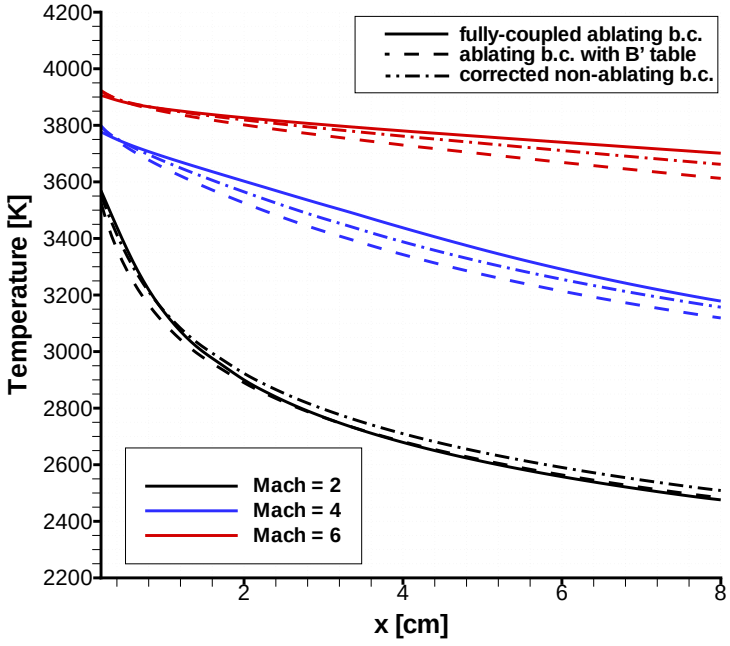

Figure 6.50: Surface temperature.

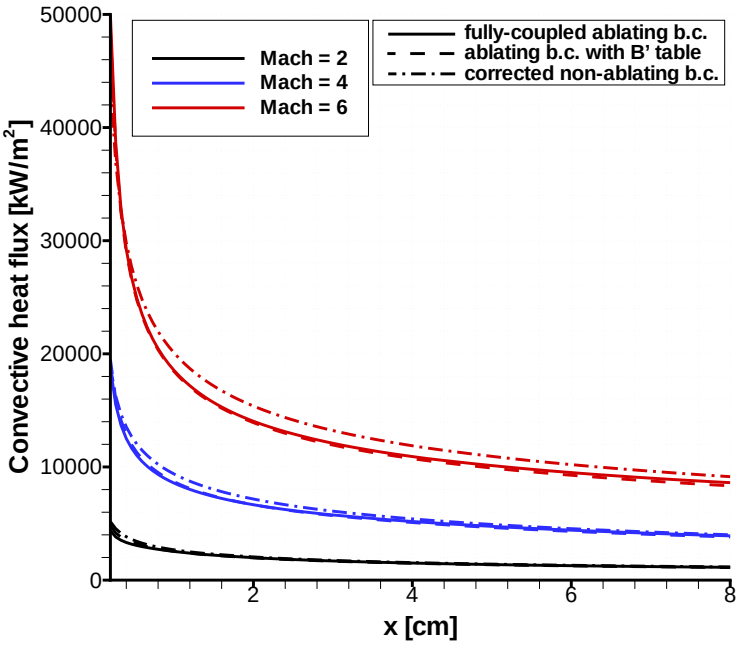

Figure 6.51: Convective heat flux.

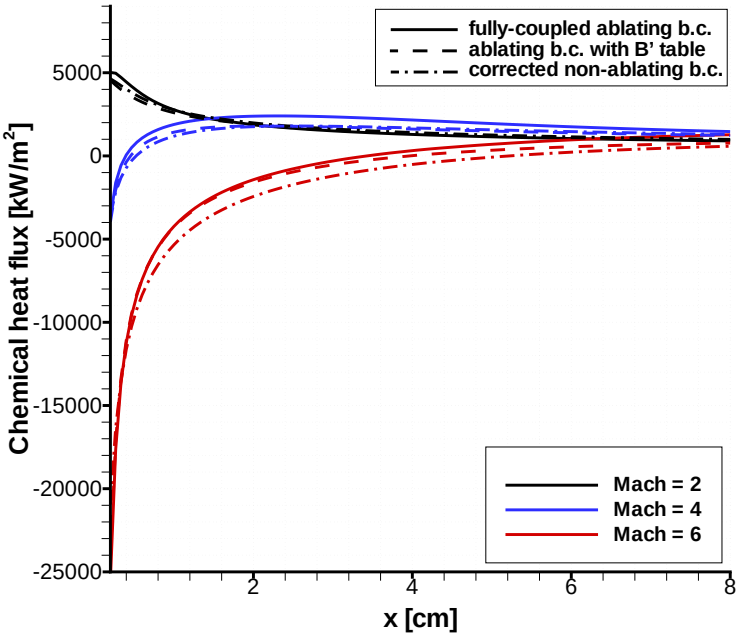

Figure 6.52: Chemical heat flux.

Figures 6.49-6.52 shows the comparison of the steady-state ablation solutions (mass blowing rate, surface temperature, wall convective and chemical heat fluxes) for different Mach numbers computed with three different boundary conditions: i) fully-coupled ablating boundary conditions with SMB and SSEB computed and solved as boundary conditions in the CFD code, ii) ablating boundary conditions coupled with thermochemical tables and transfer-coefficient SEB (in the steady-state form), Eq. (2.20), and iii) non-ablating boundary conditions coupled with thermochemical tables, transfer-coefficient SEB, and blowing correction equation (6.5).

As was noted for the isothermal case, the non-ablating approach is the one leading to major differences and the agreement between the fully-coupled and the simplified approaches gets worse as the blowing rate is increased (increasing the Mach number). However, in the present case (non-isothermal) the differences are definitely larger. Figures 6.53, 6.54, and 6.55 show the percentage error between the fully coupled approach and the two simplified approaches for the mass blowing rate, surface temperature, and convective heat flux, respectively. Figure 6.53 shows that even for the lowest Mach case the percentage error is not negligible and at the higher Mach number the error becomes very large. A similar behaviour, but with smaller percentage differences, is observed in Figure 6.54 for the convective heat flux. The comparison shows that at the highest Mach number the table-predicted mass blowing rates and heat fluxes are affected by a high degree of inaccuracy due to the increasing effect of mass blowing on boundary layer properties. In the isothermal case the differences were smaller because surface temperature was fixed and the surface energy balance was not solved. In the more realistic non-isothermal case a strong non-linear coupling exists between the surface mass and energy balances which causes the approximate solutions to produce less accurate solutions. The present comparisons have shown that this inaccuracy can be high in case of intense blowing. Looking at Figure 6.55, it is interesting to note that at the highest Mach numbers the surface temperature computed with the non-ablating boundary conditions shows the best agreement with the fully-coupled solution, while for the other parameters (mass blowing rate and heat fluxes) this happens with the ablating solution. This is due to the complex interaction between the mass and energy balances which can cause a simpler model to give better results for a specific parameter.

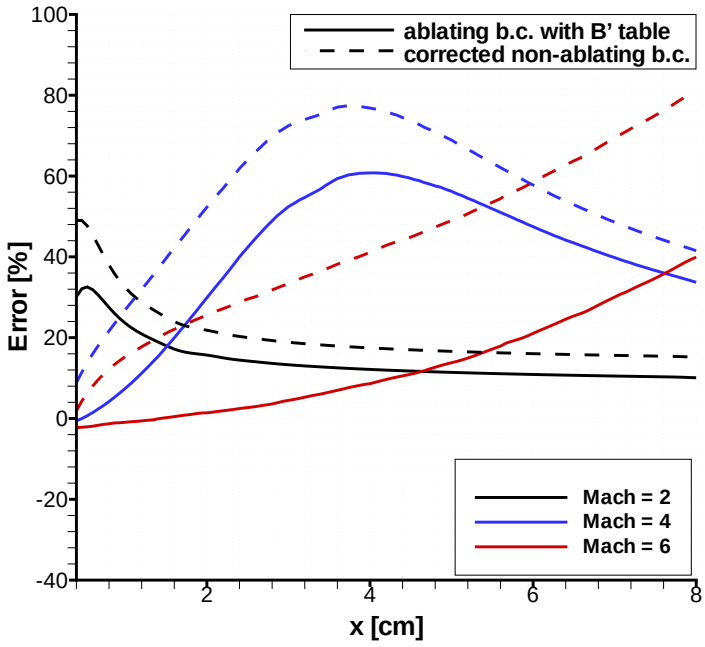

Figure 6.53: Differences on the mass blowing rate between the present method and the simplified approaches.

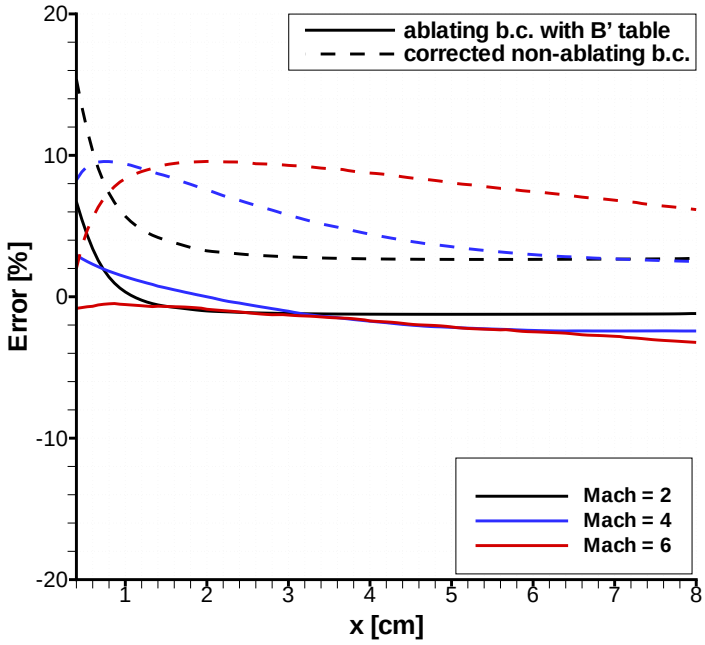

Figure 6.54: Differences on the convective heat flux between the present method and the simplified approaches.

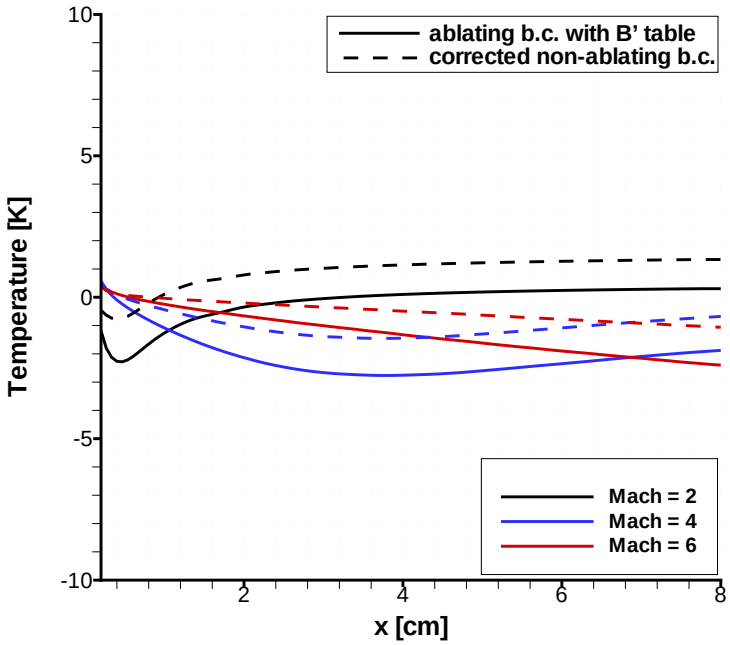

Figure 6.55: Differences on the surface temperature between the present method and the simplified approaches.

Chapter 7

Rocket nozzle applications

With the development and use of high-energy solid-propellant and harder firing conditions in large advanced solid rocket motors, graphites have found increasing application as nozzle materials because of their high-temperature thermal and physical properties, and low densities. But in spite of the advantages of these composites materials, because of the attack of carbon-carbon nozzle surface by the products of the propellant combustion during motor operation, the nozzle surface regresses by loss of material, and the nozzle throat area increases. Hence the nominal performance of the rocket motors decrease, and the resulting performance reduction must be evaluated and taken into account by the designer of motors.

The classic way to measure performance reduction is to test full-scale motors, but this takes a long time and is very expensive because tests must be repeated for every new motor. A complementary method is to establish regression models that can accurately predict the regression rates of nozzle throats, but these models require a fundamental knowledge of the major mechanisms that drive the regression rate. This chapter describes the results obtained from applying the thermochemical ablation model developed herein to describe carbon-carbon regression of large advanced solid-rocket nozzles.

7.1 Introduction

Graphite and carbon-carbon composites, which have excellent thermal and physical properties as well as low densities, are widely used as materials for rocket nozzles. However, the hostile thermochemical environment resulting from the high-performance solid propellants creates many problems to such materials. One of the serious problems is the erosion/recession of the rocket nozzle material. As the propellant of the rocket motor burns, the nozzle is exposed to the hot propel-

lant combustion products which form a turbulent boundary-layer over the nozzle surface. The hot products transfer energy to the nozzle wall, causing the surface temperature to rise and thereby increase the reactivity of the nozzle material. At high surface temperatures, heterogeneous chemical reactions occur between the nozzle material and oxidizing species such as H_2O, CO_2, and OH, present in the combustion stream. The heterogeneous reactions produce carbon monoxide CO, resulting in the thermochemical erosion of the nozzle. Such erosion is most severe at the throat due to the maximum heat-transfer rate in that region. The resulting increase in the nozzle throat area decreases the thrust and reduces the motor performance significantly in long-duration firings.

The overall rate of these reactions depends on their kinetics as well as on the rate at which the oxidizing species can diffuse across the boundary-layer to the nozzle surface. If the kinetic rates are much higher than the diffusion rates, the recession rate is determined primarily by the diffusion mechanism of oxidizing species (diffusion-controlled). The other extreme situation is that of high diffusion rates and low kinetic rates, in which case the recession is predominantly determined by the chemical kinetics (rate-controlled). The diffusional recession rate depends on such parameters as flow properties in the nozzle, chamber pressure, and concentrations of reactants. The chemical kinetics rate depends on the kinetics of the heterogeneous reactions, the concentrations of the various reactants, and especially the surface temperature of the nozzle. The surface temperature is determined by the surface energy balance which involves the heat conduction response of the C/C nozzle, the heat transfer from the hot gases to the nozzle, and the heat flux absorbed by the ablation mechanism.

The overall nozzle erosion process is extremely complex with the interplay of numerous factors including the solid-propellant composition, motor operating conditions, duration of firing, nozzle geometry and material properties, rates of diffusion of the species toward the surface through the boundary-layer, and chemical reactions at the surface and in the gas phase. In addition to the aerothermochemical processes, the erosion may have contributions from the mechanical processes caused by impact of condensed metal-oxide particles (e.g. Al_2O_3) on the nozzle surface or by the structural failure because of high thermal stresses. However, most researchers [37, 24, 50, 49] have concluded that the chemical erosion is the primary reason for the nozzle recession. Experimental studies [37, 70] on the graphite nozzle erosion using aluminized composite solid-propellant formulation indicated that the graphite removal depended primarily on the chamber pressure and the chemical attack by the combustion species H_2O and CO_2, present in the hot exhaust. A strong correlation between the surface recession rate and the mass fraction of H_2O and CO_2 was noted. The recession rate decreased with increasing aluminium content present in the composite propellants [37]. If mechanical processes (impingement of solid alumina on the nozzle surface) were significant

then the erosion should have increased with the increase in Al_2O_3 particles in the combustion stream, but on the contrary the erosion decreases. The phenomenon was attributed to the decrease in the concentrations of H_2O and CO_2 in the combustion stream for aluminized propellants.

7.2 Background

The identification and description of the major significant mechanisms happening in the nozzle regression constitute a relatively recent field of study in solid rocket technology. It has been the subject of many investigations [70, 24, 49, 50, 44, 74, 37, 40, 36], first, because of the numerous parameters to take into account: chemical propellant composition, chamber pressure, duration of firing, type, geometric form and properties (density, specific heat, thermal conductivity) of the nozzle material, among others; and, second, because of the complexity of the description of the driving phenomena, such as geometric and temperature history of the nozzle, rates of diffusion of the species through the boundary-layer, and the heterogeneous chemical reactions with the surface material. In $1960s$ and $1970s$, with limited computational resources, many investigators developed simplistic models to predict the nozzle recession rate.

Swope and Berard [70] found a direct correlation between the total concentration of the oxidizers capable of forming a CO with the material and the rate of graphite erosion. H_2O appeared to be the major contributor to graphite erosion.

Delaney et al. [24] developed a simple model for the erosion of graphite throat nozzles. The results showed that graphite nozzle erosion was limited by both process of diffusion and chemical surface reactions and that pressure was an important parameter involved in erosion.

McDonald and Hedman [50], on the basis of the results of an analytical study and analysis of short-duration test data with graphite nozzles, found that the erosion of graphite is primarily the result of a chemical surface reaction that is rate-controlled during the transiently heated period, and diffusion-controlled when surface temperature exceeds about $2000\ K$. They also found that the erosion decreased with an increase in the aluminium content in the propellants and that the hydrogen-carbon reaction was not significant with the studied propellants.

Klager [37] found, on the basis of data obtained by experimental firings on small aluminized solid rocket with graphite nozzles and of thermodynamic analysis, that graphite removal in solid rocket nozzles depended principally on pressure and on chemical attack by H_2O and CO_2, which react with the surface to give CO. The chamber flame temperature was found not to affect the graphite removal directly, and the recession rates were found, as in McDonald and Hedman, to decrease when the aluminium content in the propellant increased. A good correlation was

observed between the recession rates and the mole fraction of H_2O.
Keswani [36] conducted theoretical studies to predict recession of graphitic nozzles in different rocket motors, with different nozzle geometries and materials, at different operating pressures and temperatures, and in a wide range of propellant formulations. Recession was found to be strongly influenced by propellant composition, chamber pressure, and motor geometry, and the analysis showed that recession is due primarily to the oxidation of carbon to carbon monoxide by H_2O and CO_2. The analysis also showed that the influence of chemical kinetics is predominant only when the surface temperature is low and that the recession rate is largely determined by the diffusion rate of oxidizing species when the nozzle surface temperature has reached about $2500\ K$. The papers of Keswani and coworkers [40, 36] have completed the thesis of Keswani. Another conclusion of these works was that the total recession increases as material density decreases. It was also shown that the graphite recession process is relatively independent of gas phase reactions. The same conclusions were recently obtained by Thakre and Yang [72].
One of the most recent and more detailed model for nozzle surface recession was developed by Kuo and Keswani [40, 36]. Although their model was a significant improvement over the earlier models, it still involves several assumptions which may be removed. One of the major assumptions is that the gas-phase is modeled as being composed of a quasi-steady, compressible, isentropic, one-dimensional core-flow region and a two-dimensional, axisymmetric, quasi-steady, turbulent boundary-layer flow region. Considering the computational speed and resources available today, many of the approximations employed in previous studies can be removed. This work takes into account propellant chemistry, detailed thermodynamic and fluid-dynamic analyses, chemical kinetics in the gas phase, heterogeneous chemical reactions at the nozzle surface, rate of diffusion of the species through the boundary-layer and accurate multi-species thermophysical properties using a full Navier-Stokes approach.

7.3 Chamber equilibrium calculations

Because all previous studies have confirmed that propellant composition greatly influences nozzle regression, it is vital to identify the major products that constitute the propellant exhaust gases. Hence, the first calculations of the analysis have been made to provide the characteristics of typical propellant exhaust-gases in the combustion chamber. The hot exhaust flow stream in the nozzle consists of the combustion products of metallized AP/HTPB composite propellants. The mass fractions of the combustion species at the nozzle inlet, shown in Table 7.1, were based on chemical equilibrium calculations at a chamber pressure

Table 7.1: Nozzle inlet flow conditions: $p_0 = 70\ bar$, $T_0 = 3500\ K$

Species	Mass fractions	Gas-phase mass fractions
CO:	0.23	0.3485
CO_2:	0.02	0.0303
HCl:	0.20	0.3030
H_2:	0.01	0.0152
H_2O:	0.09	0.1364
N_2:	0.10	0.1514
OH:	0.01	0.0152
Al_2O_3:	0.34	-

of $70\ bar$. The mass fractions of all the species remain almost constant with increasing/decreasing chamber pressures with the exception of OH mass fraction which shows some variation. The stagnation temperature, T_0, and the stagnation pressure, p_0, are specified at the nozzle inlet. Five sets of chamber pressures ($50, 60, 70, 80, 90\ bar$) and the corresponding chamber temperatures were used to study the effect of motor operating parameters. However, since the chamber temperature shows only slight variation with chamber pressure it has been assumed constant. As can be seen, a certain amount of liquid alumina is formed in the combustion chamber. A single phase treatment is used in the model so that only the gaseous composition is taken into account.

7.4 Results and discussion

The governing equations with the SMB and SSEB boundary conditions have been solved numerically to predict the recession rates of C/C nozzles for various operating conditions and propellant formulations. The chemical composition used as input in the computations is listed in Table 7.1. The thermochemical properties (specific heat and enthalpy of formation) of the carbon/carbon material as a function of temperature used in the steady-state heat conduction term were obtained from Gordon and McBride database [28]. In the adopted numerical scheme the one-equation Spalart-Allmaras [68] turbulence model has been used [47].

For studying the effect of parametric variations of motor operating conditions on the nozzle erosion, the configuration used is the nozzle shown in Figure 7.1.

Since the main objective is to predict the material erosion at the nozzle throat and its vicinity, it was deemed unnecessary to simulate the entire flowfield in the rocket motor. Moreover, it is common practice to use carbon-carbon material only in the throat region where the heat flux are maximum and consequently the erosion rate reaches its peak. Five sets of chamber pressures were used and the outside nozzle wall temperature was taken at $300\ K$ in all cases. The computational domain is

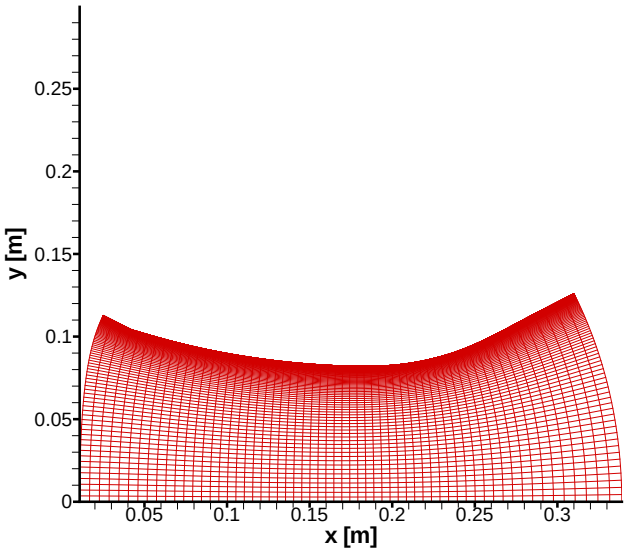

Figure 7.1: Rocket nozzle configuration under study.

subdivided into 60×150 grid points in the x and r directions, respectively. In the r direction, the grid was stretched and clustered near the nozzle surface so that the first grid point was located at y^+ less than 1 all along the nozzle length. All the results presented are in the steady-state condition.

Figures 7.2, 7.3, 7.4, and 7.5 show the entire flowfield distribution in the nozzle interior in terms of temperature, pressure, Mach number, and axial velocity using adiabatic wall boundary conditions and no surface reactions.

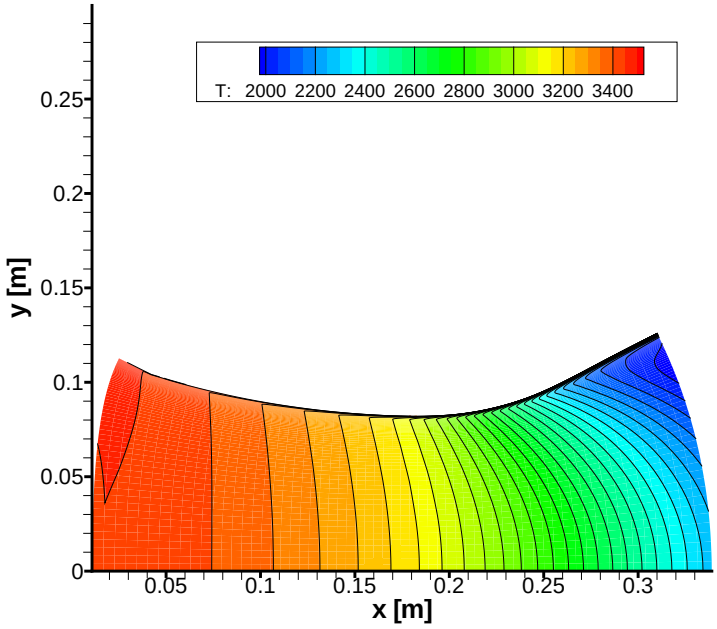

Figure 7.2: Temperature distribution in the nozzle interior ($T_0 = 3500\ K$, $p_0 = 70\ bar$, no surface reactions, adiabatic wall).

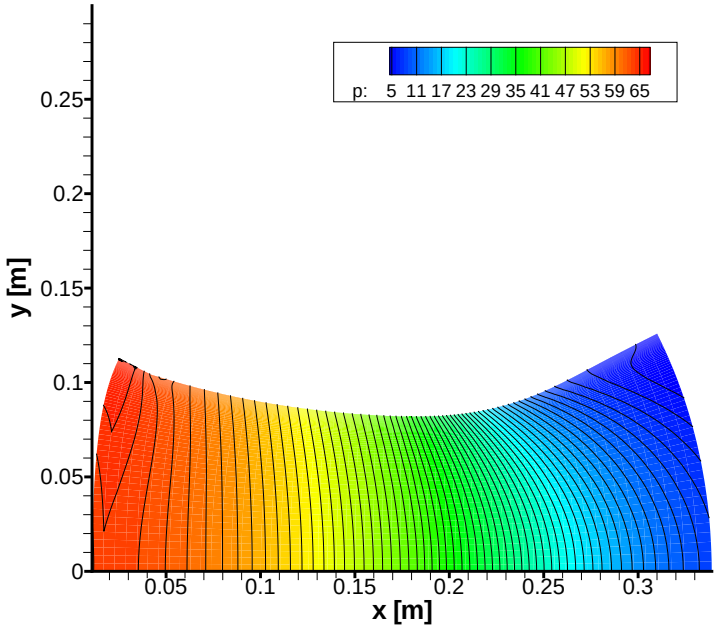

Figure 7.3: Pressure distribution in the nozzle interior ($T_0 = 3500\ K$, $p_0 = 70\ bar$, no surface reactions, adiabatic wall).

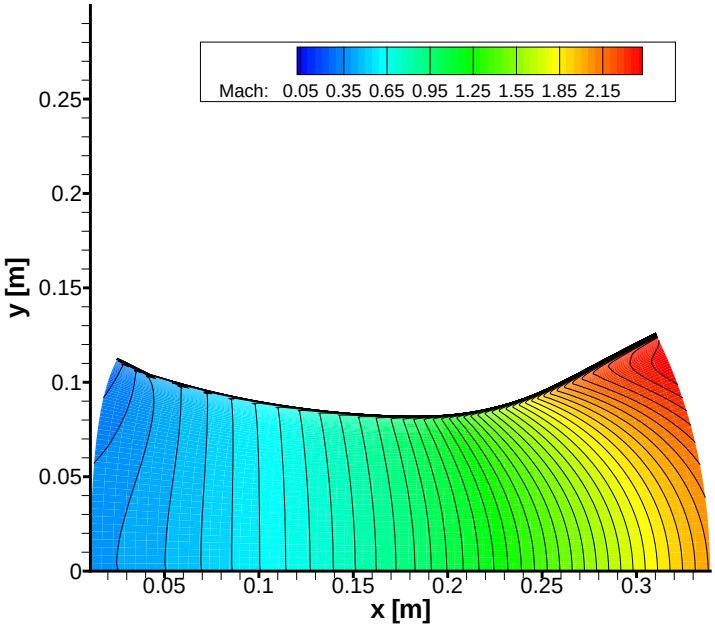

Figure 7.4: Mach distribution in the nozzle interior ($T_0 = 3500\ K$, $p_0 = 70\ bar$, no surface reactions, adiabatic wall).

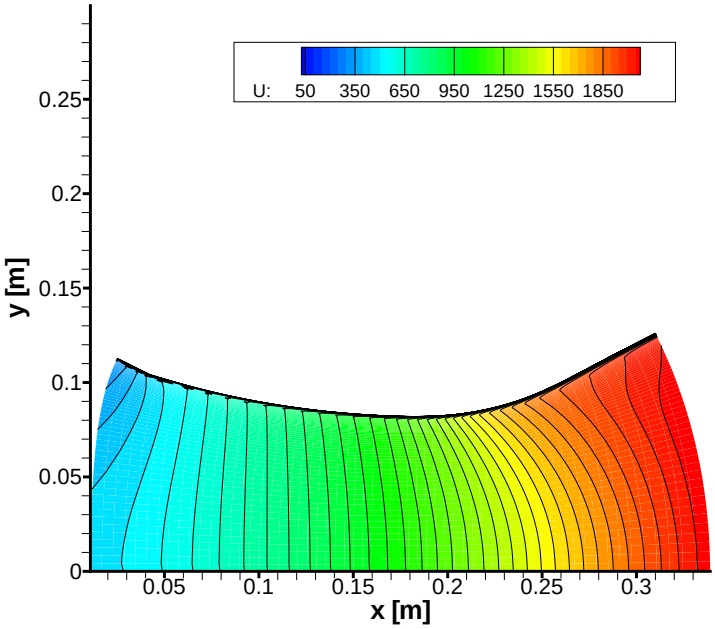

Figure 7.5: Axial velocity distribution in the nozzle interior ($T_0 = 3500\ K$, $p_0 = 70\ bar$, no surface reactions, adiabatic wall).

To simulate material erosion, the SMB and SSEB are employed with equilibrium wall condition. Researchers [50, 40, 36, 72] have found that the erosion is rate-controlled when surface temperature is below $2000 - 2500\ K$. Calculations presented in Chapter 2 have shown that, in SRM nozzle environments, the surface temperature in the throat region exceeds $2000 - 2500\ K$ after a second or less from ignition so that the nozzle erosion is essentially diffusion-controlled during the operational duration. For this reason, a surface equilibrium assumption is appropriate. As a result of heterogeneous reactions between the solid wall and the exhaust gases, CO_2, OH, and H_2O are consumed at the nozzle surface to form CO and H_2. Consequently, a concentration gradient is formed in the vicinity of the nozzle wall, wherein CO_2, OH, and H_2O diffuse towards the nozzle surface and CO and H_2 diffuse away from the surface. These surface reactions are endothermic in nature and they help reduce the nozzle surface temperature. Results obtained with the ablative boundary conditions show almost no differences in the core-flow region with the adiabatic non-ablating computations previously presented. The main differences are experienced in the boundary-layer and at the nozzle surface. Therefore our attention will be directed toward the boundary-layer structure with ablation.

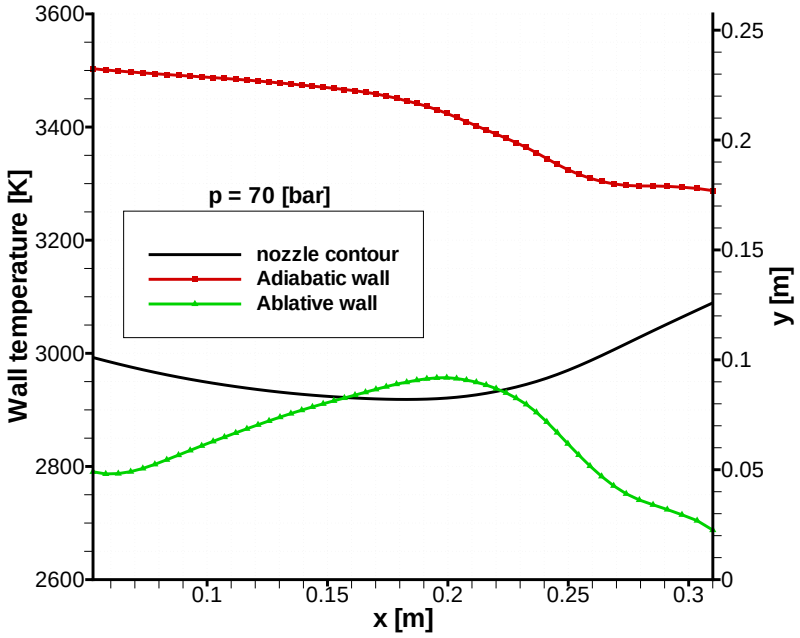

Figure 7.6: Wall temperature distribution.

Figure 7.6 shows the surface temperature distribution for the adiabatic and ablative wall condition. In the case of ablation, the surface temperature is noticeably reduced by the ablation process. Moreover, the ablative surface temperature distribution is rather different than the adiabatic profile showing a clear peak in the throat vicinity.

Figure 7.7 and 7.8 show the species mass fraction profiles in the boundary-layer at the throat section: the oxidizing species (H_2O, OH, and CO) profiles are reported in Figure 7.7 while the non-oxidizing species (CO, H_2, HCl, and N_2) profiles are reported in Figure 7.8. The mass fractions of the oxidizing

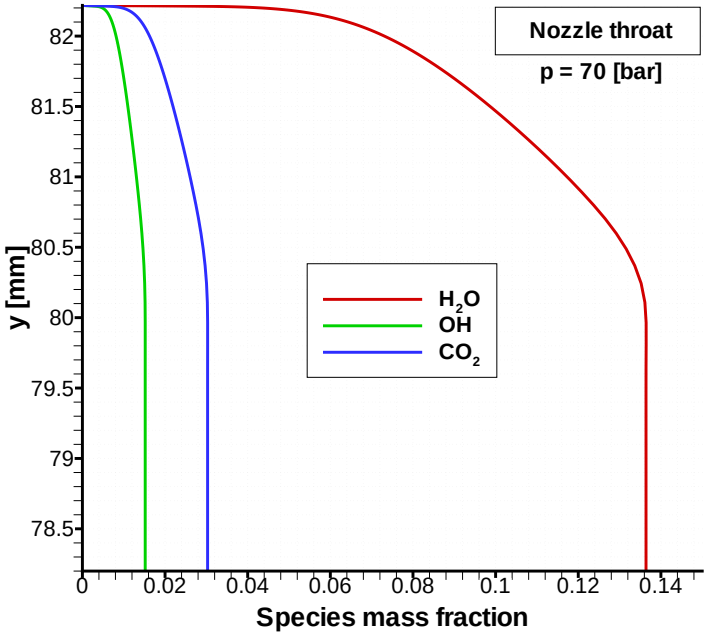

Figure 7.7: Oxidizing species profiles at throat.

species decrease from the edge of the boundary layer to nozzle surface due to their consumption in the heterogeneous reactions at the carbon-carbon surface. The gradients of the concentrations are largest near the wall since the turbulent mass diffusivity drops to zero as the viscous sublayer is approached near the wall. Since the nozzle erosion is diffusion-controlled, the concentration of these oxidizing species is vanishingly small at the nozzle surface. The species created at the surface are CO and H_2 and they are diffused away from the surface. Since these species are produced in the heterogeneous reactions at the surface, their

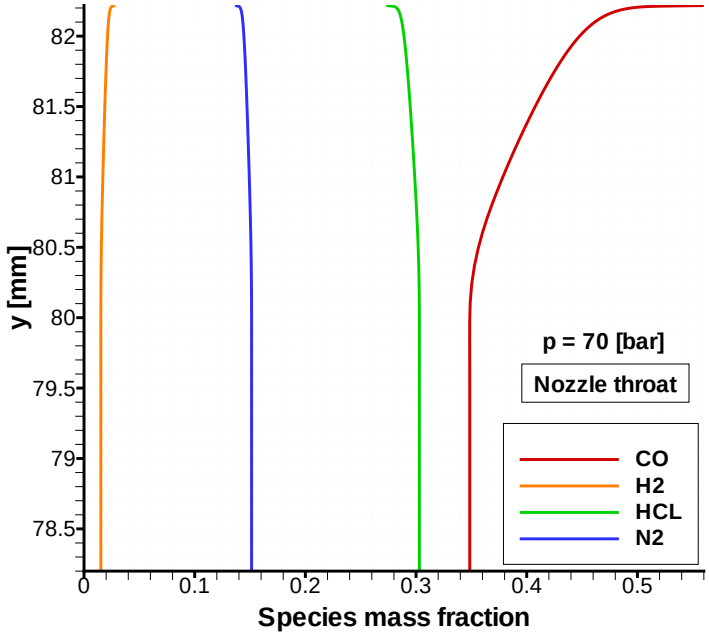

Figure 7.8: Non-oxidizing species profiles at throat.

mass fractions are maximum there. The equilibrium wall calculations show no production at all of C_3 at the surface due to the relatively high pressure and too low surface temperature. The only ablation product is therefore CO. Keswani and Kuo [36] and Thakre and Yang [72] concluded that the oxidation of carbon to CO is the principal cause of nozzle recession for nozzle surface temperatures below $3000\ K$, which are hardly exceeded in SRM nozzle. Looking at Figure 7.8, it is clear that N_2 and HCl do not participate in heterogeneous reactions, and hence their mass fractions are relatively constant across the boundary-layer. These mass fractions decrease slightly near the surface because of mass blowing at the nozzle wall. Gas-phase reactions have not been taken into account in these computations. Keswani and Kuo [36] showed that the equilibrium and frozen boundary layer profiles for the most important oxidizing species are very close one another with just slight differences. Therefore they concluded that, in general, the gas-phase reactions do not significantly influence the profiles of the major oxidizing species and hence do not affect the erosion rate. Thus, the assumption of a frozen boundary-layer is acceptable for computation of heat-transfer and recession processes in SRM nozzle applications. More recently Thakre and Yang [72] came to

the same conclusions, showing that finite-rate gas-phase reactions do not perturb the chemical composition or the temperature distribution considerably and have a very negligible effect on the erosion rate. This also justifies the use of a frozen boundary-layer assumption for nozzle recession predictions.

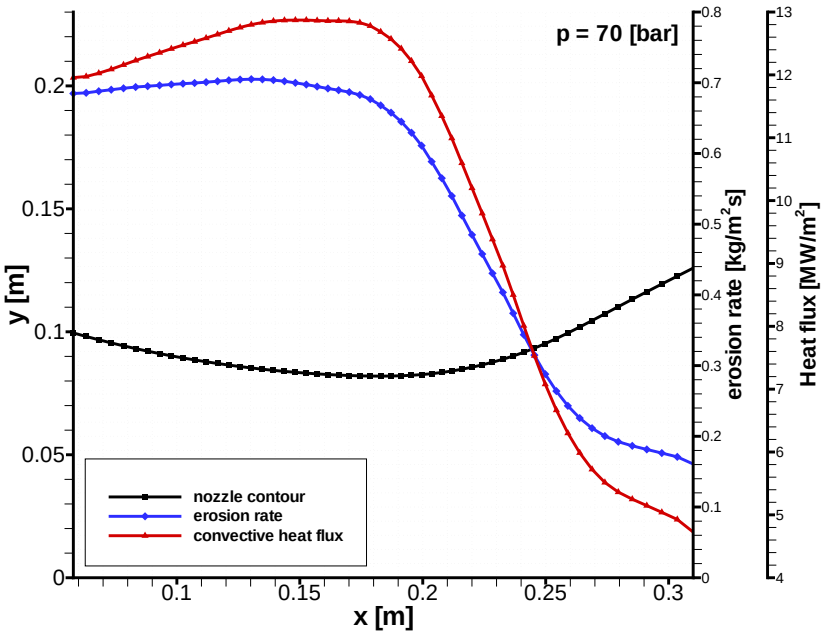

Figure 7.9: Nozzle erosion rate and wall heat flux.

For the same input conditions, Figure 7.9 shows the distribution of the thermochemical erosion rate $[kg/m^2s]$ and the surface convective heat flux $[MW/m^2]$ along the length of the nozzle. It can be noted that the erosion rate is highest a bit ahead of the throat due to maximum heat-transfer rate at that location. Researchers [40, 11] have attributed the maximum erosion at the throat to the maximum heat-transfer rate at the throat. Figure 7.9 clearly shows that the variation of erosion rate mimics the variation of heat-transfer rate all along the nozzle wall indicating a direct correlation between the two: recession and heat flux increase in the converging section of the nozzle, reach a maximum close to the throat, and decrease in the supersonic diverging section. This variation is governed by the mass flux of the flow of propellant products in the nozzle and consequently recession decreases significantly with increasing Mach number beyond unity as the mass flux decreases. Comparing Figure 7.9 with Figure 7.6 it can be seen that the peak

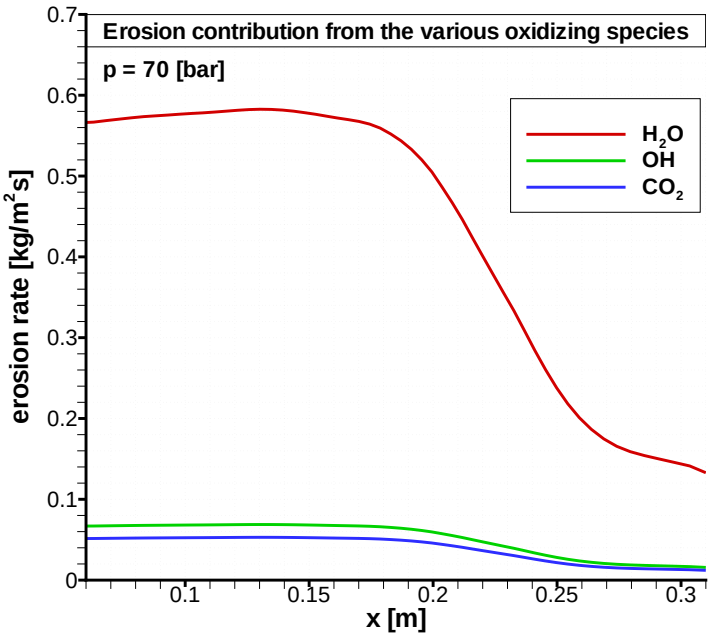

Figure 7.10: Erosion contribution from the various graphite-oxidizing species.

wall temperature is a bit after the throat section while the peak erosion rate is a bit ahead of the throat section.

Figure 7.10 shows the contributions towards the net erosion rate by the three oxidizing species which can be obtained simply by mass conservation equations:

$$\begin{aligned} C_{(s)} + H_2O &\rightleftharpoons CO + H_2 \\ C_{(s)} + OH &\rightleftharpoons CO + H \\ C_{(s)} + CO_2 &\rightleftharpoons 2CO \end{aligned} \tag{7.1}$$

From Eq. (7.1) it can be seen that a single mole of solid carbon $C_{(s)}$ can be consumed either with a mole of CO_2 or H_2O or OH. Moreover, since the mass fraction of the oxidizing species is zero at wall, the mass flux of these species diffusing to the nozzle wall reacts completely with the surface to form CO. Thus, multiplying the diffusional mass flux of the generic oxidizing species by the molecular weight of carbon and dividing by the molecular weight of the species, one obtains

the erosion mass flux contribution of that species. Figure 7.10 shows that H_2O is by far the most devastating oxidizing species followed by OH and CO_2 in that order. This results is confirmed by both theoretical [40, 36, 11, 72] and experimental studies [37, 27, 26].

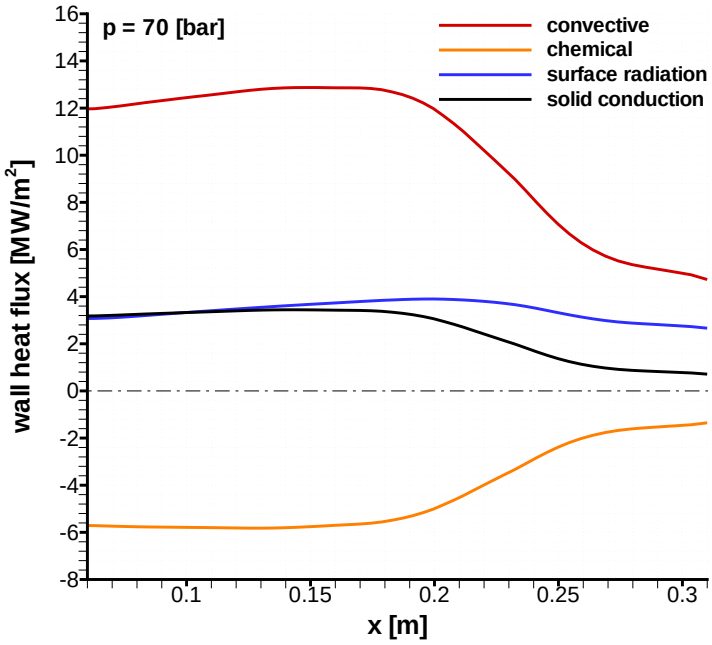

Figure 7.11: Various heat fluxes at the nozzle wall.

Figure 7.11 shows the various wall heat fluxes along the nozzle length. Since the oxidation of carbon in SRM environment is endothermic, the chemical heat flux is negative all along the nozzle length. Figure 7.11 shows that roughly 50% of the incoming convective heat flux is absorbed by the endothermic ablation process and the other 50% is partly conducted into the material and partly re-radiated from the hot surface. The energy radiated away from the surface is thus of the same order of magnitude of the energy conducted inside the material. The energy conducted into the solid shows a sharp decrease after the nozzle throat due to the sudden decrease of the convective heat flux and consequently of the erosion mass rate.

Figure 7.12 shows the influence of chamber pressure on the recession rate along the nozzle wall. The plotted results show that chamber pressure has a very strong influence on the recession rate. A change in the chamber pressure from

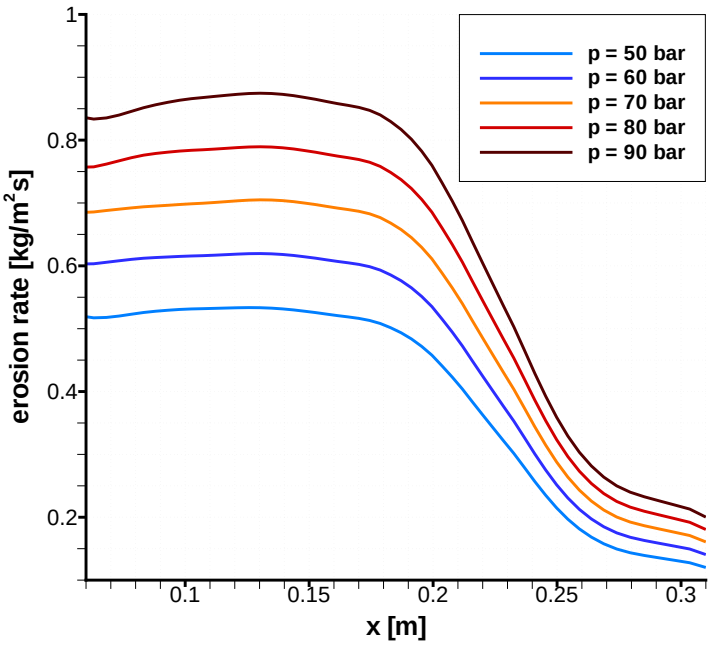

Figure 7.12: Effect of chamber pressure on erosion rate along the nozzle length.

$50\ bar$ to $90\ bar$ causes an increase in the recession rate of about 60%. An increase in pressure causes an increase in the density of the gas phase. Since the convective heat-transfer rate, and hence the mass-transfer rate, is directly proportional to density, there should be a corresponding increase in the erosion rate. Figure 7.12 substantiates this behaviour. Increase in pressure results in higher density leading to higher Reynolds, which in turn enhances the mass transport of oxidizing species across the turbulent boundary-layer. With other parameters remaining nearly constant, the linearity in the erosion rate and the motor operating pressure is clearly seen in Figure 7.13. Klager [37] conducted experimental firings on graphite SRM nozzles. He reported that the combustion product gas temperature showed no correlation with the recession rate while the chamber pressure strongly influenced the recession rate. This behaviour is confirmed by the presented numerical results.

Figure 7.14 shows the influence of chamber pressure on the surface temperature along the nozzle wall. Chamber pressure has a slight effect on surface temperature. There is, however, the tendency to shift the temperature profile downstream with increasing chamber pressure: higher pressures tend to decrease the surface temperature upstream of the throat and to increase it downstream of the throat.

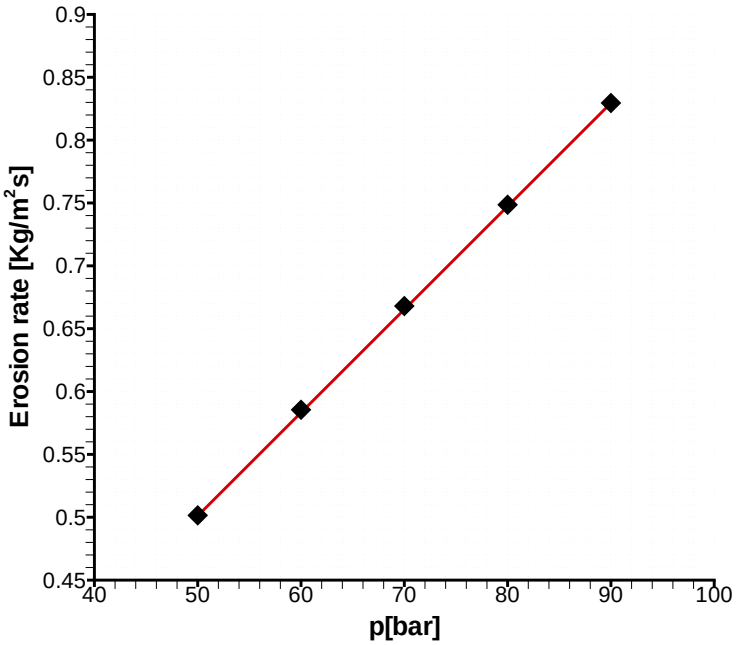

Figure 7.13: Effect of chamber pressure on erosion rate at the nozzle throat.

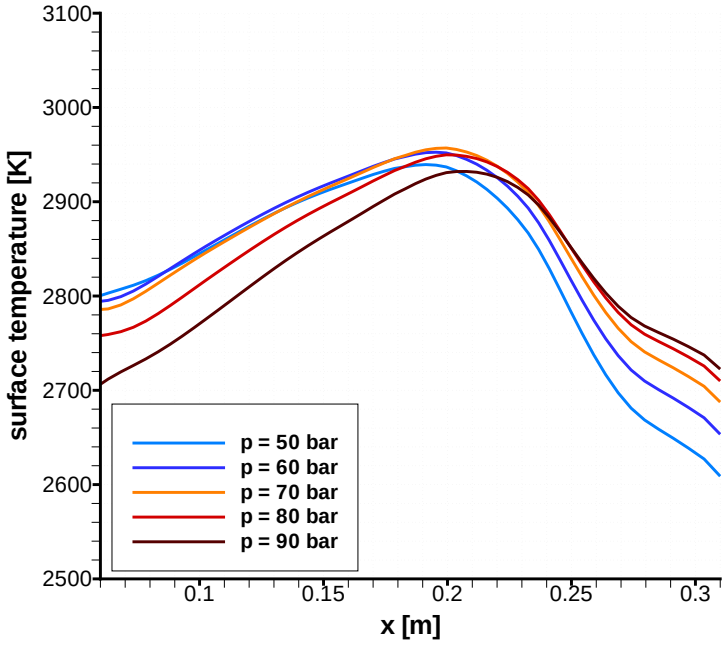

Figure 7.14: Effect of chamber pressure on surface temperature along the nozzle length.

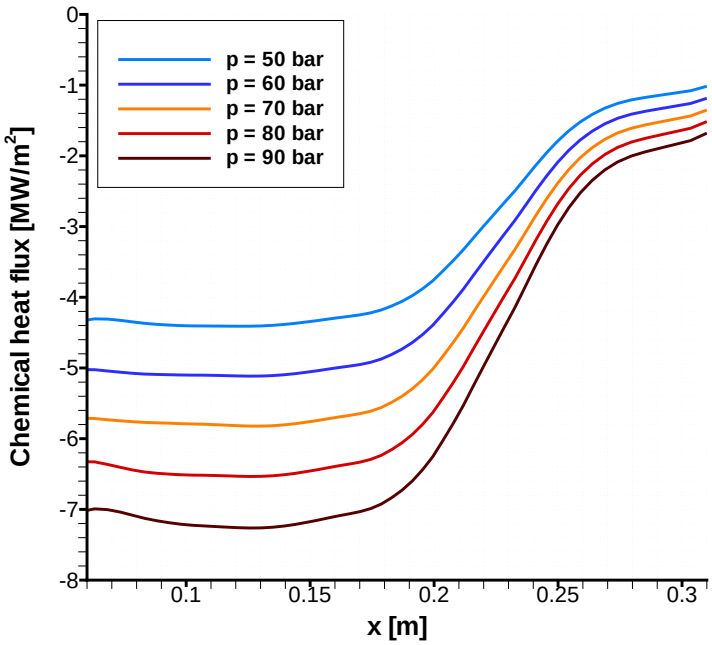

Figure 7.15: Effect of chamber pressure on surface chemical heat flux along the nozzle length.

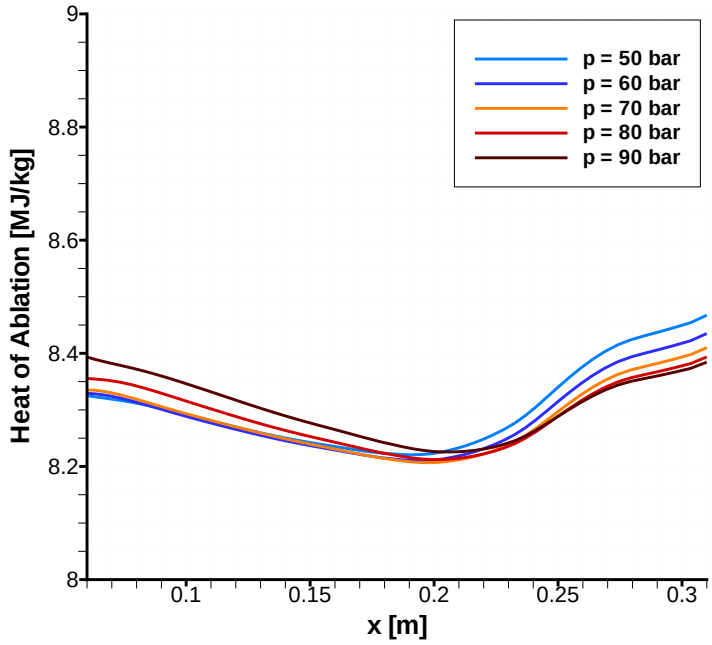

Figure 7.16: Effect of chamber pressure on heat-of-ablation along the nozzle length.

Figure 7.15 shows the influence of chamber pressure on the surface chemical heat flux along the nozzle wall. A comparison with Figure 7.12 shows that the variation of chemical heat flux mimics the variation of erosion rate all along the nozzle wall indicating a direct correlation between the two. As shown in section 5.1 the chemical heat flux represents the heat absorbed (if negative) or released (if positive) due to the surface heterogeneous reactions. It can be also expressed (see Eq. (5.9)) as the product of the mass blowing rate and the heat-of-ablation. Finally, Figure 7.16 shows the influence of chamber pressure on the heat-of-ablation which is the heat absorbed in the process of ablation per mass of TPS consumed $[MJ/kg]$. It is clear that the chamber pressure has just a slight influence on the heat-of-ablation. This explains the direct correlation between the erosion rate and the chemical heat flux. Looking at Figure 7.16 and comparing the profiles with those of Figure 7.14 it can be observed that the heat-of-ablation is influenced by surface temperature. Higher surface temperatures tend to reduce the heat-of-ablation even if its profile is almost uniform showing only a variation by a few percent along the nozzle length.

Many authors in the past [23] have correlated the recession rate with the density of the C/C composite material or bulk graphite showing higher erosion rates $[mm/s]$ with lower material densities. The model developed in this study predicts that the recession rate will be inversely proportional to the density of the nozzle material. This is evident from examining the expression for $\dot{s}$, which has the density of the nozzle material in the denominator:

$$\dot{m} = \rho_s \cdot \dot{s} \qquad \Rightarrow \qquad \dot{s} = \frac{\dot{m}}{\rho_s}$$

where $\dot{m}$ is the mass erosion rate $[kg/m^2 s]$, $\dot{s}$ is the erosion rate $[m/s]$, and ρ_s is the material density $[kg/m^3]$. Consistent with the experimental observations [23], the model predicts that the recession rate is inversely proportional to the density of the nozzle material. Looking at Figure 7.13, the erosion rate in terms of $[m/s]$ can be obtained simply dividing the mass erosion rate $[kg/m^2 s]$ by the material density. Since the diffusion process is not influenced by the thermophysical properties of the solid, C/C composite materials and various bulk graphite should have equal recession rates after the short kemical kinetics controlled time interval[1], if their densities are equal. This finding is in agreement with Geisler's experimental observation [27] that C/C and bulk graphite have equivalent thermochemical recession rates at equivalent densities.

[1] As we have seen, the chemical kinetics influences the recession rate only during a short time interval at the beginning of the recession event. After the initial phase of surface temperature rise, the recession rate is controlled mainly by the diffusion process.

Chapter 8

Conclusions

In this study, a general method is developed to examine thermo-chemical ablation of graphite and Carbon/Carbon composite material. This model includes all the relevant physics of thermo-chemical non-equilibrium flowfield and the internal heat conduction into the ablator material. The two regions, gas and solid, are fully coupled at the surface by appropriate energy and mass balances. This allows the surface conditions to be solved as part of the over-all solution. The specific application of this work is the analysis of thermal protection systems (TPS) and their complex interaction with the surrounding hot-gas flow. This problem is of critical importance for optimization of the TPS for hypersonic vehicles and SRM nozzles. TPS, in fact, are traditionally designed with one-dimensional engineering codes. Occasionally, a detailed computational solution is obtained but these solutions rarely contain the correct surface boundary conditions. To compensate for uncertainties in the analyses, a safety margin of extra TPS material is added to the final design, and the structural weight must also be increased. Clearly there is a need for more accurate, multidimensional computational tools which can be used to reduce the uncertainties in TPS analysis and to optimize the TPS distribution around the vital structures. The objective of this work is the development of an innovative material/fluid interaction tool and its integration with a CFD tool which can provide detailed modeling of these surface and near-surface physical and thermochemical phenomena. The activity leading to this final goal can be summarized into two main steps described as follows.

In the first part, a proper one-dimensional model has been selected to describe the thermal transient response of the TPS under realistic heating conditions ranging from re-entry to SRM nozzle applications. The proposed model generates a 1-D in-depth solution, but the cross sectional area of the material analysed may vary with depth (thermal stream tube). The developed code employs an implicit finite difference solution technique, which shifts its coordinate system to account for surface ablation. An important feature of this tool is the heated surface bound-

ary condition. The general solution case employs a film coefficient model which couples the external heating environment to the surface thermochemistry solution. Approximate correlation equations for the multi-component boundary-layer over an ablating material have been proposed to characterize the transfer of heat and mass across the surface. Employing the proposed boundary-layer correlations, equations are presented to characterize heat and mass transfer at the surface of an arbitrary non-charring material in an environment of arbitrary chemical composition. A numerical solution of the equations for the in-depth transient response of TPS material has been programmed with the surface boundary condition coupled to a thermochemical ablation model which accounts for heterogeneous chemical equilibrium at the ablating surface. A general theory is presented for ablation thermochemistry of TPS materials which is then implemented in a CEA-based chemical equilibrium code for generating dimensionless ablation tables. The 1-D transient model has shown excellent agreement with known analytical solutions and with the widely used CMA code. In particular this model is finalized to be used as a time-efficient engineering tool for the TPS analysis, prediction and design. Results of transient coupled solution are presented for carbon-carbon composite material in various high-temperature environments. The major result of these computations is that, despite the different kind of application ranging from rocket nozzle to Earth reentry environment, Carbon/Carbon shows a similar behaviour characterized by a quick heating and a short transient period in which surface conditions strongly vary with time. Results have shown that the surface parameters (temperature, erosion rate, heat conduction into solid) are much faster in reaching the steady conditions than the in-depth temperature profile. This permits to conclude that, for what concern the surface conditions, a steady-state assumption is acceptable to study the complex interaction between hot-gas flow and TPS material. On the contrary, if one is interested in the temperature rise inside the material and in particular at the interface with the structure, a transient solution is mandatory.

In the second part of this work, where the author concentrated much of his efforts, the interaction between the hot-gas layer and a Carbon/Carbon TPS has been studied in details assuming steady-state ablation, which has been demonstrated to be a reasonable assumption for this kind of materials. A full Navier-Stokes solver is used to model with more accuracy the heat and mass transfer mechanisms removing completely the transfer-coefficient approach (thin-film model) used in the previous coupling. To reach this goal, a general surface boundary condition with mass and energy balance for an ablating surface has been derived. A procedure based on these surface conditions has been developed and integrated with a two-dimensional axisymmetric full Navier-Stokes equation solver coupled with an equilibrium ablation model which permits both oxidation and sublimation reactions to occur on a C/C surface. Particular efforts have been made toward the

integration of the mass/energy balances and ablation model with the flow solver. The most interesting and original property of the developed numerical tool lies in the fact that it is fully coupled with the ablating boundary conditions thus permitting to remove all the commonly used mass/energy-transfer coefficients and the resulting inaccuracies. As a matter of fact, even if nowadays Computational Fluid Dynamics is common practice for re-entry and SRM nozzle applications, CFD codes rarely contain the correct surface boundary conditions to cope with ablation. Most codes, in fact, use simplistic boundary conditions (constant prescribed temperature or heat flux and with zero mass transfer) and cannot be realistically used for TPS design and analysis.

Solutions with different flowfield conditions and boundary conditions (isothermal, steady-state) have been obtained to study the effects on surface composition and ablation rate and the transition between oxidation and sublimation regimes. The effect of gas injection in the boundary layer has been studied focusing the attention on the wall heat flux and its reduction due to the ablation phenomenon. The effect of finite-rate chemistry for the ablation products has been analysed to study its effect on surface ablation. Finally, the obtained results have been compared with the most commonly used simplified approaches for coupling CFD code and surface ablation. These approaches are based on the use of thermochemical tables, heat and mass-transfer coefficients and blowing correction equations, with different degrees of simplification. The comparison of the results obtained with these simpler approaches has shown a good agreement of the solutions for the test cases analysed at the lowest blowing rates and thus validates the fully-coupled approach developed in this work. The comparison has also shown the inaccuracies introduced by the simpler methodologies which are more and more evident with increasing blowing rates and when using more complex boundary-conditions (variable surface temperature), thus demonstrating the need for more accurate CFD tools which can be used to reduce the uncertainties in TPS analysis.

As a final step, the developed tool has been applied to describe Carbon/Carbon regression of advanced solid-rocket nozzles. The hot-gas flow inside the nozzle has been simulated taking into account propellant chemistry, detailed thermodynamic and fluid-dynamic analyses, heterogeneous chemical reactions at the nozzle surface, rate of diffusion of the species through the boundary-layer and accurate multi-species thermophysical properties. The model so developed is free from many restrictive assumptions and approximations made by several researchers over the past. The results show that the erosion rate follows the trend exhibited by the heat-flux variation: recession and heat flux increase in the converging section of the nozzle, reach a maximum close to the throat, and decrease in the supersonic diverging section. This variation is governed by the mass flux of the flow of propellant products in the nozzle. The most important factors that dictate the erosion process are concentrations of the oxidizing species at the nozzle

inlet, rate of diffusion of oxidizing species toward the nozzle surface, and motor operating conditions. The results of Part I illustrated that the surface temperature of C/C nozzles increases very quickly to an elevated temperature ($\approx 2500\ K$) in few seconds. Hence, chemical kinetics, which are dominant at low surface temperatures, control the recession process only for a very short initial period of the recession event. Thereafter, the recession process is limited by the diffusion of oxidizing species to the nozzle surface. Calculated results showed that oxidation of carbon to CO is the principal cause of nozzle recession. H_2O is the dominant oxidizing species, with CO_2 and OH being of secondary importance since their concentrations are about one order of magnitude lower than that of H_2O. Consistent with experimental results, the recession rate shows an increase with increasing chamber pressure, exhibiting almost a linear correlation. This is due to the enhanced mass transport of oxidizing species across the turbulent boundary-layer. Consistent with the experimental observations, the model predicts that the recession rate is inversely proportional to the density of the nozzle material.

In conclusion, the general boundary conditions, including mass and energy balances, of chemically equilibrated gas adjacent to an ablating surface have been derived. An efficient computational procedure based on these conditions has been developed and integrated with a Navier Stokes solver. The presented model has shown a great potential and thus it is a promising tool to obtain a more accurate characterization of the coupled interaction between a hot-gas flow and an ablating surface if compared to standard approaches.

Appendix A

Governing equations

The flow of a compressible chemically reacting mixture of gases is governed by the conservation principles of mass, momentum, and energy from which a complete system of differential equations, namely the Navier-Stokes equations, can be derived. When the viscous effects can be neglected, the system reduces to the Euler equations.

A.1 Navier-Stokes equations

The complete Navier-Stokes equations for a chemically reacting viscous flow are[1] [2, 42]:

$$\begin{cases} \dfrac{\partial \rho_i}{\partial t} + \nabla \cdot (\rho_i \mathbf{v_i}) = \dot{w}_i \qquad i = 1, ..., N-1 \\ \dfrac{\partial \rho}{\partial t} + \nabla \cdot (\rho \mathbf{v}) = 0 \\ \dfrac{\partial (\rho \mathbf{v})}{\partial t} + \nabla \cdot (\rho \mathbf{v}\mathbf{v}) - \nabla \cdot \mathbf{S} = 0 \\ \dfrac{\partial (\rho e_0)}{\partial t} + \nabla \cdot (\rho e_0 \mathbf{v}) = \nabla \cdot (\mathbf{v} \cdot \mathbf{S}) - \nabla \cdot \mathbf{q} \end{cases} \tag{A.1}$$

where $\mathbf{v_i}$ is the mass motion of species i which can be expressed as:

$$\mathbf{v_i} = \mathbf{v} + \mathbf{u_i} \tag{A.2}$$

where $\mathbf{v}$ is the mass motion of the *mixture* and $\mathbf{u_i}$ is the diffusion velocity of species i. Note that for a mixture of N species only N-1 species continuity equations are needed: the N^{th} equation is given by $\sum_{i=1}^{N} \rho_i = \rho$.

[1] The volumetric forces and the volumetric heating have not been considered.

The term $\mathbf{S}$ is the stress tensor, split into the contribution of pressure forces and viscous stresses, the term $\mathbf{q}$ is the heat flux vector, and the term $\dot{w}_i$ is the source term due to chemical reaction (explained later):

$$\begin{aligned} \mathbf{S} &= -p\mathbf{I} + \mathbf{T} \\ \mathbf{q} &= -k\nabla T + \sum_{i=1}^{N} \rho_i h_i \mathbf{u_i} \end{aligned} \tag{A.3}$$

where, assuming *newtonian* flows and zero *bulk viscosity* (according to Stokes hypothesis), the viscous stress tensor can be expressed as:

$$\mathbf{T} = -\frac{2}{3}\mu(\nabla \cdot \mathbf{v})\mathbf{I} + \mu\left[\nabla\mathbf{v} + (\nabla\mathbf{v})^T\right] \tag{A.4}$$

Finally, the diffusional mass flux of the i^{th} species can be expressed using the approximation of Fick's law:

$$\mathbf{j}_i = \rho_i \mathbf{u_i} = \rho y_i \mathbf{u_i} = -\rho \mathcal{D}_{im} \nabla y_i \tag{A.5}$$

The transport coefficient μ, k, and $\mathcal{D}_{im}$ in the Eqs. (A.3), (A.4), and (A.5) are the viscosity coefficient, the thermal conductivity, and the multicomponent diffusion coefficient, respectively.

The Navier-Stokes equations (A.1) can be also written in *non-conservation* form:

$$\begin{cases} \rho\dfrac{Dy_i}{Dt} + \nabla \cdot (\rho y_i \mathbf{u_i}) = \dot{w}_i \qquad i = 1, ..., N-1 \\ \dfrac{D\rho}{Dt} + \rho\nabla \cdot \mathbf{v} = 0 \\ \rho\dfrac{D\mathbf{v}}{Dt} + \nabla p = \nabla \cdot \mathbf{T} \\ \rho\dfrac{De_0}{Dt} + \nabla \cdot (p\mathbf{v}) = \nabla \cdot (\mathbf{v} \cdot \mathbf{T}) - \nabla \cdot \mathbf{q} \end{cases} \tag{A.6}$$

wher the substantial derivative notation has been used:

$$\frac{D}{Dt} = \frac{\partial}{\partial t} + \mathbf{v} \cdot \nabla$$

A.1.1 Transport properties

A.1.1.1 Viscosity and thermal conductivity

For each chemical species the viscosity and thermal conductivity as functions of temperature are given in the form of least-square coefficients. The data for each species are fitted to the following form:

$$\ln \alpha = A \ln T + \frac{B}{T} + \frac{C}{T^2} + D$$

where α can be either the viscosity μ_i or the thermal conductivity k_i of the i^{th} species. For a multicomponent gas, such as a chemically reacting mixture, the *mixture* values of μ and k must be found from the values of μ_i and k_i of each of the chemical species i by means of the *mixture rules*. A common rule for viscosity is *Wilke's rule*, which states that:

$$\mu = \sum_{i=1}^{N} \frac{X_i \mu_i}{\sum_j X_j \phi_{ij}}, \quad \phi_{ij} = \frac{1}{\sqrt{8}} \left(1 + \frac{\mathcal{M}_i}{\mathcal{M}_j}\right)^{-1/2} \left[1 + \sqrt{\frac{\mu_i}{\mu_j}} \left(\frac{\mathcal{M}_i}{\mathcal{M}_j}\right)^{1/4}\right]^2 \tag{A.7}$$

where X_i and $\mathcal{M}_i$ are the molar fraction and the molecular weight of species i, respectively. For the thermal conductivity of a mixture, Eq. (A.7) can be used again, replacing μ and μ_i with k and k_i, respectively.

A.1.1.2 Diffusion coefficient

One of the simplest model to obtain the diffusion coefficient is that of considering a constant *Lewis* number. From its definition:

$$Le = \frac{k}{\rho \mathcal{D} c_p}, \quad \mathcal{D}_{im} = \mathcal{D} = \frac{k}{\rho c_p Le} \tag{A.8}$$

In this way a single global diffusion coefficient is used for every species. It is worth remembering that μ and k for a pure species depend only on temperature whereas $\mathcal{D}$ depends on both the temperature and the density of the gas.

A.1.2 Chemical source term

The term $\dot{w}_i$ in Eqs. (A.1) is the local rate of change of ρ_i as a result of *chemical reactions* inside the volume. The chemical source term is positive for species which are created and it is negative for species which are consumed. The dimensions of $\dot{w}_i$ are mass per unit volume per unit time.

An expression for $\dot{w}_i$ comes from the chemical rate equation (whose dimensions are moles per unit volume per unit time), couched in suitable dimensions:

$$\dot{w}_i = \mathcal{M}_i \sum_{r=1}^{R} \frac{dC_{i_r}}{dt} \tag{A.9}$$

where $\frac{dC_{i_r}}{dt}$ represent the net time rate of formation of the i^{th} species (in terms of concentrations[2]) due to the r^{th} chemical reaction and $\mathcal{M}_i$ is the molecular weight of species i. The summation is made over all the R chemical reactions involving the species i. For the general r^{th} chemical reaction of the form:

$$\sum_{i=1}^{N} \nu_{i_r}^{'} C_{i_r} \rightleftharpoons \sum_{i=1}^{N} \nu_{i_r}^{''} C_{i_r} \tag{A.10}$$

the generalized *net rate equation* is:

$$\frac{dC_{i_r}}{dt} = (\nu_{i_r}^{''} - \nu_{i_r}^{'}) \left[k_{f_r} \prod_{i=1}^{N} (C_{i_r})^{\nu_{i_r}^{'}} - k_{b_r} \prod_{i=1}^{N} (C_{i_r})^{\nu_{i_r}^{''}} \right] \tag{A.11}$$

where k_{f_r} and k_{b_r} are the forward and backward reaction rate constants for the r^{th} chemical reaction and are function of temperature only. A relation between the forward and backward reaction rate constants holds:

$$\frac{k_f}{k_b} = K_c(T) \tag{A.12}$$

where K_c is the equilibrium constant based on *concentrations* which is related to the equilibrium constant based on *partial pressures*:

$$\begin{aligned} K_c(T) &= K_p(T) \left(\frac{1}{\mathcal{R}T} \right)^{\sum_i (\nu_i^{''} - \nu_i^{'})} \\ K_p(T) &= e^{-\Delta G^0 / \mathcal{R}T} \\ \Delta G^0 &= \sum_i (\nu_i^{''} - \nu_i^{'}) G_i^0 \end{aligned}$$

where G_i^0 is the *standard state* Gibbs free energy per mole of mixture.

The chemical rate constants are generally measured experimentally. The empirical results for many reactions can be correlated using the *Arrhenius equation* form:

$$k_f = A T^b e^{-E_A / \mathcal{R}T}$$

where A, b, and E_a (the *activation energy*) are all found from experimental data.

[2] C_i is the number of moles of the i^{th} species per unit volume of mixture.

A.2 Euler equations

The *Euler* equations can be obtained neglecting the *viscous* terms due to viscosity, thermal conductivity, and mass diffusion from the *Navier-Stokes* equations (A.1):

$$\begin{cases} \dfrac{\partial \rho_i}{\partial t} + \nabla \cdot (\rho_i \mathbf{v}) = \dot{w}_i \qquad i = 1, ..., N-1 \\ \dfrac{\partial \rho}{\partial t} + \nabla \cdot (\rho \mathbf{v}) = 0 \\ \dfrac{\partial (\rho \mathbf{v})}{\partial t} + \nabla \cdot (\rho \mathbf{v}\mathbf{v}) + \nabla p = 0 \\ \dfrac{\partial (\rho e_0)}{\partial t} + \nabla \cdot (\rho e_0 \mathbf{v}) + \nabla \cdot (p\mathbf{v}) = 0 \end{cases} \tag{A.13}$$

It is well known that the Navier-Stokes equations are not hyperbolic as the addition of viscous terms changes the mathematical nature of the system by increasing its order. However, Navier-Stokes equations certainly propagate waves like Euler equations do: the viscous effects, in fact, are important only in a limited part of the flowfied, such such near walls, shock waves, and contact discontinuities. Therefore the numerical methods used to solve the Navier-Stokes equations can be an extension of those used for the Euler equations, taking advantage from their hyperbolic nature and decoupling between the convective operator and the diffusive operator.

Taking this into account, it is important to study some properties of the Euler equations before going to the Navier-Stokes equations. The Euler equations can be written in different ways and using different variables. Firstly we can distinguish between the *conservation form* and the *non-conservation form*. Eqs. (A.13) are written in *conservation form*, while the *non- conservation form* is written in substantial derivative notation:

$$\begin{cases} \rho \dfrac{Dy_i}{Dt} = \dot{w}_i \qquad i = 1, ..., N-1 \\ \dfrac{D\rho}{Dt} + \rho \nabla \cdot \mathbf{v} = 0 \\ \rho \dfrac{D\mathbf{v}}{Dt} + \nabla p = 0 \\ \rho \dfrac{De_0}{Dt} + \nabla \cdot (p\mathbf{v}) = 0 \end{cases} \tag{A.14}$$

The *non-conservation form* do dot admit discontinuous solutions; from now on, we will refer to the system (A.14) which is also called *quasi-linear* form.

A.3 Equations in terms of a/δ, v, s, y_i

Following the *lambda* scheme proposed in [54] and extended in [47] for reacting flows, the Euler equations expressed by (A.14) are written in terms of a/δ, **v**, s, y_i:

$$\begin{cases} \dfrac{Dy_i}{Dt} = \dfrac{\dot{w}_i}{\rho} \qquad i = 1, ..., N-1 \\ \dfrac{1}{c_1}\dfrac{Db}{Dt} + a\nabla\cdot\mathbf{v} - \dfrac{a}{R}\dfrac{Ds}{Dt} = \dfrac{1}{c_1}\beta \\ \dfrac{D\mathbf{v}}{Dt} + \dfrac{a}{c_1}\nabla b - \dfrac{a^2}{\gamma R}\nabla s + \dfrac{a^2}{\gamma R}\sum Q_i \nabla y_i = 0 \\ \dfrac{Ds}{Dt} = -\dfrac{1}{T}\sum \mu_i \dfrac{Dy_i}{Dt} \end{cases} \tag{A.15}$$

where $b = a/\delta$, $a = \sqrt{\gamma RT}$ is the frozen speed of sound, $\delta = (\gamma-1)/2$ and μ_i is the Gibbs free energy per unit mass (chemical potential) of the i^{th} species. The derivation of Eqs. (A.15) from Eqs. (A.14) is quite tedious and is reported in [47].

The terms c_1, β, and Q_i express the variation of γ and R due to variation of temperature T and composition y_i. Their expression is the following:

$$c_1 = d_1 \delta a_1$$

$$\beta = a c_1 \sum \left[-\frac{e_i}{RT} + \frac{\mu_i}{RT} + \frac{1}{c_1}\frac{\partial(1/\delta)}{\partial y_i} - \left(\frac{a_2}{c_1} - \frac{1}{d_1(\gamma-1)} \right) \frac{\partial \ln(\gamma R)}{\partial y_i} \right] \frac{Dy_i}{Dt}$$

$$Q_i = s_i - \frac{\partial \ln(\gamma R)}{\partial y_i} c_p \left(\frac{1}{d_1} - \frac{2a_2}{d_1 a_1} \right) - 2\frac{c_p}{d_1 a_1}\frac{\partial(1/\delta)}{\partial y_i}$$

where:

$$\begin{aligned} d_1 &= 1 + T\frac{\partial(\gamma R)}{\partial T} \\ a_1 &= \frac{1}{\delta} + \frac{2T}{d_1}\frac{\partial(1/\delta)}{\partial T} \\ a_2 &= \frac{T}{d_1}\frac{\partial(1/\delta)}{\partial T} \end{aligned}$$

The Navier-Stokes equations in terms of b, $\mathbf{v}$, s, y_i can be obtained adding the viscous terms to the Euler equations (A.15):

$$\begin{cases} \dfrac{Dy_i}{Dt} = \dfrac{\dot{w}_i}{\rho} + \dfrac{1}{\rho}\nabla\cdot(\rho\mathcal{D}_{im}\nabla y_i) \qquad i = 1, ..., N-1 \\ \dfrac{1}{c_1}\dfrac{Db}{Dt} + a\nabla\cdot\mathbf{v} - \dfrac{a}{R}\dfrac{Ds}{Dt} = \dfrac{1}{c_1}\beta \\ \dfrac{D\mathbf{v}}{Dt} + \dfrac{a}{c_1}\nabla b - \dfrac{a^2}{\gamma R}\nabla s + \dfrac{a^2}{\gamma R}\sum Q_i\nabla y_i = \dfrac{1}{\rho}\nabla\cdot\mathbf{T} \\ \dfrac{Ds}{Dt} = -\dfrac{1}{T}\sum\mu_i\dfrac{Dy_i}{Dt} + \dfrac{R}{p}(-\nabla\cdot\mathbf{q} + \nabla\mathbf{v} : \mathbf{T}) \end{cases} \tag{A.16}$$

Summing and subtracting $\dfrac{a}{\gamma R}\dfrac{Ds}{Dt}$ from the continuity equation, with $\dfrac{Ds}{Dt}$ coming from the energy equation, we obtain:

$$\frac{1}{c_1}\frac{Db}{Dt} + a\nabla\cdot\mathbf{v} - \frac{a}{\gamma R}\frac{Ds}{Dt} = \frac{1}{c_1}\beta + \frac{a}{\gamma R}(\gamma-1)V_s \tag{A.17}$$

The system can be finally written in the following form:

$$\begin{cases} \dfrac{Dy_i}{Dt} = V_{yi} \qquad i = 1, ..., N-1 \\ \dfrac{1}{c_1}\dfrac{Db}{Dt} + a\nabla\cdot\mathbf{v} - \dfrac{a}{\gamma R}\dfrac{Ds}{Dt} = V_b \\ \dfrac{D\mathbf{v}}{Dt} + \dfrac{a}{c_1}\nabla b - \dfrac{a^2}{\gamma R}\nabla s + \dfrac{a^2}{\gamma R}\sum Q_i\nabla y_i = \mathbf{V}_m \\ \dfrac{Ds}{Dt} = V_s \end{cases} \tag{A.18}$$

where the source terms are defined as follows:

$$\begin{aligned} V_{y_i} &= \frac{\dot{w}_i}{\rho} - \frac{1}{\rho}\nabla\cdot\mathbf{j}_i \\ V_b &= \frac{1}{c_1}\beta + \frac{a}{\gamma R}(\gamma-1)V_s \\ \mathbf{V}_m &= \frac{1}{\rho}\nabla\cdot\mathbf{T} \\ V_s &= -\frac{1}{T}\sum\mu_i V_{y_i} + \frac{R}{p}(-\nabla\cdot\mathbf{q} + \nabla\mathbf{v} : \mathbf{T}) \end{aligned} \tag{A.19}$$

A.4 Nondimensional form of the Navier-Stokes equations

The Navier-Stokes equations (A.18) can be nondimensionalized as follows. The nondimensional variables are defined as the ratio between the dimensional value and its reference value (expressed with the subscript r), typical of the flow considered. The reference values for nondimensioning are:

density	ρ_r
pressure	p_r
length	l_r
molecular weight	$\mathcal{M}_r = \mathcal{M}_{N_2}$
gas constant	$R_r = R_u/\mathcal{M}_{N_2}$
temperature	$T_r = p_r/(R_r\rho_r)$
velocity	$v_r = \sqrt{p_r/\rho_r}$
time	$t_r = l_r/v_r$
entropy	$s_r = R_r$
sound speed	$a_r = v_r$
shear stress tensor	$S_r = p_r$
viscous stress tensor	$T_r = p_r$
viscosity	μ_r
enthalpy	$h_r = p_r/\rho_r$
internal energy	$e_r = p_r/\rho_r$
heat flux (per unit area)	$q_r = p_r v_r$
mass flux (per unit area)	$\dot{m}_r = \rho_r v_r$
gamma	γ_r
specific heats	$c_{pr} = c_{vr} = \frac{\gamma_r}{\gamma_r - 1} R_r$
chemical source	$\omega_r = \rho_r/t_r$

The following dimensionless parameters are defined:

Reynolds number: $$Re_r = \frac{\rho_r v_r l_r}{\mu_r}$$

Prandtl number: $$Pr_r = \frac{\mu_r c_{pr}}{k_r}$$

Lewis number: $$Le_r = \frac{k_r}{\rho_r c_{pr} \mathcal{D}_r}$$

Using the Prandtl and Lewis number the reference thermal conductivity and dif-

fusion coefficient can be defined as:

$$\begin{aligned} k_r &= \mu_r \frac{c_{pr}}{Pr_r} \\ \mathcal{D}_r &= \frac{\mu_r}{Le_r Pr_r \rho_r} \end{aligned}$$

Using the same notation for dimensional and nondimensional variables, the nondimensional Navier-Stokes equations are identical to their dimensional form, expressed by Eqs. (A.18). The system can be written expressing explicitly the substantial derivative, with the subscript $()_t$ expressing partial derivative with respect to time:

$$\begin{cases} y_{i,t} + \mathbf{v} \cdot \nabla y_i = V_{yi} \qquad\qquad i = 1, ..., N^{'} = N - 1 \\ \\ \dfrac{1}{c_1} b_t + \dfrac{1}{c_1} \mathbf{v} \cdot \nabla b + a \nabla \cdot \mathbf{v} - \dfrac{a}{\gamma R} s_t - \dfrac{a}{\gamma R} \mathbf{v} \cdot \nabla s = V_b \\ \\ \mathbf{v}_t + (\mathbf{v} \cdot \nabla)\mathbf{v} + \dfrac{a}{c_1} \nabla b - \dfrac{a^2}{\gamma R} \nabla s + \dfrac{a^2}{\gamma R} \sum Q_i \nabla y_i = \mathbf{V}_m \\ \\ s_t + \mathbf{v} \cdot \nabla s = V_s \end{cases} \tag{A.20}$$

The nondimensional source terms have the following expression:

$$\begin{aligned} V_{y_i} &= \frac{\dot{w}_i}{\rho} - \frac{1}{\rho} \nabla \cdot \mathbf{j}_i \\ V_b &= \frac{1}{c_1} \beta + \frac{a}{\gamma R} (\gamma - 1) V_s \\ \mathbf{V}_m &= \frac{1}{\rho} \nabla \cdot \mathbf{T} \\ V_s &= -\frac{1}{T} \sum \mu_i V_{y_i} + \frac{R}{p} (-\nabla \cdot \mathbf{q} + \nabla \mathbf{v} : \mathbf{T}) \end{aligned} \tag{A.21}$$

with:

$$\begin{aligned} \mathbf{T} &= \frac{1}{Re_r} \mu \left[-\frac{2}{3} (\nabla \cdot \mathbf{v}) \mathbf{I} + \nabla \mathbf{v} + (\nabla \mathbf{v})^T \right] \\ \mathbf{q} &= -\frac{\gamma_r}{\gamma_r - 1} \frac{1}{Re_r P_r} k \nabla T - \frac{1}{Le_r Re_r Pr_r} \sum \rho \mathcal{D} h_i \nabla y_i \\ \mathbf{j}_i &= -\frac{1}{Pr_r Le_r Re_r} \rho \mathcal{D}_{im} \nabla y_i \end{aligned}$$

Appendix B

Lambda scheme and solving technique

The adopted technique for the numerical analysis of two-dimensional, viscous, reacting, unsteady flows is described here. To integrate the governing equations a *finite difference* approach is used. The first step to be taken is the choice of a computational grid. Obviously, the grid has to be well adapted to the geometry of the rigid bodies in the problem: grids must be so chosen that any rigid body contour is described by a grid line. Experience dictates that more accurate results are obtained if the computational grid is orthogonal so that only orthogonal grids are used here. Moreover, the finite differencing is easier and more accurate if an equally-spaced cartesian frame is adopted. Therefore, a curvilinear orthogonal grid in the physical space (obtained with conformal mapping) is transformed to a rectangular grid in the transformed space. Because the finite difference calculations are performed on this rectangular grid, it is also called the computational space. Grid created in this fashion are called *structured* grids. Since it is often useful to have more nodes in some region of the flowfield (near walls), a first transformation (*stretching*) of the computational plane is performed: the computational grid is transformed to a new grid which is still cartesian but no more equally-spaced (stretched). This intermediate grid is finally transformed to the curvilinear grid in the physical space. To summarize three planes have been defined: the physical plane (x, y) discretized with a curvilinear orthogonal grid, the intermediate plane (ξ, η) discretized with a stretched cartesian grid, and the computational plane $(\hat{x}, \hat{y})$ discretized with an equally-spaced cartesian grid. Two-dimensional problems are considered in this technique.

B.1 The λ-scheme

The governing equations derived in Appendix A and written in *quasi-linear* form in terms of b, $\mathbf{v}$, s, and y_i are now reformulated using ideas based on the concept of characteristics. Following the technique presented in [54] for two-dimensional inviscid flows and extended in [59] and [47] for viscous and reacting flows, respectively, the Navier-Stokes Eqs. (A.20) can be reformulated as follows.

Let $\mathbf{n}$ and $\boldsymbol{\tau}$ be a pair of unit vectors along the coordinate lines of a given curvilinear orthogonal grid in the physical plane (x,y) and let $\mathbf{i}$ and $\mathbf{j}$ be a pair of unit vectors of a cartesian grid in the same plane. Therefore:

$$\mathbf{v} = u\mathbf{n} + v\boldsymbol{\tau}$$

Now let be $\alpha = \alpha(x, y)$ the angle between the two orthogonal frames. Therefore:

$$\mathbf{n} = \cos\alpha\,\mathbf{i} + \sin\alpha\,\mathbf{j}, \qquad \boldsymbol{\tau} = -\sin\alpha\,\mathbf{i} + \cos\alpha\,\mathbf{j}$$

and

$$d\mathbf{n} = \boldsymbol{\tau} d\alpha, \qquad d\boldsymbol{\tau} = -d\mathbf{n}\alpha \tag{B.1}$$

We also consider a unit vectir, $\mathbf{k}$, perpendicular to the plane of motion so that $\mathbf{k} = \mathbf{i} \times \mathbf{j} = \mathbf{n} \times \boldsymbol{\tau}$. The following identities are easily proven:

$$\nabla \cdot \mathbf{v} \;=\; \mathbf{n} \cdot \nabla u + \boldsymbol{\tau} \cdot \nabla v + \mathbf{k} \times \mathbf{v} \cdot \nabla\alpha \tag{B.2}$$

$$(\mathbf{v} \cdot \nabla)\mathbf{v} \;=\; (\mathbf{v} \cdot \nabla u)\mathbf{n} + (\mathbf{v} \cdot \nabla v)\boldsymbol{\tau} + (\mathbf{v} \cdot \nabla\alpha)(u\boldsymbol{\tau} - v\mathbf{n}) \tag{B.3}$$

Finally, let $\mathbf{w}$ be an arbitrary *unit* vector. If the third of (A.20) is dot-multiplied by $\mathbf{w}$, and the result is added to the second of (A.20) and to the sum of the first i equations multiplied by $a/(\gamma R)Q_i$, a single scalar equation is obtained:

$$\begin{aligned} &\frac{1}{c_1} b_t + \mathbf{w} \cdot \mathbf{v}_t - \frac{a}{\gamma R} s_t + \frac{a}{\gamma R} \sum Q_i y_{i,t} + \\ &+(\mathbf{v} + a\mathbf{w}) \cdot \frac{\nabla b}{c_1} - \frac{a}{\gamma R}(\mathbf{v} + a\mathbf{w}) \cdot \nabla s + \frac{a}{\gamma R}(\mathbf{v} + a\mathbf{w}) \cdot \sum Q_i \nabla y_i + \\ &+\mathbf{w} \cdot [(\mathbf{v} \cdot \nabla)\mathbf{v}] + a\nabla \cdot \mathbf{v} = V_b + \mathbf{w} \cdot \mathbf{V}_m + \frac{a}{\gamma R} \sum Q_i V_{y_i} \end{aligned} \tag{B.4}$$

By using (B.2) and (B.3), (B.4) can be written in the form:

$$\begin{aligned} &\frac{1}{c_1} b_t + \mathbf{w} \cdot \mathbf{v}_t - \frac{a}{\gamma R} s_t + \frac{a}{\gamma R} \sum Q_i y_{i,t} + \\ &+(\mathbf{v} + a\mathbf{w}) \left(\frac{\nabla b}{c_1} - \frac{a}{\gamma R} \nabla s + \frac{a}{\gamma R} \sum Q_i \nabla y_i \right) + \\ &+\mathbf{w} \cdot [(\mathbf{v} \cdot \nabla u)\mathbf{n} + (\mathbf{v} \cdot \nabla v)\boldsymbol{\tau} + (\mathbf{v} \cdot \nabla\alpha)(u\boldsymbol{\tau} - v\mathbf{n})] + \\ &+a(\mathbf{n} \cdot \nabla u + \boldsymbol{\tau} \cdot \nabla v + \mathbf{k} \times \mathbf{v} \cdot \nabla\alpha) = V_b + \mathbf{w} \cdot \mathbf{V}_m + \frac{a}{\gamma R} \sum Q_i V_{y_i} \end{aligned} \tag{B.5}$$

Now let $\mathbf{w} = \mathbf{n}$, $-\mathbf{n}$, $\boldsymbol{\tau}$ and $-\boldsymbol{\tau}$ successively. Four equation are obtained from (B.5), which can be written in a simpler and symmetric form by letting:

$$\begin{aligned} \rho_1 &= b + u, & \mathbf{\Lambda}_1 &= \mathbf{v} + a\mathbf{n} \\ \rho_2 &= b - u, & \mathbf{\Lambda}_2 &= \mathbf{v} - a\mathbf{n} \\ \rho_3 &= b + v, & \mathbf{\Lambda}_3 &= \mathbf{v} + a\boldsymbol{\tau} \\ \rho_4 &= b - v, & \mathbf{\Lambda}_4 &= \mathbf{v} - a\boldsymbol{\tau} \end{aligned}$$

and

$$F = a\mathbf{k} \times \mathbf{v} \cdot \nabla\alpha, \qquad \beta = \mathbf{v} \cdot \nabla\alpha, \qquad c_{12} = (1 - c_1)/c_1$$

The four equations are:

$$\begin{aligned} &\left(\frac{1}{c_1} b_t + u_t - \frac{a}{\gamma R} s_t + \frac{a}{\gamma R} \sum Q_i y_{i,t}\right) + \\ &+\mathbf{\Lambda}_1 \left(\nabla\rho_1 - \frac{a}{\gamma R}\nabla s + \frac{a}{\gamma R} \sum Q_i \nabla y_i + c_{12}\nabla b\right) + \\ &+a\boldsymbol{\tau}\nabla v - \beta v + F = V_b + \mathbf{V}_m \cdot \mathbf{n} + \frac{a}{\gamma R} \sum Q_i V_{y_i} \end{aligned}$$

$$\begin{aligned} &\left(\frac{1}{c_1} b_t - u_t - \frac{a}{\gamma R} s_t + \frac{a}{\gamma R} \sum Q_i y_{i,t}\right) + \\ &+\mathbf{\Lambda}_2 \left(\nabla\rho_2 - \frac{a}{\gamma R}\nabla s + \frac{a}{\gamma R} \sum Q_i \nabla y_i + c_{12}\nabla b\right) + \\ &+a\boldsymbol{\tau}\nabla v + \beta v + F = V_b - \mathbf{V}_m \cdot \mathbf{n} + \frac{a}{\gamma R} \sum Q_i V_{y_i} \end{aligned}$$

$$\begin{aligned} &\left(\frac{1}{c_1} b_t + v_t - \frac{a}{\gamma R} s_t + \frac{a}{\gamma R} \sum Q_i y_{i,t}\right) + \\ &+\mathbf{\Lambda}_3 \left(\nabla\rho_3 - \frac{a}{\gamma R}\nabla s + \frac{a}{\gamma R} \sum Q_i \nabla y_i + c_{12}\nabla b\right) + \\ &+a\mathbf{n}\nabla u + \beta u + F = V_b + \mathbf{V}_m \cdot \boldsymbol{\tau} + \frac{a}{\gamma R} \sum Q_i V_{y_i} \end{aligned}$$

$$\begin{aligned} &\left(\frac{1}{c_1} b_t - v_t - \frac{a}{\gamma R} s_t + \frac{a}{\gamma R} \sum Q_i y_{i,t}\right) + \\ &+\mathbf{\Lambda}_4 \left(\nabla\rho_4 - \frac{a}{\gamma R}\nabla s + \frac{a}{\gamma R} \sum Q_i \nabla y_i + c_{12}\nabla b\right) + \\ &+a\mathbf{n}\nabla u - \beta u + F = V_b - \mathbf{V}_m \cdot \boldsymbol{\tau} + \frac{a}{\gamma R} \sum Q_i V_{y_i} \end{aligned} \tag{B.6}$$

Note that if the orthogonal frame is also cartesian, then the terms F and β vanish because $\nabla\alpha = 0$ everywhere in the flowfield. At this stage we may observe that the vectors $\mathbf{\Lambda}_i$ $(i = 1, 4)$ are two-dimensional generalizations of the characteristic slopes, λ_i, defined for one-dimensional flows [54]. Similarly, the scalars ρ_i are generalizations of the *Riemann* variables. Some additional manipulation, however, is necessary to bring the equations to a form closer to the one obtained for one-dimensional flows. We see, indeed, that (B.6) is a redundant system since the mass fractions y_i and the entropy s are provided by the first i equations and the fourth equation of (A.20), respectively, and three independent unknowns only remains: the variable b and the two velocity components u and v. Following an idea of Butler [13], the four equations (B.6) can be recombined into three, taking advantage of the orthogonality of $\mathbf{n}$ and $\boldsymbol{\tau}$.

By summing together the four equations (B.6) and subtracting the second of (A.20) multiplied by 2 and the sum of the first i equations of (A.20) multiplied by $2a/(\gamma R)Q_i$, we obtain:

$$\begin{aligned}
&\left(\frac{1}{c_1}b_t - \frac{a}{\gamma R}s_t + \frac{a}{\gamma R}\sum Q_i y_{i,t}\right) + \\
&+\frac{1}{2}\sum_{i=1}^{4}\mathbf{\Lambda}_i \cdot \left(\nabla\rho_i - \frac{a}{\gamma R}\nabla s + \frac{a}{\gamma R}\sum Q_i\nabla y_i + c_{12}\nabla b\right) + \\
-\mathbf{v}\cdot\left(\frac{\nabla b}{c_1} - \frac{a}{\gamma R}\nabla s + \frac{a}{\gamma R}\sum Q_i\nabla y_i\right) &+ F = V_b + \frac{a}{\gamma R}\sum Q_i V_{y_i} \qquad \text{(B.7)}
\end{aligned}$$

By subtracting the second of (B.6) from the first, we obtain:

$$\begin{aligned}
u_t + \frac{1}{2}\mathbf{\Lambda}_1 \cdot \left(\nabla\rho_1 - \frac{a}{\gamma R}\nabla s + \frac{a}{\gamma R}\sum Q_i\nabla y_i + c_{12}\nabla b\right) + \qquad \text{(B.8)} \\
-\frac{1}{2}\mathbf{\Lambda}_2 \cdot \left(\nabla\rho_2 - \frac{a}{\gamma R}\nabla s + \frac{a}{\gamma R}\sum Q_i\nabla y_i + c_{12}\nabla b\right) - \beta v = \mathbf{V}_m\cdot\mathbf{n}
\end{aligned}$$

and, similarly, by subtracting the fourth of (B.6) from the third, we obtain:

$$\begin{aligned}
v_t + \frac{1}{2}\mathbf{\Lambda}_3 \cdot \left(\nabla\rho_3 - \frac{a}{\gamma R}\nabla s + \frac{a}{\gamma R}\sum Q_i\nabla y_i + c_{12}\nabla b\right) + \qquad \text{(B.9)} \\
-\frac{1}{2}\mathbf{\Lambda}_4 \cdot \left(\nabla\rho_4 - \frac{a}{\gamma R}\nabla s + \frac{a}{\gamma R}\sum Q_i\nabla y_i + c_{12}\nabla b\right) + \beta u = \mathbf{V}_m\cdot\boldsymbol{\tau}
\end{aligned}$$

Finally, the first and the fourth equations of (A.20) are needed to close the system. Note that (B.7-B.9) and the first and fourth of (A.20) are all expressed in *gradient form*. The importance of this formulation resides in the way those equations can be discretized.

Now letting:

$$
\begin{aligned}
U_i &= \frac{1}{2}\mathbf{\Lambda}_i \cdot \left(\nabla \rho_i - \frac{a}{\gamma R}\nabla s + \frac{a}{\gamma R}\sum Q_i \nabla y_i + c_{12}\nabla b \right), \qquad i = 1,4 \\
U_5 &= \frac{1}{2}\mathbf{v} \cdot \left(\frac{1}{c_1}\nabla b - \frac{a}{\gamma R}\nabla s + \frac{a}{\gamma R}\sum Q_i \nabla y_i \right) \\
U_6 &= \mathbf{v} \cdot \nabla s \\
U_{7,i} &= \mathbf{v} \cdot \nabla y_i, \qquad i = 1, ..., N^{'} = N - 1 \\
V_u &= \mathbf{V}_m \cdot \mathbf{n} \\
V_v &= \mathbf{V}_m \cdot \boldsymbol{\tau} \\
V_b^{'} &= V_b + \frac{a}{\gamma R}\sum Q_i V_{y_i}
\end{aligned}
\tag{B.10}
$$

With the use of Eqs. (B.10), the system made of (B.7-B.9) plus the first and fourth equations of (A.20) can be expressed in a compact way:

$$
\begin{cases}
b_t = c_1 \left(\dfrac{a}{\gamma R} s_t - \dfrac{a}{\gamma R}\sum Q_i y_{i,t} - \displaystyle\sum_{i=1}^{4} U_i + 2U_5 - F + V_b^{'} \right) \\
u_t = -U_1 + U_2 + \beta v + V_u \\
v_t = -U_3 + U_4 - \beta u + V_v \\
s_t = -U_6 + V_s \\
y_{i,t} = -U_{7,i} + V_{y_i}, \qquad i = 1, ..., N^{'}
\end{cases}
\tag{B.11}
$$

Indeed, in the new system we have local terms, such as F, βu e βv, and source terms, such as $V_b^{'}$, V_u, V_v, V_s, and V_{y_i}. All other terms containing space derivatives express differentiations of generalized Riemann variables along directions which lie on the surface of a Mach conoid or along the direction of $\mathbf{v}$ itself. Let a Mach conoid be drawn backwards in time from a generic point, Q, to be evaluated at time $t + \Delta t$. Projecting the conoid onto the physical plane at time t, a circle is the intersection of the conoid with the physical plane. The radius of the circle is the speed of sound and its center, P, is the origin of the $\mathbf{v}$ vector ending at Q.

According to the choice of $\mathbf{n}$ and $\boldsymbol{\tau}$, four points are identified on the circle as the origin of the lines defined by the vectors $\boldsymbol{\Lambda}_i$. It is thus easy to identify from which computational cell the information proceeds, which is carried along a line parallel to one of the $\boldsymbol{\Lambda}_i$. Each one of the terms contributing to the equations, thus, can be discretized using information related to its domain of dependence.

B.2 Equations in the computational plane

It is now necessary to transform the derivatives expressed in the physical plane (x, y) into derivatives expressed in the computational plane $(\hat{x}, \hat{y})$. The computational, intermediate, and physical planes can be defined by a complex variable:

$$\hat{z} = \hat{x} + i\hat{y}$$

$$\zeta = \xi + i\eta$$

$$z = x + iy$$

In the computational plane the flowfield is a box $[0, 1] \times [0, 1]$ discretized with an equally-spaced cartesian grid. The intermediate plane ζ is obtained from the computational plane by *stretching* the coordinates x and y. The new grid is still cartesian but no more equally-spaced. This *stretching* transformation is particularly easy since the transformation functions of the two coordinates are decoupled. To obtain the flowfield in the physical plane, where the grid is curvilinear orthogonal in order to be well adapted to the geometry of the body, the transformation function $z = z(\zeta)$ is needed. In two-dimensional problems a powerful tool to create orthogonal grids around difficult bodies is represented by *conformal mapping* [55, 62]. For an orthogonal frame obtained by conformal mapping of the intermediate frame ζ onto the physical plane z, we can use the notations [53]:

$$g = \frac{d\zeta}{dz} = Ge^{-i\alpha} = \xi_x + i\eta_x = -i\xi_y + \eta_y$$

$$\phi = \phi_1 + i\phi_2 = \frac{d\log g}{d\zeta} = \frac{G_\xi}{G} - i\alpha_\xi = -i\frac{G_\eta}{G} - \alpha_\eta = -\alpha_\eta - i\alpha_\xi$$

where α is the same variable used in Eqs. (B.2) and (B.3), that is the angle between the two frames.

Now the system of Eqs. (B.10) must be explicitly expressed in terms of derivatives in the intermediate ζ plane. To do so, we note that for a scalar f the following relation holds:

$$\nabla f = f_x\mathbf{i} + f_y\mathbf{j} = G(f_\xi\mathbf{n} + f_\eta\boldsymbol{\tau})$$

where $\mathbf{n}$ and $\boldsymbol{\tau}$ are now unit vectors along the coordinate lines η and ξ, respectively. It is now possible to write the Eqs. (B.10) in the intermediate plane (ξ, η):

$$
\begin{aligned}
U_1 &= \frac{G}{2}(u+a)\left[(b+u)_\xi - \frac{a}{\gamma R}s_\xi + \frac{a}{\gamma R}\sum Q_i y_{i,\xi} + c_{12}b_\xi\right] + \\
&+ \frac{G}{2}v\left[(b+u)_\eta - \frac{a}{\gamma R}s_\eta + \frac{a}{\gamma R}\sum Q_i y_{i,\eta} + c_{12}b_\eta\right] \\
U_2 &= \frac{G}{2}(u-a)\left[(b-u)_\xi - \frac{a}{\gamma R}s_\xi + \frac{a}{\gamma R}\sum Q_i y_{i,\xi} + c_{12}b_\xi\right] + \\
&+ \frac{G}{2}v\left[(b-u)_\eta - \frac{a}{\gamma R}s_\eta + \frac{a}{\gamma R}\sum Q_i y_{i,\eta} + c_{12}b_\eta\right] \\
U_3 &= \frac{G}{2}u\left[(b+v)_\xi - \frac{a}{\gamma R}s_\xi + \frac{a}{\gamma R}\sum Q_i y_{i,\xi} + c_{12}b_\xi\right] + \\
&+ \frac{G}{2}(v+a)\left[(b+v)_\eta - \frac{a}{\gamma R}s_\eta + \frac{a}{\gamma R}\sum Q_i y_{i,\eta} + c_{12}b_\eta\right] \\
U_4 &= \frac{G}{2}u\left[(b-v)_\xi - \frac{a}{\gamma R}s_\xi + \frac{a}{\gamma R}\sum Q_i y_{i,\xi} + c_{12}b_\xi\right] + \\
&+ \frac{G}{2}(v-a)\left[(b-v)_\eta - \frac{a}{\gamma R}s_\eta + \frac{a}{\gamma R}\sum Q_i y_{i,\eta} + c_{12}b_\eta\right] \\
U_5 &= \frac{G}{2}u\left[b_\xi - \frac{a}{\gamma R}s_\xi + \frac{a}{\gamma R}\sum Q_i y_{i,\xi} + c_{12}b_\xi\right] + \\
&+ \frac{G}{2}v\left[b_\eta - \frac{a}{\gamma R}s_\eta + \frac{a}{\gamma R}\sum Q_i y_{i,\eta} + c_{12}b_\eta\right] \\
U_6 &= G(us_\xi + vs_\eta) \\
U_{7,i} &= G(uy_{i,\xi} + vy_{i,\eta}), \qquad i = 1, ..., N^{'} \\
\beta &= G(u\alpha_\xi + v\alpha_\eta) \\
F &= -aG(v\alpha_\xi - u\alpha_\eta)
\end{aligned}
\tag{B.12}
$$

Now the derivatives expressed in the intermediate plane $\zeta = (\xi, \eta)$ must be transformed into derivatives expressed in the computational plane $\hat{z} = (\hat{x}, \hat{y})$. Noting that:

$$f_\xi = f_{\hat{x}}\hat{x}_\xi, \qquad f_\eta = f_{\hat{y}}\hat{y}_\eta$$

we can finally write the Eqs. (B.12) in the computational plane:

$$
\begin{aligned}
U_1 &= \frac{1}{2}\lambda_1^x\left[(R_1^x)_{\hat{x}} - \frac{a}{\gamma R}s_{\hat{x}} + \frac{a}{\gamma R}\sum Q_i y_{i,\hat{x}} + c_{12}b_{\hat{x}}\right] + \\
&+ \frac{1}{2}\lambda_3^y\left[(R_1^x)_{\hat{y}} - \frac{a}{\gamma R}s_{\hat{y}} + \frac{a}{\gamma R}\sum Q_i y_{i,\hat{y}} + c_{12}b_{\hat{y}}\right] \\
U_2 &= \frac{1}{2}\lambda_2^x\left[(R_2^x)_{\hat{x}} - \frac{a}{\gamma R}s_{\hat{x}} + \frac{a}{\gamma R}\sum Q_i y_{i,\hat{x}} + c_{12}b_{\hat{x}}\right] + \\
&+ \frac{1}{2}\lambda_3^y\left[(R_2^x)_{\hat{y}} - \frac{a}{\gamma R}s_{\hat{y}} + \frac{a}{\gamma R}\sum Q_i y_{i,\hat{y}} + c_{12}b_{\hat{y}}\right] \\
U_3 &= \frac{1}{2}\lambda_3^x\left[(R_1^y)_{\hat{x}} - \frac{a}{\gamma R}s_{\hat{x}} + \frac{a}{\gamma R}\sum Q_i y_{i,\hat{x}} + c_{12}b_{\hat{x}}\right] + \\
&+ \frac{1}{2}\lambda_1^y\left[(R_1^y)_{\hat{y}} - \frac{a}{\gamma R}s_{\hat{y}} + \frac{a}{\gamma R}\sum Q_i y_{i,\hat{y}} + c_{12}b_{\hat{y}}\right] \\
U_4 &= \frac{1}{2}\lambda_3^x\left[(R_2^y)_{\hat{x}} - \frac{a}{\gamma R}s_{\hat{x}} + \frac{a}{\gamma R}\sum Q_i y_{i,\hat{x}} + c_{12}b_{\hat{x}}\right] + \\
&+ \frac{1}{2}\lambda_2^y\left[(R_2^y)_{\hat{y}} - \frac{a}{\gamma R}s_{\hat{y}} + \frac{a}{\gamma R}\sum Q_i y_{i,\hat{y}} + c_{12}b_{\hat{y}}\right] \\
U_5 &= \frac{1}{2}\lambda_3^x\left[\left(\frac{R_1^x + R_2^x}{2}\right)_{\hat{x}} - \frac{a}{\gamma R}s_{\hat{x}} + \frac{a}{\gamma R}\sum Q_i y_{i,\hat{x}} + c_{12}b_{\hat{x}}\right] + \\
&+ \frac{1}{2}\lambda_3^y\left[\left(\frac{R_1^y + R_2^y}{2}\right)_{\hat{y}} - \frac{a}{\gamma R}s_{\hat{y}} + \frac{a}{\gamma R}\sum Q_i y_{i,\hat{y}} + c_{12}b_{\hat{y}}\right] \\
U_6 &= \lambda_3^x s_{\hat{x}} + \lambda_3^x s_{\hat{y}} \\
U_{7,i} &= \lambda_3^x y_{i,\hat{x}} + \lambda_3^x y_{i,\hat{y}}, \qquad i = 1, ..., N' \\
\beta &= \lambda_3^x \alpha_{\hat{x}} + \lambda_3^y \alpha_{\hat{y}} \\
F &= -\frac{1}{2}\left[(\lambda_2^x - \lambda_1^x)v\alpha_{\hat{x}} - (\lambda_2^y - \lambda_1^y)u\alpha_{\hat{y}}\right]
\end{aligned}
$$

where:

$$\lambda_1^x = G\hat{x}_\xi(u+a) \qquad \lambda_2^x = G\hat{x}_\xi(u-a) \qquad \lambda_3^x = G\hat{x}_\xi u$$

$$\lambda_1^y = G\hat{y}_\eta(v+a) \qquad \lambda_2^y = G\hat{y}_\eta(v-a) \qquad \lambda_3^y = G\hat{y}_\eta v$$

and

$$R_1^x = b + u \qquad R_2^x = b - u$$

$$R_1^y = b + v \qquad R_2^y = b - v$$

It is now convenient to express in each equation the terms containing the same $\lambda_i^{x,y}$ in order to approximate the derivatives with *upwind* differences, either forward or backward according to the sign of $\lambda_i^{x,y}$. By letting:

$$\begin{aligned}
f_1^x &= -\frac{1}{2}\lambda_1^x \left[(R_1^x)_{\hat{x}} - v\alpha_{\hat{x}} - \frac{a}{\gamma R} s_{\hat{x}} + \frac{a}{\gamma R} \sum Q_i y_{i,\hat{x}} + c_{12} b_{\hat{x}} \right] \\
f_2^x &= -\frac{1}{2}\lambda_2^x \left[(R_2^x)_{\hat{x}} + v\alpha_{\hat{x}} - \frac{a}{\gamma R} s_{\hat{x}} + \frac{a}{\gamma R} \sum Q_i y_{i,\hat{x}} + c_{12} b_{\hat{x}} \right] \\
f_3^x &= -\lambda_3^x (v_{\hat{x}} + u\alpha_{\hat{x}}) \qquad \text{(B.13)} \\
f_4^x &= -\lambda_3^x s_{\hat{x}} \\
f_i^x &= -\lambda_3^x y_{i,\hat{x}}, \qquad i = 1, ..., N'
\end{aligned}$$

and

$$\begin{aligned}
f_1^y &= -\frac{1}{2}\lambda_1^y \left[(R_1^y)_{\hat{y}} + u\alpha_{\hat{y}} - \frac{a}{\gamma R} s_{\hat{y}} + \frac{a}{\gamma R} \sum Q_i y_{i,\hat{y}} + c_{12} b_{\hat{y}} \right] \\
f_2^y &= -\frac{1}{2}\lambda_2^y \left[(R_2^y)_{\hat{y}} - u\alpha_{\hat{y}} - \frac{a}{\gamma R} s_{\hat{y}} + \frac{a}{\gamma R} \sum Q_i y_{i,\hat{y}} + c_{12} b_{\hat{y}} \right] \\
f_3^y &= -\lambda_3^y (u_{\hat{y}} - v\alpha_{\hat{y}}) \qquad \text{(B.14)} \\
f_4^y &= -\lambda_3^y s_{\hat{y}} \\
f_i^y &= -\lambda_3^y y_{i,\hat{y}}, \qquad i = 1, ..., N'
\end{aligned}$$

Finally the system can be written in its final form:

$$\begin{cases} b_t = c_1 \left(f_1^x + f_2^x + f_1^y + f_2^y + V_b^{'} + \dfrac{a}{\gamma R} s_t - \dfrac{a}{\gamma R} \sum Q_i y_{i,t} \right) \\ u_t = f_1^x - f_2^x + f_3^y + V_u \\ v_t = f_1^y - f_2^y + f_3^x + V_v \\ s_t = f_4^x + f_4^y + V_s \\ y_{i,t} = f_i^x + f_i^y + V_{y_i}, \qquad i = 1, ..., N^{'} \end{cases} \tag{B.15}$$

we recall the expression of the source terms:

$$\begin{aligned} V_b^{'} &= V_b + \frac{a}{\gamma R} \sum Q_i V_{y_i} = \frac{1}{c_1}\beta + \frac{a}{\gamma R}(\gamma - 1) V_s + \frac{a}{\gamma R} \sum Q_i V_{y_i} \\ V_u &= \mathbf{V}_m \cdot \mathbf{n} = \frac{1}{\rho}(\nabla \cdot \mathbf{T}) \cdot \mathbf{n} \\ V_v &= \mathbf{V}_m \cdot \boldsymbol{\tau} = \frac{1}{\rho}(\nabla \cdot \mathbf{T}) \cdot \boldsymbol{\tau} \\ V_s &= -\frac{1}{T} \sum \mu_i V_{y_i} + \frac{R}{p}(-\nabla \cdot \mathbf{q} + \nabla \mathbf{v} : \mathbf{T}) \\ V_{y_i} &= \frac{\dot{w}_i}{\rho} - \frac{1}{\rho} \nabla \cdot \mathbf{j}_i \end{aligned} \tag{B.16}$$

with:

$$\mathbf{T} = \frac{1}{Re_r} \mu \left[-\frac{2}{3}(\nabla \cdot \mathbf{v})\mathbf{I} + \nabla \mathbf{v} + (\nabla \mathbf{v})^T \right] \tag{B.17}$$

$$\mathbf{q} = -\frac{\gamma_r}{\gamma_r - 1} \frac{1}{Re_r P_r} k \nabla T - \frac{1}{Le_r Re_r Pr_r} \sum \rho \mathcal{D} h_i \nabla y_i \tag{B.18}$$

$$\mathbf{j}_i = -\frac{1}{Pr_r Le_r Re_r} \rho \mathcal{D}_{im} \nabla y_i \tag{B.19}$$

To complete the transformation from the physical plane to the computational plane the viscous terms must be transformed in terms of derivatives in the computational plane. It is therefore necessary to express $\nabla \cdot \mathbf{q}$, $\nabla \cdot \mathbf{j}_i$, $(\nabla \cdot \mathbf{T}) \cdot \mathbf{n}$, $(\nabla \cdot \mathbf{T}) \cdot \boldsymbol{\tau}$, and $\Phi = \nabla \mathbf{v} : \mathbf{T}$ in the computational plane.

The following expressions are taken from [59] and [47]. Firstly $\nabla\mathbf{v}$ is evaluated:

$$\begin{aligned}\nabla\mathbf{v} &= G(\mathbf{v}_\xi\mathbf{n}+\mathbf{v}_\eta\boldsymbol{\tau}) = \\ &= G\left[(u\mathbf{n}+v\boldsymbol{\tau})_\xi\mathbf{n}+(u\mathbf{n}+v\boldsymbol{\tau})_\eta\boldsymbol{\tau}\right] = \\ &= G\left[(u_\xi-v\alpha_\xi)\mathbf{nn}+(u_\eta-v\alpha_\eta)\mathbf{n}\boldsymbol{\tau}+(v_\xi+u\alpha_\xi)\boldsymbol{\tau}\mathbf{n}+(v_\eta+u\alpha_\eta)\boldsymbol{\tau}\boldsymbol{\tau}\right]\end{aligned}$$

now letting:

$$\begin{aligned}e_{11} &= G(u_\xi-v\alpha_\xi) = G(\hat{x}_\xi u_{\hat{x}}+v\phi_2) \\ e_{12} &= \frac{1}{2}G(u_\eta+v_\xi-v\alpha_\eta+u\alpha_\xi) = \frac{1}{2}G(\hat{y}_\eta u_{\hat{y}}+\hat{x}_\xi v_{\hat{x}}+v\phi_1-u\phi_2) \\ e_{22} &= G(v_\eta+u\alpha_\eta) = G(\hat{y}_\eta v_{\hat{y}}-u\phi_1)\end{aligned}$$

The following expressions hold:

$$\nabla\mathbf{v}+(\nabla\mathbf{v})^T = 2\left[e_{11}\mathbf{nn}+e_{12}(\mathbf{n}\boldsymbol{\tau}+\boldsymbol{\tau}\mathbf{n})+e_{22}\boldsymbol{\tau}\boldsymbol{\tau}\right] \tag{B.20}$$

$$\nabla\cdot\mathbf{v} = e_{11}+e_{22} \tag{B.21}$$

therefore we can express the viscous stress tensor from Eq. (B.17):

$$\mathbf{T} = T_{11}\mathbf{nn}+T_{12}(\mathbf{n}\boldsymbol{\tau}+\boldsymbol{\tau}\mathbf{n})+T_{22}\boldsymbol{\tau}\boldsymbol{\tau}$$

where:

$$\begin{aligned}T_{11} &= \frac{2\mu}{3Re_r}(2e_{11}-e_{22}) \\ T_{12} &= \frac{2\mu}{3Re_r}e_{12} \\ T_{22} &= \frac{2\mu}{3Re_r}(2e_{22}-e_{11})\end{aligned}$$

finally obtaning, using (B.1):

$$\begin{aligned}\nabla\cdot\mathbf{T} &= \nabla\cdot\left[T_{11}\mathbf{nn}+T_{12}(\mathbf{n}\boldsymbol{\tau}+\boldsymbol{\tau}\mathbf{n})+T_{22}\boldsymbol{\tau}\right] = \\ &= G\left[T_{11\xi}\mathbf{n}+T_{11}(\alpha_\xi\boldsymbol{\tau}+\alpha_\eta\mathbf{n})+T_{12\xi}\boldsymbol{\tau}+\right. \\ &\quad \left.+T_{12\eta}\mathbf{n}+2T_{12}(\alpha_\eta\boldsymbol{\tau}-\alpha_\xi\mathbf{n})+T_{22\eta}\boldsymbol{\tau}-T_{22}(\alpha_\xi\boldsymbol{\tau}+\alpha_\eta\mathbf{n})\right] = \\ &= G\left[\hat{x}_\xi T_{11\hat{x}}+\hat{y}_\eta T_{12\hat{y}}-(T_{11}-T_{22})\phi_1+2T_{12}\phi_2\right]\mathbf{n}+ \\ &+ G\left[\hat{x}_\xi T_{12\hat{x}}+\hat{y}_\eta T_{22\hat{y}}-(T_{11}-T_{22})\phi_2+2T_{12}\phi_1\right]\boldsymbol{\tau}\end{aligned} \tag{B.22}$$

and from the symmetry of $\mathbf{T}$:

$$\nabla\mathbf{v}:\mathbf{T} = \frac{1}{2}(\nabla\mathbf{v}+\nabla\mathbf{v}^T):\mathbf{T} = T_{11}e_{11}+2T_{12}e_{12}+T_{22}e_{22}$$

from which we obtain the expression of Φ:

$$\Phi = \frac{\mu}{Re_r}\left[2(e_{11}^2 + 2e_{12}^2 + e_{22}^2) - \frac{2}{3}(e_{11}+e_{22})^2\right] \tag{B.23}$$

Finally, we obtain the heat flux vector (B.18) and the mass flux vector (B.19) and their divergence. The heat flux vector $\mathbf{q}$ becomes:

$$\begin{aligned}
\mathbf{q} &= q_1\mathbf{n} + q_2\boldsymbol{\tau} \\
q_1 &= -G\left[\frac{\gamma_r}{\gamma_r - 1}\frac{k}{Re_r Pr_r}\hat{x}_\xi T_{\hat{x}} + \frac{1}{Le_r Re_r Pr_r}\sum \rho\mathcal{D}\hat{x}_\xi h_i y_{i,\hat{x}}\right] \\
q_2 &= -G\left[\frac{\gamma_r}{\gamma_r - 1}\frac{k}{Re_r Pr_r}\hat{y}_\eta T_{\hat{y}} + \frac{1}{Le_r Re_r Pr_r}\sum \rho\mathcal{D}h_i\hat{y}_\eta y_{i,\hat{y}}\right]
\end{aligned}$$

and its divergence, using (B.1):

$$\begin{aligned}
\nabla\cdot\mathbf{q} &= \nabla q_1\cdot\mathbf{n} + \nabla q_2\cdot\boldsymbol{\tau} + q_1\nabla\cdot\mathbf{n} + q_2\nabla\cdot\boldsymbol{\tau} = \\
&= G(q_{1\xi} + q_{2\eta} + q_1\alpha_\eta + q_2\alpha_\xi) = \\
&= G(\hat{x}_\xi q_{1\hat{x}} + \hat{y}_\eta q_{2\hat{y}} - q_1\phi_1 + q_2\phi_2)
\end{aligned} \tag{B.24}$$

The mass flux vector $\mathbf{j}_i$ is:

$$\begin{aligned}
\mathbf{j}_i &= j_{i1}\mathbf{n} + j_{i2}\boldsymbol{\tau} \\
j_{i1} &= -\frac{G}{Pr_r Re_r Le_r}\rho\mathcal{D}\hat{x}_\xi y_{i\hat{x}} \\
j_{i2} &= -\frac{G}{Pr_r Re_r Le_r}\rho\mathcal{D}\hat{y}_\eta y_{i\hat{y}}
\end{aligned}$$

and its divergence:

$$\nabla\cdot\mathbf{j}_i = G(\hat{x}_\xi j_{i1\hat{x}} + \hat{y}_\eta j_{i2\hat{y}} - j_{i1}\phi_1 + j_{i2}\phi_2) \tag{B.25}$$

The source terms $V_b^{'}$, $\mathbf{V}_m$, V_s, and V_{y_i} can be finally evaluated in the computational plane $\hat{z}$ with the use of Eqs. (B.22), (B.23), (B.24) and (B.25).

B.3 Two-Dimensional axisymmetric problems

The same two-dimensional equations (A.20) can be used for axisymmetric problem with the addition of some terms; therefore the effect of axisymmetry is treated as a source term. The axisymmetric operators (gradient, divergence, etc.), denoted with $()_a$, can be expressed as a function their planar counterpart, denoted with $()_p$. Following the work presented [59] and [47], the final results are shown here.

We now introduce three unit vectors **i**, **j**, and **k** along the axial, radial, and azimuthal direction, respectively, to define a cartesian frame in the physical plane. Using the relations between planar and axisymmetric operators, the equations of motion (A.20) remain unchanged for the axisymmetric problem, except for the second of (A.20), which has the added term $\frac{a}{y}(\mathbf{v}\cdot\mathbf{j})$ on the right-end side, and the source terms, whose expression is illustrated below. In the computational plane, the first of (B.15) becomes:

$$(b_t)_a = (b_t)_p + c_1 A$$

where:

$$\begin{aligned} A &= a e_{33} \qquad\qquad (B.26)\\ e_{33} &= \frac{\mathbf{v}\cdot\mathbf{j}}{y} = \frac{u\sin\alpha + v\cos\alpha}{y} \end{aligned}$$

Now the viscous terms must be derived for the axisymmetric case. Noting that:

$$(\nabla\mathbf{v})_a = (\nabla\mathbf{v})_p + e_{33}\mathbf{kk}$$

the (B.20-B.21) become:

$$\begin{aligned} (\nabla\mathbf{v} + \nabla\mathbf{v}^T)_a &= (\nabla\mathbf{v} + \nabla\mathbf{v}^T)_p + 2e_{33}\mathbf{kk}\\ (\nabla\cdot\mathbf{v})_a &= (\nabla\cdot\mathbf{v})_p + e_{33} \end{aligned}$$

consequently we can express $\mathbf{T}$ from Eq. (B.17):

$$\mathbf{T} = (T_{11})_a\mathbf{nn} + (T_{12})_a(\mathbf{n}\boldsymbol{\tau} + \boldsymbol{\tau}\mathbf{n}) + (T_{22})_a\boldsymbol{\tau}\boldsymbol{\tau} + (T_{33})_a\mathbf{kk}$$

where:

$$\begin{aligned} (T_{11})_a &= \frac{2\mu}{3Re_r}(2e_{11} - e_{22} - e_{33})\\ (T_{12})_a &= \frac{2\mu}{3Re_r}e_{12}\\ (T_{22})_a &= \frac{2\mu}{3Re_r}(2e_{22} - e_{11} - e_{33})\\ (T_{33})_a &= \frac{2\mu}{3Re_r}(2e_{33} - e_{11} - e_{22}) \end{aligned}$$

Finally we obtain the expression for Φ:

$$(\Phi)_a = (\Phi)_p + \frac{4\mu}{3Re_r}\left[e_{33}^2 - e_{33}(e_{11} + e_{22})\right]$$

and for the source term V_s from (B.16):

$$\begin{aligned}(V_s)_p &= -\frac{1}{T}\sum \mu_i (V_{yi})_p + \frac{R}{p}\left[(\Phi)_p - (\nabla\cdot\mathbf{q})_p\right] \\ (V_s)_a &= -\frac{1}{T}\sum \mu_i (V_{yi})_a + \frac{R}{p}\left[(\Phi)_a - (\nabla\cdot\mathbf{q})_p + \frac{1}{y}(q_1\cos\alpha + q_2\sin\alpha)\right]\end{aligned}$$

and for the source term V_{yi} from (B.16):

$$\begin{aligned}(V_{yi})_p &= \frac{\dot{w}_i}{\rho} - \frac{1}{\rho}(\nabla\cdot\mathbf{j}_i)_p \\ (V_{yi})_a &= \frac{\dot{w}_i}{\rho} - \frac{1}{\rho}\left[(\nabla\cdot\mathbf{j}_i)_p + \frac{1}{y}(j_{i1}\cos\alpha + j_{i2}\sin\alpha)\right]\end{aligned}$$

Note that $(\mathbf{q})_a = (\mathbf{q})_p$ and $(\mathbf{j}_i)_a = (\mathbf{j}_i)_p$, since $(\nabla f)_a = (\nabla f)_p$ for a generic scalar f. Lastly we must derive the expression for $\mathbf{V}_m$:

$$(\mathbf{V}_m)_p = \frac{1}{\rho}(\nabla\cdot\mathbf{T})_p \tag{B.27}$$

now lettting:

$$\begin{aligned}T_{xy} &= (\mathbf{T}\cdot\mathbf{i})\cdot\mathbf{j} = T_{11}\sin\alpha\cos\alpha + T_{12}(\cos^2\alpha - \sin^2\alpha) - T_{22}\sin\alpha\cos\alpha \\ T_{yy} &= (\mathbf{T}\cdot\mathbf{j})\cdot\mathbf{j} = T_{11}\sin^2\alpha + 2T_{12}\sin\alpha\cos\alpha - T_{22}\cos^2\alpha\end{aligned}$$

the following relation is obtained:

$$\begin{aligned}(\mathbf{V}_m)_a = (\mathbf{V}_m)_p &+ \frac{1}{\rho y}\left[T_{xy}\cos\alpha + (T_{yy} - T_{33})\sin\alpha\right]\mathbf{n} + \\ &- \frac{1}{\rho y}\left[T_{xy}\sin\alpha + (T_{33} - T_{yy})\cos\alpha\right]\boldsymbol{\tau}\end{aligned}$$

and expressing the terms explicitly:

$$\begin{aligned}(\mathbf{V}_m)_a = (\mathbf{V}_m)_p &+ \frac{2\mu}{\rho R e_r}\left[\frac{(e_{11} - e_{33})\sin\alpha + e_{12}\cos\alpha}{y}\right]\mathbf{n} + \\ &+ \frac{2\mu}{\rho R e_r}\left[\frac{(e_{22} - e_{33})\cos\alpha + e_{12}\sin\alpha}{y}\right]\boldsymbol{\tau}\end{aligned}$$

The axisymmetric expression for the source terms $(V_s)_a$, $(V_{yi})_a$, and $(\mathbf{V}_m)_a$ have been obtained.

B.4 Time-marching finite difference method

The code is based on the explicit two-level (*predictor-corrector*) scheme [52, 54], patterned on the well-known MacCormack scheme and having second-order accuracy in both space and time. The convective terms are discretized with *upwind* differences, either forward or backward according to the sign of $\lambda_i^{x,y}$. The diffusive terms are treated as source terms, discretized explicitly by second-order *central* differences.

Let $t = k\Delta t$, $\hat{x} = n\Delta\hat{x}$, and $\hat{y} = m\Delta\hat{y}$. Knowing all the values at level k, solution at level $k + 1/2$ (***predictor***) is obtained as follows:

$$\begin{cases} (y_i)_{nm}^{k+\frac{1}{2}} = (y_i)_{nm}^{k} + (y_{i,t})_{nm}^{k}\frac{\Delta t}{2} \\ (s)_{nm}^{k+\frac{1}{2}} = (s)_{nm}^{k} + (s_t)_{nm}^{k}\frac{\Delta t}{2} \\ (b)_{nm}^{k+\frac{1}{2}} = (b)_{nm}^{k} + (b_t)_{nm}^{k}\frac{\Delta t}{2} \\ (u)_{nm}^{k+\frac{1}{2}} = (u)_{nm}^{k} + (u_t)_{nm}^{k}\frac{\Delta t}{2} \\ (v)_{nm}^{k+\frac{1}{2}} = (v)_{nm}^{k} + (v_t)_{nm}^{k}\frac{\Delta t}{2} \end{cases} \tag{B.28}$$

To evaluate the time derivatives $(y_{i,t})_{nm}^{k}$, $(s_t)_{nm}^{k}$, $(b_t)_{nm}^{k}$, $(u_t)_{nm}^{k}$, and $(v_t)_{nm}^{k}$ at level k, the (B.15) are used. Only the discretized form of f_1^x is shown here since the other quantities f_p^q $(p = 1, 2, 3, 4, i;\ q = x, y)$ are discretized following the same logic. The f_1^x approximation at the first level (*predictor*) is the following:

$$\begin{aligned} (f_1^x)_{nm}^{k} = &-\frac{1}{4\Delta\hat{x}}\left[(\lambda_1^x)_{n'm}^{k} + (\lambda_1^x)_{n''m}^{k}\right]\left[(R_1^x)_{n'm}^{k} - (R_1^x)_{n''m}^{k}\right] + \\ &+\frac{1}{4\Delta\hat{x}}\left[(\lambda_1^x)_{n'm}^{k}(v)_{n'm}^{k} + (\lambda_1^x)_{n''m}^{k}(v)_{n''m}^{k}\right]\left[(\alpha)_{n'm}^{k} - (\alpha)_{n''m}^{k}\right] + \\ &+\frac{1}{4\Delta\hat{x}}\left[(\lambda_1^x)_{n'm}^{k}(\frac{a}{\gamma R})_{n'm}^{k} + (\lambda_1^x)_{n''m}^{k}(\frac{a}{\gamma R})_{n''m}^{k}\right]\left[(s)_{n'm}^{k} - (s)_{n''m}^{k}\right] + \\ &-\frac{1}{4\Delta\hat{x}}\sum_i\left[(\lambda_1^x)_{n'm}^{k}(\frac{aQ_i}{\gamma R})_{n'm}^{k} + (\lambda_1^x)_{n''m}^{k}(\frac{aQ_i}{\gamma R})_{n''m}^{k}\right]\left[(y_i)_{n'm}^{k} - (y_i)_{n''m}^{k}\right] + \\ &-\frac{1}{4\Delta\hat{x}}\left[(\lambda_1^x)_{n'm}^{k}(c_{12})_{n'm}^{k} + (\lambda_1^x)_{n''m}^{k}(c_{12})_{n''m}^{k}\right]\left[(b)_{n'm}^{k} - (b)_{n''m}^{k}\right] \end{aligned} \tag{B.29}$$

where the index n' and n'' are defined as follows:

$$(\lambda_1^x)_{nm}^{k} \geq 0 \ \Rightarrow \begin{cases} n' = n \\ n'' = n-1 \end{cases} \qquad (\lambda_1^x)_{nm}^{k} < 0 \ \Rightarrow \begin{cases} n' = n+1 \\ n'' = n \end{cases}$$

The Eq. (B.29) is obtained from the first of (B.13) discretizing the spatial derivatives with *upwind* differences, either forward or backward according to the sign

of $(\lambda_1^x)_{nm}^k$. The terms multiplying the space derivatives are substituted with their average value between the two nodes. A special treatment is needed when the sign of $(\lambda_1^x)_{nm}^k$ changes between n' and n''. In that case the local value of $(\lambda_1^x)_{nm}^k$ is used and the (B.29) becomes:

$$\begin{aligned}(f_1^x)_{nm}^k = &-\frac{1}{2\Delta\hat{x}}(\lambda_1^x)_{nm}^k\left[(R_1^x)_{n'm}^k-(R_1^x)_{n''m}^k\right]+\\ &+\frac{1}{2\Delta\hat{x}}(\lambda_1^x)_{nm}^k(v)_{nm}^k\left[(\alpha)_{n'm}^k-(\alpha)_{n''m}^k\right]+\\ &+\frac{1}{2\Delta\hat{x}}(\lambda_1^x)_{nm}^k(\frac{a}{\gamma R})_{nm}^k\left[(s)_{n'm}^k-(s)_{n''m}^k\right]+\\ &-\frac{1}{2\Delta\hat{x}}\sum_i(\lambda_1^x)_{nm}^k(\frac{aQ_i}{\gamma R})_{nm}^k\left[(y_i)_{n'm}^k-(y_i)_{n''m}^k\right]+\\ &-\frac{1}{2\Delta\hat{x}}(\lambda_1^x)_{nm}^k(c_{12})_{nm}^k\left[(b)_{n'm}^k-(b)_{n''m}^k\right]\end{aligned} \tag{B.30}$$

The diffusive terms, according to their nature, are discretized by central differences [56]. For example, the mass flux vector components j_{i1} and j_{i2} are discretized as follows:

$$\begin{aligned}(j_{i1})_{nm}^k &= -\frac{(G)_{nm}}{Pr_rRe_rLe_r}(\rho)_{nm}^k(\mathcal{D})_{nm}^k(\hat{x}_\xi)_n\frac{(y_i)_{n'm}^k-(y_i)_{n''m}^k}{2\Delta\hat{x}}\\ (j_{i2})_{nm}^k &= -\frac{(G)_{nm}}{Pr_rRe_rLe_r}(\rho)_{nm}^k(\mathcal{D})_{nm}^k(\hat{y}_\eta)_m\frac{(y_i)_{nm'}^k-(y_i)_{nm''}^k}{2\Delta\hat{y}}\end{aligned}$$

and the divergence of the mass flux vector $\mathbf{j}_i$ is:

$$\begin{aligned}(\nabla\cdot\mathbf{j}_i)_{nm}^k = (G)_{nm}\Bigg[&(\hat{x}_\xi)_n\frac{(j_{i1})_{n'm}^k-(j_{i1})_{n''m}^k}{2\Delta\hat{x}}-(j_{i1})_{nm}^k(\phi_1)_{nm}+\\ &+(\hat{y}_\eta)_m\frac{(j_{i2})_{nm'}^k-(j_{i2})_{nm''}^k}{2\Delta\hat{y}}+(j_{i2})_{nm}^k(\phi_2)_{nm}\Bigg]\end{aligned} \tag{B.31}$$

with

$$\begin{cases} n'=n+1\\ n''=n-1\end{cases}\qquad\qquad\begin{cases} m'=m+1\\ m''=m-1\end{cases}$$

All the other diffusive terms are evaluated following the same logic. Finally, the terms which do not contain space derivatives, such the chemical source term (A.9) or the added term for axisymmetric problems (B.26), are explicitly evaluated at level k. To summarize, the time derivatives at level k can be evaluated using the (B.15) and expressions like (B.29) and (B.31) for the convective terms and the

diffusive terms, respectively. Finally (B.28) can be used to obtain the values at level $k+1/2$. Note that since the variable b is an implicit function of temperature, the value of T at level $k+1/2$ is obtained from the value of b at the same level using the Newton's iterative procedure. From the knowledge of $(T)_{nm}^{k+1/2}$ and of $(y_i)_{nm}^{k+1/2}$, the ratio of specific heats $(\gamma)_{nm}^{k+1/2}$ and the frozen speed of sound $(a)_{nm}^{k+1/2}$ can be evaluated.

Solution at the second level $k+1$ (***corrector***) is obtained using the same equations (B.28), with $k+1/2$ instead of k:

$$\begin{cases} (y_i)_{nm}^{k+1} = (y_i)_{nm}^{k+\frac{1}{2}} + (y_{i,t})_{nm}^{k+\frac{1}{2}} \frac{\Delta t}{2} \\ (s)_{nm}^{k+1} = (s)_{nm}^{k+\frac{1}{2}} + (s_t)_{nm}^{k+\frac{1}{2}} \frac{\Delta t}{2} \\ (b)_{nm}^{k+1} = (b)_{nm}^{k+\frac{1}{2}} + (b_t)_{nm}^{k+\frac{1}{2}} \frac{\Delta t}{2} \\ (u)_{nm}^{k+1} = (u)_{nm}^{k+\frac{1}{2}} + (u_t)_{nm}^{k+\frac{1}{2}} \frac{\Delta t}{2} \\ (v)_{nm}^{k+1} = (v)_{nm}^{k+\frac{1}{2}} + (v_t)_{nm}^{k+\frac{1}{2}} \frac{\Delta t}{2} \end{cases} \tag{B.32}$$

The time derivatives at level $k+1/2$, needed to obtain the solution at level $k+1$, are obtained from the (B.15) with F_p^q instead of f_p^q. The F_p^q are defined as follows:

$$\begin{aligned} (F_p^x)_{nm}^{k+\frac{1}{2}} &= 2(f_p^x)_{nm}^{k+\frac{1}{2}} - (f_p^x)_{n'm}^{k} \\ (F_p^y)_{nm}^{k+\frac{1}{2}} &= 2(f_p^y)_{nm}^{k+\frac{1}{2}} - (f_p^y)_{nm'}^{k} \end{aligned} \tag{B.33}$$

where

$$\begin{aligned} (\lambda_p^x)_{nm}^k > 0 \Rightarrow n' = n-1 \qquad & (\lambda_p^x)_{nm}^k < 0 \Rightarrow n' = n+1 \\ (\lambda_p^y)_{nm}^k > 0 \Rightarrow m' = m-1 \qquad & (\lambda_p^y)_{nm}^k < 0 \Rightarrow m' = n+1 \end{aligned}$$

The diffusive terms are evaluated with expressions like (B.31) with $k+1/2$ instead of k. In the discretized form of the equations, the metric terms are also present: $(G)_{nm}$, $(\alpha)_{nm}$ $(\phi_1)_{nm}$, and $(\phi_2)_{nm}$. Their expression in discrete form can be found in [59].

Thanks to the B.33, the technique is second-order accurate both in space and time even if two-nodes finite differences are being used. The method has some advantages over other techniques. One is simplicity, which is also responsible for reducing computational time. Another is easiness in handling boundary points and boundary conditions. Both sets of equations (B.28) and (B.32), in addition to local terms, contain terms (the f_p^q) which express physical contributions from one side or the other. Terms which express contribution from outside, are not computed from inside the computational region. They must be determined using some appropriate, physical boundary condition. The calculation at boundary

points, therefore, is not affected by arbitrariness and no errors are introduced at the boundaries.

The time step Δt is determined from the CFL (Courant-Friedrick-Lewis) condition with a special correction for the viscous case. The time step is evaluated as follows:

$$\Delta t = \frac{c_s}{\hat{\lambda}_{max}\Delta\hat{x}}, \qquad \hat{\lambda}_{max} = max(\lambda_i^x \Delta\hat{x}, \lambda_i^y \Delta\hat{y}), \quad i = 1, ..., 3 \tag{B.34}$$

where c_s is the Courant number of the scheme, limited to 2 as shown in [25] (a typical value is between 0.5 and 2.0). For viscous flows the stability analysis is more complex, and the following expression is used [67]:

$$\Delta t = \frac{c_s}{\tilde{\lambda}_{max}}, \qquad \tilde{\lambda}_{max} = max(\frac{8\Delta x^2}{Re_r}, \frac{\Delta y^2}{Re_r}) \tag{B.35}$$

where Re_r is the reference Reynolds number. The local time step Δt is the smallest among (B.34) and (B.35). For transient problems, the time step must be the same everywhere and therefore the smallest Δt evaluated in the flowfield is used for every node. If steady-state solutions are sought, a way of reducing the computational time consists of using, for each node, the maximum time step permitted by the CFL conditions. A *local* time step, different for each node, is therefore used to speed-up convergence to the steady-state solution. For chemically reacting flows, the computational time can be reduced using special techniques such as *point implicit* or *operator splitting*. Details on these techniques can be found in [58].

Appendix C

Difference form of the in-depth energy equation

The in-depth energy balance in the moving coordinate system has been derived in chapter 1:

$$\rho c_p \left(\frac{\partial T}{\partial t}\right)_x = \frac{1}{A}\frac{\partial}{\partial x}\left(kA\frac{\partial T}{\partial x}\right)_t + \rho c_p \left(\frac{\partial T}{\partial x}\right)_t \dot{s} \qquad \text{(C.1)}$$

which holds for the most general case (variable cross-section area and variable properties). In chapter 2 the finite-difference method for the energy equation has been described for the simpler case of planar surface, constant properties and constant nodal size. Here the difference form of the equation for the most general case represented by Eq. (C.1) will be described.

C.1 Interior nodes

The differential form of Eq. (C.1) is the following:

$$\begin{aligned}\rho_n c_{p_n}\frac{T_n^{'} - T_n}{\Delta t} &= \frac{1}{\Delta x_n A_n}\left[-\alpha_{n+1}(T_n^{'} - T_{n+1}^{'} + T_n - T_{n+1}) + \alpha_{n-1}(T_{n-1}^{'} - T_n^{'} + T_{n-1} - T_n)\right] \\ &+ \frac{\rho_n c_{p_n}\dot{s}}{4\Delta x_n}\left(T_{n+1}^{'} - T_{n-1}^{'} + T_{n+1} - T_{n-1}\right) \qquad \text{(C.2)}\end{aligned}$$

multiplying (C.2) through by $4\Delta x_n \Delta t A_n$ to eliminate the denominators, and collecting all the terms involving the unknowns $T_n^{'}$ on the left hand side results in:

$$\begin{aligned}
-\Delta t(4\alpha_{n-1} - \rho_n c_{p_n} \dot{s} A_n) T_{n-1}^{'} \quad &+ \quad (4\rho_n c_{p_n} \Delta x_n A_n + 4\Delta t \alpha_{n+1} + 4\Delta t \alpha_{n-1}) T_n^{'} \\
-\Delta t(4\alpha_{n+1} + \rho_n c_{p_n} \dot{s} A_n) T_{n+1}^{'} \quad &= \\
\Delta t(4\alpha_{n-1} - \rho_n c_{p_n} \dot{s} A_n) T_{n-1} \quad &+ \quad (4\rho_n c_{p_n} \Delta x_n A_n - 4\Delta t \alpha_{n+1} - 4\Delta t \alpha_{n-1}) T_n \\
+\Delta t(4\alpha_{n+1} + \rho_n c_{p_n} \dot{s} A_n) T_{n+1} &
\end{aligned} \tag{C.3}$$

where:

$$\alpha_{n+1} = \left(\frac{\Delta x_{n+1}}{k_{n+1} A_{n+1}} + \frac{\Delta x_n}{k_n A_n} \right)^{-1}, \qquad \alpha_{n-1} = \left(\frac{\Delta x_{n-1}}{k_{n-1} A_{n-1}} + \frac{\Delta x_n}{k_n A_n} \right)^{-1} \tag{C.4}$$

The terms ρ_n, k_n, and c_{p_n} represent the density, thermal conductivity, and specific heat of the material for the n-node, respectively. The term A_n is the cross-section area of the n-node and Δx_n is the nodal size of the n-node (which is fixed in size but may vary from node to node).

C.2 The surface node

The energy input to the first node ($n = 1$) will be left simply as q_c, which will replace the terms of the form:

$$\alpha_{n+1}(T_n - T_{n+1}) + \alpha_{n-1}(T_{n-1} - T_n) = q_c A_n$$

$$\alpha_{n+1}(T_n^{'} - T_{n+1}^{'}) + \alpha_{n-1}(T_{n-1}^{'} - T_n^{'}) = q_c^{'} A_n$$

Thus we have the energy difference equation for the first node as:

$$\begin{aligned}
\rho_n c_{p_n} \frac{T_n^{'} - T_n}{\Delta t} &= \frac{1}{\Delta x_n A_n} \left[-2\alpha_{n+1}(T_n^{'} - T_{n+1}^{'} + T_n - T_{n+1}) + q_c^{'} A_n + q_c A_n \right] \\
+ \quad \frac{\rho_n c_{p_n} \dot{s}}{4\Delta x_n} &\left[\left(1 - \frac{\alpha_{n+1}}{\alpha_{n-1}} \right) (T_{n+1}^{'} - T_n^{'} + T_{n+1} - T_n) - \frac{A_n}{\alpha_{n-1}} (q_c^{'} + q_c) \right]
\end{aligned} \tag{C.5}$$

multiplying (C.5) through by $4\Delta x_n \Delta t A_n$ to eliminate the denominators, and collecting all the terms involving the unknowns $T_n^{'}$ on the left hand side results in:

$$\begin{aligned}
&\left[4\rho_n c_{p_n}\Delta x_n A_n + 8\Delta t\alpha_{n+1} + \rho_n c_{p_n}\dot{s}\Delta t A_n\left(1-\frac{\alpha_{n+1}}{\alpha_{n-1}}\right)\right] \quad T_n^{'} \\
&\qquad -\Delta t\left[8\alpha_{n+1} + \rho_n c_{p_n}\dot{s}A_n\left(1-\frac{\alpha_{n+1}}{\alpha_{n-1}}\right)\right] \quad T_{n+1}^{'} \quad = \\
&\left[4\rho_n c_{p_n}\Delta x_n A_n - 8\Delta t\alpha_{n+1} - \rho_n c_{p_n}\dot{s}\Delta t A_n\left(1-\frac{\alpha_{n+1}}{\alpha_{n-1}}\right)\right] \quad T_n \\
&\qquad +\Delta t\left[8\alpha_{n+1} + +\rho_n c_{p_n}\dot{s}A_n\left(1-\frac{\alpha_{n+1}}{\alpha_{n-1}}\right)\right] \quad T_{n+1} \\
&\qquad +A_n\Delta t\left[4-\rho_n c_{p_n}\dot{s}\left(\frac{A_n}{\alpha_{n-1}}\right)\right](q_c^{'}+q_c) \qquad \text{(C.6)}
\end{aligned}$$

C.3 The last node

The last node does not conduct energy to an adjacent node. Hence the conduction term is replaced by a temperature-potential convective transfer communicating with a "reservoir" at temperature T_{res}:

$$\alpha_{n+1}(T_n - T_{n+1}) + \alpha_{n-1}(T_{n-1} - T_n) = h_{res}(T_n - T_{res})A_n$$

$$\alpha_{n+1}(T_n^{'} - T_{n+1}^{'}) + \alpha_{n-1}(T_{n-1}^{'} - T_n^{'}) = h_{res}(T_n^{'} - T_{res})A_n$$

Thus we have the energy difference equation for the last node as:

$$\begin{aligned}
\rho_n c_{p_n}\frac{T_n^{'}-T_n}{\Delta t} &= \frac{1}{\Delta x_n A_n}\left[2\alpha_{n-1}(T_{n-1}^{'} - T_n^{'} + T_{n-1} - T_n) - h_{res}A_n(T_n^{'} + T_n - 2T_{res})\right] \\
+ \quad \frac{\rho_n c_{p_n}\dot{s}}{4\Delta x_n}&\left[\left(1-\frac{\alpha_{n-1}}{\alpha_{n+1}}\right)(T_n^{'} - T_{n-1}^{'} + T_n - T_{n-1}) - \left(\frac{h_{res}A_n}{\alpha_{n+1}}\right)(T_n^{'} + T_n) + 2\frac{h_{res}}{\alpha_{n+1}}T_{res}A_n\right]
\end{aligned}$$

(C.7)

multiplying (C.7) through by $4\Delta x_n \Delta t A_n$ to eliminate the denominators, and collecting all the terms involving the unknowns $T_n^{'}$ on the left hand side results in:

$$
\begin{aligned}
-\Delta t \left[8\alpha_{n-1} - \rho_n c_{p_n} \dot{s} A_n \left(1 - \frac{\alpha_{n-1}}{\alpha_{n+1}} \right) \right] \quad T'_{n-1} \quad + \\
\left[4\rho_n c_{p_n} \Delta x_n A_n + 8\Delta t \alpha_{n-1} + 4\Delta t h_{res} A_n - \rho_n c_{p_n} \dot{s} \Delta t A_n \left(1 - \frac{h_{res} A_n}{\alpha_{n+1}} - \frac{\alpha_{n-1}}{\alpha_{n+1}} \right) \right] \quad T'_n \quad = \\
\Delta t \left[8\alpha_{n-1} - \rho_n c_{p_n} \dot{s} A_n \left(1 - \frac{\alpha_{n-1}}{\alpha_{n+1}} \right) \right] \quad T_{n-1} \quad + \\
\left[4\rho_n c_{p_n} \Delta x_n A_n - 8\Delta t \alpha_{n-1} - 4\Delta t h_{res} A_n + \rho_n c_{p_n} \dot{s} \Delta t A_n \left(1 - \frac{h_{res} A_n}{\alpha_{n+1}} - \frac{\alpha_{n-1}}{\alpha_{n+1}} \right) \right] \quad T_n \quad + \\
2A_n \Delta t h_{res} T_{res} \left[4 + \rho_n c_{p_n} \dot{s} \left(\frac{A_n}{\alpha_{n+1}} \right) \right]
\end{aligned}
\tag{C.8}
$$

C.4 Equations for coefficients in energy equation array

The coefficients A_n, B_n, C_n, and D_n in the array of Eq. (2.8) are determined by Equations (C.3), (C.6), and (C.8).

For nodes in the ablating material except the first and last, from Eq. (C.3):

$$
\begin{cases}
A_n &= -\Delta t (4\alpha_{n-1} - \rho_n c_{p_n} \dot{s} A_n) \\
B_n &= (4\rho_n c_{p_n} \Delta x_n A_n + 4\Delta t \alpha_{n+1} + 4\Delta t \alpha_{n-1}) \\
C_n &= -\Delta t (4\alpha_{n+1} + \rho_n c_{p_n} \dot{s} A_n) \\
D_n &= -A_n T_{n-1} + (4\rho_n c_{p_n} \Delta x_n A_n - 4\Delta t \alpha_{n+1} - 4\Delta t \alpha_{n-1}) T_n - C_n T_{n+1}
\end{cases}
\tag{C.9}
$$

For the surface node of the ablating material ($n = 1$), from Eq. (C.6):

$$\begin{cases} A_1 &= 0 \\ B_1 &= \left[4\rho_n c_{p_n}\Delta x_n A_n + 8\Delta t\alpha_{n+1} + \rho_n c_{p_n}\dot{s}\Delta t A_n\left(1-\frac{\alpha_{n+1}}{\alpha_{n-1}}\right)\right] \\ C_1 &= \Delta t\left[8\alpha_{n+1} + \rho_n c_{p_n}\dot{s}A_n\left(1-\frac{\alpha_{n+1}}{\alpha_{n-1}}\right)\right] \\ D_1 &= \left[4\rho_n c_{p_n}\Delta x_n A_n - 8\Delta t\alpha_{n+1} - \rho_n c_{p_n}\dot{s}\Delta t A_n\left(1-\frac{\alpha_{n+1}}{\alpha_{n-1}}\right)\right]T_1 \\ &- C_1 T_2 + A_n\Delta t\left[4-\rho_n c_{p_n}\dot{s}\left(\frac{A_n}{\alpha_{n-1}}\right)\right](q_c^{'}+q_c) = \mathcal{F}(q_{cond}^{'}) \end{cases} \tag{C.10}$$

For the last node ($n = N$), from Eq. (C.8):

$$\begin{cases} A_N &= -\Delta t\left[8\alpha_{n-1} - \rho_n c_{p_n}\dot{s}A_n\left(1-\frac{\alpha_{n-1}}{\alpha_{n+1}}\right)\right] \\ B_N &= \left[4\rho_n c_{p_n}\Delta x_n A_n + 8\Delta t\alpha_{n-1} + 4\Delta t h_{res}A_n - \rho_n c_{p_n}\dot{s}\Delta t A_n\left(1-\frac{h_{res}A_n}{\alpha_{n+1}}-\frac{\alpha_{n-1}}{\alpha_{n+1}}\right)\right] \\ C_N &= 0 \\ D_N &= -A_1 T_{N-1} \\ &+ \left[4\rho_n c_{p_n}\Delta x_n A_n - 8\Delta t\alpha_{n-1} - 4\Delta t h_{res}A_n + \rho_n c_{p_n}\dot{s}\Delta t A_n\left(1-\frac{h_{res}A_n}{\alpha_{n+1}}-\frac{\alpha_{n-1}}{\alpha_{n+1}}\right)\right]T_N \\ &+ 2A_n\Delta t h_{res}T_{res}\left[4+\rho_n c_{p_n}\dot{s}\left(\frac{A_n}{\alpha_{n+1}}\right)\right] \end{cases} \tag{C.11}$$

Note that if there are one or more non-ablating back-up materials (such as insulators or structural materials) the finite difference equations have the same form expressed in Eqs. (C.3), (C.6), and (C.8) without the convection term (that is $\dot{s} = 0$).

A particular treatment is adopted for the last ablating node since the rear boundary of this node is stationary with respect to a fixed coordinate system while the front boundary is stationary with respect to the moving coordinate system. Within this node, therefore, a variation occurs between the moving and fixed coordinate system. Since the last node is a shrinking node (this special treatment is adopted only for the last node) the $\dot{s}$ term for this node is taken as half its value.

Bibliography

[1] *User's Manual: Aerotherm Charring Material Thermal Response and Ablation Program*. Aerotherm Div., Acurex Corp., Mountain View, CA., 1987.

[2] J. D. Anderson. *Hypersonic and High Temperature Gas Dynamics*. AIAA, Reston, Virginia, 2000.

[3] Anon. *Mars Environmental Survey (MESUR) Science Objectives and Mission Description*. MESUR Study Office Rept., NASA Ames Research Center, 1991.

[4] D. R. Bartz. Heat transfer from rapidly accelerating flow of rocket combustion cases and from heated air. *Advances in Heat Transfer*, Vol. 2, J. P. Hartnett and T. F. Irvine Jr., eds. New York: Academic Press. 1965.

[5] B. A. Bhutta and C. H. Lewis. New technique for low-to-high altitude predictions of ablative hypersonic flowfields. *Journal of Spacecraft and Rockets*, 29(1), 1992.

[6] B. A. Bhutta and C. H. Lewis. Low-to-high altitude predictions of three-dimensional ablative hypersonic flowfields. *Journal of Spacecraft and Rockets*, 30(4), 1993.

[7] D. Bianchi, E. Martelli, F. Nasuti, and M. Onofri. Study of isothermal ablation. In Proc. 2nd European Conference for Aerospace Sciences, June 2007, Bruxelles.

[8] D. Bianchi, E. Martelli, and M. Onofri. Practical navier-stokes computation of flowfields with ablation products injection. In Proc. 5th European Workshop on Thermal Protection Systems and Hot Structures, May 2006, ESA SP-631. Noordwijk, The Netherlands, ESA-ESTEC.

[9] D. Bianchi, F. Nasuti, E. Martelli, and M. Onofri. A numerical approach for high-temperature flows over ablating surfaces. In Proc. 39th AIAA Thermophysics Conferece, June 2007, Miami, FL.

[10] B. F. Blackwell and R. E. Hogan. One-dimensional ablation using landau transformation and finite control volume procedure. *Journal of Thermophysics and Heat Transfer*, Vol. VIII, No. 2, 1994.

[11] V. Borie, J. Brulard, and G. Lengelle. Aerothermochemical analysis of carbon-carbon nozzle regression in solid-propellant rocket motors. *Journal of Propulsion*, 5(6), 1989.

[12] J. J. Brogan. A numerical method of solution for heat conduction in composite slabs with a receding surface. Lockheed Missiles and Space Division, Lockheed Aircraft Corp., LMSD 288204, Sunnyvale, CA, 1960.

[13] D. S. Butler. The numerical solution of hyperbolic systems of partial differential equation in three indipendent variables. *Proc. R. Soc.*, (255A):232–252, 1960.

[14] M. W. Chase, C. A. Davies, J. R. Downey, D. J. Frurip, R. A. McDonald, and A. N. Syverud. Jannaf thermodynamic tables (third ed., pts. i-ii). *Journal of Physical and Chemical Reference Data*, Vol. 14, Suppl. 1, Americal Chemical Society, Washington, DC., 1985.

[15] Y. K. Chen and W. D. Henline. Hypersonic nonequilibrium navier-stokes solutions over an ablating graphite nosetip. *Journal of Spacecraft and Rockets*, 31(5), 1994.

[16] Y. K. Chen, W. D. Henline, and M. E. Tauber. Mars pathfinder trajectory based heating and ablation calculations. *Journal of Spacecraft and Rockets*, 32(2), 1995.

[17] Y. K. Chen and F. S. Milos. Ablation and thermal response program for spacecraft heatshield analysis. *Journal of Spacecraft and Rockets*, 36(3), 1999.

[18] Y. K. Chen and F. S. Milos. Two-dimensional implicit thermal response and ablation program for charring materials. *Journal of Spacecraft and Rockets*, 38(4), 2001.

[19] Y. K. Chen and F. S. Milos. Navier-stokes solutions with finite rate ablation for planetary mission earth reentries. *Journal of Spacecraft and Rockets*, 42(6), 2005.

[20] Y. K. Chen and F. S. Milos. Multidimensional effects on heatshield thermal response for the orion crew module. 2007. 39th AIAA Thermophysics Conference, Miami, FL.

[21] Y. K. Chen, F. S. Milos, D. C. Reda, and D. A. Stewart. Graphite ablation and thermal response simulation under arc-jet flow conditions. 36th AIAA Thermophysics Conference, Orlando, FL, June 2003.

[22] J. D. Cox. *CODATA Key Values for Thermodynamics*. Hemisphere Publishing Corp., New York, 1989.

[23] B. S. DeHoff. An overview of carbon/carbon recession prediction technology. Presented at the JANNAF Carbon/Carbon Nozzle Technology Workshop II, Oct. 1980, Monterey, CA.

[24] L. J. Delaney, L. C. Eagleton, and W. H. Jones. A semiquantitative prediction of the erosion of graphite nozzle inserts. *AIAA Journal*, 2(8), 1964.

[25] B. Gabutti. On two upwind finite-difference scheme for hyperbolic equations in non-conservative form. *Computer and Fluids*, 11:207–230, 1983.

[26] R. L. Geisler. The prediction of graphite rocket nozzle recession rates. Presented at the JANNAF Propulsion Meeting, New Orleans, LA, May 1981. CPIA Publication 342.

[27] R. L. Geisler. The relationship between solid propellant formulation variables and nozzle recession rates. Presented at the JANNAF Rocket Nozzle Technology Subcommittee Workshops, July 12-13, 1978, Lancaster, CA.

[28] S. Gordon and B. J. McBride. Computer program for calculation of complex chemical equilibrium compositions and applications. NASA RP 1311, 1994.

[29] R. N. Gupta. Aerothermodynamic analysis of stardust sample return capsule with coupled radiation and ablation. *Journal of Spacecraft and Rockets*, 37(4), 2000.

[30] L. V. Gurvich, I. V. Veyts, and C. B. Alcock. *Thermodynamic Properties of individual Substances*. Vol.1, Pts. 1-2, Fourth ed., Hemisphere Publishing Corp., New York, 1989.

[31] M. A. Havstad and R. M. Ferencz. Comparison of surface chemical kinetic models for ablative reentry of graphite. *Journal of Thermophysics and Heat Transfer*, 16(4), 2002.

[32] W. M. Kays. *Convective Heat and Mass Transfer*. McGraw-Hill Book Co., New York, 1980.

[33] R. M. Kendall, E. P. Bartlett, R. A. Rindal, and C. B. Moyer. An analysis of the chemically reacting boundary layer and charring ablator. part i: Summary report. NASA CR 1060, 1968.

[34] R. M. Kendall and R. A. Rindal. An analysis of the chemically reacting boundary layer and charring ablator. part v: A general approach to the thermochemical solution of mixed equilibrium-nonequilibrium, homogeneous or heterogeneous systems. NASA CR 1064, 1968.

[35] R. M. Kendall, R. A. Rindal, and E. P. Bartlett. Thermochemical ablation. AIAA Paper 65–642, 1965.

[36] S. T. Keswani and K. K. Kuo. Validation of an aerothermochemical model for graphite nozzle recession and heat-transfer processes. *Combustion Science and Technology*, 42, 1986.

[37] K. Klager. The interaction of the efflux of solid propellants with nozzle materials. *Propellants and Explosives*, 2, 1977.

[38] D. W. Kuntz, B. Hassan, and D. L. Potter. Iterative approach for coupling fluid/thermal predictions of ablating hypersonic vehicles. AIAA Paper 99–3460, June 1999.

[39] D. W. Kuntz, B. Hassan, and D. L. Potter. Predictions of ablating hypersonic vehicles using an iterative coupled fluid/thermal approach. *Journal of Thermophysics and Heat Transfer*, 15(2), 2001.

[40] K. K. Kuo and S. T. Keswani. A comprehensive theoretical model for carbon-carbon composite recession. *Combustion Science and Technology*, 42, 1985.

[41] H. G. Landau. Heat conduction in a melting solid. *Quarterly of Applied Math*, 8(1), 1950.

[42] J. H. Lee. Basic governing equations for flight regimes of aeroassisted orbital transfer vehicles. *Progress in Astronautics and Aeronautics*, 96, 1985.

[43] L. Lees. Convective heat transfer with mass addition and chemical reactions. *Third AGARD Colloquium on Combustion and Propulsion*, Pergamon Press, New York, 1959.

[44] J. C. Lewis, I. J. Floyd, and F. C. Cowlard. A laboratory investigation of carbon-gas-reactions of relevance to rocket nozzle erosion. AGARD CP-52, Feb. 1959.

[45] J. H. Lundell and R. R. Dickey. Ablation of graphitic materials in the sublimation regime. *AIAA Journal*, 13(8), 1975.

[46] K. N. Marsh, A. Das, M. Frenkel, N. M. Gadalla, and R. C. Wilhoit. *TRC Thermodynamic Tables, Non-Hydrocarbons (Vols. I-VIII) and Hydrocarbons (Vols. I-XII)*. Thermodynamics Research Center, Texas A&M University, College Station, TX, 1988.

[47] E. Martelli. *Studio della Fluidodinamica Interna di Ugelli Propulsivi di Tipo Dual Bell*. 2005. PhD Thesis (in Italian), Dept. of Mechanics and Aeronautics, Univ. of Rome "La Sapienza", Rome, Italy.

[48] B. J. McBride, S. Gordon, and M. A. Reno. Thermodynamic data for fifty reference elements. NASA TP 3287, 1993.

[49] P. A. McCuen, J. W. Schaefer, R. E. Lundberg, and R. M. Kendall. A study of solid-propellant rocket motor exposed materials behavior. *Air Force Rocket Propulsion Lab, AFRPL-TR-65-33*, 1965.

[50] A. J. McDonald and P. O. Hedman. Erosion of graphite in solid-propellant combustion gases and effects on heat transfer. *AIAA Journal*, 3(7), 1965.

[51] F. S. Milos and D. J. Rasky. Review of numerical procedures for computational surface thermochemistry. *Journal of Thermophysics and Heat Transfer*, 8(1), 1994.

[52] G. Moretti. The λ-scheme. *Comput. Fluids*, 7:191–205, 1979.

[53] G. Moretti. Analisi matematica. Hoepli, Milano, 1981. II ed.

[54] G. Moretti. A technique for integrating two-dimensional euler equations. *Computer and Fluids*, 15(1):59–75, 1987.

[55] G. Moretti. Orthogonal grids around difficoult bodies. *AIAA Journal*, 30(4):933–938, 1992.

[56] G. Moretti, M. F., and M. Onofri. Shock boundary layer interactions computed by a shock fitting technique. In *Lecture Nn in Physics*, volume 414, pages 345–349. Springer-Verlag, Berlin, 1993.

[57] C. B. Moyer and R. A. Rindal. An analysis of the chemically reacting boundary layer and charring ablator. part ii: Finite difference solutions for the in-depth response of charring materials considering surface chemical and energy balances. NASA CR 1061, 1968.

[58] H. N. Najm, P. S. Wyckoff, and O. M. Knio. A semi-implicit numerical scheme for reacting flows. 1. stiff chemistry. *Journal of Computational Physics*, 143:381–402, 1998.

[59] F. Nasuti. *Analisi Numerica di Fenomeni di Separazione in Ugelli Propulsivi*. 1995. PhD Thesis (in Italian), Dept. of Mechanics and Aeronautics, Univ. of Rome "La Sapienza", Rome, Italy.

[60] F. Nasuti. *A Multi-Block Shock-Fitting Technique to Solve Steady and Unsteady Compressible flows*. Armfield S., Morgan P., Srinivas K., Springer-Verlag, Berlin, 2003.

[61] F. Nasuti and M. Onofri. Analysis of unsteady supersonic viscous flows by a shock fitting technique. *AIAA Journal*, 34(7), 1996.

[62] F. Nasuti, M. Onofri, and M. Valorani. Orthogonal grid generation for internal flows by conformal mapping. In *Numerical Methods in Laminar and Turbulent Flow*, volume VIII–1, pages 1359–1369. Pineridge Press, Swansea, UK, 1993.

[63] D. Olynick, Y. K. Chen, and M. E. Tauber. Aerothermodynamics of the stardust sample return capsule. *Journal of Spacecraft and Rockets*, 36(3), 1999.

[64] C. Park, J. T. Howe, and R. L. Jaffe. Review of chemical-kinetics problems of future nasa missions, ii: Mars entries. *Journal of Thermophysics and Heat Transfer*, 8(1), 1994.

[65] T. J. Poinsot and S. K. Lele. Boundary conditions for direct simulations of compressible viscous flows. *Journal of Computational Physics*, 101:104–129, 1992.

[66] V. Quan. Quasi-steady solution for ablation-erosion heat transfer. *Journal of Spacecraft and Rockets*, 7:355–357, 1970.

[67] P. J. Roache. Computational fluid dynamics. Hermosa Publishers, 1976. Albuquerque, NM, USA.

[68] P. R. Spalart and S. R. Allmaras. A one-equation turbulence model for aerodynamic flow. *La Recherche Aerospatiale*, 1:5–21, 1994.

[69] D. B. Spalding. *Convective Mass Transfer, an Introduction*. Edward Arnold, London, 1963.

[70] L. W. Swope and M. F. Berard. Effect of solid-rocket propellant formulations and exhaust-gas chemistries on the erosion of graphite nozzles. *AIAA Solid Propellant Rocket Conference*. Palo Alto, CA., Jan.1964.

[71] M. E. Tauber and G. P. Meneses. Aerothermodynamics of transatmospheric vehicles. AIAA Paper 86–1257, June 1986.

[72] P. Thakre and V. Yang. A comprehensive model to predict and mitigate the erosion of carbon-carbon/graphite rocket nozzles. 33rd AIAA/ASME/SAE/ASEE Joint Propulsion Conference and Exhibit, Cincinnati, OH, July 2007.

[73] K. W. Thompson. Time dependent boundary conditions for hyperbolic systems. *Journal of Computational Physics*, 68:1–24, 1987.

[74] H. Tong, G. J. Hartman, E. K. Chu, and A. J. Murphy. Afrpl graphite performance prediction program-improved capability for the design and ablation performance prediction of advanced air force solid propellant rocket nozzles. Air Force Rocket Propulsion Lab., Final Rept. AFRPL TR-76-70, Dec. 1976.

[75] S. V. Zhluktov and A. Takashi. Viscous shock-layer simulation of airflow past ablating blunt body with carbon surface. *Journal of Thermophysics and Heat Transfer*, 13(1), 1999.